A NUMERICAL STUDY OF ENTROPY GENERATION, HEAT AND MASS TRANSFER IN BOUNDARY LAYER FLOWS

A THESIS SUBMITTED TO THE UNIVERSITY OF KWAZULU-NATAL
FOR THE DEGREE OF DOCTOR OF PHILOSOPHY
IN THE COLLEGE OF AGRICULTURE, ENGINEERING & SCIENCE

By
Mohammed Hassan Mohammed Almakki
School of Mathematics, Statistics & Computer Science
November 2018

Contents

Abstract

This study lies at the interface between mathematical modelling of fluid flows and numerical methods for differential equations. It is an investigation, through modelling techniques, of entropy generation in Newtonian and non-Newtonian fluid flows with special focus on nanofluids. We seek to enhance our current understanding of entropy generation mechanisms in fluid flows by investigating the impact of a range of physical and chemical parameters on entropy generation in fluid flows under different geometrical settings and various boundary conditions. We therefore seek to analyse and quantify the contribution of each source of irreversibilities on the total entropy generation.

Nanofluids have gained increasing academic and practical importance with uses in many industrial and engineering applications. Entropy generation is also a key factor responsible for energy losses in thermal and engineering systems. Thus minimizing entropy generation is important in optimizing the thermodynamic performance of engineering systems.

The entropy generation is analysed through modelling the flow of the fluids of interest using systems of differential equations with high nonlinearity. These equations provide an accurate mathematical description of the fluid flows with various boundary conditions and in different geometries. Due to the complexity of the systems, closed form solutions are not available, and so recent spectral schemes are used to solve the equations. The methods of interest are the spectral relaxation method, spectral quasilinearization method, spectral local linearization method and the bivariate spectral quasilinearization method. In using these methods, we also check and confirm various aspects such as the accuracy, convergence, computational burden and the ease of deployment of the method. The numerical solutions provide useful insights about the physical and chemical characteristics of nanofluids. Additionally, the numerical solutions give insights into the sources of

irreversibilities that increases entropy generation and the disorder of the systems leading to energy loss and thermodynamic imperfection. In Chapters 2 and 3 we investigate entropy generation in unsteady fluid flows described by partial differential equations. The partial differential equations are reduced to ordinary differential equations and solved numerically using the spectral quasilinearization method and the bivariate spectral quasilinearization method. In the subsequent chapters we study entropy generation in steady fluid flows that are described using ordinary differential equations. The differential equations are solved numerically using the spectral quasilinearization and the spectral local linearization methods.

Declaration

The work presented in this dissertation is my original work under the supervision of Prof. P. Sibanda in the School of Mathematics, Statistics, & Computer Science, University of KwaZulu-Natal, Pietermaritzburg campus, from March 2016 to November 2018.

No portion of this work has been submitted in any form to any university or institution of learning for any degree or qualification. Where use has been made of the work of others it is duly acknowledged.

Signature:..... .....

Mohammed H. M. Alamkki Date

Signature:..... .....

Prof. P. Sibanda Date

This thesis is dedicated to my wife Rihab Abdelrahman.

Acknowledgments

I give deep and huge glory to God, He made my dream to study for a PhD degree come to pass.

I would like to express my deepest gratitude to my supervisor Precious Sibanda, for his incredible support, continuous encouragement, and patience throughout my PhD journey. He provided me with an excellent atmosphere for doing research. His valuable comments substantially contributed to my academic growth in all aspects, including writing skills and future career plans. I have learned so much from him and I truly cannot thank him enough.

Grateful thanks go to Prof. S.S Motsa for his insightful comments, invaluable help, and guidance on spectral methods and computation.

I am grateful to my mentor Dr. Sabyasachi Mondal for his great assistance and support, particularly in the early stages of my PhD, which helped me to understand the difficult concepts in fluid dynamics.

I am grateful to Dr. Hiranmoy Mondal for his wonderful assistance, interesting discussions and comments during the second project of my PhD.

My sincere thanks to my best friend Ahamed Hassan for his lovely character that made the office an enjoyable atmosphere; hence assisting in overcoming the stress of PhD research life. I would like to thank the administrative and academic staff in the School of Mathematics, Statistics, & Computer Science, University of KwaZulu-Natal, Pietermaritzburg Campus.

I am grateful to the Center of Excellence–Mathematical and Statistical Sciences (CoE-MaSS) for their generous financial support.

I humbly thank my parents for their love and support. I also thank my sisters and brothers for

giving me endless amounts of pleasure, enjoyment and encouragement.

Finally, I would like to say a special thank you to my soulmate, partner and wife Rihab Abdelrahman who always provides me with unconditional love and endless support. Her caring and encouragement are the reasons for every single success.

List of Publications

M. Almakki, S. Dey, S. Mondal and P. Sibanda. On Unsteady Three-Dimensional Axisymmetric MHD Nanofluid Flow with Entropy Generation and Thermo-Diffusion Effects on a Non-Linear Stretching Sheet. *Entropy*, vol. 19, no. 7, p. 168, 2017.

I provided the numerical solution of the flow equations using the spectral quasilinearization method, analysed the results and drafted the paper.

M. Almakki, S. K. Nandy, S. Mondal, P. Sibanda, and D. Sibanda. A model for entropy generation in stagnationpoint flow of non-Newtonian Jeffrey, Maxwell, and Oldroyd-B nanofluids. *Heat Transfer-Asian Research*, 48:24-41; 2019.

I modified an existing fluid model and solved the equations, interpreted the results and drafted the paper.

M. Almakki, H. Mondal, P. Sibanda, and N. Haroun. Entropy generation in MHD flow of viscoelastic nanofluids with homogeneous-heterogeneous reaction, partial slip and nonlinear thermal radiation. *Journal of Thermal Engineering*, accepted February-2018.

I developed the model, used the spectral quasilinearization method to solve the system of equations and drafted the paper.

Signature: ....

Mohammed. H. M. Almakki Date

Chapter 1

Introduction

Over the last few decades, there has been a growing interest and need to study the flow characteristics and behaviour of non-Newtonian nanofluids. These fluids play a key role in many industrial, biomedical and transportation applications [1]. Despite having a broad range of applications, the physics of non-Newtonian nanofluids is not as well understood as that of Newtonian flows, because it is considerably more complex. To elaborate, neither the Navier-Stokes equation nor any single constitutive relationship provides an adequate comprehensive description of nanofluids [2]. In this study, we investigate theoretically the flow of a number of non-Newtonian nanofluids; namely viscoelastic nanofluid, Casson nanofluid, Jeffery nanofluids, Maxwell nanofluids, Oldroyd-B nanofluids and micropolar nanofluids. The viscoelastic nanofluid has an elastic-like behaviour with a certain yield stress indicating that it behaves as a solid when the applied shear stress is less than the yield stress and behaves as a liquid when the applied shear stress is higher than the yield stress.

The primary concern in this study is the mathematical modelling and study of entropy generation in the chosen non-Newtonian nanofluids under various conditions and in different geometries. Entropy generation affects the thermal performance of thermodynamic systems such as found in refrigeration, thermal power conversion, and heat transfer and storage [3]. In this regard, minimizing entropy generation is a desirable outcome because high entropy is an intrinsic cause of thermal performance degradation. Thus, the analysis of entropy generation is undertaken in an attempt to optimize the thermodynamic performance of engineering systems and devices [4]. This optimization is typically realized by achieving a dynamic balance or trade–off among different competing

irreversibilities in the thermodynamic system [3].

In the literature, there are numerous studies of entropy generation, heat and mass transfer in Newtonian fluids, including [5–8]. These studies have investigated the impact of entropy generation, heat and mass transfer in Newtonian fluids in different geometries and with various boundary conditions using different fluid models and solution methods to solve the underlying equations. Recently, there have been rapid developments in the study of entropy generation in non-Newtonian fluids using the second law of thermodynamics, which captures many mechanisms that account for irreversibility in thermodynamic systems. In particular we note [2], who investigated entropy generation, heat and mass transfer in a Jeffrey nanofluid over a linearly stretching sheet, using the Keller-box method was used to solve the system of equations. Magnetohydrodynamic (MHD) flow over a stretching sheet was studied by Butta et al. [9], who analysed the effect of entropy generation in viscoelasticity MHD flow over a stretching plate immersed in a permeable medium. Abolbashari et al. [10] investigated entropy generation in a Casson nanofluid flow induced by a stretching surface. Qing et al. [11] also studied entropy generation in a Casson nanofluid, but theirs was subject to chemical reaction and nonlinear thermal radiation.

The aim of this study is to investigate entropy generation in both Newtonian and non-Newtonian nanofluids for different geometrical settings and subject to various boundary conditions. The chemical and physical behaviours of the nanofluids are examined by carefully analysing the influence and impact of various physical and chemical parameters. Due to the high complexity of the fluid models presented in this study, recent, robust and rapidly converging methods are used to provide reliable approximate solutions. In particular, the systems of highly nonlinear, coupled, differential equations describing the nanofluid flows are solved numerically using linearization and spectral methods.

1.1 Heat and mass transfer

The heat and mass transfer in various fluid flows is investigated in this thesis. A crucial aspect of modern engineering designs is considering heat transfer. In power production and chemical processing, size of equipment is determined primarily by the heat-transfer rates that can be attainable. For instance, the design and operation of devices such as air-conditioners and refrigeration systems must take into account efficiencies in the heat exchanges. In many types of equipment a successful design makes provision for maintaining reasonable temperatures through adequate transfer of heat away from the heat source to the ambient fluid. Sophisticated modems devices which depend on adequate heat transfer include large equipment such as high-speed aircraft, and atmosphere reentry vehicles, as well as compact electronic components and rocket nozzles. The study of heat transfer entails understanding the physical processes whereby thermal energy is transferred as a result of a temperature gradient. There are three different processes by which energy is transported; conduction, convection and radiation.

Conduction is the mechanism of heat transfer that takes place between particles immediately adjacent to one another or through molecular action, supplemented by free flow of electrons from a high temperature region to a low temperature region [12]. The rate of heat transfer via conduction is a function of the temperature difference, the material involved and its thickness [12]. Throughout a layer, the rate of heat conduction is proportionally related to the heat transfer area and the temperature differences, and is inversely related to the thickness of the layer. In mathematical notation this is stated as

$$Q_{\text{cond}} = -kA\frac{dT}{dy}. \tag{1.1}$$

Equation (1.1) represents Fourier's law of heat conduction, where k and A are the thermal conductivity of the material and heat transfer area, respectively, and dT/dy represents the temperature gradient in the $y-$direction. Equation (1.1) appears in the energy equations that are used in this study.

In convection, the thermal energy transport is influenced by the relative motions within the fluid,

so the resultant heat transfer occurs between the layers of a fluid [12]. The rate of heat transfer via convention is proportionally related to the temperature difference, which is expressed by Newton's law of cooling,

$$\dot{Q_{\text{conv}}} = h_{\text{conv}} A_s \Big(T_s - T_\infty \Big), \tag{1.2}$$

where h_{conv} and A_s are the heat transfer coefficient and surface area, respectively, and $T_s - T_\infty$ represents the temperature difference across the layer. Equation (1.2) appears in the energy and the mass transport equations shown in this thesis.

Solid bodies as well as liquids and gases emit thermal energy in the form of electromagnetic waves and absorb similar energy from neighboring bodies [12]. This type of heat transfer is known as thermal radiation. It is explained further in Section 1.3.

Many fluid flows involve mass transfer. The transport of one constituent chemical species from a region of higher concentration to that of a lower concentration constitutes mass transfer [13]. As an everyday example, a lump of sugar added to a cup of black coffee eventually dissolves and then the sugar molecules diffuse uniformly throughout the coffee. Mass transfer has a central role in almost all industrial processes [13]. Typical examples include the removal of pollutants from plant discharge streams by absorption, the stripping of gases from waste water, or neutron diffusion within nuclear reactors. When a system contains two or more components whose concentrations vary from point to point, there is a natural tendency for mass to be transferred, so as to minimize concentration differences within the system [12]. Mass transfer occurs both through the bulk fluid motion (mass convection) and through diffusion [12].

The rate of mass diffusion of species b is proportionally related to the concentration gradient in the specific direction [12].

$$m_{diff} = -D_{ab} b \frac{dC_b}{dy}, \tag{1.3}$$

where D_{ab} and C_b are the mass diffusion coefficient and mass concentration of species b, respec-

tively. Further, dC_b/dy is the concentration gradient in the $y-$direction. Equation (1.3) is called Fick's law. Equation (1.3) appears in the energy and the mass transport equations.

The rate of mass convection is obtained as

$$m_{\text{conv}} = h_{mass} B_s \Big(Cs - C_\infty \Big), \tag{1.4}$$

where A_s and h_{mass} are the surface area and mass transfer coefficients, respectively, and $C_s - C_\infty$ is concentration difference. Equation (1.4) is a component of the energy and the mass transport equations. Heat and mass transfer share many similarities; thus, for a particular geometry, they are expressed in a similar mathematical form [14].

1.2 Nanofluids

This study pays special attention to nanofluid flows over various surfaces. A nonfluid contains solid nanometer–sized particles [15]. The study of nanofluids has attracted considerable interest due to their novel properties, which make them potentially useful in a number of industrial applications including power generation, micromanufacturing, ventilation and air-conditioning, as well as medical applications in cancer treatment [16]. Yu and Xie [17] reported significant progress in methods of preparation and evaluation of the stability of nanofluids. In addition, they reported a wide variety of present and possible future applications of nanofluids. Some applications of nanofluids in transportation, residential and commercial sectors were investigated by Ghadimi et al. [18]. The behaviour and rheological characteristics of nanofluids is important in determining their suitability for various industrial applications. One characteristic is that the suspension of nanoparticles in base fluids, such as oil, water or ethylene, gives rise to higher convective heat transfer and thermal conductivity coefficients than for the base fluids alone,. The convective heat transfer enhancement can be attributed, in part, to the Brownian motion of nanoparticles. Buongiorno [15] proposed a model to investigate the effect of Brownian diffusion, fluid drainage, thermophoresis, inertia, Magnus effect and gravity on the thermal conductivity and viscosity of a nanofluid flow without turbulence. That study showed that Brownian motion and thermophoresis are the most significant mechanisms

that improve the thermophysical properties of the fluid. Kuznetsov and Nield [19] extended the Pohlhausen-Kuiken-Bejan problem using the Buongiorno model [15]. They presented an analytic solution for a model of the convective flow of a nanofluid over a vertical plate, in which they had incorporated particle Brownian motion and thermophoresis. The results showed that the solution depended on Brownian motion, the Prandtl number and thermophoresis. An unsteady flow over a shrinking sheet with wall suction was studied by Rohni et al. [20]. The study used a water based nanofluid with different types of nanoparticles. They found that the wall mass has significant impact on the fluid flow and heat transfer. Gireesha and Rudraswamy [21] presented an analysis of heat transfer near the stagnation point of an MHD fluid flow over a porous stretching sheet. The flow was subject to particle Brownian motion, a non-uniform source/sink and thermophoresis, and the effects of a chemical reaction was also taken into account. They concluded that a chemical reaction has substantial impact on the fluid flow.

The convective boundary condition is derived from the Fourier law of heat conduction applied to a solid boundary, together with Newton's law of cooling. Heat transfer associated with convective boundary conditions is important in thermal energy storage, the transpiration cooling process, material drying, gas turbines, etc. Heat transfer in magnetohydrodynamic (MHD) nanofluid flow past a linear stretching sheet with thermal radiation was considered by Makinde and Aziz [22]. Their analysis showed that the Prandtl number, Brownian motion, magnetic field, thermophoresis and the thermal radiation parameters have a significant effect on the transport of heat and solutes in boundary layers. The convective flow of a nanofluid was investigated by, among others, [23–25]. In some earlier studies, for instance, [26–28], it was assumed that the nanoparticle distribution was uniform across the nanofluid. In reality, however, there are slip velocities between the nanoparticles and the fluid molecules owing to, among other factors, particle Brownian motion, thermophoresis, and migration of nanoparticles from hotter to colder regions. Noghrehabadi et al. [29] considered the influence of the slip velocity on heat and mass transfer in a nanofluid flow over a continuously stretching sheet. They found that the slip velocity and theromphoresis have a positive contribution to the Nusselt number. A model of heat transfer and boundary layer flow of an MHD nanofluid flow over a porous stretching surface was given by Ibrahim and Shankar [30], who used it to investigate

thermal radiation and the slip condition.

The focus of most earlier studies concerned idealized nanofluids, with constant properties. However, recently there has been a growing trend to study nanofluids with variable properties that depend on the temperature and the nanoparticle volume fraction. Noghrehabadi and Behseresht [31] studied the influence of nanoparticle concentration on the mixed convective nanofluid flow over a vertical cone in a permeable medium. The model considered nanoparticle slip, thermophoresis and Brownian motion. The thermal conductivity and the viscosity of a nanofluid are a function of the volume fraction of nanoparticles. The results showed that the heat transfer coefficient increased with the viscosity parameter, while the opposite behaviour was noted with changes in thermal conductivity. Recently, three-dimensional steady flow near the stagnation point of a bionanofluid flow with thermal convective and zero nanoparticle flux was studied by Amirsom et al. [32].

1.3 Thermal radiation

Thermal radiation is central to investigating the behaviour of fluid flow as it is a key mechanism for heat transfer [33]. Thermal radiation is a type of electromagnetic radiation emitted by all bodies that is generated when the body's internal energy is converted to electromagnetic radiation by the movement of electrons and protons in the material [33]. Solar thermal radiation heats Earth through absorption and the excitation of thermal energy in electrons and atomic nuclei [33]. The thermal radiation emitted from Earth has a lower intensity than that emitted by the sun. The balance between heating by incoming solar radiation and cooling by Earth's outgoing radiation is the primary process that determines Earth's overall temperature [33]. Thermal radiation increases in power, and frequency, with increasing temperature [33].

Thermal radiation has been conisdered in previous studies. Abbasi et al. [34] considered the flow and behaviour of an MHD Jeffrey nanofluid along a linear stretching sheet subject to thermal radiation for prescribed heat and nanoparticle concentration flux conditions. The effects of thermal radiation in MHD nanofluid flow across two horizontal rotating plates was studied by

Sheikholeslami et al. [35].

Thermal radiation is often approximated using the Rosseland approximation [36], with the heat flux q_r given by

$$q_r = -\frac{\partial T^4}{\partial y}\left(\frac{4\sigma^*}{3k^*}\right), \tag{1.5}$$

where k^* and σ^* are the Rosseland mean spectral absorption coefficient and the Stefan–Boltzmann constant, respectively. If the temperature differences are small, T^4 can be expanded using the the Taylor series about T_∞, to obtain

$$T^4 \approx -3T_\infty^4 + 4T_\infty^3. \tag{1.6}$$

In this way, the relative heat flux can be written as

$$q_r = -\frac{\partial T}{\partial y}\left(\frac{16\sigma^* T_\infty^3}{3k^*}\right). \tag{1.7}$$

Equation (1.7) is an integral part of the energy equation used in Chapters 2 to 6.

1.4 Entropy generation

The investigation of entropy generation in fluid flows is an integral part of this thesis. The performance of engineering and thermal devices is affected by irreversible processes that lead to increase in system entropy and a reduction in thermal efficiency [37]. For this reason it is important to determine the conditions that minimize entropy generation and maximize the system efficiency. The first and the second laws of thermodynamics can be used to analyse the irreversibilities in the form of entropy generation. However, calculations based on the second laws are more useful since the thermal efficiency is expressed as a ratio of the actual thermal efficiency [37]. Some factors that are responsible for irreversibilities include heat transfer, mass diffusion and viscous dissipation. Most energy-critical applications such as cooling systems, solar power collectors and geothermal energy systems depend on entropy generation. The study of fluids is important for understanding the flow processes that optimize entropy generation and the quality of energy to be preserved in

any process. Studies on entropy generation in stretching sheets with thermal radiation and viscous dissipation were reported recently by Rashidi et al. [38], who investigated the entropy generation on MHD blood flow caused by peristaltic waves. They used an analytic method with a perturbation technique to solve the system of flow equations. Entropy generation in a non-Newtonian Carreau nanofluid flow over a shrinking sheet with thermal radiation was studied by Bhatti et al. [39]. The successive linearization method with Chebyshev spectral collocation method was used to solve the system of equations. The study gave an indication of the effect of thermal radiation and the Prandtl number on temperature profiles. Magherbi et al. [40] studied entropy generation and its minimization in double diffusive convective two-dimensional fluid flow. Their study determined the total irreversibility in mixed convective flow. Entropy generation and the impact of the Bejan number on double diffusive unsteady MHD fluid flow past a vertical plate immersed in a permeable medium was sutdied by Butt and Ali [41]. The exact solutions were obtained using the Laplace transformation technique. The thermal radiation was taken into account. Other related studies, include [10, 11, 42, 43].

1.5 Unsteady flows

In Chapters 2 and 3 we are concerned with the solution of equations for unsteady fluid flows. Unsteady flow is flow in which the fluid properties may vary with both time and space. It is necessary to consider unsteady flows when assessing the impact of a flood wave moving down a river or when assessing surges and bores. Examples of unsteady flows include translatory waves that cause water particles to move in the direction of the flow [44]. Translatory waves are often encountered in streams and open channels. Oscillatory waves are another type wave, in which water particles oscillate but do not display appreciable movement in the direction of the wave. When the velocity of flow changes suddenly and impulsively, it can take some time for the flow to become fully steady [45]. This leads to oscillatory waves.

Obtaining solutions for unsteady flow is, unfortunately, a mathematically challenging task, consequently, many prior studies have been limited in scope to steady self-similar flows [46]. Lok et al.

[47] presented an analysis of heat transfer near the stagnation point on a double-infinite vertical plate flow of a micropolar fluid. They assumed that the unsteadiness due to the impulsive motion of the fluid from the sheet either increased or reduced the sheet temperature far from the sheet. The system of equations was solved numerically using th Keller-box method. An incompressible, unsteady three-dimensional and mixed convection stagnation point flow in porous body was investigated by Chamkha amd Ahamed [48]. The flow was subject to heat generation/absorption and a magnetic field, while a chemical reaction was assumed to be significant. Three characteristics were considered, which were decelerating flow, the steady-state case and accelerating flow. The system of equations was solved numerically using the tri-diagonal implicit finite differences method. An unsteady mixed convection flow and heat transfer in a viscous fluid flow near the stagnation point of a heated vertical body immersed in a permeable medium was investigated by Seshadri et al. [49], who used a finite difference scheme to solve the system of the equations. Alharbi and Hassanien [45] investigated two-dimensional unsteady laminar boundary-layer stagnation point with heat transfer along a horizontal plate placed in a permeable medium. The flow was subject to buoyancy forces and viscous dissipation. The system was solved numerically using the finite difference scheme. The effect of heat absorption or generation and a first order chemical reaction on unsteady MHD flow over a vertical cone was studied by Ravindran et al. [50]. The quasilinearization method with an implicit finite difference scheme was used to solve the system of equations.

1.6 Methods of solution

The heat and mass transfer in boundary layer flow through an unsteady or steady stretching sheet is modelled using systems of nonlinear equations. Solving the systems is challenging because they are generally highly coupled, nonlinear equations. This in general, precludes the existence of closed-form solutions. In recent years, various numerical methods have been used to solve systems of coupled, nonlinear equations. These include some analytic and non-perturbation techniques such as Adomian's decomposition method and Lyapunov's artificial small parameter method. However, if the system is highly nonlinear, these methods may not work or may be inefficient

[51]. In addition, some of the methods have small convergence regions and rely on the existence of a small or large embedded parameter [51]. The Adomian decomposition and the homotopy analysis method are useful for nonlinear problems [52–55]. They can be used to solve both ordinary and partial differential equations that do not contain very large or very small parameters. Nonetheless, analytical approaches have limitations when used to solve nonlinear systems.

In the literature, there are popular numerical methods such as the Runge-Kutta schemes [56], element free Galerkin method [57], finite elements method [58], the Keller-box method [59] and finite differences method [60], which have been used to find approximate solutions of highly nonlinear coupled systems. These methods have some disadvantages, such as requiring many grid points for approximating the solutions accurately, being computationally expensive and possibly not being very effective in scenarios involving discontinuities, singularities and problems with multiple solutions [61].

In this study, Chebyshev pseudospectral methods are used to solve nonlinear boundary layer flow problems modelled by systems of ordinary and partial differential equations. Motsa et al. [62] proposed the spectral relaxation and the spectral quasilinearization methods to find solutions for unsteady boundary layer flow problems. The linearization method was used successfully for boundary layer flow problems described by nonlinear ordinary differential equations [63]. These methods generally give better accuracy compared to those from finite element and finite differences methods. Parabolic equations have been solved using the bivariate spectral quasilinearization method, Motsa et al. [64]. The system of nonlinear equations was solved using Lagrange interpolation polynomials as basis functions. Motsa and Shateyi [65] used the successive linearization method for the equations describing an unsteady boundary layer flow. To obtain accurate solutions using the spectral relaxation method technique, the original nonlinear equations were linearized and the successive linearization method with the Chebyshev pseudospectral method applied iteratively. This method has proved to be effective for the boundary layer problems, by Shateyi and Motsa [66].

1.6.1 The spectral relaxation method

The spectral relaxation method is an iterative scheme for solving a system of nonlinear differential equations. This method was introduced by Motsa [67] to solve nonlinear boundary value problems and has been used successfully to solve chaotic and hyperchaotic systems [68, 69]. To use the method a simple rearrangement of the equations may be necessary. An approach, similar to the Gauss-Seidel scheme is used to decouple the equations, which are then integrated by using the Chebyshev pseudo-spectral collocation method [70–72]. These studies suggested that this method is convergent, numerically stable, reliable, and useful for nonlinear boundary layer flow problems. The numerical scheme for the spectral relaxation method for the conservation equations of a fluid is described in brief below.

Assume that the momentum is F, the temperature is T and the concentration is C and $\eta \in [a,b]$, where η is an independent variable. In general, the system of equations may be written as

$$\Upsilon_i = \Big[F,T,C\Big] = 0, \quad \text{for} \quad i = \Big(f,\theta,\phi\Big) \tag{1.8}$$

where $\Upsilon_f, \Upsilon_\theta, \Upsilon_\phi$ are nonlinear operators in the momentum, temperature and the concentration equations, respectively, where F,T and C are expressed as

$$F = \left\{f, \frac{\partial f}{\partial \eta}, \frac{\partial^2 f}{\partial \eta^2}, \ldots \frac{\partial^p f}{\partial \eta^p}\right\},\ T = \left\{\theta, \frac{\partial \theta}{\partial \eta}, \frac{\partial^2 \theta}{\partial \eta^2}, \ldots \frac{\partial^p \theta}{\partial \eta^p}\right\},\ P = \left\{\phi, \frac{\partial \phi}{\partial \eta}, \frac{\partial^2 \phi}{\partial \eta^2}, \ldots \frac{\partial^p \phi}{\partial \eta^p}\right\}, \tag{1.9}$$

where p is pth derivative. Now the system of equations can be written as a combination of linear and nonlinear terms as

$$L_i[F,T,C] + N_i[F,T,C] = H_i(\eta) \tag{1.10}$$

where L and N are linear and nonlinear components, respectively, and $H_i(\eta)$ represents an unknown function of η.

For illustrative purposes, assume that the system is restricted to two-point boundary conditions,

such as

$$\sum_{p=0}^{n_i-1}\sum_{j=1}^{m}\beta_{\nu,j}^{p}\Upsilon_i^p(a)=K_{a,\nu},\quad \nu=1,2,...,m_a,$$
$$\sum_{p=0}^{n_i-1}\sum_{j=1}^{m}\gamma_{\sigma,j}^{p}\Upsilon_i^p(b)=K_{b,\sigma},\quad \sigma=1,2,...,m_b, \tag{1.11}$$

where $\beta_{\nu,j}^{p}$ and $\gamma_{\sigma,j}^{p}$ represent the constant coefficients of Υ_i^p at the boundary conditions, p is pth derivative and m_a and m_b represent the total number of specified boundary conditions in $[a,b]$, respectively. Starting from initial approximations we obtain the iterative schemes:

$$\begin{aligned}
&L_f\Big[F_{r+1},T_r,C_r\Big]+F_{r+1}N_f\Big[F_r,T_r,C_r\Big]=H_f-N_f\Big[F_r,T_r,C_r\Big],\\
&L_\theta\Big[F_{r+1},T_{r+1},C_r\Big]+\theta_{r+1}N_\theta\Big[F_{r+1},T_r,C_r\Big]=H_\theta-N_\theta\Big[F_{r+1},T_r,C_r\Big],\\
&L_\phi\Big[F_{r+1},T_{r+1},C_{r+1}\Big]+\phi_{r+1}N_\phi\Big[F_{r+1},T_{r+1},C_r\Big]=H_\phi-N_\phi\Big[F_{r+1},T_{r+1},C_r\Big],
\end{aligned} \tag{1.12}$$

where r is the previous iteration and $r+1$ is the current iteration. Equation (1.12) is analogous to the Gauss-Siedel relaxation method, which also updates solutions in the subsequent equation. These equations are integrated by using the spectral collocation method. We use the Gauss-Lobatto points

$$\xi_i=\cos\Big(\frac{\pi i}{N}\Big),\quad i=1,2,...,N,-1\le\xi\le 1, \tag{1.13}$$

where N is the number of collocation points. The systems of equations is considered in the domain $[0,L]$ instead of $[0,\infty)$; where L is the boundary condition at infinity and L should be a large number. Therefore, $[0,L]$ is transformed to $[-1,1]$ using the linear formula $\eta=\frac{L(x+1)}{2}$. The differentiation matrix $\mathbf{D}$ is used to estimate the derivatives of the unknown functions, which are given by

$$\frac{d\Upsilon_i}{d\eta}=\sum_{k=0}^{N}\mathbf{D}_{sk}\Upsilon_i\xi_k=\mathbf{D}\Upsilon_i,\quad s=1,2,3,...,N, \tag{1.14}$$

where $\mathbf{D}=2D/(b-a)$ and $\Upsilon=\Big[\Upsilon(\xi_0),\Upsilon(\xi_1),\Upsilon(\xi_2),...,\Upsilon(\xi_N)\Big]^T$ represents the vector function at the collocation points. The higher derivatives are defined as powers of $\mathbf{D}$, thence

$$\frac{d^p\Upsilon_i}{d\eta^p}=\mathbf{D}^p\Upsilon_i. \tag{1.15}$$

Now equation (1.10) can be expressed as

$$\sum_{p=0}^{n_i} \alpha_i^p \Upsilon_i^p + N_i\Big[F,T,C\Big] = H_i, \tag{1.16}$$

where α_i^p are the coefficients of Υ_i^p which appears in f, θ and ϕ equations. Using equation (1.16), the iteration schemes in equation (1.12) can be written as

$$\sum_{p=0}^{n_i} \alpha_i^p \Upsilon_{i,r+1} + \Upsilon_{i,r+1} N_i\Big[F_{r+1},T_{r+1},C_r\Big] = H_i - \sum_{p=0}^{n_i} \alpha_i^p \Upsilon_{i,r} - N_i\Big[F_{r+1},T_{r+1},C_r\Big]. \tag{1.17}$$

Applying equation (1.13) on equation (1.17) which will satisfy the boundary conditions. Thus the spectral relaxation iteration schemes may now be defined as

$$\sum_{p=0}^{n_i} \alpha_i^p \mathbf{D}^p \Upsilon_{i,r+1} + \Upsilon_{i,r+1} N_i\Big[\mathbf{F}_{r+1},\mathbf{T}_{r+1},\mathbf{C}_r\Big] =$$
$$\mathbf{H}_i - \sum_{p=0}^{n_i} \alpha_i^p \mathbf{D}^p \Upsilon_{i,r} - N_i\Big[\mathbf{F}_{r+1},\mathbf{T}_{r+1},\mathbf{C}_r\Big]. \tag{1.18}$$

The boundary conditions now become

$$\sum_{p=0}^{n_i-1} \beta_{\nu,i}^p \sum_{k=0}^{N} \mathbf{D}_{N_k}^p \Upsilon_{i,r+1}(\xi_k) = K_{a,\nu}, \quad \nu = 1,2,3,\ldots,m_a,$$
$$\sum_{p=0}^{n_i-1} \gamma_{\sigma,i}^p \sum_{k=0}^{N} \mathbf{D}_{N_k}^p \Upsilon_{i,r+1}(\xi_k) = K_{b,\sigma}, \quad \sigma = 1,2,3,\ldots,m_b. \tag{1.19}$$

For more details regarding the spectral relaxation method for a system contain m equations see [67, 69].

1.6.2 The spectral and bivariate quasilinearization methods

The spectral quasilinearization method is a generalisation of the Newton-Raphson quasilinearization method developed by Bellman and Kalaba [73] to solve a nonlinear system of partial differential equations. In spectral quasilinearization method, the system of equations is linearized using the Taylor series by assuming that the difference between the current and the previous iteration is small. Then, the Chebyshev spectral collocation method is used to integrate the linear equations. This method has been used successfully to solve numerous fluid problems [63, 74]. It gives

accurate results with rapid convergence, according to Motsa et al. [62]. However, the spectral quasilinearization method is limited in the sense that it cannot be used for systems involving space and time, besides it requires high number of grid points.

The bivariate spectral quasilinearization method is proposed by Motsa et al. [64] to extend the spectral quasiliearization method by considering the space and time. The collocation is applied to the space variable while the finite difference is applied to discretize the time variable. The bivariate spectral quasilinearization method requires fewer grid points without compromising the accuracy and convergence [71, 75]. This method has been used successfully to solve nonlinear evolution partial differential equations Motsa et al. [64]. Motsa and Ansari [76] used the bivariate quasilinearization method to solve the equations for the flow of a non-Newtonian power-law nanofluid past a linearly stretching sheet. Makanda et al. [77] investigated the effect of viscous dissipation and radiation in magnetohydrodynamic (MHD) flow of a Casson fluid with partial slip past a porous medium stretching sheet. The boundary layer problem was solved using the bivariate spectral quasilinearization method. In Chapter 3, the bivariate spectral quasilinearization method is used to solve a problem in which the unsteadiness results from a time dependent free stream velocity.

1.7 Thesis objectives

The primary objective of this study is to investigate entropy generation in Newtonian and non-Newtonian nanofluid flows in different geometries and subject to various boundary conditions. Due to the high complexity of the mathematical models involved, recently developed robust and fast-converging methods are used to provide reliable approximate solutions. Systems of highly nonlinear, coupled differential equations describing the flows are solved numerically using spectral methods.

The aim of the thesis is to present mathematical models for both steady and unsteady MHD incompressible nanofluid flow over both linear and nonlinear stretching surfaces. We further present a generalized mathematical model that captures the flow characteristics of three important non-

Newtonian nanofluids, namely the Jeffrey, Maxwell and Oldroyd-B nanofluids.

A secondary objective is to verify the reliability of the spectral relaxation method, the spectral local linearization method, spectral quasilinearization method and the bivariate spectral quasilinearization method in terms of accuracy, convergence, computational time, together with their performance in response to changing parameters.

In the thesis we seek to study the impact of key physical parameters including Brownian motion, thermal radiation, and thermophoresis parameters and the Reynold and Brinkman numbers on the velocity, temperature, concentration profiles and entropy generation.

1.8 Thesis structure

The first part of the remainder of this thesis, comprising Chapters 2 and 3, is concerned with the solution of coupled nonlinear partial differential equations that describe unsteady boundary layer flow. In the next part, Chapters 4 to 6 deal with the solution of nonlinear ordinary differential equations.

In Chapter 2 we study the entropy generation rate in the unsteady laminar three-dimensional MHD axisymmetric nanofluid flow over a nonlinear stretching sheet, taking into account a chemical reaction and thermal radiation. The nanofluid particle volume fraction at the wall is passively controlled. The spectral quasilinearization method is used to solve the model equations.

In Chapter 3 we analyse the effect of entropy generation at the stagnation point for the flow of an unsteady MHD micropolar nanofluid along a linear permeable sheet. The flow is subject to viscous dissipation. Thermophoesis, nanoparticle Brownian motion, a chemical reaction and thermal radiation are also considered. The bivariate spectral quasilinearization method is used to solve a highly coupled system of nonlinear partial differential equations.

In Chapter 4 entropy generation and the impact of the Bejan number in a steady MHD viscoelastic nanofluid flow in homogeneous and heterogeneous reactions are considered using the spectral

quasilinearization method. The effect of the slip velocity, chemical reactions and the nonlinear thermal radiation on the fluid flows are considered.

In Chapter 5 presents a model to describe the flow of a Casson nanofluid with a binary chemical reaction. The study considers the impact of thermal radiation, viscous dissipation, Brownian motion, temperature ratio and thermophoresis on the flow structure and the heat transfer properties of the fluid. The spectral quasilinearization method is used to solve the flow equations.

In Chapter 6 we investigate entropy generation, and heat and mass transfer in Jeffrey, Maxwell and Oldroyd-B laminar nanofluid boundary-layer flows near a stagnation point. Three spectral methods are used to solve the model equations. The residual errors are used to determine the most appropriate solution method.

Finally, in Chapter 7, we conclude the study by summarizing and discussing the major findings.

Chapter 2

On unsteady three-dimensional axisymmetric MHD nanofluid flow with entropy generation and thermo-diffusion effects

In this chapter, we study entropy generation in a three-dimensional axisymmetric nanofluid flow over a nonlinear stretching sheet. Thermal radiation and a chemical reaction are considered to be significant. It is assumed that there is no mass flux across the wall and the magnetic field and chemical reaction are dependent on time and the stretching surface. The spectral quasilinearization method is used to solve the flow equations.

entropy

MDPI

Article

On Unsteady Three-Dimensional Axisymmetric MHD Nanofluid Flow with Entropy Generation and Thermo-Diffusion Effects on a Non-Linear Stretching Sheet

Mohammed Almakki [1], Sharadia Dey [1,2,*], Sabyasachi Mondal [1] and Precious Sibanda [1]

[1] School of Mathematics, Statistics and Computer Science, University of KwaZulu-Natal, Private Bag X01, Scottsville, 3209 Pietermaritzburg, South Africa; m.almakki1977@gmail.com (M.A.); sabya.mondal.2007@gmail.com (S.M.); sibandap@ukzn.ac.za (P.S.)

[2] DST-NRF Centre of Excellence in Mathematical and Statistical Sciences (CoE-MaSS), Private Bag 3, Wits, 2050 Johannesburg, South Africa

* Correspondence: sharadiadey1985@gmail.com; Tel.: +27-83-580-1328

Academic Editors: Giulio Lorenzini and Omid Mahian
Received: 22 February 2017; Accepted: 12 April 2017; Published: 12 July 2017

Abstract: The entropy generation in unsteady three-dimensional axisymmetric magnetohydrodynamics (MHD) nanofluid flow over a non-linearly stretching sheet is investigated. The flow is subject to thermal radiation and a chemical reaction. The conservation equations are solved using the spectral quasi-linearization method. The novelty of the work is in the study of entropy generation in three-dimensional axisymmetric MHD nanofluid and the choice of the spectral quasi-linearization method as the solution method. The effects of Brownian motion and thermophoresis are also taken into account. The nanofluid particle volume fraction on the boundary is passively controlled. The results show that as the Hartmann number increases, both the Nusselt number and the Sherwood number decrease, whereas the skin friction increases. It is further shown that an increase in the thermal radiation parameter corresponds to a decrease in the Nusselt number. Moreover, entropy generation increases with respect to some physical parameters.

Keywords: unsteady 3D axisymmetric nanofluid; entropy generation; spectral quasi-linearization method

1. Introduction

The study of unsteady nanofluid flow, heat and mass transfers along a nonlinear stretching surface has received considerable attention during the last few years because of several applications in engineering processes, such as in materials manufacturing through extrusion, glass-fiber and paper production. Similarly, unsteady mixed convection in boundary layer flows have received attention with a large number of studies focusing on heat and mass transfer characteristics in nanofluids (Dessie et al. [1]). Nanofluids have increased thermal conductivity and convective heat transfer performance as compared to base fluids such as water and oils. The notion of a nanofluid was introduced by Choi [2] when he proposed the suspension of nanoparticles in a base fluid like water, oil or an ethylene-glycol mixture. These common base fluids have lower thermal conductivity, which is increased when nanoparticles are added. The increase in the thermal conductivity was explained by Buongiorno [3] in terms of the effect of particle Brownian motion and thermophoresis. Nanofluids have several applications due to the unique chemical and physical properties of the constituent nanoparticles. For instance, nanofluids have been used in applications that require high-performance

cooling systems such as hot rolling, glass fiber production, rubber and the manufacture of metallic sheets [4].

Heat transfers due to free and mixed convection have several applications, for instance in electronic cooling, heat exchangers, etc. The study of axisymmetric magnetohydrodynamics (MHD) flow and heat transfer of power law fluid along an unsteady radially-stretching sheet was carried out by Ahmed et al. [5]. The conservation equations are solved analytically and numerically. Mohammadiun et al. [6] derived an exact solution of axisymmetric stagnation-point flow and heat transfer along a stationary infinite circular cylinder of a steady viscous compressible fluid with constant heat flux. The general self-similar solution was obtained with constant wall heat flux. The solutions of the system were obtained for different Reynolds numbers, compressibility factors and Prandtl numbers. Xiao et al. [7] proposed a mathematical model for heat convection in the presence of Brownian motion of nanoparticles where the physical properties of the fluid are predicted by the mean of fractal geometry. Thermal conductivity was found to have a positive and negative relation with concentration and the size of nanoparticles, respectively. The model output was found to be in good agreement with experimental data. Cai et al. [8] presented a review of research conducted on thermal conductivity and convective heat transfer in nanofluids by using fractal models and fractal-based techniques. Cai et al. [8] presented a model that considered the fractal distribution of nanoparticle sizes and heat convection between the fluid and the nanoparticles. Additionally, the heat transfer in nanofluids was modeled using three fractal-based models. The models were used to derive formulas for predicting the heat flux for boiling heat transfer. The predictions were found to be in a good agreement with the experimental data.

Shankar et al. [9] studied MHD flow, heat and mass transfer in a nanofluid flow along a stretching boundary with a non-uniform heat source/sink. The system of equations was solved using the Keller-box method. MHD effects in heat transfer have applications in science and technology. In MHD flow, the induced currents in the fluid generate forces, which in turn modify the flow field. Shahzad et al. [10] presented the exact solution for the MHD flow and heat transfer for a viscous incompressible fluid and a nonlinear sheet stretching radially in a porous medium.

Thermal radiation is important in the flow of a fluid, and consequently, the effects of thermal radiation on heat and mass transfer have been extensively studied. Ahmad et al. [11] considered the effect of thermal radiation on the steady MHD axisymmetric stagnation point flow of a viscous incompressible micropolar fluid along a shrinking sheet. The system of equations was solved numerically using an algorithm based on finite difference approximations. They found that the thickness of the thermal boundary layer becomes thinner as the thermal radiation parameter increased. The effect of melting heat transfer and second order slip with thermal radiation for a stagnation point flow was examined by Mabood et al. [12]. Singh et al. [13] analyzed unsteady MHD flow of a viscous incompressible fluid over a permeable stretching sheet and took into account the effect of thermal radiation.

In practical applications, mass transfer occurs due to molecular diffusion of species in homogeneous and heterogeneous chemical reactions (Sarada et al. [14]). The properties of the fluid can be affected by the diffusion of the species, which can either be generated or absorbed by the fluid. For this reason, the study of a chemical reaction in a fluid flow has attracted many researchers. Sarada et al. [14] analyzed the influence of a chemical reaction on unsteady MHD flow of a viscous incompressible fluid passing through an infinite vertical porous plate with varying suction.

The study of the unsteady flow of a viscous incompressible fluid along a linear stretching with a chemical reaction was investigated by Hunegnaw et al. [15]. They used a shooting technique and a fourth-order Runge–Kutta integration scheme combined with the Newton–Raphson method to solve the conservation equations. Barik [16] presented a study of the effects of a chemical reaction on unsteady rotating MHD flow in a porous medium with a heat source.

Entropy generation plays a vital role in the study of heat transfer processes. Entropy is a measure of the randomness or molecular disorder of a system. In accordance with the second law of thermodynamics, the entropy of a system always increases during an irreversible process and

remains constant during a reversible process, that is entropy generation (E_{gen}) is always positive for an irreversible process and zero for reversible process. The performance of any engineering system is degraded by irreversibility, and entropy generation is a measure of the magnitude of the irreversibility of the process.

Entropy generation is disregarded in most of the studies reviewed earlier. In this work, the mechanisms for generating entropy are connected to heat transfer, fluid friction irreversibility, magnetic field and mass transfer. The pioneering work in the analysis of entropy generation was done by Bejan [17]. Subsequently, entropy generation in MHD Casson nanofluid flow in the proximity of a stagnation point was investigated by Qing et al. [18]. The findings suggested a positive correlation between entropy generation and an increase in the Brinkman number, Reynolds number, Hartmann number and porosity. The study of entropy generation with MHD flow peristaltic blood of nanofluid across a porous medium was considered by Rashidi et al. [19]. The system was solved numerically using the homotopy perturbation method (HPM). The entropy generation of MHD an Eyring–Powell nanofluid flow towards a permeable stretching surface in the presence of nonlinear thermal radiation was investigated by Bhatti et al. [20]. The successive linearization method (SLM) and Chebyshev spectral collocation method are used. Rashidi et al. [21] studied entropy generation in nanofluid flow along a permeable stretching surface near the stagnation point with heat generation/absorption and a convective boundary condition. Bhatti et al. [22] used the successive linearization method (SLM) to study the entropy generation on non-Newtonian Carreau nanofluid over a shrinking sheet. The thermal radiation and magnetohydrodynamics (MHD) are taken into account. The idea of entropy generation in nanofluids is a growing area of research, and recent studies have examined different source terms and flow geometries [23].

The spectral quasi-linearization method (SQLM) has not been previously used to solve equations for three-dimensional axisymmetric MHD nanofluid flow. Moreover, to the best of the authors' knowledge, entropy generation in this type of fluid flow has not been previously studied. The aim of the study is to analyze thermo-diffusion effects in three-dimensional axisymmetric MHD nanofluid flow, heat and mass transfers over a nonlinearly circular stretching sheet with entropy generation. The flow is subjected to thermal radiation and a chemical reaction. The conservation equations are solved numerically using the spectral quasi-linearization method [24]. The SQLM combines fast convergence with accuracy. The method has been used in recent boundary layer flow and heat transfer studies, such as [24,25]. In addition, the nanofluid boundary condition suggested by Nield and Kuznetsov [26] is adopted where it is assumed that the nanoparticle mass flux at the wall vanishes. The results are found to be in good agreement with previously published work, such as Mustafa et al. [27].

2. Problem Formulation

Consider the unsteady three-dimensional MHD flow of an incompressible viscous flow of nanofluid. A cylindrical coordinate system (r, θ, z) is used. The velocity of the stretching sheet is assumed to be nonlinear along the radial direction. It is assumed that there is no nanoparticle flux across the wall, and the surface is stretching along the z-direction. In the ambient fluid, the temperature, solute concentration and nanoparticle concentration are denoted by T_∞, C_∞ and ψ_∞, respectively (see Figure 1). Here, C_w, T_w and ψ_w represent the solute concentration, constant temperature and nanoparticle concentration respectively on the wall. The variable magnetic field intensity is denoted by $B(r,t)$ where t represents time. The magnetic field acts in the positive z-direction normal to the sheet. In this study, $B(r,t)$ generalizes the magnetic field term provided previously in [9,10] to:

$$B(r,t) = \frac{B_0 r^{(n-1)/2}}{\sqrt{1-\lambda t}}, \tag{1}$$

where B_0 is the uniform magnetic field strength, $n > 0$ is the power-law index or stretching sheet parameter and λ represents the unsteadiness parameter.

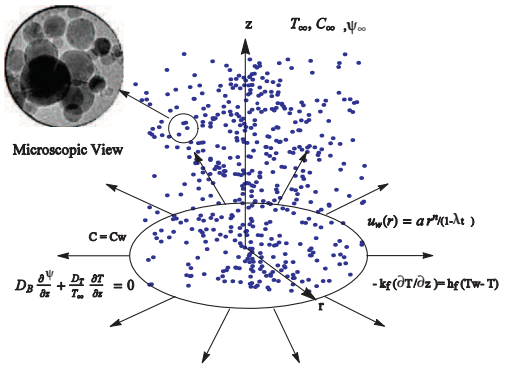

Figure 1. Physical configuration and coordinate system.

The equations for the conservation of momentum, energy, mass and nanoparticle volume fraction, considering the boundary layer assumptions presented above, can be obtained [27,28] as:

$$\frac{\partial u}{\partial r} + \frac{u}{r} + \frac{\partial w}{\partial z} = 0, \tag{2}$$

$$\frac{\partial u}{\partial t} + u\frac{\partial u}{\partial r} + w\frac{\partial u}{\partial z} = \nu_f \frac{\partial^2 u}{\partial z^2} - \frac{\sigma B^2(r,t)u}{\rho_f}, \tag{3}$$

$$\frac{\partial T}{\partial t} + u\frac{\partial T}{\partial r} + w\frac{\partial T}{\partial z} = \alpha_f \frac{\partial^2 T}{\partial z^2} + \tau\left[D_B \frac{\partial \psi}{\partial z}\frac{\partial T}{\partial z} + \frac{D_T}{T_\infty}\left(\frac{\partial T}{\partial z}\right)^2\right] + D_{TC}\frac{\partial^2 C}{\partial z} - \frac{1}{\rho_f c_p}\frac{\partial q_r}{\partial z}, \tag{4}$$

$$\frac{\partial C}{\partial t} + u\frac{\partial C}{\partial r} + w\frac{\partial C}{\partial z} = D_s \frac{\partial^2 C}{\partial z^2} + D_{CT}\frac{\partial^2 T}{\partial z} - R(r,t)(C - C_\infty), \tag{5}$$

$$\frac{\partial \psi}{\partial t} + u\frac{\partial \psi}{\partial r} + w\frac{\partial \psi}{\partial z} = D_B \frac{\partial^2 \psi}{\partial z^2} + \frac{D_T}{T_\infty}\frac{\partial^2 T}{\partial z^2}, \tag{6}$$

where u and w represent the fluid velocity components in r and z directions, respectively; ν_f, σ and ρ_f are the kinematic viscosity, electrical conductivity and the density of the fluid, respectively; $\alpha_f = k_f/(\rho c_p)_f$ is the thermal diffusivity, c_p is the heat capacity, D_B is the Brownian diffusion coefficient, D_T is the thermophoretic diffusion coefficient; $\tau = (\rho c_p)_s/(\rho c_p)_f$ the ratio of effective heat capacity of the nanoparticle material to heat capacity of the fluid; D_{CT} and D_{TC} are the Soret and Dufour diffusivities, D_s is the solute diffusivity and $R(r,t)$ is the chemical reaction.

The quantity q_r is the relative heat flux. Applying the Rosseland approximation, [29], q_r can be expressed as:

$$q_r = -\frac{4\sigma^*}{3K^*}\frac{\partial T^4}{\partial z}, \tag{7}$$

In Equation (7), σ^* is the Stefan–Boltzmann constant while K^* is the Rosseland mean spectral absorption coefficient. If the variation in temperature across the flow is small, T^4 may be expanded using the Taylor series about T_∞, which yields:

$$T^4 \approxeq 4T_\infty^3 T - 3T_\infty^4. \tag{8}$$

Substituting Equation (8) in Equation (7), the relative heat flux becomes:

$$q_r = -\frac{16\sigma^* T_\infty^3}{3K^*}\frac{\partial T}{\partial z}. \tag{9}$$

To simplify the mass equation, the chemical reaction $R(r,t)$ must be a constant. This condition holds if $R(r,t)$ has the following form:

$$R(r,t) = R_0 \frac{ar^{n-1}}{1-\lambda t}, \tag{10}$$

where R_0 is constant and $a > 0$ is the stretching constant.

The boundary conditions considered (see [27]) are:

$$\begin{aligned} u = u_w(r) = \frac{ar^n}{1-\lambda t},\ -k_f \frac{\partial T}{\partial z} = h_f(T_w - T), \\ D_B \frac{\partial \psi}{\partial z} + \frac{D_T}{T_\infty}\frac{\partial T}{\partial z} = 0,\ C = C_w \quad \text{at } z = 0, \\ u \to 0,\ T \to T_\infty,\ C \to C_\infty \text{ and} \\ \psi \to \psi_\infty \text{ as } z \to \infty, \end{aligned} \tag{11}$$

where $k_f = k_0\sqrt{1-\lambda t}$ is the thermal conductivity of the base fluid where k_0 is a constant. A similarity solution of the energy equation can be obtained if the Biot number,

$$Bi = \frac{h_f}{k_0}\sqrt{\frac{\nu_f}{ar^{(n-1)}}}, \tag{12}$$

is a constant. This condition is satisfied if the heat transfer coefficient, h_f, is proportional to $r^{(n-1)/2}$. Thus, the heat transfer coefficient is expressed as $h_f = b_0 r^{(n-1)/2}$, where b_0 is a constant. The Biot number can be obtained as $Bi = h_0\sqrt{(\nu_f/a)}/k_0$.

Equations (2)–(6) are converted into coupled ordinary differential equations by using the following similarity variables (see [27]):

$$\begin{aligned} \eta = \sqrt{\frac{a}{\nu_f(1-\lambda t)}} r^{(n-1)/2} z,\ \theta(\eta) = \frac{T - T_\infty}{T_w - T_\infty}, \\ S(\eta) = \frac{C - C_\infty}{C_w - C_\infty},\ \phi(\eta) = \frac{\psi - \psi_\infty}{\psi_\infty}. \end{aligned} \tag{13}$$

The system of Equations (2)–(6) is transformed to:

$$f''' + \frac{(n+3)}{2} f f'' - n f'^2 - A\left(f' + \frac{1}{2}\eta f''\right) - Haf' = 0, \tag{14}$$

$$\left(1 + Nr\right)\frac{1}{Pr}\theta'' - \frac{A}{2}\eta\theta' + \frac{n+3}{2} f\theta' + Nb\phi'\theta' + Nt\theta'^2 + Nd\, S'' = 0, \tag{15}$$

$$\frac{1}{Sc} S'' - \frac{A}{2}\eta S' + \frac{(n+3)}{2} f S' - R_0 S + Ld\, \theta'' = 0, \tag{16}$$

$$\phi'' - \frac{A}{2} Sc\, \eta\phi' + \frac{n+3}{2} Sc\, f\phi' + \frac{Nt}{Nb}\theta'' = 0, \tag{17}$$

subject to the boundary conditions:

$$\begin{aligned} f(0) = 0,\quad f'(0) = 1 \text{ and } f'(\infty) \to 0, \\ \theta'(0) = -Bi(1 - \theta(0)),\ \theta(\infty) \to 0, \\ S(0) = 1,\ S(\infty) \to 0, \\ Nb\phi'(0) + Nt\theta'(0) = 0 \text{ and } \phi(\infty) \to 0. \end{aligned} \tag{18}$$

The parameters in Equations (14)–(17) are given by:

$$A = \frac{\lambda}{ar^{n-1}},\ Ha = \frac{\sigma B_0^2}{a\rho_f},\ Pr = \frac{\nu_f}{\alpha},\ Nr = \frac{16\sigma^* T_\infty^3}{3k_f K^*},$$
$$Nb = \frac{\tau D_B \phi_\infty}{\nu_f}, Nt = \frac{\tau(T_w - T_\infty)D_T}{\nu_f T_\infty},$$
$$Nd = \frac{D_{TC}(C_w - C_\infty)}{\nu_f(T_w - T_\infty)},\ Sc = \frac{\nu_f}{D_B},$$
$$R_0 = \frac{(1-\lambda t)R(x,t)}{ar^{n-1}} \text{ and } Ld = \frac{D_{CT}(T_w - T_\infty)}{\nu_f(C_w - C_\infty)}, \tag{19}$$

where A is the unsteadiness parameter, Ha is the Hartmann number, Pr is the Prandtl number, Nr is the thermal radiation parameter, Nb is the Brownian motion parameter, Nt is the thermophoresis parameter, Nd is the modified Dufour parameter, Sc is the Schmidt number, R_0 is a constant and Ld is the modified Soret parameter.

The skin friction coefficient C_f, the Nusselt number Nu_r and the Sherwood number Sh_r can be expressed as:

(i) Skin-fraction coefficient:

$$C_f Re^{1/2} = f''(0), \tag{20}$$

where $Re = \frac{u_w(r)r}{\nu_f}$ is the Reynolds number.

(ii) Nusselt number:

$$Nu = \frac{rh_w}{k_f(T_w - T_\infty)}, \tag{21}$$

where h_w represents surface heat flux, which can be obtained by:

$$h_w = -\left[k_f + \frac{16\sigma^* T_\infty^3}{3K^*}\right]\left(\frac{\partial T}{\partial z}\right)_{z=0}. \tag{22}$$

Equation (21) becomes:

$$-(1+Nr)\theta'(0) = Re^{-1/2} Nu_r \tag{23}$$

(iii) The Sherwood number for solute concentration equation is:

$$Sh_r = \frac{rh_m}{D_s(C_w - C_\infty)}, \tag{24}$$

where:

$$h_m = -D_s\left(\frac{\partial C}{\partial z}\right)_{z=0}, \tag{25}$$

where h_m is the surface mass flux. Equation (24) can be written as:

$$-S'(0) = Re_r^{-(1/2)} Sh_r \tag{26}$$

The mass flux is zero due to the nanoparticle boundary condition used, and for this reason, it is not possible to define the Sherwood number for nanoparticle concentration at the wall.

3. Entropy Generation Analysis

Entropy generation suggests a wastage of energy; thus, minimization of entropy production is often a major objective. Entropy generation analysis can be used as an effective tool for the identification of causes of inefficiency in any system and offers scope for the improvement in the design of any device or process. The limitation of global energy resources provides an impetus for re-examining energy production systems and consumption patterns (Arikoglu et al. [30]). From a theoretical perspective, the second law of thermodynamics is utilized to study energy producing, converting and consuming systems. The volumetric rate of local entropy generation for a nanofluid along with thermal radiation and a magnetic field can be expressed as (see [18,22,23]:

$$E_{gen} = \underbrace{\frac{k}{\widetilde{T}_\infty^2}\left(\left(\frac{\partial \widetilde{T}}{\partial z}\right)^2 + \frac{16\sigma^* \widetilde{T}_\infty^3}{3K^*}\left(\frac{\partial \widetilde{T}}{\partial z}\right)^2\right)}_{1^{\text{st}}\text{ part}} + \underbrace{\frac{\mu}{\widetilde{T}_\infty}\left(\frac{\partial \widetilde{u}}{\partial z}\right)^2}_{2^{\text{nd}}\text{ part}} + \underbrace{\frac{\sigma B_0^2}{\widetilde{T}_\infty}\widetilde{u}^2}_{3^{\text{rd}}\text{ part}} + \underbrace{\frac{RD_B}{\psi_\infty}\left(\frac{\partial \psi}{\partial z}\right)^2 + \frac{RD_B}{\widetilde{T}_\infty}\left(\frac{\partial T}{\partial z}\right)\left(\frac{\partial \psi}{\partial z}\right)}_{4^{\text{th}}\text{ part}} \tag{27}$$

In Equation (27), the entropy generation is stated in four parts. The first part is entropy generation due to heat transfer irreversibility; the second part is the entropy generation due to the viscous dissipation irreversibility; the third part is the entropy generation due to the applied magnetic field irreversibility; and the fourth part is due to the diffusive irreversibility.

We define the entropy generation number as the ratio of the local volumetric entropy generation rate E_{gen} to a characteristic rate of entropy generation E_0, that is,

$$N_G = \frac{E_{gen}}{E_0}, \tag{28}$$

where:

$$E_0 = \frac{k_f (T_w - T_\infty)^2}{T_\infty^2 r^2}. \tag{29}$$

Using Equations (27)–(29), the non-dimensional entropy generation can be represented as:

$$\begin{aligned} N_G = {} & Re\left(1 + Nr\right)\theta'^2(\eta) + \frac{BrRe}{\Omega} f''^2 + \frac{Br\left(Ha\right)^2}{\Omega} f'^2 \\ & + \frac{Re\Sigma}{\Omega^2}\phi'^2(\eta) + \frac{Re\Sigma}{\Omega}\theta'(\eta)\phi'(\eta), \end{aligned} \tag{30}$$

where $Re, Nr, Br, \Omega, Ha, \Sigma$ are the Reynolds number, the thermal radiation parameter, Brinkman number, dimensionless temperature difference, Hartmann number and the diffusive parameter, respectively. These parameters are expressed by the following relations:

$$Br = \frac{\mu u_w^2(r)}{k_f \Delta T}, \Omega = \frac{\Delta T}{T_\infty} = \frac{T_w - T_\infty}{T_\infty}, \Sigma = \frac{RD_B \psi_\infty}{k_f}. \tag{31}$$

4. Method of Solution

The quasi-linearization method (QLM) is a generalization of the Newton–Raphson method (Bellman and Kalaba [31]). The derivation of the QLM is based on the linearization of the nonlinear components of the governing equations using the Taylor series assuming that the difference between the value of the unknown function is negligible between the current iteration, $r + 1$, and the previous iteration, r.

Applying the quasi-linearization scheme to Equations (14)–(17) with the boundary conditions, Equation (18), yields the following iterative schemes:

$$a_{0,r}f'''_{r+1} + a_{1,r}f''_{r+1} + a_{2,r}f'_{r+1} + a_{3,r}f_{r+1} = R_f, \tag{32}$$
$$b_{0,r}\theta''_{r+1} + b_{1,r}\theta'_{r+1} + b_{2,r}\theta_{r+1} + b_{3,r}f_{r+1} + b_{4,r}S''_{r+1} + b_{5,r}\phi'_{r+1} = R_\theta, \tag{33}$$
$$c_{0,r}S''_{r+1} + c_{1,r}S'_{r+1} + c_{2,r}S_{r+1} + c_{3,r}f_{r+1} + c_{4,r}\theta''_{r+1} = R_S, \tag{34}$$
$$d_{0,r}\phi''_{r+1} + d_{1,r}\phi'_{r+1} + d_{2,r}f_{r+1} + d_{3,r}\theta''_{r+1} = R_\phi, \tag{35}$$

subject to

$$\begin{aligned} &f_{r+1}(0) = 0,\ f'_{r+1}(0) = 1,\ f'_{r+1}(\infty) \to\ 0,\\ &\theta'_{r+1}(0) = -Bi(1-\theta_{r+1}(0)),\ \theta_{r+1}(\infty) \to\ 0,\\ &S_{r+1}(0) = 1,\ S_{r+1}(\infty) \to\ 0,\\ &Nb\phi'_{r+1}(0) + Nt\theta'_{r+1}(0) = 0, \text{ and } \phi_{r+1}(\infty) \to\ 0, \end{aligned} \tag{36}$$

where the coefficients in Equations (32)–(35) are obtained as:

$$\begin{aligned} &a_{0,r} = 1,\ a_{1,r} = \left(\frac{n+3}{2}\right)f_r - \frac{A}{2}\eta,\\ &a_{2,r} = -2nf'_r - A - Ha,\ a_{3,r} = \left(\frac{n+3}{2}\right)f''_r, \end{aligned} \tag{37}$$

$$\begin{aligned} &b_{0,r} = \left(1+Nr\right)\frac{1}{Pr},\\ &b_{1,r} = \left(\frac{n+3}{2}\right)f_r - \frac{A}{2}\eta + Nb\phi'_r + 2Nt\theta'_r,\\ &b_{2,r} = 0,\ b_{3,r} = \left(\frac{n+3}{2}\right)\theta'_r,\\ &b_{4,r} = Nd,\ b_{5,r} = Nb\theta'_r, \end{aligned} \tag{38}$$

$$\begin{aligned} &c_{0,r} = \frac{1}{Sc},\ c_{1,r} = \left(\frac{n+3}{2}\right)f_r - \frac{A}{2}\eta,\ c_{2,r} = -R_0,\\ &c_{3,r} = \left(\frac{n+3}{2}\right)S'_r,\ c_{4,r} = Ld, \end{aligned} \tag{39}$$

$$\begin{aligned} &d_{0,r} = 1,\ d_{1,r} = \left(\frac{n+3}{2}\right)Sc\ f_r - \frac{A}{2}Sc\ \eta,\\ &d_{2,r} = \left(\frac{n+3}{2}\right)Sc\ \phi'_r,\ d_{3,r} = \frac{Nt}{Nb}. \end{aligned} \tag{40}$$

A Chebyshev pseudo-spectral method [24] was used to solve Equations (32)–(35). The Chebyshev interpolating polynomial defined by Equation (41) is used with Gauss–Lobatto points [32,33] to define the unknown functions where:

$$x_i = \cos\left(\frac{\pi i}{N}\right), \quad i = 0, 1, ..., N; \quad -1 \le x_i \le 1. \tag{41}$$

The variable N in Equation (41) is the number of collocation points. A truncated domain $[0, L]$ is used to approximate the semi-infinite domain to facilitate computations. The parameter L represents the boundary condition at infinity. In order to model the behavior of the flow at infinity, the parameter L should be a large number. The domain $[0, L]$ is transformed into $[-1, 1]$ using the linear transformation $\eta = \frac{L(x+1)}{2}$.

The spectral collocation method is used to construct a differentiation matrix to approximate the derivative of unknown variables at the collocation points as a matrix vector product:

$$\frac{dF_r^{(1)}}{d\eta}(\eta_j) = \sum_{k=0}^{N} \mathbf{D}_{jk} f(\eta_k) = \mathbf{D}F_m, j = 0, 1, 2, ..., N, \tag{42}$$

where $\mathbf{D} = 2D/L$ and $F = \left[f(\eta_0), f(\eta_1), f(\eta_1), ..., f(\eta_N)\right]^T$ represent the vector function at the collocation points. The high order derivatives are given as powers of $\mathbf{D}$, such as:

$$F_r^{(p)} = \mathbf{D}^p F_r, \tag{43}$$

where p is the order of the derivative. Spectral collocation is applied at r using the differentiation matrix $\mathbf{D}$ in order to approximate derivatives of unknown functions in Equations(32)–(35) with Equation (36), which yields:

$$\mathbf{A}_{1,1}\mathbf{f} + \mathbf{A}_{1,2}\boldsymbol{\theta} + \mathbf{A}_{1,3}\mathbf{S} + \mathbf{A}_{1,4}\boldsymbol{\phi} = R_f, \tag{44}$$

$$\mathbf{A}_{1,2}\mathbf{f} + \mathbf{A}_{2,2}\boldsymbol{\theta} + \mathbf{A}_{2,3}\mathbf{S} + \mathbf{A}_{2,4}\boldsymbol{\phi} = R_\theta, \tag{45}$$

$$\mathbf{A}_{1,3}\mathbf{f} + \mathbf{A}_{2,3}\boldsymbol{\theta} + \mathbf{A}_{3,3}\mathbf{S} + \mathbf{A}_{3,4}\boldsymbol{\phi} = R_S, \tag{46}$$

$$\mathbf{A}_{1,4}\mathbf{f} + \mathbf{A}_{2,4}\boldsymbol{\theta} + \mathbf{A}_{3,4}\mathbf{S} + \mathbf{A}_{4,4}\boldsymbol{\phi} = R_\phi. \tag{47}$$

Here:

$$\begin{aligned} &\mathbf{A}_{1,1} = a_{0,r}\mathbf{D}^3 + \mathbf{diag}(a_{1,r})\mathbf{D}^2 + \mathbf{diag}(a_{2,r})\mathbf{D} + \mathbf{diag}(a_{3,r})\mathbf{I}, \\ &\mathbf{A}_{1,2} = 0, \mathbf{A}_{1,3} = 0, \mathbf{A}_{1,4} = 0, \end{aligned} \tag{48}$$

$$\begin{aligned} &\mathbf{A}_{2,1} = \mathbf{diag}(b_{3,1})\mathbf{I}, \\ &\mathbf{A}_{2,2} = \mathbf{diag}(b_{0,r})\mathbf{D}^2 + \mathbf{diag}(b_{1,r})\mathbf{D} + \mathbf{diag}(b_{2,r})\mathbf{I}, \\ &\mathbf{A}_{2,3} = \mathbf{diag}(b_{4,r})\mathbf{D}^2, \mathbf{A}_{2,4} = \mathbf{diag}(b_{5,r})\mathbf{D}, \end{aligned} \tag{49}$$

$$\begin{aligned} &\mathbf{A}_{3,1} = \mathbf{diag}(c_{3,r})\mathbf{I}, \mathbf{A}_{3,2} = \mathbf{diag}(c_{4,r})\mathbf{D}^2, \\ &\mathbf{A}_{3,3} = c_{0,r}\mathbf{D}^2 + \mathbf{diag}(c_{1,r})\mathbf{D} + (c_{2,r})\mathbf{I} \text{ and} \\ &\mathbf{A}_{3,4} = 0, \end{aligned} \tag{50}$$

$$\begin{aligned} &\mathbf{A}_{4,1} = \mathbf{diag}(d_{2,r})\mathbf{I}, \mathbf{A}_{4,2} = \mathbf{diag}(d_{3,r})\mathbf{D}^2, \\ &\mathbf{A}_{4,3} = 0, \mathbf{A}_{4,4} = \mathbf{diag}(d_{0,r})\mathbf{D} + \mathbf{diag}(d_{1,r})\mathbf{D}, \end{aligned} \tag{51}$$

$$\mathbf{R}_f = \left(\frac{n+3}{2}\right)\mathbf{f_r}\mathbf{f_r''} - n\left(\mathbf{f_r'}\right)^2, \ \mathbf{R}_\phi = \left(\frac{n+3}{2}\right) Sc\ \mathbf{f_r}\boldsymbol{\phi}_\mathbf{r}', \tag{52}$$

$$\mathbf{R}_s = \left(\frac{n+3}{2}\right)\mathbf{f_r}\mathbf{S_r'} \text{ and } \mathbf{R}_\phi = \left(\frac{n+3}{2}\right) Sc\ \mathbf{f_r}\boldsymbol{\phi}_\mathbf{r}', \tag{53}$$

where **diag**() represents diagonal matrices of order $(N+1)\times(N+1)$, $\mathbf{I}$ is an $(N+1)\times(N+1)$ identity matrix and $\mathbf{f}, \boldsymbol{\theta}, \mathbf{S}$ and $\boldsymbol{\phi}$ are the values of functions f, θ, S and ϕ, respectively. Equations (44)–(47) are solved as a matrix system using the SQLM scheme where the iteration is started with initial approximate solutions obtained as:

$$\begin{aligned} &f_0(\eta) = 1 - \exp(-\eta), \ \ \theta_0(\eta) = \left(\frac{Bi}{1+Bi}\right)\exp(-\eta), \\ &S_0(\eta) = \exp(-\eta) \text{ and} \\ &\phi_0(\eta) = -\left(\frac{Nt}{Nb}\right)\left(\frac{Bi}{1+Bi}\right)\exp(-\eta). \end{aligned} \tag{54}$$

The above equations can be expressed in matrix form as follows:

$$\begin{bmatrix} \mathbf{A}_{11} & \mathbf{A}_{12} & \mathbf{A}_{13} & \mathbf{A}_{14} \\ \mathbf{A}_{21} & \mathbf{A}_{22} & \mathbf{A}_{23} & \mathbf{A}_{24} \\ \mathbf{A}_{31} & \mathbf{A}_{32} & \mathbf{A}_{33} & \mathbf{A}_{34} \\ \mathbf{A}_{41} & \mathbf{A}_{42} & \mathbf{A}_{43} & \mathbf{A}_{44} \end{bmatrix} \begin{bmatrix} F_{r+1} \\ \Theta_{r+1} \\ S_{r+1} \\ \Phi_{r+1} \end{bmatrix} = \begin{bmatrix} \mathbf{R}_f \\ \mathbf{R}_\theta \\ \mathbf{R}_s \\ \mathbf{R}_\phi \end{bmatrix} \tag{55}$$

5. Results and Discussion

The study investigated entropy generation in an unsteady three-dimensional MHD nanofluid along a nonlinear stretching sheet and considered the influence of thermal radiation and a chemical reaction. The conservation equations are solved numerically using the spectral quasi-linearization method (SQLM). The SQLM has been used in a limited number of studies to solve boundary layer flow, heat and mass transfer problems [34]. The physical parameters in this paper are mostly chosen from the literature, for example in the papers [21,26,27,35].

A comparison with previously published results is shown in Table 1 when $A = 0, Ha = 0$, Nr = 0, $Nd = 0$ and $Ld = 0$ (i.e., in the absence of unsteadiness parameter, Hartmann number, the thermal radiation number, Dufour parameter and Soret parameter, respectively). These results are comparable to those of Mustafa et al. [27], which validates this numerical method.

Table 1. Current Nusselt number $-\theta'(0)$ compared with Mustafa et al. [27].

n	*Nt*	*Sc*	*Pr*	Mustafa et al. [27]	Present Results
0.5	0.1	20	5	1.9112911	1.91068095
	0.5			1.2170065	1.21659065
	0.7			0.9815765	0.98122822
1.0	0.5	5	5	1.6914582	1.69104675
		10		1.4740787	1.47375172
		20		1.2861370	1.28590965
2.5	0.5	20	0.7	0.6619164	0.66986678
			5	1.4784288	1.47847763
			7	1.5758736	1.57604858

To demonstrate further the convergence of the SQLM, Figures 2–5 show the effect of the number of collocation points on the accuracy of the solutions obtained for the velocity, temperature, solute concentration and nanoparticle concentration profiles, respectively.

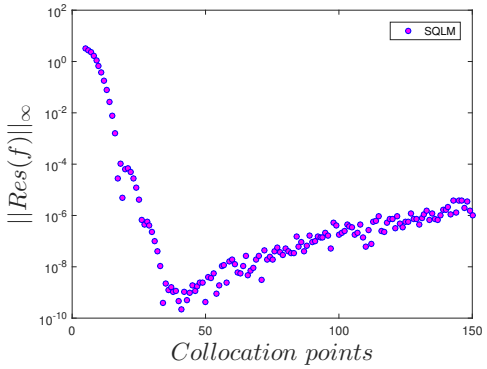

Figure 2. Effects of the number of collocation points number on the residual error of the velocity profile $||Res(f)||_\infty$ when $n = 3, A = 0.3, Pr = 7, Ha = 0.5, Nr = 0.2, Nb = 0.5, Nt = 0.5, Nd = 0.02, Ld = 0.02, Sc = 7, R_0 = 0.3, Bi = 0.2$.

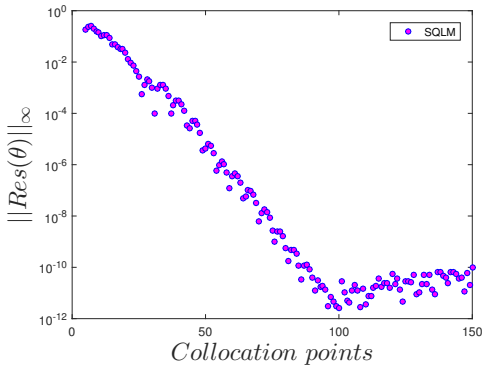

Figure 3. Effects of the number of collocation points number on the residual error of the temperature profile $||Res(\theta)||_\infty$ when $n = 3, A = 0.3, Pr = 7, Ha = 0.5, Nr = 0.2, Nb = 0.5, Nt = 0.5, Nd = 0.02, Ld = 0.02, Sc = 7, R_0 = 0.3, Bi = 0.2$.

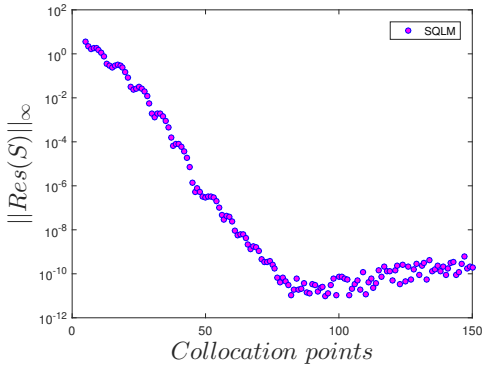

Figure 4. Effects of the number of collocation points number on the residual error of the solute concentration profile $||Res(S)||_\infty$ when $n = 3, A = 0.3, Pr = 7, Ha = 0.5, Nr = 0.2, Nb = 0.5, Nt = 0.5, Nd = 0.02, Ld = 0.02, Sc = 7, R_0 = 0.3, Bi = 0.2$.

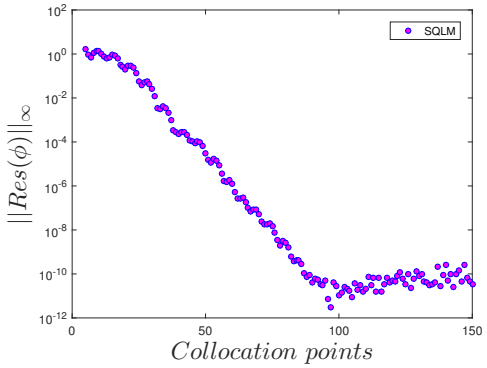

Figure 5. Effects of the number of collocation points number on the residual error of the nanoparticle concentration profile $||Res(\phi)||_\infty$ when $n = 3, A = 0.3, Pr = 7, Ha = 0.5, Nr = 0.2, Nb = 0.5, Nt = 0.5, Nd = 0.02, Ld = 0.02, Sc = 7, R_0 = 0.3, Bi = 0.2$.

It was found that an increase in the number of collocation points results in a reduction of residual error. However, after a certain point (the point at which an optimal residual error is obtained), an increase in the number of collocation points does not have a significant effect on residual error.

In Figure 2, it is observed that the optimal residual error for the velocity profile is around 10^{-9}, which is achieved when the number of the collocation points is within the range 30 and 40; beyond that range, the accuracy starts declining. From Figures 3 and 5, it is noted that the optimal residual errors for the temperature and nanoparticle concentration profiles, respectively, are found around 10^{-12} when the number of collocation points is within 100 and 120. Figure 4 shows that the optimal residual of the solute concentration profile occurs approximately at 10^{-11} when the number of collocation points is between 80 and 100. It is interesting to note that there is no magic number of collocation points that induces the optimal residual errors for all of the physical properties. Additionally, there is variability in the behavior of the decline of the accuracy after the range at which the optimal residuals are obtained; for instance, in Figure 2, the accuracy of the solution of the velocity profile declines much faster as compared to the accuracy of the solution of temperature, solute concentration and nanoparticle concentration profiles respectively shown in Figures 3–5. Overall, these results demonstrate the accuracy and convergence of the SQLM technique.

Table 2 shows the computed skin friction, heat transfer and the mass transfer coefficients, which are represented by $-f''(0), |-\theta'(0)|$ and $|-S'(0)|$, respectively, for various values of n, A, Ha, Nr and Pr. It is observed that the skin friction decreases as n increases, whereas the heat transfer coefficient and mass transfer increase with increasing n with other parameters fixed. It is also noted that the skin friction reduces as A increases while the heat and mass transfer rates decrease. The skin friction, heat and mass transfer rates vary inversely with Ha and appear to be independent of changes in Nr, while the heat transfer rate decreases with the increase in Nr. The same result also holds for the skin friction and the mass transfer with respect to Pr. The heat transfer increases when Pr increases.

Table 2. Skin friction coefficient, heat transfer coefficient and mass transfer coefficient for $Nb = 0.5$, $Nt = 0.5, Nd = 0.02, Ld = 0.02, Sc = 7, R_0 = 0.3, Bi = 0.2$.

n	A	Ha	Nr	Pr	$-f''(0)$	$-\theta'(0)$	$-S'(0)$
1					1.43922866	−0.16417529	−2.89107257
2	0.3	0.5	0.2	7	1.70034047	−0.16661752	−3.16939593
4					2.12897896	−0.16969131	−3.66539915
	−0.5				1.77701012	−0.17085800	−3.72686482
3	0	0.5	0.2	7	1.87092985	−0.16944779	−3.54329048
	0.5				1.96353732	−0.16749470	−3.34434681
		1.5			2.17151786	−0.16755905	−3.37606776
3	0.3	2.5	0.2	7	2.39114443	−0.16678981	−3.33136800
		5			2.86708560	−0.16495200	−3.23526081
			1		1.92657387	−0.16615306	−3.42533294
3	0.3	0.5	1.5	7	1.92657387	−0.16464481	−3.42514164
			2		1.92657387	−0.16310964	−3.42504767
				4	1.92657387	−0.16585371	−3.42553409
3	0.3	0.5	0.2	5	1.92657387	−0.16708464	−3.42554096
				9	1.92657387	−0.16894896	−3.42668462

In Table 3 it is noted that for small values of the Biot number, small changes in the Biot number correspond to a large changes in the maximum temperature. In contrast, with high values of the Biot number, a large change in the Biot number does not appear to affect the maximum temperature significantly.

Table 3. Effects of the Biot number on the maximum temperature.

Biot Number	Maximum Temperature	Change in Maximum Temperature
0.1	0.1264	
0.9	0.3401	169.07
2	0.5218	53.43
5	0.7377	41.38
10	0.853	15.63
50	0.9678	13.46

The parameter n plays an important role in fluid flow. A fluid is called pseudoplastic fluid when $n < 1$ and dilatant fluid when $n > 1$. It is a Newtonian fluid when $n = 1$. A fluid is shear-thinning or shear-thickening according as $n < 1$ or $n > 1$. The effect of n on the fluid velocity, temperature and solute concentration profiles, respectively, is shown in Figures 6–8. Figure 6 illustrates the velocity profile (f') with the variation in the stretching sheet parameter keeping other parameters fixed. The magnitude of the radial component of the velocity decreases with increasing n. In contrast, n has a significant impact on η and the velocity components u and w, respectively. Figure 7 shows that an increases in n leads to a decrease in the thickness of the thermal boundary layer. As a result, the temperature decreases with increasing n and an increase in the heat transfer rate from the sheet. Increasing n increases the deformation rate from the wall to the fluid. Figure 8 shows the effect of n on the solute concentration when the other parameters take fixed values. It is noticed that increases in the non-linear stretching lead to a decrease in the solutal concentration.

Figures 9 and 10 describe the effects of unsteadiness parameter A on the temperature and the solute concentration profiles, respectively. Two cases have been studied, namely $A < 0$ and $A > 0$. From Figure 9, it is observed that the temperature increases with increasing values of $A > 0$. A similar effect is observed for $A < 0$. That the temperature decreases, as moving far away from the stretching sheet in the dynamics region due to the increase of the unsteadiness parameter. Physically, the decrease of temperature can be attributed to heat lostfrom the sheet as a result of the increase in the unsteadiness. Similar properties of solute concentration profiles are observed in Figure 10.

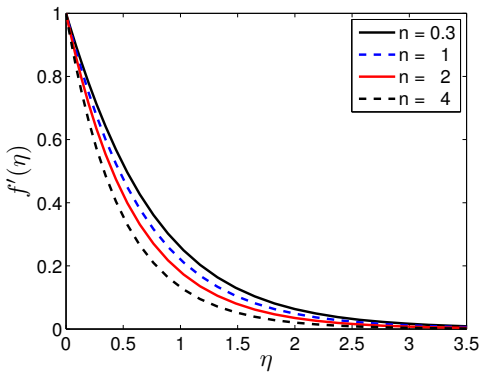

Figure 6. Effects of the stretching parameter n on $f'(\eta)$ when $A = 0.3, Ha = 0.5, Nr = 0.2, Pr = 7, Nb = 0.5, Nt = 0.5, Nd = 0.02, Sc = 7, R_0 = 0.3, Ld = 0.02, Bi = 0.2$.

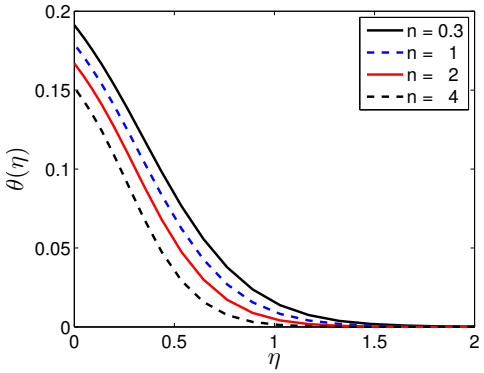

Figure 7. Effects of the stretching parameter n on $\theta(\eta)$ where $A = 0.3, Ha = 0.5, Nr = 0.2, Pr = 10, Nb = 0.5, Nt = 0.5, Nd = 0.02, Sc = 7, R_0 = 0.3, Ld = 0.02, Bi = 0.2$.

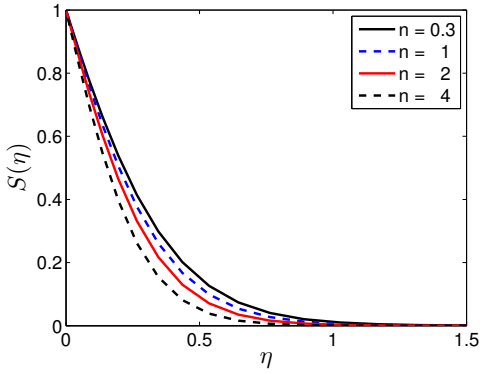

Figure 8. Effects of the stretching parameter n on $S(\eta)$ for $A = 0.3, Ha = 0.5, Nr = 0.2, Pr = 7, Nb = 0.5, Nt = 0.5, Nd = 0.02, Sc = 7, R_0 = 0.3, Ld = 0.02, Bi = 0.2$.

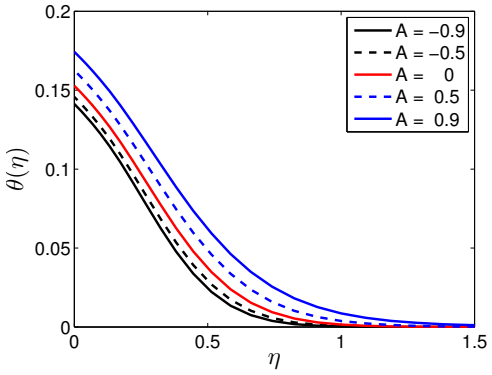

Figure 9. Effects of the unsteadiness parameter (A) on $\theta(\eta)$ for $n = 3, Ha = 0.5, Nr = 0.2, Pr = 7, Nb = 0.5, Nt = 0.5, Nd = 0.02, Sc = 7, R_0 = 0.3, Ld = 0.02, Bi = 0.2$.

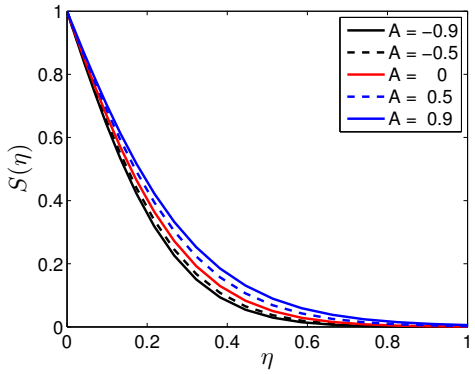

Figure 10. Effects of the unsteadiness parameter (A) on $S(\eta)$ when $n = 3, Ha = 0.5, Nr = 0.2, Pr = 7, Nb = 0.5, Nt = 0.5, Nd = 0.02, Sc = 7, R_0 = 0.3, Ld = 0.02, Bi = 0.2$.

Figures 11 and 12 demonstrate the behavior of several values of the Hartmann number on the velocity and temperature profiles when the other physical parameters are fixed. Figure 11 shows that the dimensionless radial component of the velocity decreases as the Hartmann number increases. This is an indication of a Lorentz force slowing the motion of the fluid in the radial direction. Consequently, the boundary layer thickness increases. The physical implication is that the momentum of the fluid flow may be controlled through an applied magnetic field. Figure 12 shows that the temperature increases with an increase in the Hartmann number due to the effect of the transverse magnetic field in the fluid. It is also worth noting that the application of the magnetic field affects the thermal boundary layer thickness positively in the sense that the thickness of the thermal boundary increases in the presence of a magnetic field.

Figure 13 shows how the temperature profiles vary with the thermal radiation parameter. The temperature increases with increased thermal radiation, which is in line with physical observations regarding the impact of increasing thermal radiation.

Figure 14 presents the influence of the Prandtl number on the temperature profiles. As the Prandtl number increases, the temperature decreases. Smaller Prandtl numbers suggest a fluid with higher thermal conductivities; hence, heat diffuses more rapidly from the heated surface than in the case of fluids with higher Prandtl numbers.

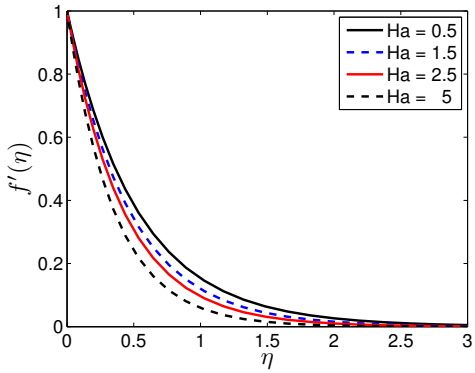

Figure 11. Effects of the Hartmann number (Ha) on $f'(\eta)$ for $n = 3, A = 0.3, Nr = 0.2, Pr = 7, Nb = 0.5, Nt = 0.5, Nd = 0.02, Sc = 7, R_0 = 0.3, Ld = 0.02, Bi = 0.2$.

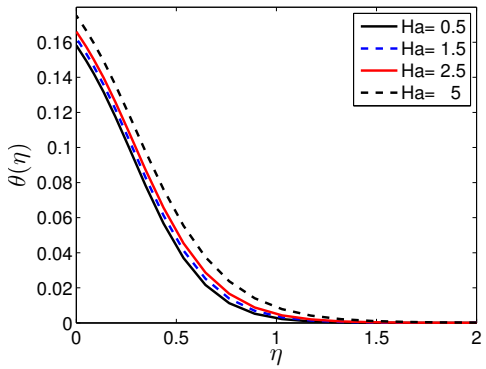

Figure 12. Effects of the Hartmann number (Ha) on $\theta(\eta)$ when $n = 3, A = 0.3, Nr = 0.2, Pr = 7, Nb = 0.5, Nt = 0.5, Nd = 0.02, Sc = 7, R_0 = 0.3, Ld = 0.02, Bi = 0.2$.

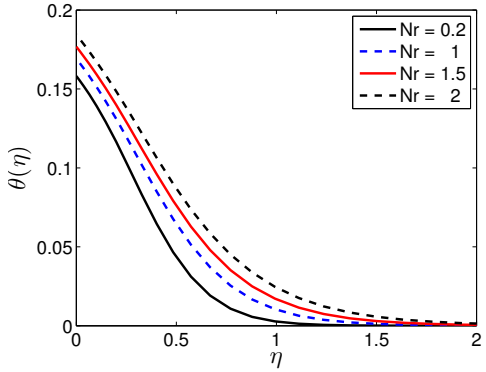

Figure 13. Effects of the thermal radiation parameter (Nr) on $\theta(\eta)$ where $n = 3, A = 0.3, Ha = 0.5, Pr = 7, Nb = 0.5, Nt = 0.5, Nd = 0.02, Sc = 7, R_0 = 0.3, Ld = 0.02, Bi = 0.2$.

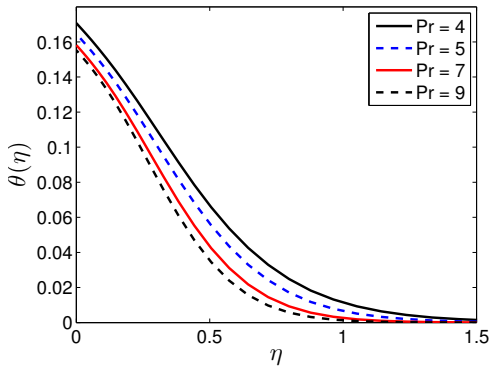

Figure 14. Effects of the Prandtl number (Pr) on $\theta(\eta)$ for $n = 3, A = 0.3, Ha = 0.5, Nr = 0.2, Nb = 0.5, Nt = 0.5, Nd = 0.02, Sc = 7, R_0 = 0.3, Ld = 0.02, \beta_i = 0.2$.

Figure 15 illustrates the behavior of the temperature profiles with different values of the thermophoresis parameter, Nt, when the other parameter are fixed. It is observed that the temperature increases as the thermophoresis parameter increases because the thermal boundary layer increases with increases in the thermophoresis parameter.

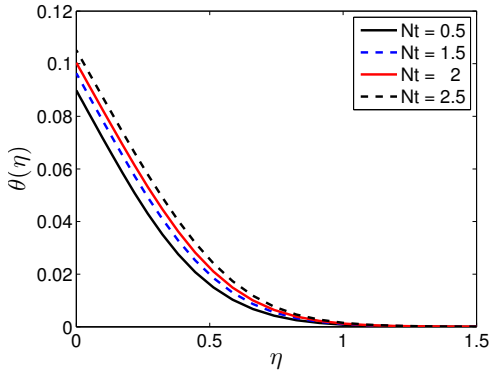

Figure 15. Effects of the thermophoresis parameter (Nt) on $\theta(\eta)$ for $n = 3, A = 0.3, Ha = 0.5, Nr = 0.2, Pr = 7, Nb = 0.5, Nd = 0.02, Sc = 7, R_0 = 0.3, Ld = 0.02, Bi = 0.2$.

Figure 16 demonstrates the influence of the Schmidt number on the solute concentration profile with fixing the other parameters. It is noticed that the solute concentration decreases as the Schmidt number increases.

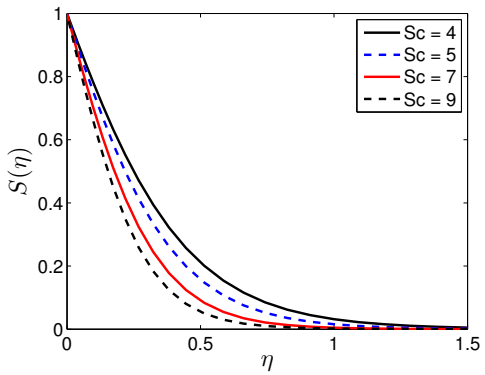

Figure 16. Effects of the Schmidt number (Sc) on $S(\eta)$ for $n = 3, A = 0.3, Ha = 0.5, Nr = 0.2, Pr = 7, Nb = 0.5, Nt = 0.5, R_0 = 0.3, Bi = 0.2$.

Figure 17 shows the relation between the Biot number Bi and the temperature profiles. The Biot number can be perceived as the ratio of internal (conductive) resistance of solid to external (convective resistance). Here, it is found that temperature increases with the increase in the Biot number. An increase in the Biot number causes a stronger convection, and this leads to higher surface temperatures. Further, for sufficiently large values of the Biot number, the temperature approaches its maximum value.

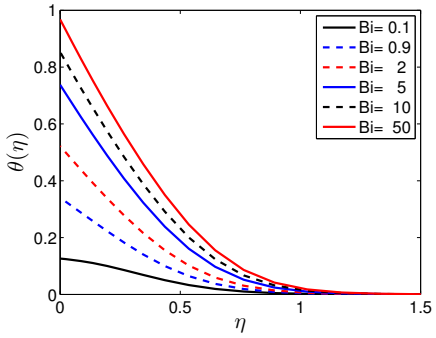

Figure 17. Effects of the Biot number (Bi) on $\theta(\eta)$ for $n = 3, A = 0.3, Ha = 0.5, Nr = 0.2, Pr = 7$, $Nb = 0.5, Nt = 0.5, Nd = 0.02, Sc = 7, R_0 = 0.3, Ld = 0.02$.

Figure 18 shows that high values of the stretching sheet parameter n lead to a reduction in the thickness of the nanoparticle concentration boundary layer thickness up to a certain value of η. Beyond this critical distance, the opposite trend is observed. In Figure 19, we observe a similar pattern of nanoparticle concentration profiles as in Figures 9 and 10. In Figure 20, the nanoparticle concentration profiles increase with the thermophoresis parameter. Similar results are shown in Figure 21 for the Brownian motion parameter. In Figure 22, it is observed that increasing the Schmidt number reduces the nanoparticle concentration profile. The Schmidt number Sc has an opposite effect on the Brownian diffusion coefficient. When D_B is small, the penetration depth of the nanoparticle concentration profiles becomes shorter. Thus, as the Schmidt number increases, the penetration depth becomes shorter. Moreover, the increase in Sc results in a decrease in the concentration rate, as well as the heat transfer rate.

It is interesting to note that Figures 23–27 suggest different ways of controlling the entropy generation. Figure 23 shows the effect of the Reynolds number on the entropy generation N_G. It is observed that entropy generation increases with the increase in the Reynolds number. This observation could be explained by the increase in random eddies, vortices and flow fluctuation in the fluid, which are associated with increasing Re. As a consequence, the heat transfer increases, which, in turn, enhances the entropy generation. The entropy generation number increases in the proximity of the sheet due to a decrease in the fluid friction. Reducing the Reynolds number induces a reduction in the entropy generation number.

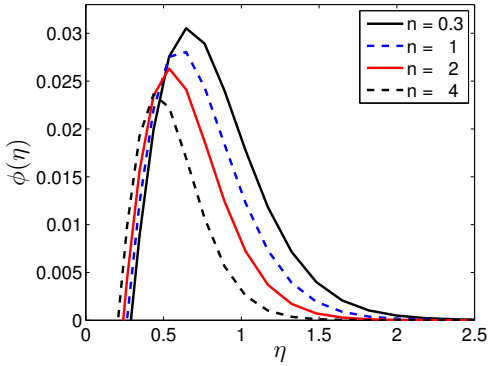

Figure 18. Effects of the stretching parameter (n) on $\phi(\eta)$ when $A = 0.3, Ha = 0.5, Nr = 0.2, Pr = 7$, $Nb = 0.5, Nt = 0.5, Nd = 0.02, Sc = 7, R_0 = 0.3, Ld = 0.02, Bi = 0.2$.

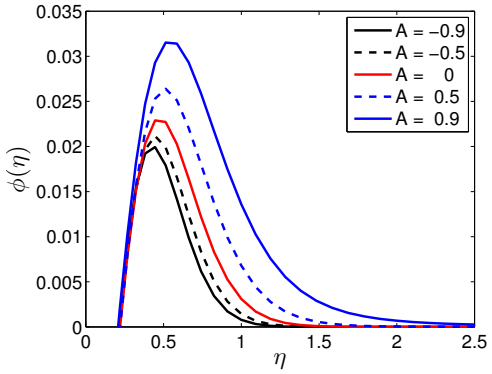

Figure 19. Effects of the unsteadiness parameter (A) on $\phi(\eta)$ for $n = 3, Ha = 0.5, Nr = 0.2, Pr = 7, Nb = 0.5, Nt = 0.5, Nd = 0.02, Sc = 7, R_0 = 0.3, Ld = 0.02, Bi = 0.2$.

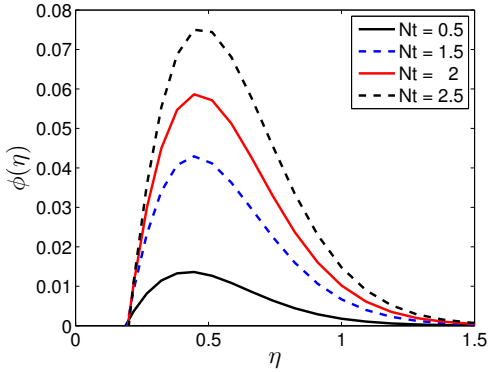

Figure 20. Effects of the thermophoresis parameter (Nt) on $\phi(\eta)$ for $n = 3, A = 0.3, Ha = 0.5, Nr = 0.2, Pr = 7, Nb = 0.5, Nd = 0.02, Sc = 7, R_0 = 0.3, Ld = 0.02, Bi = 0.2$.

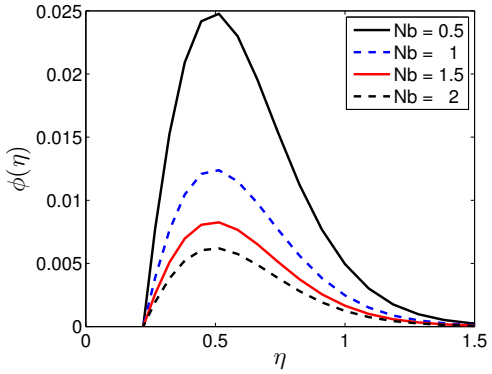

Figure 21. Effects of the Brownian motion parameter (Nb) on $\phi(\eta)$ when $n = 3, A = 0.3, Ha = 0.5, Nr = 0.2, Pr = 7, Nt = 0.5, Nd = 0.02, Sc = 7, R_0 = 0.3, Ld = 0.02, Bi = 0.2$.

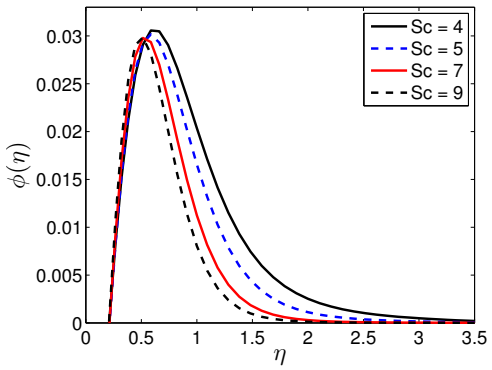

Figure 22. Effects of the Schmidt number (Sc) on $\phi(\eta)$ for $n = 3, A = 0.3, Ha = 0.5, Nr = 0.2$, $Pr = 7, Nb = 0.5, Nt = 0.5, R_0 = 0.3, Bi = 0.2$.

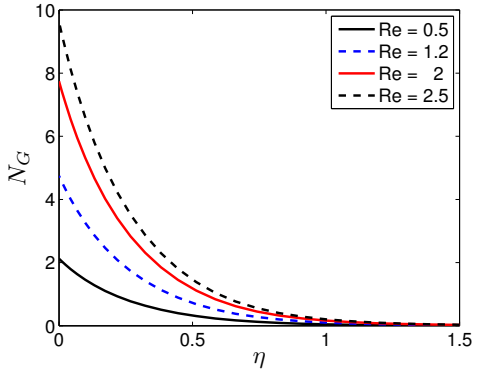

Figure 23. Effects of the Reynolds number Re on the entropy generation number N_G when $Nr = 0.2$, $Br = 1, \Omega = 1, Ha = 0.5$ and $\Sigma = 0.5$.

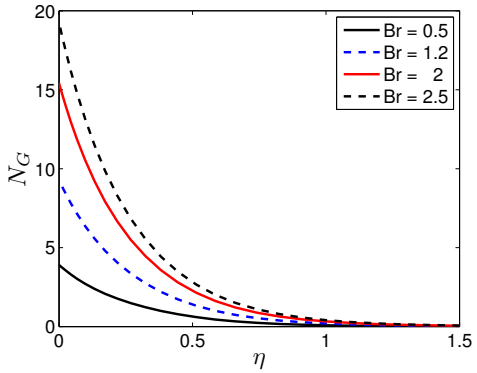

Figure 24. Effects of Brinkman number Br on the entropy generation number N_G when $Re = 2$, $Nr = 0.2, \Omega = 1, Ha = 0.5$ and $\Sigma = 0.5$.

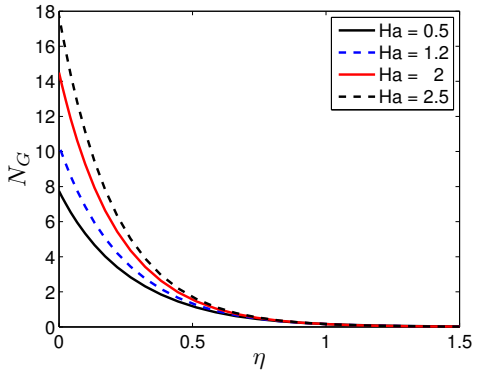

Figure 25. Effects of Hartmann number Ha on the entropy generation number N_G when $Re = 2$, $Nr = 0.2, Br = 1, \Omega = 1$ and $\Sigma = 0.5$.

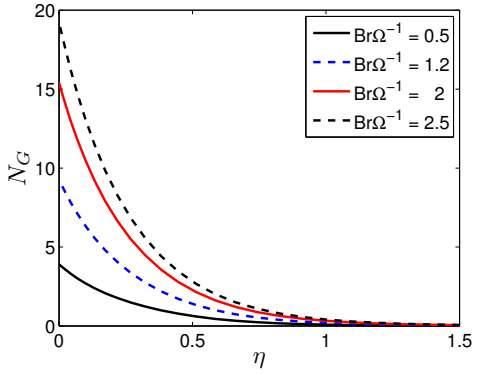

Figure 26. Effects of the Brinkman group parameter $Br\Omega^{-1}$ on the entropy generation number N_G when $Re = 2, Nr = 0.2, Br = 1$ and $\Sigma = 0.5$.

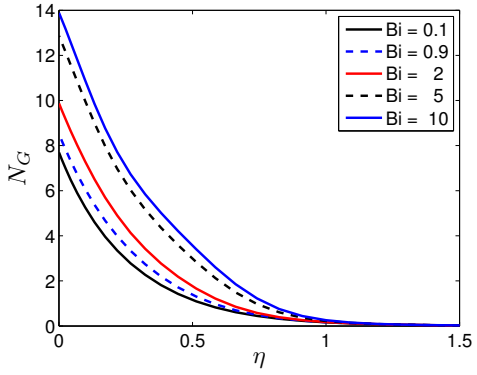

Figure 27. Effects of Biot number Bi on the entropy generation number N_G when $Re = 2$, $Nr = 0.2$, $Br = 1, Ha = 0.5, \Omega = 1$ and $\Sigma = 0.5$.

Figure 24 shows entropy generation with the Brinkman number. The Brinkman number is a measure of the importance of heat produced by viscous heating relative to heat transported by molecular conduction. An increase in the Brinkman number causes an increase in the entropy generation in the vicinity of the sheet. Heat produced by viscous dissipation dominates over heat transported by molecular conduction in the proximity of the sheet. In the vicinity of the sheet,

significant heat generation occurs within the layers of the moving fluid particles, which in turn increases the entropy generation number by enhancing the degree of disorder of the system. This gradually fades with the distance from the sheet.

The influence of the Hartmann number on the entropy generation number is given in Figure 25. In close proximity to the sheet, an increase in the Hartmann number corresponds to a noticeable increase in the entropy generation, whereas far from the sheet, the increase in the Hartmann number has rather negligible impact on entropy generation. This change in entropy generation number in response to the Hartmann number is related to the increase in the resistance of the fluid motion due to an increase in the Hartmann number. This variation in entropy generation with the Hartmann number can be attributed to higher heat transfer rates, which result in an increase of the entropy generation number. However, far from the sheet, the effect of the Hartmann number is insignificant, causing a corresponding insignificant entropy generation.

Figure 26 displays the entropy generation with the Brinkman parameter ($Br\Omega^{-1}$). An increase in $Br\Omega^{-1}$ results in a remarkable increase in the entropy generation number in the area surrounding the sheet. The increase in the entropy generation number around the sheet due to the increase in $Br\Omega^{-1}$ can be related to a decrease in the fluid friction caused by increasing $Br\Omega^{-1}$. Moreover, Equation (31) suggests that the increase in $Br\Omega^{-1}$ results in an increase in the sheet velocity, which affects the fluid in the surroundings of the sheet and that explains, in part, the noticeable effect of $Br\Omega^{-1}$ on the entropy generation proximity of the sheet and the negligible effect in the further region. Figure 27 demonstrates the relation between the Biot number and the entropy generation number. The entropy generation number increases prominently in the proximity of the sheet as the Biot number increases. On the contrary, the Biot number has an insignificant effect on the entropy generation number far away from the sheet.

Figure 28 demonstrates how the skin friction $-f''(0)$ varies according to different values of the magnetic field parameter Ha and the stretching sheet parameter n. It is observed that $-f''(0)$ increases with increasing values of Ha and n.

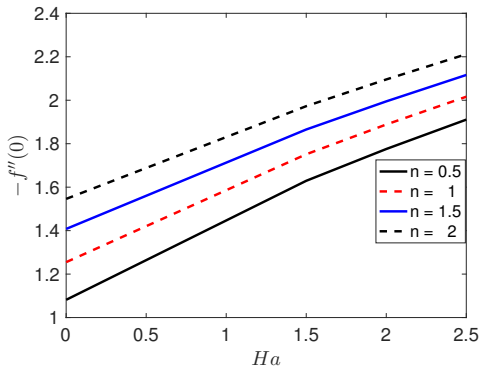

Figure 28. Effect of the magnetic field Ha and the stretching sheet parameter n on the skin friction $-f''(0)$ when $A = 0.3, Pr = 7, Nr = 0.2, Nb = 0.5, Nt = 0.5, Nd = 0.02, Ld = 0.02, Sc = 7, R_0 = 0.3, Bi = 0.2$.

The variation in the Nusselt number $-\theta'(0)$ due to the thermophoresis number Nt and the stretching sheet parameter n is graphed in Figure 29. It is noticed that with increasing values of Nt and n, $-\theta'(0)$ decreases.

Figure 30 displays the change in the Sherwood number $-S'(0)$ caused by the effect of the Schmidt number Sc and the stretching sheet parameter n. It is observed that $-S'(0)$ increases as Sc and n increase.

The changing of the Nusselt number $-\theta'(0)$ due to the effect of the Prandtl number Pr, and the thermal radiation parameter Nr is exhibited in Figure 31. The figure depicts that the $-\theta'(0)$ is an increasing function of Pr and Nr.

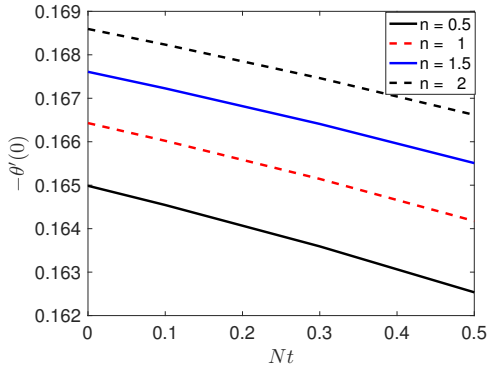

Figure 29. Effect of the thermophoresis number (Nt) and the stretching sheet parameter (n) on the Nusselt number ($-\theta'(0)$) when $A = 0.3, Ha = 0.5, Pr = 7, Nr = 0.2, Nb = 0.5, Nd = 0.02, Ld = 0.02, Sc = 7, R_0 = 0.3, Bi = 0.2$.

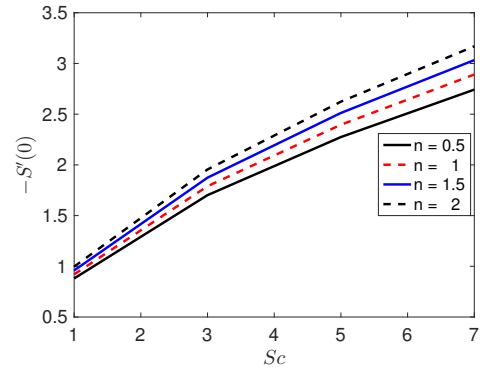

Figure 30. Effect of the Schmidt number Sc and the stretching sheet parameter n on the Sherwood number $-S'(0)$ when $A = 0.3, Ha = 0.5, Pr = 7, Nr = 0.2, Nb = 0.5, Nd = 0.02, Ld = 0.02, Nt = 0.5, R_0 = 0.3, Bi = 0.2$.

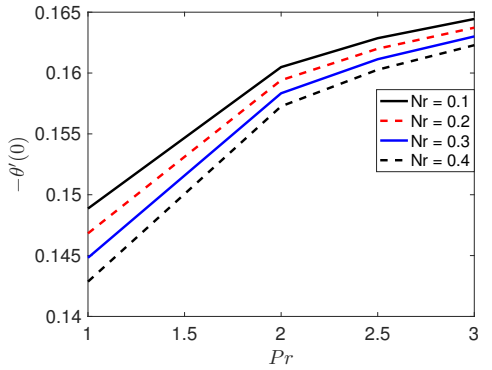

Figure 31. Effect of the Prandtl number Re and the thermal radiation parameter Nr on the Nusselt number $-\theta'(0)$ when $n = 3, A = 0.3, Ha = 0.5, Sc = 7, Nb = 0.5, Nd = 0.02, Ld = 0.02, Nt = 0.5, R_0 = 0.3, Bi = 0.2$.

6. Conclusions

A mathematical formulation and analysis of the entropy generation rate in an unsteady three-dimensional axisymmetric MHD nanofluid flow over a non-linear stretching sheet subject to thermal radiation and a chemical reaction has been presented. The influence of different physical parameters on the entropy generation number has been demonstrated and discussed in detail. From the discussion, the following outcomes may be inferred:

1. The heat transfer rate increases with increasing sheet stretching.
2. An increase in the Reynolds number and the Brinkman number corresponds to a significant increase in the entropy generation number. Therefore, it can be ascertained that the entropy generation number is highly affected by viscous dissipation when the nanofluid flow has a large Reynolds number.
3. An increase in the Biot and Hartmann numbers corresponds to a significant increase in the entropy generation number in the vicinity of the sheet surface. The significance of the Biot and Hartmann numbers gradually fades with distance from the sheet.
4. The entropy generation rate can be minimized by controlling the physical parameters.
5. The number of collocation points has a significant influence on the accuracy of the solutions.

Acknowledgments: The authors would like to thank the University of KwaZulu-Natal, DST-NRF Centre of Excellence in Mathematical and Statistical Sciences (CoE-MaSS) and Claude Leon Foundation, South Africa, for the financial support. Furthermore, the authors are thankful to the reviewers for their valuable comments and suggestions, which have improved the quality of this paper.

Author Contributions: Sabyasachi Mondal proposed the main idea and design framework. Mohammed Almakki carried out the numerical simulations and the first draft of this paper. Sharadia Dey and Precious Sibanda revised the draft, done some write-up and checked the calculations. All authors contributed equally in the analysis of the results.

Conflicts of Interest: The authors declare no conflict of interest.

Abbreviations

The following abbreviations are used in this manuscript:

r, θ, z	cylindrical polar coordinate axes
B_0	magnetic field strength ($kg{\cdot}s^{-2}A^{-1}$)
u	velocity in radial direction ($m{\cdot}s^{-1}$)
n, λ	constants
w	velocity in axial direction ($m{\cdot}s^{-1}$)
ν_f	kinematic viscosity (m^2s^{-1})
T	temperature variable (K)
σ	electrical conductivity ($\Omega^{-1}m^{-1}$)
T_w	temperature of fluid at sheet (K)
ρ_f	density of fluid ($kg{\cdot}m^{-3}$)
T_∞	ambient temperature of fluid (K)
α_f	thermal diffusion of fluid (m^2s^{-1})
C	solute concentration of fluid ($kg{\cdot}m^{-3}$)
C_W	solute concentration at wall ($kg{\cdot}m^{-3}$)
C_∞	solute concentration far away from the disk ($kg{\cdot}m^{-3}$)
ψ	nanoparticle concentration
ψ_W	nanoparticle concentration at wall
ψ_∞	nanoparticle concentration far away from the disk

τ	ratio of nanoparticle heat capacity
D_B	Brownian mention coefficient ($kg{\cdot}m^{-1}s^{-1}$)
D_T	Thermophoretic diffusion coefficient ($kg{\cdot}m^{-1}s^{-1}K^{-1}$)
D_{TC}	Dufour diffusion coefficient
c_p	specific heat ($m^2s^{-2}K^{-1}$)
k_f	thermal conductivity ($W{\cdot}m^{-1}K^{-1}$)
q_r	radiative heat flux ($kg{\cdot}m^{-2}$)
D_s	solute diffusion coefficient
D_{CT}	Soret diffusion coefficient
R	chemical reaction parameter
$(\rho c_p)_s$	heat capacity of the nanoparticle
$(\rho c_p)_f$	heat capacity of fluid
σ^*	Stefan–Boltzmann constant
K^*	mean absorption coefficient
R_0, a	constants
k_0, b_0	constants
h_f	heat transfer coefficient ($W{\cdot}m^{-2}\ K^{-1}$)
Bi	Biot number
η	dimensionless variable
θ	dimensionless temperature
S	dimensionless solute concentration
ϕ	dimensionless nanoparticle concentration
f	dimensionless velocity
A	unsteadiness parameter
Ha	Hartmann number
Nr	thermal radiation parameter
Pr	Prandtl number
Nb	Brownian mention parameter
Nt	Thermophoresis parameter
Nd	Dufour parameter
Sc	Schmidt number
Ld	Soret parameter
C_f	skin friction coefficient
Nu_r	Nusselt number
Sh_r	Sherwood number
$u_w(r)$	velocity of the stretching sheet
Re	Reynolds number
h_w	heat flux ($W{\cdot}m^{-2}$)
h_m	mass flux ($kg{\cdot}m^{-2}s^{-1}$)
E_{gen}	volumetric entropy generation per unit length ($W{\cdot}m^{-3}\ K^{-1}$)
E_0	dimensionless entropy generation rate
Br	Brinkman number
Ω	dimensionless parameter
Ha	Hartmann number
Σ	diffusive constant parameter
ΔT	difference between $(T_W - T_\infty)(K)$

References

1. Dessie, H.; Kishan, N. Unsteady MHD flow of heat and mass transfer of nanofluids over stretching sheet with a non-uniform heat/source/sink considering viscous dissipation and chemical reaction. *Int. J. Eng. Res. Afr.* **2015**, *14*, doi:10.4028/www.scientific.net/JERA.14.1.
2. Chol, S. Enhancing thermal conductivity of fluids with nanoparticles. *ASME Publ. FED* **1995**, *231*, 99–106.
3. Buongiorno, J. Convective transport in nanofluids. *J. Heat Transf.* **2006**, *128*, 240–250.

4. Ahmed, N.; Goswami, J.; Barua, D. Effects of chemical reaction and radiation on an unsteady MHD flow past an accelerated infinite vertical plate with variable temperature and mass transfer. *Indian J. Pure Appl. Math.* **2013**, *44*, 443–466.
5. Ahmed, J.; Mahmood, T.; Iqbal, Z.; Shahzad, A.; Ali, R. Axisymmetric flow and heat transfer over an unsteady stretching sheet in power law fluid. *J. Mol. Liq.* **2016**, *221*, 386–393.
6. Mohammadiun, H.; Rahimi, A.; Kianifar, A. Axisymmetric stagnation-point flow and heat transfer of a viscous, compressible fluid on a cylinder with constant heat flux. *Sci. Iran.* **2013**, *20*, 185–194.
7. Xiao, B.; Yang, Y.; Chen, L. Developing a novel form of thermal conductivity of nanofluids with Brownian motion effect by means of fractal geometry. *Powder Technol.* **2013**, *239*, 409–414.
8. Cai, J.; Hu, X.; Xiao, B.; Zhou, Y.; Wei, W. Recent developments on fractal-based approaches to nanofluids and nanoparticle aggregation. *Int. J. Heat Mass Transf.* **2017**, *105*, 623–637.
9. Shankar, B.; Yirga, Y. Unsteady heat and mass transfer in MHD flow of nanofluids over stretching sheet with a non-uniform heat source/sink. *Int. J. Math. Comput. Sci. Eng.* **2013**, *7*, 1267–1275.
10. Shahzad, A.; Ali, R.; Khan, M. On the exact solution for axisymmetric flow and heat transfer over a nonlinear radially stretching sheet. *Chin. Phys. Lett.* **2012**, *29*, 084705.
11. Ahmad, S.; Ashraf, M.; Syed, K. Effects of thermal radiation on MHD axisymmetric stagnation point flow and heat transfer of a micropolar fluid over a shrinking sheet. *World Appl. Sci. J.* **2011**, *15*, 835–848.
12. Mabood, F.; Shafiq, A.; Hayat, T.; Abelman, S. Radiation effects on stagnation point flow with melting heat transfer and second order slip. *Results Phys.* **2017**, *7*, 31–42.
13. Prasad, K.; Vaidya, H.; Vajravelu, K.; Datti, P.; Umesh, V. Axisymmetric mixed convective MHD flow over a slender cylinder in the presence of chemically reaction. *Int. J. Appl. Mech. Eng.* **2016**, *21*, 121–141.
14. Sarada, K.; Shanker, B. The effect of chemical reaction on an unsteady MHD free convection flow past an infinite vertical porous plate with variable suction. *Int. J. Eng. Mod. Res.* **2013**, *3*, 725–735.
15. Hunegnaw, A.; Kishan, N. Unsteady MHD heat and mass transfer flow over stretching sheet in porous medium with variable properties considering viscous dissipation and chemical reaction. *Am. Chem. Sci. J.* **2014**, *4*, 901–917.
16. Barik, R. Heat and Mass Transfer Effects on Unsteady MHD Flow through an Accelerated Isothermal Vertical Plate Embedded in Porous Medium in the Presence of Heat Source and Chemical Reaction. *Eur. J. Adv. Eng. Technol.* **2016**, *3*, 56–61.
17. Bejan, A. *Entropy Generation Minimization: The Method of Thermodynamic Optimization of Finite-Size Systems and Finite-Time Processes*; CRC Press: Boca Raton, FL, USA, 1995.
18. Qing, J.; Bhatti, M.M.; Abbas, M.A.; Rashidi, M.M.; Ali, M.E.S. Entropy generation on MHD Casson nanofluid flow over a porous stretching/shrinking surface. *Entropy* **2016**, *18*, 123.
19. Rashidi, M.M.; Bhatti, M.M.; Abbas, M.A.; Ali, M.E.S. Entropy generation on MHD blood flow of nanofluid due to peristaltic waves. *Entropy* **2016**, *18*, 117.
20. Bhatti, M.M.; Abbas, T.; Rashidi, M.M.; Ali, M.E.S.; Yang, Z. Entropy generation on MHD eyring—Powell nanofluid through a permeable stretching surface. *Entropy* **2016**, *18*, 224.
21. Rashidi, M.; Mohammadi, F.; Abbasbandy, S.; Alhuthali, M. Entropy generation analysis for stagnation point flow in a porous medium over a permeable stretching surface. *J. Appl. Fluid Mech.* **2015**, *8*, 753–765.
22. Bhatti, M.M.; Abbas, T.; Rashidi, M.M.; Ali, M.E.S. Numerical simulation of entropy generation with thermal radiation on MHD Carreau nanofluid towards a shrinking sheet. *Entropy* **2016**, *18*, 200.
23. Freidoonimehr, N.; Rahimi, A.B. Comment on "Effects of thermophoresis and Brownian motion on nanofluid heat transfer and entropy generation" by M. Mahmoodi, Sh. Kandelousi, Journal of Molecular Liquids, 211 (2015) 15–24. *J. Mol. Liq.* **2016**, *216*, 99–102.
24. Agbaje, T.; Mondal, S.; Makukula, Z.; Motsa, S.; Sibanda, P. A new numerical approach to MHD stagnation point flow and heat transfer towards a stretching sheet. *Ain Shams Eng. J.* **2016**, in press.
25. Kaladhar, K.; Motsa, S.; Srinivasacharya, D. Mixed Convection Flow of Couple Stress Fluid in a Vertical Channel with Radiation and Soret Effects. *J. Appl. Fluid Mech.* **2016**, *9*, 43–50.
26. Nield, D.; Kuznetsov, A. The onset of convection in a horizontal nanofluid layer of finite depth: A revised model. *Int. J. Heat Mass Transf.* **2014**, *77*, 915–918.
27. Mustafa, M.; Khan, J.A.; Hayat, T.; Alsaedi, A. Analytical and numerical solutions for axisymmetric flow of nanofluid due to non-linearly stretching sheet. *Int. J. Non Linear Mech.* **2015**, *71*, 22–29.

28. Sajid, M.; Hayat, T.; Asghar, S.; Vajravelu, K. Analytic solution for axisymmetric flow over a nonlinearly stretching sheet. *Arch. Appl. Mech.* **2008**, *78*, 127–134.
29. Pal, D. Heat and mass transfer in stagnation-point flow towards a stretching surface in the presence of buoyancy force and thermal radiation. *Meccanica* **2009**, *44*, 145–158.
30. Arikoglu, A.; Ozkol, I.; Komurgoz, G. Effect of slip on entropy generation in a single rotating disk in MHD flow. *Appl. Energy* **2008**, *85*, 1225–1236.
31. Bellman, R.E.; Kalaba, R.E. *Quasilinearization and Nonlinear Boundary-Value Problems*; RAND Corporation: New York, NY, USA, 1965.
32. Canuto, C.; Hussaini, M.Y.; Quarteroni, A.M.; Thomas, A., Jr. *Spectral Methods in Fluid Dynamics*; Springer: Berlin/Heidelberg, Germany, 2012.
33. Trefethen, L.N. *Spectral Methods in MATLAB*; SIAM: Oxford, UK, 2000.
34. Motsa, S.; Sibanda, P.; Shateyi, S. On a new quasi-linearization method for systems of nonlinear boundary value problems. *Math. Methods Appl. Sci.* **2011**, *34*, 1406–1413.
35. Rashidi, M.; Abelman, S.; Mehr, N.F. Entropy generation in steady MHD flow due to a rotating porous disk in a nanofluid. *Int. J. Heat Mass Transf.* **2013**, *62*, 515–525.

Chapter 3

Entropy generation in unsteady MHD micropolar nanofluid flow with viscous dissipation and thermal radiation

In Chapter 2, we studied the entropy generation in Newtonian fluid flow which is described by a system of ordinary differential equations. Despite being more complex than Newtonian fluids, non-Newtonian fluids have significantly more uses in industry. This chapter extends the work in Chapter 2 to a non-Newtonian fluid flow which is described by partial differential equations.

In this chapter we consider entropy generation in unsteady two-dimensional magneto-micropolar nanofluid flow along a linear stretching sheet in a porous medium with heat generation and a chemical reaction. The flow is subject to viscous dissipation and thermal radiation. Thermophoesis and nanoparticle Brownian motion are taken into account. The bivariate spectral quasiliearization method is used solve the model equations.

Entropy generation in unsteady magneto-micropolar nanofluid flow with viscous dissipation and thermal radiation

M. Almakki, H.Mondal*and P. Sibanda

School of Mathematics, Statistics and Computer Science University of KwaZulu-Natal

Pietermaritzburg Private Bag X01

Scottsville 3209, South Africa

August 28, 2018

Abstract

We investigate entropy generation in magneto-micropolar nanofluid flow, particle deposition and thermal radiation effects on boundary layer flow over a stretching sheet with heat generation and a chemical reaction. A novel feature of this study is the investigation of entropy generation in a combined micropolar nanofluid and the use of the recently developed bivariate spectral quasiliearization method to solve the conservation equations. It is found that the method converges fast and accurate results can be achieved with this new method. The results show that entropy generation can be controlled to a degree by controlling the Brinkman and Reynold number.

Keyword: Micropolar, Nanofluids; Entropy generation; Thermal radiation; viscous dissipation

1 Introduction

The MHD micropolar nanofluid flow with a stretching surface has gained increasing importance during recent years owing to the great variety of applications it has on engineering and geophysics. The non-Newtonian fluids help us to understand the behaviour of a wide variety of fluids including micropolar fluids. The viscosity is mainly used to characterize the thickness of a fluid, its behaviors like of non-Newtonian fluids. The micropolar fluids are regarded as isotropic-polar fluids with negligence of the deformation of molecules. Physically, this model can capture the independent rotation of the molecules of the fluids and the local vorticity. A fluid represented by such a model can exhibit body couples, couple stresses, and exhibit microrotational and microinertial effects. This occurs in thermal energy storage, aerodynamic extrusion of polymer sheets, petroleum reservoirs. Magneto-micropolar fluids can be used to model body fluids including cerebral-spinal fluid. Hassanien et al. [1] investigated the micropolar fluid flow along a non-isothermal stretching sheet with suction/blowing. A Numerical methods have been applied to solve microploar fluids [2]. Hsiao [3] studied the influence of MHD flow of micropolar fluid subject to heat and mass transfer with viscous dissipation over permeable medium. Das [4] proposed a model to consider the influence of thermal radiation and the first order chemical radiation of MHD micropolar fluid. The small perturbation approximation is used to solve the system.

In this study, the entropy generation mechanisms are made dependent on many factors namely, magneto-micropolar fluid field, heat transfer, fluid friction irreversibility and mass transfer. Entropy quantifies the

*Corresponding author's email id: hiranmoymondal@yahoo.com

disorder of the molecules of a system. Entropy is related to the thermal performance of engineering systems as it is proportional to the irreversible processes which are responsible for the degraded performance.

Srinivasacharya et al. [5] studied entropy generation and heat transfer in MHD flow of micropolar fluid. The finite difference methods are used to solve the system. Related studies, include among others [6, 7, 8, 9, 10, 11, 12].

The objective of this paper is to study magneto-micropolar nanofluid flow past permeable a stretching sheet subject to a chemical reaction, thermal radiation and heat generation. The primary aim is to investigate entropy generation of micropolar nanofluid flow over a stretching sheet. Such a study, is important in, for example, materials processing. The solutions of the transformed conservation equations are obtained using the bivariate spectral quasiliearization method [13, 14]. The significance of fluid and physical parameters on the flow and entropy generation fields is elaborated.

2 Problem formulation

Consider the unsteady laminar two-dimensional MHD flow of a magneto-micropolar fluid along a linear permeable sheet in the xy–plane. The x–axis is parallel to the vertical surface and y–axis is perpendicular to the surface. The flow is subject to viscous dissipation. Thermophoesis, nanoparticle Brownian motion, the chemical reaction and the thermal radiation are considered to be significant. A magnetic field of strength B_0 is exerted in a transverse trend to the flow. The uniform surface and ambient temperatures are given by $T_w(x)$ and T_∞ respectively, while $C_w(x)$ is the concentration close to the surface and C_∞ represents the ambient concentration where $C_w(x)>C_\infty$ and $T_w(x)>T_\infty$. Assumed that $u_w(x)$ is the velocity, concentration $C_w(x)$ and the temperature $T_w(x)$ of the shrinking sheet are linear function. The flow configuration is represented in Figure (1).

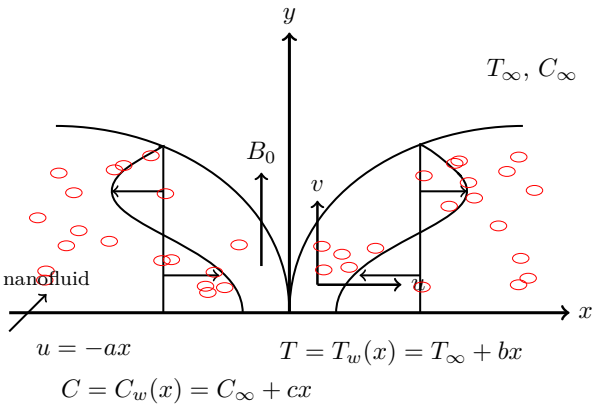

Figure 1: Physical configuration.

The equations that describe such micropolar fluid flow are (see [15, 16, 17])

(i) The continuity equation

$$\frac{\partial u}{\partial x} + \frac{\partial v}{\partial y} = 0. \tag{1}$$

(ii) The momentum equation

$$\frac{\partial u}{\partial t} + u\frac{\partial u}{\partial x} + v\frac{\partial u}{\partial y} = \left(\frac{k_1^*}{\rho} + \nu\right)\frac{\partial^2 u}{\partial y^2} + \frac{k_1^*}{\rho}\frac{\partial N}{\partial y} - \frac{\sigma B_0^2}{\rho}u + g\beta_c(C - C_\infty) + g\beta_t(T - T_\infty). \tag{2}$$

(iii) The angular momentum equation

$$\rho j\left(\frac{\partial N}{\partial t}+u\frac{\partial N}{\partial x}+v\frac{\partial N}{\partial y}\right)=\frac{\partial^2 N}{\partial y^2}\gamma-k_1^*\left(2N+\frac{\partial u}{\partial y}\right). \tag{3}$$

(iv) The energy equation

$$\frac{\partial T}{\partial t}+u\frac{\partial T}{\partial x}+v\frac{\partial T}{\partial y}=\frac{\mu}{\rho c_p}\left(\frac{\partial u}{\partial y}\right)^2+\alpha\frac{\partial^2 T}{\partial y^2}+\frac{1}{\rho c_p}\frac{16\sigma^* T_\infty^3}{3k^*}\frac{\partial^2 T}{\partial y^2}+\frac{\gamma}{\rho c_p}\left(\frac{\partial N}{\partial y}\right)^2+\frac{Q}{\rho c_p}(T-T_\infty)$$
$$+\tau\left(D_B\frac{\partial T\partial C}{\partial y^2}+\frac{D_T}{T_\infty}\left(\frac{\partial T}{\partial y}\right)^2\right). \tag{4}$$

(v) The mass diffusion equation

$$\frac{\partial C}{\partial t}+u\frac{\partial C}{\partial x}+v\frac{\partial C}{\partial y}=\frac{D_T}{T_\infty}\frac{\partial^2 T}{\partial y^2}+D_B\frac{\partial^2 C}{\partial y^2}-R(C-C_\infty), \tag{5}$$

where u is the velocity along the x–direction, t is the time variable , v is the velocity along the y– direction, ν is the kinematic viscosity, k_1^* represents the vortex viscosity, N angular velocity of the microroration, which is rotation in x, y–directions, σ represents the electrical conductivity, j represents the microinertia density and γ represents the spin gradient viscosity. Moreover, $\alpha=(k_f/\rho c_p)$ is the thermal diffusion which represents the ratio between the effective thermal conductivity and the effective specific heat, σ^* is steaffan-Boltzman constant, k^* represents mean absorption coefficient, Q represents the volumetric rate of heat generation, $\tau=(\rho c)_p/(\rho c)_f$ is proportion between the effective heat capacity of the nanofluid and the heat capacity of the base fluid, D_T and D_B are thermophoretic diffusion coefficient and the Brownian mention coefficient; respectively, and R represents the chemical reaction. The spin gradient viscosity γ, is proportion to the viscosity and micro-inertia such that $\gamma=j\left(\mu+0.5k_1^*\right)$ (see [18]) where $j=\nu/a$.

The auxiliary conditions are

$$u=u_w=-ax,\ v=v_w,\ T=T_w(x)=bx+T_\infty,\ N=-n\frac{\partial u}{\partial y},\ C=C_w=cx+C_\infty\ \text{ as }\ y=0,$$
$$u\to 0,\ v\to 0,\ N\to 0,\ C\to C_\infty,\ T\to T_\infty\ \text{ as }\ y\to\infty, \tag{6}$$

where $a,\ b,\ c>0$, u_w is the shrinking velocity, $v_w=v_0x$ is the variable suction/injection velocity with v_0 begin a constant and when $k_1^*=0$ the fluid is viscous. The boundary parameter n takes values in the range $[0,1]$ with $n=0$ implying that the microelements at the boundary are unable to rotate and there is a low concentration of the nanoparticles. When $n=\frac{1}{2}$, the anti-symmetric stress tensor vanishes and the concentration of the nanoparticles is low. When $n=1$, the flow becomes turbulent.

The conservation equations are reduced to a dimensionless form using the following variables (see [16]):

$$\psi=(a\nu)^{1/2}\xi^{1/2}xf(\eta,\xi),\quad \eta=\left(\frac{a}{\nu}\right)^{1/2}\xi^{-1/2}y,\ \xi=1-e^{\zeta},\quad \zeta=at,$$
$$N=\left(\frac{a}{\nu}\right)^{1/2}\xi^{-1/2}axh(\eta,\xi),\ \theta(\eta,\xi)=\frac{T-T_\infty}{T_w-T_\infty},\quad \phi(\eta,\xi)=\frac{C-C_\infty}{C_w-C_\infty}. \tag{7}$$

Thus, the system of Eqs. (1)–(5) is transformed to

$$(1+K)f'''+Kh'+0.5(1-\xi)\eta f''+\xi(ff''-f'^2-Ha^2f'+\omega_t\theta+\omega_c\phi)=\frac{\partial f'}{\partial\xi}(1-\xi)\xi, \tag{8}$$
$$\left(1+\frac{K}{2}\right)h''+0.5(1-\xi)(h+\eta h')+\xi(fh'-f'h)-\xi(2h+f'')K=\frac{\partial h}{\partial\xi}(1-\xi)\xi, \tag{9}$$

$$\frac{Nr+1}{Pr}\theta'' + 0.5(1-\xi)\eta\theta' + \xi(f\theta' - f'\theta) + \xi Nb\theta'\phi' + \xi Nt\theta'^2 + Ecf''^2 + \xi Q_0\theta + \frac{Ec}{\xi}\Big(1+\frac{K}{2}\Big)h'^2 = \frac{\partial\theta}{\partial\xi}(1-\xi)\xi, \tag{10}$$

$$\frac{1}{Sc}\phi'' + 0.5(1-\xi)\eta\phi' + \xi(f\phi' - f'\phi) + \xi\frac{Nt}{Nb}\theta'' - \xi R_0\phi = \frac{\partial\phi}{\partial\xi}(1-\xi)\xi, \tag{11}$$

with boundary conditions (see [16]) given by

$$f(0,\xi) = s,\ f'(0,\xi) = 1,\ h(0,\xi) = -nf''(0,\xi),\ \theta(0,\xi) = 1,\ \phi(\xi,0) = 1,\ f'(\infty,\xi)\to 0,$$
$$h(\infty,\xi)\to 0,\ \theta(\infty,\xi)\to 0,\ \phi(\infty,\xi)\to 0. \tag{12}$$

where $0 \le \xi \le 1$, primes denote the derivative related to η and $s = v_0 x/(a\nu)^{1/2}\xi^{1/2}$. The parameters in Eqs. (8)–(11) are defined as follows

$$K = \frac{k_1^*}{\mu},\ Ha = B_0\sqrt{\frac{\sigma}{\rho a}},\ Nr = \frac{16\sigma^* T_\infty^3}{3kk^*},\ \omega_t = \frac{g\beta_t\Big(T_w - T_\infty\Big)x/\nu^2}{u_w^2\nu^2},\ Pr = \frac{\nu}{\alpha},$$
$$Sc = \frac{\nu}{D_B}, \omega_c = \frac{g\beta_c\Big(C_w - C_\infty\Big)x/\nu^2}{u_w^2\nu^2},\ Ec = \frac{a^2 x}{bc_p},\ Nb = \frac{\tau(C_w - C_\infty)D_B}{\nu},$$
$$Nt = \frac{\tau(T_w - T_\infty)D_T}{\nu T_\infty},\ Q_0 = \frac{Q(T_w - T_\infty)}{abx\rho c_p},\ R_0 = \frac{R(C_w - C_\infty)}{acx}, \tag{13}$$

where K represents the material parameter, Ha represents the Hartmann number, ω_t represents the temperature Grashof number, ω_c represents the concentration Grashof number Nr,Nb, Pr and Nt are the thermal radiation parameter, the Brownian mention parameter, the Prandtl number and the Thermophoresis parameter respectively, Ec is the Eckert number, Q_0 represents the heat generation parameter, Sc represents the Schmidt number and R_0 represents chemical reaction parameter.

The skin friction coefficient along the x–axis C_{f_x}, the Nusselt number Nu_x and the Sherwood number Sh_x are the most significant physical quantities, such that:

$$C_f = \frac{\tau_w}{\rho u_w^2(x)}, \tag{14}$$

where

$$\tau_w = \left((\mu + k_1^*)\frac{\partial u}{\partial y} + k_1^* N\right)_{y=0}. \tag{15}$$

Thus

$$C_{f_x}Re^{1/2} = f''(0,\xi)\Big(1 + (1-n)K\Big)\xi^{-1/2}, \tag{16}$$

where $\frac{u_w(x)x}{\nu} = Re$ represents Reynolds number. However, the Nusselt number

$$Nu_x = \frac{xh_w}{k_f(T_w - T_\infty)}, \tag{17}$$

where h_w represents the surface heat flux, which is given as:

$$h_w = -\left(k_f + \frac{16\sigma^* T_\infty^3}{3k^*}\right)\left(\frac{\partial T}{\partial y}\right)_{y=0}. \tag{18}$$

Eq. (17) becomes as

$$Nu_x Re^{-1/2} = -\xi(1+Nr)\theta'(0,\xi). \tag{19}$$

Finally, the Sherwood number is

$$Sh_x = \frac{xh_m}{\rho D_B(C_w - C_\infty)}, \tag{20}$$

where h_m represents the surface mass flux, which can be obtained from

$$h_m = -\rho D_B\Big(\frac{\partial C}{\partial y}\Big)_{y=0}, \tag{21}$$

hence, Eq. (20) becomes as

$$Sh_x Re^{-1/2} = -\xi^{-1/2}\phi'(0,\xi). \tag{22}$$

3 Entropy generation analysis

Entropy generation is dependent on the reversibility of a specified procedure. In an isolated system, entropy tends to increase with time, but remains steady for reversible reactions. Due to the increasing use application of nanofluids and nanoparticles in engineering and medical applications, it is imperative to investigate and study the impact of these nanoparticles on entropy generation on real life, [19]. This study focus on entropy generation along the sheet of magneto-micropolar nanofluids.

The volumetric rate of local entropy generation S'''_{gen}, which is given for two-dimensional flow as below

$$S'''_{gen} = \underbrace{\frac{1}{T_\infty^2}\Big(k_f + \frac{16\sigma^* T_\infty^3}{3k^*}\Big)\Big(\frac{\partial T}{\partial y}\Big)^2}_{S_{th}} + \underbrace{\frac{\sigma B_0^2}{T_\infty}u^2}_{S_m} + \underbrace{\frac{\mu(1+K)}{T_\infty}\Big(\frac{\partial u}{\partial y}\Big)^2}_{S_{dis}} + \underbrace{\frac{\gamma}{T_\infty}\Big(\frac{\partial N}{\partial y}\Big)^2}_{S_{rot}} + \underbrace{\frac{RD}{C_\infty}\Big(\frac{\partial C}{\partial y}\Big)^2 + \frac{RD}{T_\infty}\Big(\frac{\partial T}{\partial y}\frac{\partial C}{\partial y}\Big)}_{S_{dif}}. \tag{23}$$

Eq. (23) reveals that the entropy generation is a contribution of sixth sources. The first source is caused by heat transfer or the thermal radiation, heat transfer irreversibility (HTI), (S_{th}), the second source is caused by the magnetic field (S_m); the third is caused by viscous dissipation (S_{dis}); the fourth is caused by micro-rotation (S_{rot}) and the fifth and sixth terms are caused by mass transfer (S_{dif}). Therefore, the volumetric rate of local entropy generation is obtained as a linear combination of $(S_{th}), (S_m), (S_{dis}), (S_{rot})$ and (S_{dif}) such that

$$S'''_{gen} = (S_{th}) + (S_m) + (S_{dis}) + (S_{rot}) + (S_{dif}). \tag{24}$$

It is suitable to write the entropy generation number (N_G) as a ratio between (S'''_{gen}) and a rate of entropy generation (S'''_0) where S'''_0 given as([20])

$$S'''_0 = \frac{k_f(T_w - T_\infty)^2}{T_\infty^2 x^2}. \tag{25}$$

The characteristic entropy generation rate S'''_0 demonstrates the optimal entropy generation at which the thermodynamic performance of a system is optimized [21]. Finding S'''_0 requires solving an optimization problem which is constrained by the irreversible operations of the system. The physical characteristics of the system is varied until a minimum entropy generation is found Bejan [21].

The entropy generation number N_G can be obtained as

$$N_G = \frac{S'''_{gen}}{S'''_0} = Re\xi^{-1}(1+Nr)\theta'^2 + \frac{ReBr}{\Omega}\left(\xi^{-1}(1+K)f''^2 + \xi^{-2}(1+K/2)h'^2 + Ha^2 f'^2\right) + Re\Sigma\left(\frac{\chi}{\Omega}\right)^2\xi^{-1}\phi'^2 + Re\Sigma\frac{\chi}{\Omega}\xi^{-1}\theta'\phi', \tag{26}$$

where χ is the concentration difference, Br, Ω, Σ are the Brinkman number, the temperature difference and a constant parameter, respectively. These can be expression as:

$$Br = \frac{\mu^2 u_w^2(x)}{k_f \Delta T},\ \Omega = \frac{\Delta T}{T_\infty} = \frac{T_w - T_\infty}{T_\infty},\ \Sigma = \frac{C_\infty RD}{k_f},\quad \chi = \frac{\Delta C}{C_\infty} = \frac{C_w - C_\infty}{C_\infty}, \tag{27}$$

where R and D are the ideal gas and mass diffusion, respectively. In equation (26), there are five irreversibility sources that contribute to the entropy generation number, hence N_G may be re-written as $N_G = S_{th} + S_m + S_{dis} + S_{rot} + S_{dif}$, where

$$S_{th} = Re\xi^{-1}(1+Nr)\theta'^2,\ S_m = \frac{ReBrHa^2 f'^2}{\Omega},\ S_{dis} = \frac{ReBr\xi^{-1}(1+K)f''^2}{\Omega},$$
$$S_{rot} = \frac{ReBr\xi^{-2}(1+K/2)h'^2}{\Omega},\ S_{dif} = Re\Sigma\left(\frac{\chi}{\Omega}\right)^2\xi^{-1}\phi'^2 + Re\Sigma\frac{\chi}{\Omega}\xi^{-1}\theta'\phi'. \tag{28}$$

The fraction of irreversibility from each source can be obtained by dividing the irreversibility source by the total irreversibility leading to non-dimensional parameters, such as

$$\gamma_{th} = \frac{S_{th}}{N_G},\ \gamma_m = \frac{S_m}{N_G},\ \gamma_{dis} = \frac{S_{dis}}{N_G},\ \gamma_{rot} = \frac{S_{rot}}{N_G},\ \gamma_{dif} = \frac{S_{dif}}{N_G}, \tag{29}$$

where γ_{th} is the fraction of irreversibility due to thermal diffusion, γ_m is the fraction of irreversibility due to magnetic field, γ_{dis} is the fraction of irreversibility due to viscous dissipation, γ_{rot} is the fraction of irreversibility due to micro-rotation and γ_{dif} is the fraction irreversibility due to concentration diffusion.

4 Methods of solution

The numerical scheme used to solve Eqs. (8)–(11) with Eq. (12) is described. The momentum equations are simplified using quasi-liearization. The resulting linear PDEs are, then solved using a spectral collocation method. This method has been used successfully to solve non-linear evolution PDEs [13]. Spectral methods produce approximations with high accuracy using comparatively few grid points since they construct the desired approximations from all available function values; [22, 23].

The quasi-linearization method is an iteration-based procedure derived from the Taylor series that is used to approximate unknown function and its derivatives. The iterative nature of the quasi-linearization method implies that previous estimates are denoted using the subscript r and new estimates are denoted by using the subscript $r+1$ where r is the iteration index.

Using the quasi-linearization method on Eqs. (8)–(11) with Eq. (12) result in expanded linear PDEs

$$a_{0,r}f'''_{r+1}+a_{1,r}(\eta,\xi)f''_{r+1}+a_{2,r}(\eta,\xi)f'_{r+1}+a_{3,r}(\eta,\xi)f_{r+1}+a_{4,r}h'_{r+1}+a_{5,r}(\eta,\xi)\theta_{r+1}+$$
$$a_{6,r}(\eta,\xi)\phi_{r+1}-\xi(1-\xi)\frac{\partial f'}{\partial\xi}=R_{1,r}(\eta,\xi), \tag{30}$$
$$b_{0,r}h''_{r+1}+b_{1,r}(\eta,\xi)h'_{r+1}+b_{2,r}(\eta,\xi)h_{r+1}+b_{3,r}(\eta,\xi)f_{r+1}+b_{4,r}(\eta,\xi)f'_{r+1}+b_{5,r}(\eta,\xi)f''_{r+1}-$$
$$\xi(1-\xi)\frac{\partial h}{\partial\xi}=R_{2,r}(\eta,\xi), \tag{31}$$
$$c_{0,r}\theta''_{r+1}+c_{1,r}(\eta,\xi)\theta'_{r+1}+c_{2,r}(\eta,\xi)\theta_{r+1}+c_{3,r}(\eta,\xi)f_{r+1}+c_{4,r}(\eta,\xi)f'_{r+1}+c_{5,r}(\eta,\xi)f''_{r+1}+$$
$$c_{6,r}(\eta,\xi)h'_{r+1}+c_{7,r}(\eta,\xi)\phi'_{r+1}-\xi(1-\xi)\frac{\partial\theta}{\partial\xi}=R_{3,r}(\eta,\xi), \tag{32}$$
$$d_{0,r}\phi''_{r+1}+d_{1,r}(\eta,\xi)\phi'_{r+1}+d_{2,r}(\eta,\xi)\phi_{r+1}+d_{3,r}(\eta,\xi)f_{r+1}+d_{4,r}(\eta,\xi)f'_{r+1}+d_{5,r}(\eta,\xi)\theta''_{r+1}-$$
$$\xi(1-\xi)\frac{\partial\phi}{\partial\xi}=R_{4,r}(\eta,\xi). \tag{33}$$

The boundary conditions can be expressed as

$$f_{r+1}(0,\xi)=s,\ f'_{r+1}(0,\xi)=1,\ \theta_{r+1}(0,\xi)=1,\ h_{r+1}(0,\xi)=-nf''_{r+1}(0,\xi),\ \phi_{r+1}(0,\xi)=1,$$
$$f'_{r+1}(\infty,\xi)\to 0,\ h_{r+1}(\infty,\xi)\to 0,\ \theta_{r+1}(\infty,\xi)\to 0,\ \phi_{r+1}(\infty,\xi)\to 0, \tag{34}$$

where the coefficients in Eqs. (30)–(33) are

$$a_{0,r}=(1+K),\ a_{1,r}(\eta,\xi)=\frac{\eta}{2}(1-\xi)+\xi f_r,\ a_{2,r}(\eta,\xi)=-2\xi f'_r-\xi Ha^2,$$
$$a_{3,r}(\eta,\xi)=\xi f''_r,\ a_{4,r}(\eta,\xi)=K,\ a_{5,r}(\eta,\xi)=\xi w_t,\ a_{6,r}(\eta,\xi)=\xi w_c, \tag{35}$$
$$b_{0,r}=(1+K/2),\ b_{1,r}(\eta,\xi)=\frac{\eta}{2}(1-\xi)+\xi f_r, b_{2,r}(\eta,\xi)=\frac{1}{2}(1-\xi)-\xi f'_r-2\xi K,\ b_{3,r}(\eta,\xi)=\xi h'_r,$$
$$b_{4,r}(\eta,\xi)=-\xi h_r,\ b_{5,r}=-\xi K, \tag{36}$$
$$c_{0,r}=\frac{1+Nr}{Pr},\ c_{1,r}(\eta,\xi)=\frac{\eta}{2}(1-\xi)+\xi f_r+\xi Nb\phi'_r+2\xi Nt\theta'_r, c_{2,r}(\eta,\xi)=-\xi f'_r+\xi Q_0,$$
$$c_{3,r}(\eta,\xi)=\xi\theta'_r,\ c_{4,r}(\eta,\xi)=-\xi\theta_r,\ c_{5,r}(\eta,\xi)=2Ecf''_r,$$
$$c_{6,r}(\eta,\xi)=\frac{2Ec}{\xi}(1+K/2)h'_r,\ c_{7,r}(\eta,\xi)=\xi Nb\theta'_r, \tag{37}$$
$$d_{0,r}=\frac{1}{Sc},\ d_{1,r}(\eta,\xi)=\frac{\eta}{2}(1-\xi)+\xi f_r,\ d_{2,r}(\eta,\xi)=-\xi f'_r-\xi R_0,$$
$$d_{3,r}(\eta,\xi)=\xi\phi'_r,\ d_{4,r}(\eta,\xi)=-\xi\phi_r,\ d_{5,r}(\eta,\xi)=\frac{Nt}{Nb}\xi, \tag{38}$$

$$\mathbf{R}_{1,r}(\eta,\xi)=\xi f_r f''_r-\xi f'^2_r,\ \mathbf{R}_{2,r}(\eta,\xi)=\xi(f_r h'_r-f'_r h_r),$$
$$\mathbf{R}_{3,r}(\eta,\xi)=\xi(f_r\theta'_r-f'_r\theta_r)+\xi Nt\theta'^2_r+\xi Nb\theta'_r\phi'_r+Ecf''^2_r+\frac{Ec}{\xi}(1+K/2)h'^2_r,$$
$$\mathbf{R}_{4,r}(\eta,\xi)=\xi(f_r\phi'_r-f'_r\phi_r). \tag{39}$$

A wide variety of methods that can be used to solve the linear system (30)–(33). In this study, Chebyshev spectral collocation subject to bivariate Lagrange interpolation is used due to the high accuracy associated with this method. The discretization is done through the Gauss-Lobatto collocation points are:

$$\tau_i=\cos\left(\frac{i\pi}{N_\eta}\right),\ \zeta_j=\cos\left(\frac{j\pi}{N_\xi}\right)$$
$$\text{for } i=0,1,...,N_\eta \text{ and } j=0,1,...,N_\xi. \tag{40}$$

The domain of η and ξ, which are $[0, L]$ and $[0, 1]$ respectively, are transformed to $[-1, 1]$ by means of a linear transformation. Now, consider the approximation functions given by

$$f(\eta,\xi) \approx \sum_{i=0}^{N_\eta}\sum_{j=0}^{N_\xi} f(\tau_i,\zeta_j)L_i(\tau)L_j(\zeta), \quad h(\eta,\xi) \approx \sum_{i=0}^{N_\eta}\sum_{j=0}^{N_\xi} h(\tau_i,\zeta_j)L_i(\tau)L_j(\zeta), \tag{41}$$

$$\theta(\eta,\xi) \approx \sum_{i=0}^{N_\eta}\sum_{j=0}^{N_\xi} \theta(\tau_i,\zeta_j)L_i(\tau)L_j(\zeta), \quad \phi(\eta,\xi) \approx \sum_{i=0}^{N_\eta}\sum_{j=0}^{N_\xi} \phi(\tau_i,\zeta_j)L_i(\tau)L_j(\zeta), \tag{42}$$

where L_i and L_j denote the standard Lagrange interpolation polynomials. The derivatives related to η and ξ can be estimated at the collocation points using the Chebyshev differentiation matrices. The resulting approximation of the pth derivative of f can be expressed as

$$\left.\frac{\partial^p f_{r+1,i}}{\partial^p \eta}\right|_{\eta=\eta_i} = \left(\frac{2}{\eta_e}\right)^p \sum_{k=0}^{N_\eta} D^p_{j,k} f_{r+1,i}(\tau_k,\zeta_i) = \mathbf{D}^p \mathbf{f}_{r+1,i}, \tag{43}$$

where η_e is chosen large enough to capture the conditions at infinity. $\mathbf{D} = (2/\eta_e)[D_{j,k}]$ for $j, k = 0, 1, ..., N_\eta$ where $[D_{j,k}]$ denotes an $(N_\eta + 1) \times (N_\eta + 1)$ Chebyshev derivative matrix and $F_{r+1,i}$ is a vector defined as

$$\mathbf{F}_{r+1,i} = \Big[F_{r+1,i}(\tau_0), F_{r+1,i}(\tau_1), ... , F_{r+1,i}(\tau_{N_\eta})\Big]^T. \tag{44}$$

The approximations of the derivative with respect to ζ at the collocation points are computed similarly as:

$$\left.\frac{\partial f_{r+1}}{\partial \xi}\right|_{\xi=\xi_i} = 2\sum_{k=0}^{N_\xi} d_{i,k} f_{r+1}(\tau_k,\zeta_k), \tag{45}$$

where $[d_{i,k}]$ is an $(N_\xi + 1) \times (N_\xi + 1)$ Chebyshev derivative matrix.

The above detailed procedure is used to compute approximations for the derivatives of h, θ and ϕ related to η and ξ at the collocation points.

Eqs. (30)–(33) can be written as

$$\begin{aligned}
&A^i_{1,1}\mathbf{F}_{r+1,i} - \xi(1-\xi)\sum_{j=0}^{N_\xi} d_{i,j}\mathbf{D}\mathbf{F}_{r+1,j} + A^i_{1,2}\mathbf{H}_{r+1,i} + A^i_{1,3}\mathbf{\Theta}_{r+1,i} + A^i_{1,4}\mathbf{\Phi}_{r+1,i} = \mathbf{R}_{1,r},\\
&A^i_{2,1}\mathbf{F}_{r+1,i} + A^i_{2,2}\mathbf{H}_{r+1,i} - \xi(1-\xi)\sum_{j=0}^{N_\xi} d_{i,j}\mathbf{H}_{r+1,j} = \mathbf{R}_{2,r},
\end{aligned} \tag{46}$$

$$\begin{aligned}
&A^i_{3,1}\mathbf{F}_{r+1,i} + A^i_{3,2}\mathbf{H}_{r+1,i} + A^i_{3,3}\mathbf{\Theta}_{r+1,i} - \xi(1-\xi)\sum_{j=0}^{N_\xi} d_{i,j}\mathbf{\Theta}_{r+1,j} + A^i_{3,4}\mathbf{\Phi}_{r+1,i} = \mathbf{R}_{3,r},\\
&A^i_{4,1}\mathbf{F}_{r+1,i} + A^i_{4,3}\mathbf{\Theta}_{r+1,i} + A^i_{4,4}\mathbf{\Phi}_{r+1,i} - \xi(1-\xi)\sum_{j=0}^{N_\xi} d_{i,j}\mathbf{\Phi}_{r+1,j} = \mathbf{R}_{4,r},
\end{aligned} \tag{47}$$

where

$$\begin{aligned}
&A^i_{1,1} = a^i_{0,r}\mathbf{D}^3 + a^i_{1,r}\mathbf{D}^2 + a^i_{2,r}\mathbf{D} + a^i_{3,r},\ A^i_{1,2} = a^i_{4,r}\mathbf{D},\ A^i_{1,3} = a^i_{5,r},\ A^i_{1,4} = a^i_{6,r},\\
&A^i_{2,2} = b^i_{0,r}\mathbf{D}^2 + b^i_{1,r}\mathbf{D} + b^i_{2,r},\ A^i_{2,1} = b^i_{3,r} + b^i_{4,r}\mathbf{D} + b^i_{5,r}\mathbf{D}^2,\\
&A^i_{3,3} = c^i_{0,r}\mathbf{D}^2 + c^i_{1,r}\mathbf{D} + c^i_{2,r},\ A^i_{3,1} = c^i_{3,r} + c^i_{4,r}\mathbf{D} + c^i_{5,r}\mathbf{D}^2,\ A_{3,2} = c^i_{6,r}\mathbf{D},\ A^i_{3,4} = c^i_{7,r}\mathbf{D},\\
&A^i_{4,4} = d^i_{0,r}\mathbf{D}^2 + d^i_{1,r}\mathbf{D} + d^i_{2,r},\ A^i_{4,1} = d^i_{3,r} + d^i_{4,r}\mathbf{D},\ A^i_{4,3} = d^i_{5,r}\mathbf{D}^2,
\end{aligned} \tag{48}$$

with $a^i_{k,r}$ $(k = 0, 1, 2, .., 6)$ and $R_{1,r} = [R_{1,r}(\tau_0), R_{1,r}(\tau_1), \ldots, R_{1,r}(\tau_{N_x})]^T$.

In matrix notation assume that (see Appendix A).
The solution is found to be

$$\mathbf{FF} = \mathbf{AA}^{-1}\mathbf{RR}, \tag{49}$$

where

$$\begin{aligned}
&B^{(i,i)}_{1,1} = A^i_{1,1} - \xi(1-\xi)d_{i,i}\mathbf{D},\ B^{(i,i)}_{1,2} = A^i_{1,2},\ B^{(i,i)}_{1,3} = A^i_{1,3},\ B^{(i,i)}_{1,4} = A^i_{1,4},\\
&B^{(i,i)}_{2,1} = A^i_{2,1},\ B^{(i,i)}_{2,2} = A^i_{2,2} - \xi(1-\xi)d_{i,i}\mathbf{I},\ B^{(i,i)}_{2,3} = A^i_{2,3},\ B^{(i,i)}_{2,4} = A^i_{2,4},\\
&B^{(i,i)}_{3,1} = A^i_{3,1},\ B^{(i,i)}_{3,2} = A^i_{3,2},\ B^{(i,i)}_{3,3} = A^i_{3,3} - \xi(1-\xi)d_{i,i}\mathbf{I},\ B^{(i,i)}_{3,4} = A^i_{3,4},\\
&B^{(i,i)}_{4,1} = A^i_{4,1},\ B^{(i,i)}_{4,2} = A^i_{4,2},\ B^{(i,i)}_{4,3} = A^i_{4,3},\ B^{(i,i)}_{4,4} = A^i_{4,4} - \xi(1-\xi)d_{i,i}\mathbf{I},\\
&B^{(i,j)}_{1,1} = -\xi(1-\xi)d_{i,j}\mathbf{D},\ B^{(i,j)}_{2,2} = -\xi(1-\xi)d_{i,j}\mathbf{I},\\
&B^{(i,j)}_{3,3} = -\xi(1-\xi)d_{i,j}\mathbf{I},\ B^{(i,j)}_{4,4} = -\xi(1-\xi)d_{i,j}\mathbf{I},\quad i \neq j,
\end{aligned} \tag{50}$$

and $\mathbf{I}$ represents an $(N_\eta + 1) \times (N_\eta + 1)$ identity matrix

5 Convergence analysis

In this section, we seek to determine the accuracy of the method through the calculation of the absolute difference between the successive approximate values of the solutions and their derivatives.

Fig. (2)(a) shows the absolute differences of the successive approximate values for $f(\eta,\xi), h(\eta,\xi), \theta(\eta,\xi)$, $\phi(\eta,\xi)$ versus the iterations. It is observed that the solution the absolute difference decreases to $\approx 10^{-14}$ after the fifth iterations. Fig. (2)(a) shows the absolute difference of the successive values for the derivatives $f'(\eta,\xi), h'(\eta,\xi), \theta'(\eta,\xi), \phi'(\eta,\xi)$ versus the iterations. It is noted that the absolute difference decreases to $\approx 10^{-13}$ at sixth iterations

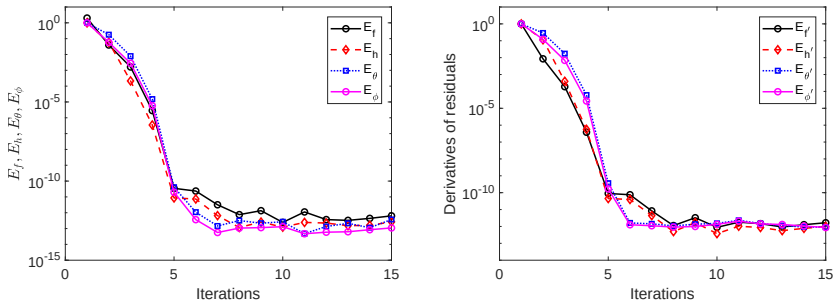

Figure 2: Convergence graph of (a) $f(\eta,\xi), h(\eta,\xi), \theta(\eta,\xi)$ and $\phi(\eta,\xi)$ and (b) $f'(\eta,\xi), h(\eta,\xi), \theta'(\eta,\xi)$ and $\phi'(\eta,\xi)$

6 Results and discussion

The system described by equations (8)–(11) and (12) is solved by the bivariate spectral quasiliearization method for selected parameter values. The iteration is started from initial approximations which satisfy Eq.

(12), namely:

$$f_0(\eta,\xi) = s + 1 - \exp(-\eta), \quad h_0(\eta,\xi) = \Big(\exp(-\eta)\Big)n, \tag{51}$$

$$\theta_0(\eta,\xi) = \exp(-\eta), \quad \phi_0(\eta,\xi) = \exp(-\eta). \tag{52}$$

We studied the importance of physical parameters for instance the Grashof number (related to temperature) ω_t, the heat generation parameter Q_0, the material parameter K, the Eckert number Ec and the Grashof number (related to concentration) ω_c on the velocity $f'(\eta,\xi)$, $h(\eta,\xi)$ microrotation or angular velocity, temperature $\theta(\eta,\xi)$, concentration $\phi(\eta,\xi)$ and the volumetric entropy generation $N_G(\eta,\xi)$ on the micropolar nanofluid. The values of K and ξ are 1 and 0.2 respectively, which are specified in [16]. Unless stated otherwise, values of the rest of parameters for a micropolar laminar fluid flow are $Nb = Nt = 0.5, \omega_t = \omega_c = 1, Nr = 0.2$, $Ha = 0.5, Sc = 0.94, Pr = 6.8$, $s = 1, Ec = 0.1, Q_0 = 0.1, n = 0.5, R_0 = 0.3$ ([3, 16]).

Table 1 (see Appendix B) represents the computed skin friction $f''(0,\xi)$, heat transfer $\theta'(0,\xi)$ and the mass transfer $\phi'(0,\xi)$ for different values of K, Nt, Nb and R_0. It is noted that K has a positive relation with heat transfer and skin friction; however, increased values of K has a negative impact on mass transfer and fixing the other parameters. Moreover, we observe that $f''(0,\xi)$ increases as Nt increases while $\theta'(0,xi)$ and $\phi'(0,\xi)$ rates reduce. The skin friction and heat transfer rate vary inversely with Nb whereas Nb has positive effect on mass transfer rate. The same result holds for $f''(0,\xi)$, $\theta'(0,\xi)$ and $\phi'(0,\xi)$ respect to R_0.

Figs. 3(a) and (b) show the behaviour of velocity and angular momentum profiles for various values of K. We found that the value of material parameter has a positive relation with the velocity profile. It can be clearly noted from Fig. 3(b) that the angular momentum $h(\xi,\eta)$ decreases when $0 \leq \eta \leq 1$. And in regions further from the sheet the angular momentum remains unchanged ($\eta > 1$).

The variation of temperature and concentration profiles respect to Eckert number Ec is shown in Figs. 4(a) and (b). The temperature is a positive function with the Eckert number. From Fig. 4(b), it is found that the the concentration distribution is inversely related to the Eckert number when $0 \leq \eta \leq 1$ whereas the opposite behavior is noted when $\eta > 1$.

The changes in the concentration and temperature profiles with varying values of Nr are illustrated in Figs. 5(a) and (b). Fig. 5(a) shows that Nr has a positive relation with temperature profiles, therefore the boundary layer becomes thickness. In the proximity of the surface, the temperature distribution has a negative slope indicating heat transfer from the surface to the ambient fluid. Fig. 5(b) shows that $\phi(\eta,\xi)$ decrease at a certain values of η.

Figs. 6(a), (b) and (c) depicte the velocity, angular momentum and concentration profiles for different solutal buoyancy parameter or local concentration Grashof number ω_c. From Fig. 6(a) it is noted thatthe velocity profiles increase as the concentration Grashof number increases. Further, we observe a peak near the plate for $\eta = 1.5$ and the peak diminishes as ω_c is reduced. From Figs. 6(b) and (c), it is noted that an increment in the solutal Grashof number leads to reduction in the angular momentum and concentration profiles; respectively across the boundary layers. Thus, the thickness of the angular and solutal boundary layer decrease.

The behavioral relationship of the velocity and angular momentum profiles in response to the local Grashof number ω_t is shown in Figs. 7 (a) and (b). The figure indicates that the temperature of the thermal boundary layer is enhanced by the local Grashof number which is a phenomenon that can be attributed to the cooling down of the plate as a result of transferring the temperature by the free convection current to the free stream from the plate. With regard to the effect of the parameter ω_t on the angular momentum, Fig. 7 (b) shows that the angular momentum increases with high values of ω_t, peaks at 2 and it falls down until vanishes outside the boundary layer. This observation can be traced back to the fact that high values of ω_t generate strong buoyancy force which, in turns, generate high kinetic energy consumed in negating the flow resistance and as a consequence the angular velocity overshoot.

Fig. 8(a) illustrates the impact of the of the heat generation/absorption parameter Q_0 on the temperature profile. The figure indicates that an increase in the temperature profile in response to an increase in Q_0 in the case where the boundary layer generates heat. On the other hand, if the boundary layer absorbs heat, the temperature profiles decreases noticeably with an increase in Q_0. Fig. 8(b) depicts the impact of

the chemical reaction R_0 on the concentration profiles. It is observed that the chemical reaction negatively impacts the concentration profiles causing the density of the nanoparticle species to drop.

The profiles for the velocity $f'(\eta,\xi)$, angular momentum $h(\eta,\xi)$, temperature $\theta(\eta,\xi)$ and concentration $\phi(\eta,\xi)$ are given in Figs. 9(a), (b), (c) and (d), respectively. It is observed that ξ causes the velocity distribution to deteriorate but not to a very remarkable degree (cf. Fig. 9(a)). However, the effect of ξ on the angular momentum is rather noticeable especially in the proximity of the sheet (cf. Fig. 9(b)). A similar observation is noted for the case of the temperature where it is also found that ξ negatively influence the temperature especially in regions close to the stretching sheet (cf. Fig. 9(c)). The concentration distribution decreases with increasing ξ too (cf Fig. 9(d)).

The changes in velocity, angular momentum, temperature and concentration fields associated with different values of the thermophoretic parameters Nt are given in 10 (a), (b), (c) and (d), respectively. We observe that Nt is an increasing function on the velocity, angular momentum, temperature and concentration fields. Thus, we notice that Nt has a positive effect on the thickness of thermal boundary layer.

Brownian motion occurs in nanofluid systems which affects the heat transfer properties of the systems especially when the sizes of the nanoparticle species are close to the nanometer scale in which case the influence of the nanoparticle on heat transfer is very remarkable. Figs. 11 (a) and (b) show the impact of Brownian motion on the temperature distribution and the volume fraction of nanoparticles. Further, we found that nanoparticle volume fraction deteriorates with the values of Nr increase whereas temperature profile is positively affected by Nr.

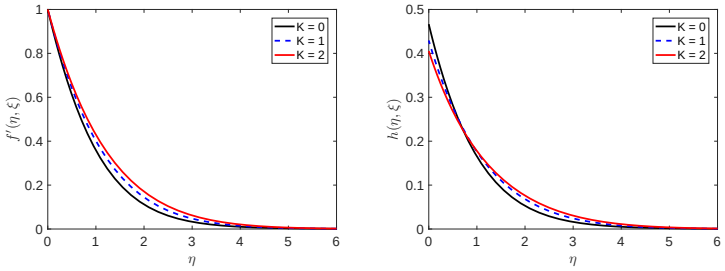

Figure 3: Effect of K on (a) the velocity profile $f'(\eta,\xi)$ and (b) the Angular momentum $h(\eta,\xi)$.

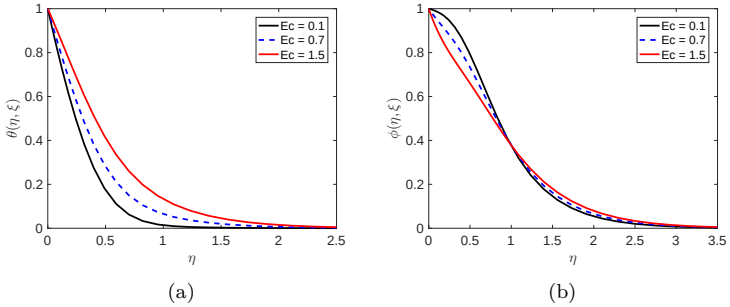

Figure 4: Effect of Ec on (a) the temperature profiles $\theta(\eta,\xi)$, and (b) the concentration profiles $\phi(\eta,\xi)$.

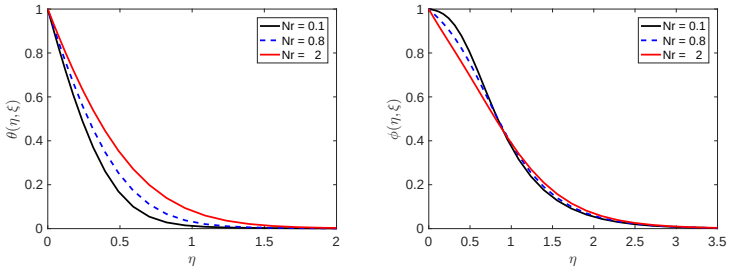

(a) (b)

Figure 5: Effect of Nr on (a) the temperature profiles $\theta(\eta,\xi)$, and (b) the concentration profiles $\phi(\eta,\xi)$.

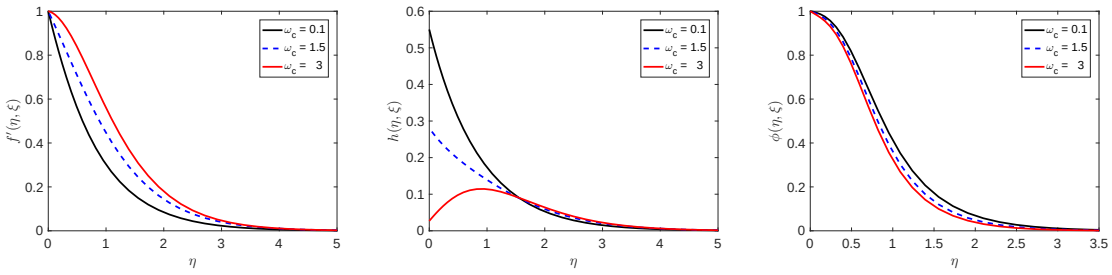

(a) (b) (c)

Figure 6: Effect of ω_c on (a) the velocity profile $f'(\eta,\xi)$, (b) the angular momentum $h(\eta,\xi)$, and (c) the concentration profiles $\phi(\eta,\xi)$.

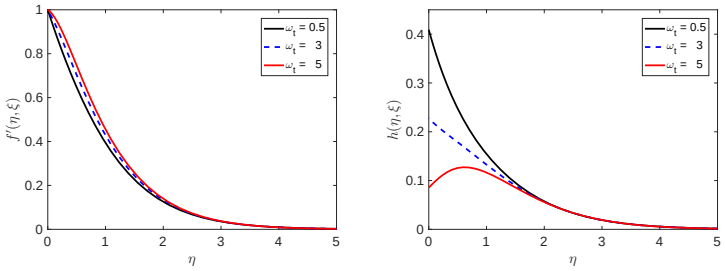

(a) (b)

Figure 7: Effect of ω_t on (a) the velocity profile $f'(\eta,\xi)$, and (b) the angular momentum $h(\eta,\xi)$.

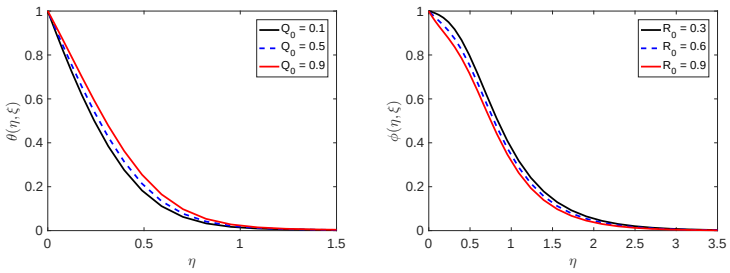

(a) (b)

Figure 8: Effect of Q_0 and R_0 on (a) the temperature profiles $\theta(\eta,\xi)$, and (b) the concentration profiles $\phi(\eta,\xi)$ respectively.

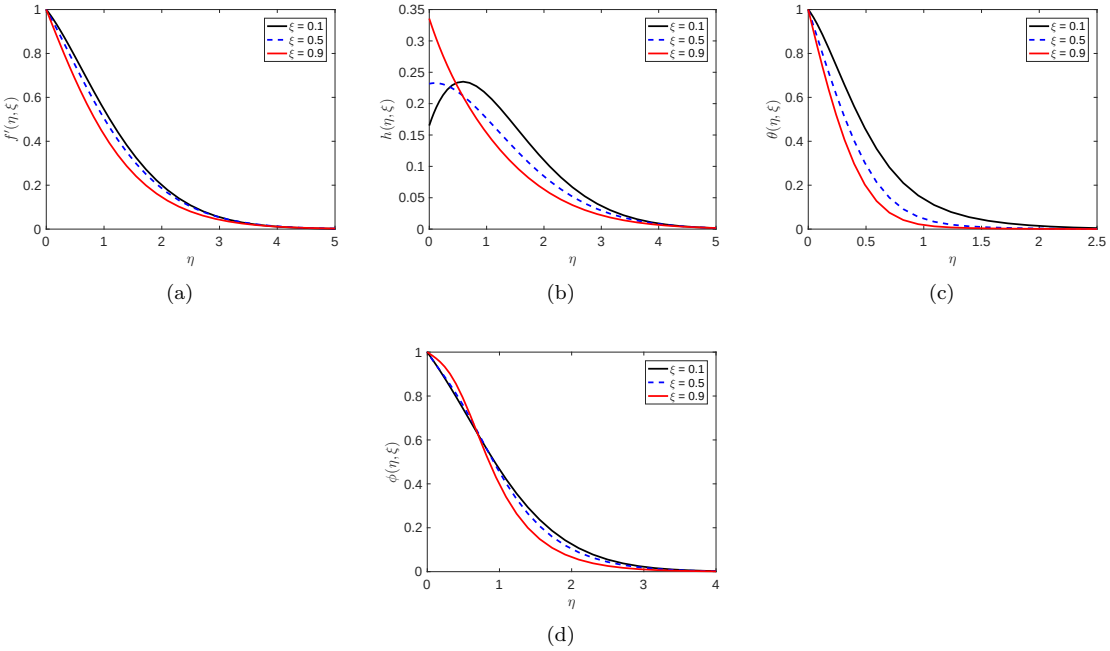

(a) (b) (c)

(d)

Figure 9: Effect of ξ on (a) the velocity profile $f'(\eta,\xi)$, (b) the angular momentum $h(\eta,\xi)$, (c) the temperature profile $\theta(\eta,\xi)$, and (d) the concertation profile $\phi(\eta,\xi)$.

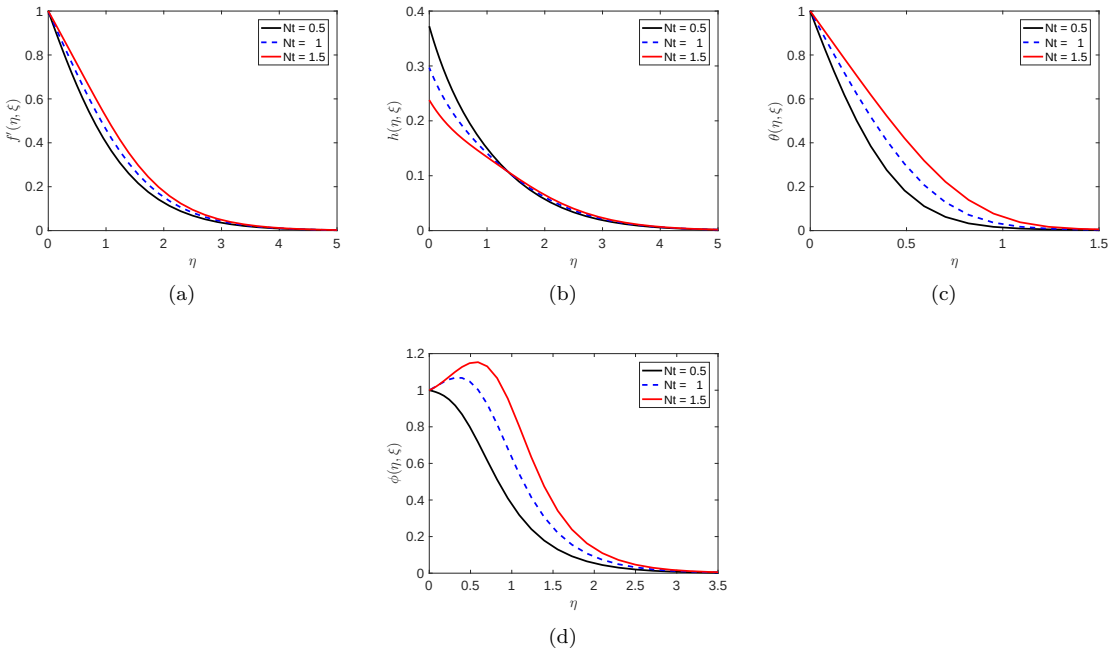

Figure 10: Effect of Nt on (a) the velocity profile $f'(\eta,\xi)$, (b) the angular momentum $h(\eta,\xi)$, (c) the temperature profiles $\theta(\eta,\xi)$, and (d) the concentration profiles $\phi(\eta,\xi)$

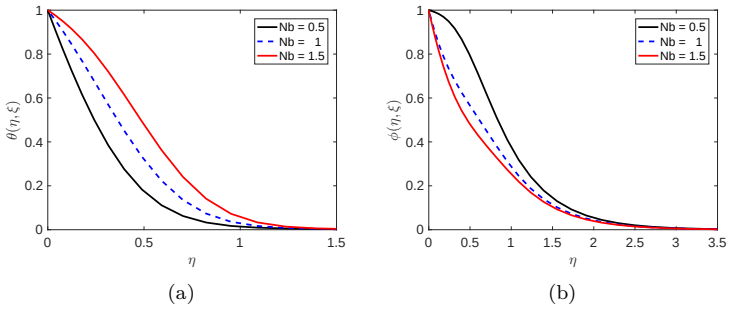

Figure 11: Effect of Nb on (a) the temperature profiles $\theta(\eta,\xi)$, and (b) the concentration profiles $\phi(\eta,\xi)$

The changes of the skin-friction coefficient $f''(0,\xi)$, Nusselt number $\theta'(0,\xi)$ and Sherwood number $\phi'(0,\xi)$ with the Prandtl number for varying values of thermal radiation parameter Nr are shown in Fig. 12. Figs. 12 (a) and (b) describe the changes in the skin-friction coefficient and local Nusselt number with varying Pr and Nr. We observe that the increasing values of Prandtl number improve $f''(0,\xi)$ and degrade $\theta'(0,\xi)$ for all the values of Nr. Moreover, We observe that Nr has a positive relation with $f''(0,\xi)$ whereas the opposite is seen in the case the local Nusselt number. From Fig. 12(c), we observe that the Sherwood number has a positive relation with the Prandtl number and thermal radiation parameter.

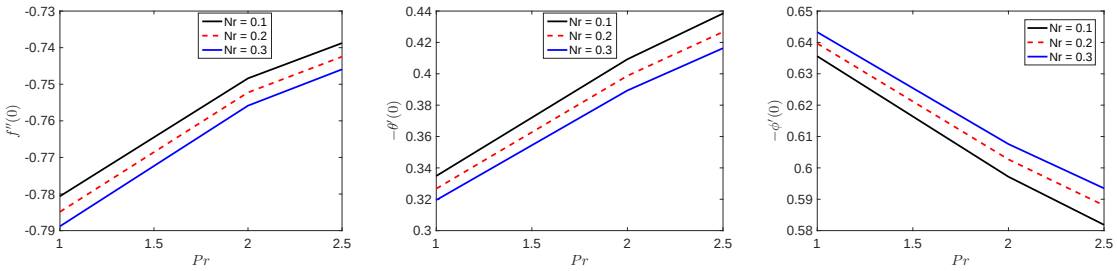

Figure 12: Effect of Nr and Pr (a) the skin friction $f''(0,\xi)$,(b) the Nusselt number $-\theta'(0,\xi)$, and (c) the Sherwood number $-\phi'(0,\xi)$.

Entropy generation, which is an important attribute of the flow is discussed below. The entropy generation is influenced by the quantum and changes in the physical characteristics of the fluid and the porous medium as can be seen in equation (26). We consider how physical parameters such as the Reynolds number, the material parameter K and the Brinkman number Br. The impact of varying Reynolds number, material parameter and Brinkman number on entropy generation is presented in Figs. 13 (a), (b) and (c), respectively. The Reynolds number has a positive impact on entropy generation. A reduction in entropy generation is observed with an increase in K as shown in Fig. 13(b). This is due to the fact that both velocity and angular momentum increases within the stretching sheet decrease as material parameter increases. The importance of viscous dissipation and fluid conduction are determined by the Brinkman number Br. With increasing Br, viscous dissipation produces more heat which is manifested in the graphs of the temperature profiles. As Brinkman number increases, entropy generation increases.Since the entropy generation is responsible for the irreversibility and our analysis has shown that in the neighborhood of the sheet the entropy generation is substantially high in comparison with other regions, it can be concluded that the sheet is a strong source of irreversibility and the thermodynamics imperfections.

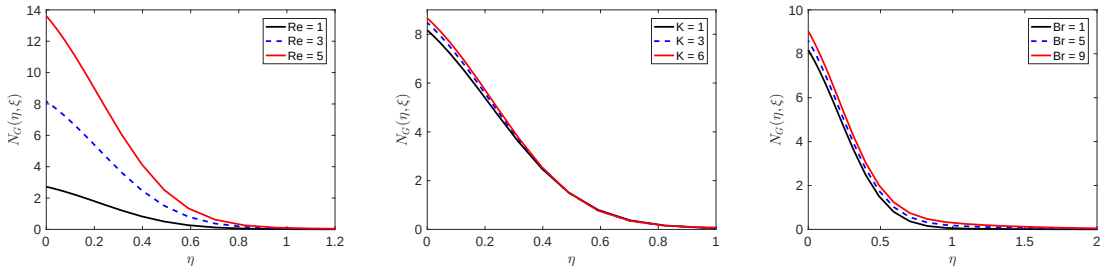

Figure 13: Effect of (a) the Reynolds number Re,(b) the material parameter K, and (c) the Brinkman number Br on the entropy generation profiles.

As mentioned in section (3), there are five sources of irreversibility, namely thermal diffusion, the magnetic field, viscous dissipation, the micro-rotation and concentration diffusion. In figure (14), the contribution of each source to the total irreversibility is given as a function of distance from the sheet. Firstly, it is observed, though not very noticeable, that at the proximity of the sheet all sources of irreversibility contribute positively to the total irreversibility. Close to the sheet, it is observed that the irreversibility due to the thermal diffusion (γ_{th}) has a positive and remarkable contribution to the total irreversibility. The irreversibility due to the

thermal diffusion (λ_{th}) is dominant around the sheet due to the temperature gradient and the high motion of the nanoparticle. Close to the surface, the irreversibility due to viscous dissipation has comparative influence because the velocity gradients are comparative high. Move closer to the sheet, the irreversibility due to viscous dissipation (λ_{dis}) takes over and becomes the dominate source of irreversibility. In contrast, moving away from the sheet the irreversibility due to the micro-rotation (γ_{rot}) takes over and becomes the dominant source of irreversibility as the temperature drops. The contribution of irreversibility due to thermal diffusion decreases moving away from the sheet due to a decrease in the temperature gradients. The combined effect of the increase in the micro-rotation and the decrease in temperature gradient leads to the dominance of the irreversibility in the regions far from the sheet. It is worth noting that the magnitude of irreversibility due to the magnetic field (λ_m) and concentration diffusion (λ_{dif}) is very low.

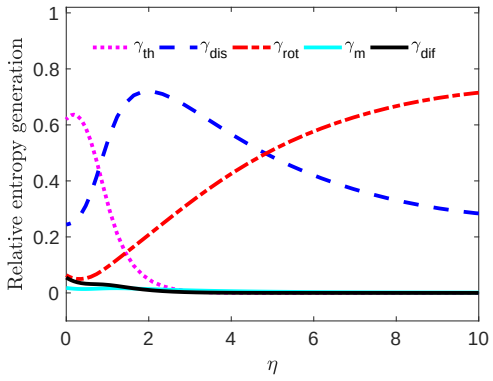

Figure 14: The impact of each source of irreversibility

7 Conclusion

In this study we have investigated heat and mass transfer and entropy generation in a micropolar nanofluid flow. The system of equations were solved using the bivariate spectral quasiliearization method. The novelty is the investigation of entropy generation in an imcompressible micropolar nanofluid flow over a permeable sheet subject to viscous dissipation and thermal radiation. The main results of the analysis are,

- The fluid velocity, concentration and temperature distribution increase when thermophoresis parameter increases.
- The Brownian motion parameter has a positive impact on the temperature profiles whereas the increase in the Brownian motion parameter deteriorates the concentration profiles.
- The Nusselt number and skin-friction coefficient increase with an increasing thermal radiation parameter whereas the opposite is case for the Sherwood number.
- The entropy generation increases with increasing Reynolds and Brinkman numbers.
- The surface is hugely responsible for the irreversibility.
- The entropy generation due to thermal diffusion is the most dominant source of entropy generation

Acknowledgement:

The authors are grateful to DST-NRF Centre of Excellence-Mathematical and Statistical Sciences, the Claude Leon Foundation, DST-NRF Centre of Excellence-Mathematical and Statistical Sciences and the University of KwaZulu-Natal for financial support.

References

[1] I. Hassanien, R. Gorla, Heat transfer to a micropolar fluid from a non-isothermal stretching sheet with suction and blowing, Acta Mechanica 84 (1-4) (1990) 191–199.

[2] R. Bhargava, S. Sharma, H. S. Takhar, O. A. Bég, P. Bhargava, Numerical solutions for micropolar transport phenomena over a nonlinear stretching sheet, Nonlinear Anal. Model. Control 12 (2007) 45–63.

[3] K.-L. Hsiao, Micropolar nanofluid flow with mhd and viscous dissipation effects towards a stretching sheet with multimedia feature, International Journal of Heat and Mass Transfer 112 (2017) 983–990.

[4] K. Das, Effect of chemical reaction and thermal radiation on heat and mass transfer flow of mhd micropolar fluid in a rotating frame of reference, International journal of heat and mass transfer 54 (15) (2011) 3505–3513.

[5] D. Srinivasacharya, K. H. Bindu, Effect of magnetic field on entropy generation due to micropolar fluid flow in a rectangular duct, Procedia Engineering 127 (2015) 1150–1157.

[6] D. Srinivasacharya, K. H. Bindu, Entropy generation in a micropolar fluid flow through an inclined channel, Alexandria Engineering Journal 55 (2) (2016) 973–982.

[7] S. Jangili, N. Gajjela, O. A. Beg, Mathematical modeling of entropy generation in magnetized micropolar flow between co-rotating cylinders with internal heat generation, Alexandria Engineering Journal 55 (3) (2016) 1969–1982.

[8] S. Jangili, S. Adesanya, J. Falade, N. Gajjela, Entropy generation analysis for a radiative micropolar fluid flow through a vertical channel saturated with non-darcian porous medium, International Journal of Applied and Computational Mathematics 3 (4) (2017) 3759–3782.

[9] M. Afridi, M. Qasim, O. Makinde, Second law analysis of boundary layer flow with variable fluid properties, Journal of Heat Transfer 139 (10) (2017) 104505.

[10] A. Muhammad, O. D. Makinde, Thermodynamics analysis of unsteady mhd mixed convection with slip and thermal radiation over a permeable surface, in: Defect and Diffusion Forum, Vol. 374, Trans Tech Publ, 2017, pp. 29–46.

[11] S. O. Adesanya, O. D. Makinde, Irreversibility analysis in a couple stress film flow along an inclined heated plate with adiabatic free surface, Physica A: Statistical Mechanics and its Applications 432 (2015) 222–229.

[12] S. Das, S. Chakraborty, R. Jana, O. Makinde, Entropy analysis of nanofluid flow over a convectively heated radially stretching disk embedded in a porous medium, Journal of Nanofluids 5 (1) (2016) 48–58.

[13] S. Motsa, V. Magagula, P. Sibanda, A bivariate chebyshev spectral collocation quasilinearization method for nonlinear evolution parabolic equations, The Scientific World Journal 2014.

[14] G. Makanda, S. Shaw, P. Sibanda, Effects of radiation on mhd free convection of a casson fluid from a horizontal circular cylinder with partial slip in non-darcy porous medium with viscous dissipation, Boundary Value Problems 2015 (1) (2015) 75.

[15] A. Ishak, R. Nazar, I. Pop, Mixed convection stagnation point flow of a micropolar fluid towards a stretching sheet, Meccanica 43 (4) (2008) 411–418.

[16] A. Aurangzaib, A. Kasim, S. S. Mohammad NlF, Soret and dufour effects on unsteady mhd flow of a micropolar fluid in the presence of thermophoresis deposition particle, World Applied Sciences Journal 21 (5) (2013) 766–73.

[17] N. Sandeep, C. Sulochana, Dual solutions for unsteady mixed convection flow of mhd micropolar fluid over a stretching/shrinking sheet with non-uniform heat source/sink, Engineering Science and Technology, an International Journal 18 (4) (2015) 738–745.

[18] Y. Kim, Thermal boundary layer flow of a micropolar fluid past a wedge with constant wall temperature, Acta mechanica 138 (1) (1999) 113–121.

[19] A. Bejan, Entropy generation minimization: The new thermodynamics of finite-size devices and finite-time processes, Journal of Applied Physics 79 (3) (1996) 1191–1218.

[20] M. A. Abbas, Y. Bai, M. M. Rashidi, M. M. Bhatti, Analysis of entropy generation in the flow of peristaltic nanofluids in channels with compliant walls, Entropy 18 (3) (2016) 90.

[21] A. Bejan, Entropy generation minimization, Advanced Engineering Thermodynamics (2016) 531–600.

[22] J. S. Hesthaven, S. Gottlieb, D. Gottlieb, Spectral methods for time-dependent problems, Vol. 21, Cambridge University Press, 2007.

[23] J. P. Boyd, Chebyshev and Fourier spectral methods, Courier Corporation, 2001.

Appendix A

$$
\mathbf{AA} = \left[\begin{array}{cccc|cccc|c|c}
B_{1,1}^{(0,0)} & B_{1,2}^{(0,0)} & B_{1,3}^{(0,0)} & B_{1,4}^{(0,0)} & B_{1,1}^{(0,1)} & & & & \ddots & B_{1,1}^{(0,N_\xi)} \\
B_{2,1}^{(0,0)} & B_{2,2}^{(0,0)} & B_{2,3}^{(0,0)} & B_{2,4}^{(0,0)} & & B_{2,2}^{(0,1)} & & & \ddots & & B_{2,2}^{(0,N_\xi)} \\
B_{3,1}^{(0,0)} & B_{3,2}^{(0,0)} & B_{3,3}^{(0,0)} & B_{3,4}^{(0,0)} & & & B_{3,3}^{(0,1)} & & \ddots & & & B_{3,3}^{(0,N_\xi)} \\
B_{4,1}^{(0,0)} & B_{4,2}^{(0,0)} & B_{4,3}^{(0,0)} & B_{4,4}^{(0,0)} & & & & B_{4,4}^{(0,1)} & \ddots & & & & B_{4,4}^{(0,N_\xi)} \\
\hline
B_{1,1}^{(1,0)} & & & & B_{1,1}^{(1,1)} & B_{1,2}^{(1,1)} & B_{1,3}^{(1,1)} & B_{1,4}^{(1,1)} & \ddots & B_{1,1}^{(1,N_\xi)} \\
& B_{2,2}^{(1,0)} & & & B_{2,1}^{(1,1)} & B_{2,2}^{(1,1)} & B_{2,3}^{(1,1)} & B_{2,4}^{(1,1)} & \ddots & & B_{2,2}^{(1,N_\xi)} \\
& & B_{3,3}^{(1,0)} & & B_{3,1}^{(1,1)} & B_{3,2}^{(1,1)} & B_{3,3}^{(1,1)} & B_{3,4}^{(1,1)} & \ddots & & & B_{3,3}^{(1,N_\xi)} \\
& & & B_{4,4}^{(1,0)} & B_{4,1}^{(1,1)} & B_{4,2}^{(1,1)} & B_{4,3}^{(1,1)} & B_{4,4}^{(1,1)} & \ddots & & & & B_{4,4}^{(1,N_\xi)} \\
\hline
\ddots & & & & \ddots & & & & \cdots & \ddots \\
& \ddots & & & & \ddots & & & \cdots & & \ddots \\
& & \ddots & & & & \ddots & & \cdots & & & \ddots \\
& & & \ddots & & & & \ddots & \cdots & & & & \ddots \\
\hline
B_{1,1}^{(N_\xi,0)} & & & & B_{1,1}^{(N_\xi,1)} & & & & \ddots & B_{1,1}^{(N_\xi,N_\xi)} & B_{1,2}^{(N_\xi,N_\xi)} & B_{1,3}^{(N_\xi,N_\xi)} & B_{1,4}^{(N_\xi,N_\xi)} \\
& B_{2,2}^{(N_\xi,0)} & & & & B_{2,2}^{(N_\xi,1)} & & & \ddots & B_{2,1}^{(N_\xi,N_\xi)} & B_{2,2}^{(N_\xi,N_\xi)} & B_{2,3}^{(N_\xi,N_\xi)} & B_{2,4}^{(N_\xi,N_\xi)} \\
& & B_{3,3}^{(N_\xi,0)} & & & & B_{3,3}^{(N_\xi,1)} & & \ddots & B_{3,1}^{(N_\xi,N_\xi)} & B_{3,2}^{(N_\xi,N_\xi)} & B_{3,3}^{(N_\xi,N_\xi)} & B_{3,4}^{(N_\xi,N_\xi)} \\
& & & B_{4,4}^{(N_\xi,0)} & & & & B_{4,4}^{(N_\xi,1)} & \ddots & B_{4,1}^{(N_\xi,N_\xi)} & B_{4,2}^{(N_\xi,N_\xi)} & B_{4,3}^{(N_\xi,N_\xi)} & B_{4,4}^{(N_\xi,N_\xi)}
\end{array}\right],
$$

$$
\mathbf{FF} = \left[\begin{array}{c}
\mathbf{F}_0 \\ \mathbf{H}_0 \\ \mathbf{\Theta}_0 \\ \mathbf{\Phi}_0 \\ \hline
\mathbf{F}_1 \\ \mathbf{H}_1 \\ \mathbf{\Theta}_1 \\ \mathbf{\Phi}_1 \\ \hline
\vdots \\ \vdots \\ \vdots \\ \vdots \\ \hline
\mathbf{F}_{N_\xi} \\ \mathbf{H}_{N_\xi} \\ \mathbf{\Theta}_{N_\xi} \\ \mathbf{\Phi}_{N_\xi}
\end{array}\right], \qquad
\mathbf{RR} = \left[\begin{array}{c}
\mathbf{R}_{1,0} \\ \mathbf{R}_{2,0} \\ \mathbf{R}_{3,0} \\ \mathbf{R}_{4,0} \\ \hline
\mathbf{R}_{1,1} \\ \mathbf{R}_{2,1} \\ \mathbf{R}_{3,1} \\ \mathbf{R}_{4,1} \\ \hline
\vdots \\ \vdots \\ \vdots \\ \vdots \\ \hline
\mathbf{R}_{1,N_\xi} \\ \mathbf{R}_{2,N_\xi} \\ \mathbf{R}_{3,N_\xi} \\ \mathbf{R}_{4,N_\xi}
\end{array}\right]. \tag{53}
$$

Appendix B

Table 1: Computed $f''(0,\xi)$, $-\theta'(0,\xi)$ and $-\phi'(0,\xi)$ with various values of K, Nt, Nb and R_0 when $\xi = 0.2, \omega_t = \omega_c = 1, Nr = 0.2$, $Ha = 0.5, Sc = 0.94, Pr = 6.8$, $s = 1, Ec = 0.1, Q_0 = 0.1, n = 0.5$

K	Nt	Nb	R_0	$C_{f_x}R^{1/2}$	$Re^{-1/2}Nu_x$	$Re^{-1/2}Sh_x$
0.2				−0.915452	1.519181	0.853184
1	0.5	0.5	0.3	−0.858733	1.541030	0.850256
2.5				−0.792516	1.562133	0.848537
	0.5			−0.858733	1.541030	0.850256
1	1	0.5	0.3	−0.848969	1.286133	0.751045
	1.5			−0.839054	1.132108	0.707963
		0.2		−0.848848	1.652673	0.528010
1	0.5	0.5	0.3	−0.858733	1.541030	0.850256
		1		−0.860131	1.345855	0.979923
			0.1	−0.858106	1.542271	0.834545
1	0.5	0.5	0.3	−0.858733	1.541030	0.850256
			1	−0.861379	1.531537	0.909714

Chapter 4

Entropy generation in viscoelastic nanofluids with homogeneous-heterogeneous reaction, partial slip and nonlinear thermal radiation

In Chapter 3, we studied the entropy generation in non-Newtonian fluid flow. In this chapter we take into account the impact homogeneous-heterogeneous chemical reactions and neglect the partial slip between nanoparticles and the fluid molecules.

We assume the boundary layer flow of a viscoelastic nanofluid over a stretching sheet with nonlinear thermal radiation. We provide some analysis of the impact of the Bejan number on the viscoelastic nanofluid flow. A nonlinear thermal radiation is assumed. The spectral quasilinearization method is used to solve the flow equations.

Entropy generation in MHD flow of viscoelastic nanofluids with homogeneous-heterogeneous reaction, partial slip and nonlinear thermal radiation

M. Almakki,[1] H. Mondal,[1]* P.Sibanda,[1] N. Haroun[1]

ABSTRACT

We investigate the combined effects of homogeneous and heterogeneous reactions in the boundary layer flow of a viscoelastic nanofluid over a stretching sheet with nonlinear thermal radiation. The incompressible fluid is electrically conducting with an applied a transverse magnetic field. The conservation equations are solved using the spectral quasi-linearization method. This analysis is carried out in order to enhance the system performance, with the source of entropy generation and the impact of Bejan number on viscoelastic nanofluid due to a partial slip in homogeneous and heterogeneous reactions flow using the spectral quasi-linearization method. Various fluid parameters of interest such as entropy generation, Bejan number, fluid velocity, shear stress heat and mass transfer rates are studied quantitatively and their behaviors are depicted graphically. A comparison of the entropy generation due to the heat transfer and the fluid friction is made with the help of the Bejan number. Among the findings reported in this study is that the entropy generation has a significant impact in controlling the rate of heat transfer in the boundary layer region.

KEYWORD:

Nanofluids; Viscoelastic fluid; Homogeneous–Heterogeneous reactions; Nonlinear thermal radiation

INTRODUCTION

In recent years, nanofluids have attracted a considerable amount of interest due to their novel properties that make them potentially useful in a number of industrial applications including transportation, power generation, micro-manufacturing, thermal therapy for cancer treatment, chemical and metallurgical sectors, heating, cooling, ventilation, and air-conditioning. The term nanofluid is used to refer to a solid-liquid mixture with a continuous phase, Choi [1]. Nanofluids are used in many areas including oil extraction, cancer therapy and safer surgery by cooling. The two-dimensional boundary layer flow in porous media caused by a stretching surface has received considerable attention because such flows arise in many applications such as in paper industry, aerodynamic extrusion of plastic sheets, hot rolling, wire drawing, glass-fiber production and the manufacture of polymer and rubber sheets, Fisher [2]. Makinde et al. [3] investigated nanofluid flow over a linear stretching sheet with thermophoresis and particle Brownian motion. The Brownian motion and thermophoresis lead to an increase in the rate of heat transfer. However, the opposite was observed in the case of the rate of mass transfer. The effect of an applied magnetic field on nanofluids has substantial applications in chemistry, physics and engineering. These include cooling of continuous filaments, in the process of drawing, annealing and thinning of copper wire. Drawing such strips through an electrically conducting fluid subject to a magnetic field can control the rate of cooling and stretching, thereby furthering the desired characteristics of the

[1]School of Mathematics, Statistics and Computer Science,University of KwaZulu-Natal, Private Bag X01, Scottsvile, Pietermaritzburg-3209, South Africa

[2]Corresponding author: hiranmoymondal@yahoo.co.in (H. Mondal)

final product. Such an application of a linearly stretching sheet of incompressible viscous flow of MHD was discussed by Chamka [4].

It is a well-established fact that all bodies emit thermal radiation when their temperature is greater that zero. The greater the bodies temperature, the greater the thermal radiation. As a result of thermal radiation, when two bodies come in contact with each other, the hotter one transmits heat to the less hotter one until the reach the same temperature. The previously stated sentences on thermal radiation is an informed statement of Prevostis Theory of thermal radiation which is regarded as the corner of motion theory of thermal radiation; please refer to Putley [5] for elaborate details. Heat transfer and viscous dissipation of MHD nanaofluid flow through a permeable stretching/shrinking sheet was investigated by Sandeep et al. [6]. Raju et al. [7] was scrutinized the influence of the thermal radiation on ferrofluid across a flat plate within slip velocity and aligned magnetic field. The effects of thermal radiation in presence of MHD of nanofluid flow throughout two horizontal rotating plates was studied by Mohsen et al. [8]. They pointed out that Nusselt number has remarkable relation with thermal radiation. The common approach prior studies [6, 7, 8] to nonlinear temperature is to simplify it using Taylor serious up to a certain order and accept a truncated error. Consequently, the complexity of the analysis of a thermal radiation model reduces substantially. The linear approximation of the nonlinear temperature may lead to inconsistency with realistic practical applications in industry and engineering as the thermal radiation, which is a function of temperature, may be far from being linear in reality. Recent studies attempt at overcoming the over simplified approach of prior studies to nonlinear thermal radiation by considering it as the fourth power of the temperature and the nonlinearity was not resolved using Taylor series. The current study employ the same approach to nonlinear thermal radiation as [9, 10].

Many chemically reacting systems involve both homogeneous and heterogeneous reactions, with examples occurring in combustion, catalysis and biochemical processes. The interaction between the homogeneous reactions in the bulk of the fluid and heterogeneous reactions occurring on some catalytic surfaces is generally very complex, and is involved in the production and consumption of reactant pieces at different rates both within the fluid and the catalytic surfaces. The first study on homogeneous and heterogeneous reactions in boundary layer flow was addressed by Chaudhary et al [11]. They presented a simple model of homogeneous-heterogeneous reactions for forced convection near leading edge of the plate. Merkin [12] used the same model to considered the problem of a homogeneous reaction defined by cubic auto-catalysis and the heterogeneous reaction by a first order process in the boundary layer flow of a viscous fluid past a flat plate. A numerical study of the Homogeneous-heterogeneous reactions in micropolar fluid flow from a permeable stretching or shrinking sheet in a porous medium was conducted by Shaw et al. [13]. The study shown that the solutions are possible for all positive values of the stretching parameter, while solutions are possible only for a limited range of values for shrinking surface. Goyal et al. [14] studied the boundary layer flow and heat transfer of viscoelastic nanofluids past a stretching sheet with partial slip condition. A homogeneous-heterogeneous reactions on boundary layer flow of fluid at a stagnation point over a porous stretching sheet take into account the partial slip condition was discussed by Mariam et al. [15]. Bachok et al. [16] examined the homogeneous-heterogeneous reactions boundary layer flow close to the stagnation point past a stretching surface. The analytic solution of the homogeneous-heterogeneous reactions on Powell-Eyring fluid flow through a stretching sheet was addressed by Hayat et al. [17].

Entropy quantifies the molecular disorder (randomness) of systems. The second low of thermodynamics indicates that the entropy generation is positively correlated with the irreversible processes; that is, entropy generation (E_{gen}) is always positive during irreversible processes. On contrary, the entropy of a system stays unchanged during reversible processes. Since the performance of engineering systems deteriorate by irreversible process, it follows that the entropy generation affects the performance of such systems negatively. Therefore, the entropy generation is sometimes regarded as a measure of the magnitude of the irreversiblity of a process. Little attention has been paid to the study of entropy generation and the impact of the Bejan number (Be) on the viscoelastic nanofluid. This study the mechanisms for generating entropy are related to heat transfer, magnetic field, fluid friction irreversibility and mass transfer. Mirzazadeh et al. [18] studied the concept of entropy generation and the impact of the Bejan number (Be) on viscoelastic fluid past rotating cylinders. The application of the second law analysis to viscoelastic MHD flow through a stretching sheet was scrutinized by Soraya et al. [19]. Adnan et al. [20] analyzed the influence of viscoelasticity on entropy generation over a stretching plate.

The motivation of the present study is to investigate the entropy generation and Bejan number for steady two-

dimensional MHD flow, heat and mass transfer of an incompressible viscoelastic nanofluids over a linearly stretching sheet with homogeneous-heterogeneous chemical reaction and thermal radiation. To the best of the authors knowledge no paper in the research has so far studied entropy generation and Bejan number in viscoelastic nanofluid over a stretching sheet with homogeneous-heterogeneous reaction. The present study has many applications in cooling of metallic plate, movement of biological fluids, melt spinning, heat exchangers technology, and oceanography. Precisely, both entropy generation and Bejan number are play a major role in controlling the rate of heat transfer in the proximity of the sheet. The conversations equations are solved using the spectral quasi-linearization method (SQLM). The behavior of velocity, temperature, nanoparticles volume fraction, entropy generation and Bejan number are studied and visualize graphically.

MATHEMATICAL FORMULATION OF THE PROBLEM

Consider an incompressible, steady two-dimensional and hydrodynamics laminar flow of a viscoelastic fluid flow over a linear stretching sheet subject to the magnetic field and homogeneous–heterogeneous chemical reactions. The flow field is sibject to the effect of external transverse magnetic field of stretching B_0. The flow of viscoelastic fluid is restricted to region $(y>0)$ and the stagnation point is fixed at $x=0$. The wall and ambient temperature of the stretching sheet are defined as T_w and T_∞ respectively. C_a and C_b are the concentrations homogeneous and heterogeneous reactions for species A and B respectively. In addition the concentration at the ambient is defined as C_∞. The velocity near stretching sheet denoted by $U(x)=u_w(x)=cx$, where c represents stretching rate and $c>0$. This study considers the interaction between two different types of chemical reaction; such as, a homogeneous (bulk) and a heterogeneous (on sheet) reactions through a boundary layer flow. The reaction between species A and B is given by (see [11, 12])

$$A+2B\rightarrow 3B, \quad \text{rate}=k_1C_aC_b^2, \tag{1}$$
$$A\rightarrow B, \quad \text{rate}=k_sC_a. \tag{2}$$

Using these assumptions, and the usual boundary layer approximation, the system of equations for the viscoelastic nanofluid are given by:

$$\frac{\partial u}{\partial x}+\frac{\partial v}{\partial y}=0, \tag{3}$$
$$u\frac{\partial u}{\partial x}+v\frac{\partial u}{\partial y}=\nu\frac{\partial^2 u}{\partial y^2}-\frac{k_0}{\rho}\left[u\frac{\partial^3 u}{\partial x\partial y^2}+v\frac{\partial^3 u}{\partial y^3}+\frac{\partial u}{\partial x}\frac{\partial^2 u}{\partial y^2}-\frac{\partial u}{\partial y}\frac{\partial^2 u}{\partial x\partial y}\right]-\frac{\sigma B_0^2}{\rho}u, \tag{4}$$
$$u\frac{\partial T}{\partial x}+v\frac{\partial T}{\partial y}=\alpha_m\nabla^2 T+\tau\left[D_B\frac{\partial C_b}{\partial y}.\frac{\partial T}{\partial y}+\frac{D_T}{T_\infty}\left(\frac{\partial T}{\partial y}\right)^2\right]-\frac{1}{\rho c_p}\frac{\partial q_r}{\partial y}, \tag{5}$$
$$u\frac{\partial C_a}{\partial x}+v\frac{\partial C_a}{\partial y}=D_A\frac{\partial^2 C_a}{\partial y^2}-k_1C_aC_b^2, \tag{6}$$
$$u\frac{\partial C_b}{\partial x}+v\frac{\partial C_b}{\partial y}=D_B\frac{\partial^2 C_b}{\partial y^2}+\frac{D_T}{T_\infty}\frac{\partial^2 T}{\partial y^2}+k_1C_aC_b^2, \tag{7}$$

where $\alpha_m=k_f/(\rho c_p)_f$ and $\tau=(\rho c_p)_s/(\rho c_p)_f$. Suppose $\theta_w=T_w/T_\infty$. Then the temperature can be written as

$$T=T_\infty\left[1+\left(\theta_w-1\right)\theta\right].$$

The nonlinear thermal relation q_r is relative to heat flux. Applying the Rosseland approximation [9], q_r can be written as

$$q_r=-\frac{4\sigma^*}{3k^*}\frac{\partial T^4}{\partial y}=-\frac{16\sigma^*}{3k^*}T^3\frac{\partial T}{\partial y}. \tag{8}$$

The boundary conditions are:

$$u = U + k_1^* \nu \frac{\partial u}{\partial y}, \;\; v = 0, \;\; T = T_w, \;\; D_A \frac{\partial C_a}{\partial y} = k_s C_a, \;\; D_B = \frac{\partial C_b}{\partial y} = -k_s C_a \quad \text{at} \quad y = 0,$$
$$u = 0, \;\; T = T_\infty, \;\; C_a \to C_\infty, \;\; C_b \to 0 \quad \text{at} \quad y \to \infty. \tag{9}$$

To simplify the equations we introduce the following similarity transformations:

$$\eta = \sqrt{\frac{c}{\nu}} y, \;\; u = cx f'(\eta), \;\; v = -\sqrt{c\nu} f(\eta),$$
$$\theta(\eta) = \frac{T - T_\infty}{T_w - T_\infty}, \;\; \xi(\eta) = \frac{C_a}{C_\infty}, \;\; \phi(\eta) = \frac{C_b}{C_\infty}. \tag{10}$$

The system of equations (3)–(7) is transformed to:

$$f''' + f f'' - f'^2 + \alpha\left(f''^2 - 2f' f''' + f f''''\right) - Ha^2 f' = 0, \tag{11}$$
$$\left[1 + Nr\left\{1 + (\theta_w - 1)\theta\right\}^3\right]\theta'' + 3Nr(\theta_w - 1)\left\{1 + (\theta_w - 1)\theta\right\}^2 \theta'^2 + Pr f \theta' + Pr\left(Nb\theta'\phi' + Nt\theta'^2\right) = 0, \tag{12}$$
$$\xi'' + Scf\xi' - KSc\xi\phi^2 = 0, \tag{13}$$
$$\frac{1}{\varepsilon Sc}\left(\phi'' + \frac{Nt}{Nb}\theta''\right) + f\phi' + K\xi\phi^2 = 0, \tag{14}$$

subject to the boundary conditions

$$f(0) = 0, \;\; f'(0) = 1 + \lambda f''(0), \;\; \theta(0) = 1, \;\; \xi'(0) = K_s\xi(0), \;\; \phi'(0) = -\varepsilon K_s \xi(0),$$
$$f'(\infty) = 0, \;\; \theta(\infty) = 0, \;\; \xi(\infty) = 1, \;\; \phi(\infty) = 0, \tag{15}$$

where a prime refers to differentiation respect to η, $\lambda = k_1^* \nu\sqrt{c/\nu}$, $K_s = k_s/\left(D_A\sqrt{c/\nu}\right)$ and $\varepsilon = D_A/D_B$. The non-dimensional parameters appearing in Equations (11)–(14) are defined as

$$\alpha = \frac{ck_0}{\nu}, \;\; Ha^2 = \frac{\sigma B_0^2}{\rho c}, \;\; Pr = \frac{\mu c_p}{k_f},$$
$$Nr = \frac{16\sigma^* T_\infty^3}{3k^* k_f}, \;\; Nb = \frac{\tau D_B C_\infty}{\nu}, \;\; Nt = \frac{\tau D_T\left(T_w - T_\infty\right)}{\nu T_\infty},$$
$$K = \frac{k_1 C_\infty^2}{c}, \;\; Sc = \frac{\nu}{D_B}, \;\; \varepsilon = \frac{D_A}{D_B}. \tag{16}$$

Although in many practical scenarios the sizes of the diffusion coefficient of the chemical species of A and B are not equal, they could be of a comparable size. Thus, it is not unrealistic to assume that $D_A = D_B$ (consequently, $\varepsilon = 1$), [21]. This assumption leads to

$$\xi(\eta) + \phi(\eta) = 1. \tag{17}$$

Consequently, Equations (13) and (14) can be reduced to a single equation as follows

$$\xi'' - \frac{Nt}{Nb}\theta'' + Scf\xi' - ScK\xi(1 - \xi)^2 = 0, \tag{18}$$

with boundary conditions

$$\xi'(0) = K_s\xi(0), \quad \xi(\infty) = 1. \tag{19}$$

Hence, the system in Equations (11)–(14) becomes

$$f''' + ff'' - f'^2 + \alpha(f''^2 - 2f'f''' + ff'''') - Ha^2 f' = 0, \tag{20}$$

$$\left[1 + Nr\left\{1 + (\theta_w - 1)\theta\right\}^3\right]\theta'' + 3Nr(\theta_w - 1)\left\{1 + (\theta_w - 1)\theta\right\}^2\theta'^2 + Prf\theta' + Pr\left(Nt\theta'^2 - Nb\xi'\theta'\right) = 0, \tag{21}$$

$$\xi'' - \frac{Nt}{Nb}\theta'' + Scf\xi' - ScK\xi(1-\xi)^2 = 0, \tag{22}$$

with the new boundary conditions

$$f(0) = 0, \quad f'(0) = 1 + \lambda f''(0), \quad f'(\infty) = 0, \quad \theta(0) = 1, \quad \theta(\infty) = 0, \quad \xi'(0) = K_s\xi(0), \quad \xi(\infty) = 1. \tag{23}$$

The skin friction coefficient C_f, the local Nusselt number Nu_x and the Sherwood number Sh_x are the most significant physical quantities which are given by

$$C_f = \frac{\tau_w}{\rho u_w^2}, \quad Nu_x = \frac{xh_w}{k\left(T_w - T_\infty\right)} \text{ and } Sh_x = \frac{xh_m}{D_B C_\infty}, \tag{24}$$

where τ_w, h_w and h_m are given by

$$\tau_w = \mu\left(\frac{\partial u}{\partial y}\right)_{y=0}, \quad h_w = -k\left(\frac{\partial T}{\partial y}\right)_{y=0} \text{ and } h_m = -D_B\left(\frac{\partial C_a}{\partial y}\right)_{y=0}. \tag{25}$$

Using Equation (9) and Equation (25) the Equation (24) becomes as:

$$C_f Re^{1/2} = f''(0), \quad Re^{-1/2}Nu_x = -\left(1 + Nr\theta_w^3\right)\theta'(0) \text{ and } Re^{-1/2}Sh_x = -\xi'(0). \tag{26}$$

where $Re = \frac{U(x)x}{\nu}$.

ENTROPY GENERATION ANALYSIS

Entropy measures the chaos of a certain system. Entropy generation depends on procedures reversibility. In isolated systems, it is usually the case where there is a rise in entropy over time for reversible reactions. In present days, the applications of nanofluids in medical and engineering settings, have increased substantially which give more credits to the studies which investigate the influence of nanoparticles on entropy generation, [22, 23]. In this study the focus is on entropy generation in the viscoelastic nanofluid.

The volumetric rate of local entropy generation, which is based on the second law of thermodynamics, is given by

$$E_{gen} = \frac{k_f}{T_\infty^2}\left(\left(\frac{\partial T}{\partial y}\right)^2 + \frac{16\sigma^* T^3}{3k^* k_f}\left(\frac{\partial T}{\partial y}\right)^2\right) + \frac{\sigma B_0^2}{T_\infty}u^2 + \frac{RD}{T_\infty}\left(\frac{\partial T}{\partial y}\frac{\partial C_a}{\partial y}\right) + \frac{RD}{C_\infty}\left(\frac{\partial C_a}{\partial y}\right)^2, \tag{27}$$

where in Equation (27), the first term is irreversibility caused by heat transfer, the second term is the entropy generation due to the influence of the magnetic field and the third and fourth terms are irreversibility caused by diffusion effect. The characteristic entropy generation rate is

$$E_0 = \frac{k_f\left(\Delta T\right)^2}{x^2 T_\infty^2}. \tag{28}$$

By using Equation (28) and Equation (10) the entropy generation in dimensionless is given by

$$N_G = Re\left\{1+Nr\left(1+\chi\theta\right)^3\right\}\theta'^2 + \frac{ReBrHa^2}{\chi}f'^2 + \frac{Re\Sigma}{\chi^2}\xi'^2 + \frac{Re\Sigma}{\chi}\theta'\xi'. \tag{29}$$

The numbers and parameters in Equation (29) can be obtained as

$$\begin{aligned} Re &= \frac{u_w(x)x}{\nu},\ \ Br = \frac{\mu u_w^2(x)}{k_f\Delta T}, \Delta T = T_w - T_\infty, \\ \Sigma &= \frac{C_\infty RD}{k_f},\ \ \chi = \left(\theta_w - 1\right), \end{aligned} \tag{30}$$

Equation (29) can be obtained as a summation of the entropy generation number caused by the heat transfer (N_1) and the entropy generation number caused by both diffusive irreversibility and magnetic field (N_2). That is $N_G = N_1 + N_2$, where

$$N_1 = Re\left\{1+Nr\left(1+\chi\theta\right)^3\right\}\theta'^2,\ \ N_2 = \frac{ReBrHa^2}{\chi}f'^2 + \frac{Re\Sigma}{\chi^2}\xi'^2 + \frac{Re\Sigma}{\chi}\theta'\xi'. \tag{31}$$

The heat transfer irreversibility, diffusive irreversibility and the magnetic field all contribute to entropy generation. It is therefore worthwhile investigating the conditions under which heat transfer dominates entropy generation. To investigate this question, the Bejan (Be) number is defined as the ratio of entropy generation due to heat transfer and the entropy generation number.

$$Be = \frac{N_1}{N_G} = \frac{1}{1+\Phi}, \tag{32}$$

where $\Phi = \frac{N_2}{N_1}$ represents the irreversibility ratio. Depending on Φ, different factors contribute differently on entropy generation. When $0 \leq \Phi < 1$, heat transfer is the most dominant factor in entropy generation. When $\Phi > 1$, the irreversibility diffusive with the magnetic effects dominate on entropy generation. When $\Phi = 1$ heat transfer and diffusion with magnetic effects contributes equally on entropy generation. The Bejan number takes values in range $[0,1]$ (see [22, 24, 25, 26, 27, 28]). At the extreme when $Be = 1$ the irreversibility of heat transfer dominates. On the other extreme when $Be = 0$ the combined effects of diffusion and magnetic field dominates the irreversibility. When $Be = 0.5$, the contribution of heat transfer in entropy generation is the same as the combined contribution of diffusion and magnetic field in entropy generation. Additionally, the Bejan number Be is considered at the best values of the parameters at which the entropy generation its minimum.

METHODS OF SOLUTION

The quasi-linearization method (QLM) represents the general form of the Newton-Raphson method (Bellman and Kalaba [29]). The concept of the QLM is linearization the nonlinear system of equations using the Taylor series by assumption that the difference between the current iteration, $r+1$, and the previous iteration, r is negligible.

Implementing the quasi-linearization scheme to Equations (20)–(22) subject to the boundary conditions (23), gives the iterative schemes:

$$a_{0,r}f''''_{r+1} + a_{1,r}f'''_{r+1} + a_{2,r}f''_{r+1} + a_{3,r}f'_{r+1} + a_{4,r}f_{r+1} = R_f, \tag{33}$$

$$b_{0,r}\theta''_{r+1} + b_{1,r}\theta'_{r+1} + b_{2,r}\theta_{r+1} + b_{3,r}f_{r+1} + b_{4,r}\xi'_{r+1} = R_\theta, \tag{34}$$

$$c_{0,r}\xi''_{r+1} + c_{1,r}\xi'_{r+1} + c_{2,r}\xi_{r+1} + c_{3,r}f_{r+1} + c_{4,r}\theta''_{r+1} = R_\xi, \tag{35}$$

subject to

$$f_{r+1}(0)=0,\ \ f'_{r+1}(0)=1+\lambda f''_{r+1}(0),\ \ f'_{r+1}(\infty)=0,\ \ \theta_{r+1}(0)=1,$$
$$\theta_{r+1}(\infty)=0,\ \ \xi'_{r+1}(0)=K_s\xi_{r+1}(0),\quad \xi_{r+1}(\infty)=1. \tag{36}$$

The coefficients in Equations (33)–(35) are:

$$a_{0,r}=\alpha f_r,\ a_{1,r}=1-2\alpha f'_r,\ a_{2,r}=f_r+2\alpha f''_r,$$
$$a_{3,r}=-2f'_r-2\alpha f'''_r-Ha^2,\ a_{4,r}=f''_r+\alpha f''''_r,$$
$$b_{0,r}=1+Nr\Big[1+\big(\theta_w-1\big)\theta_r\Big]^3,$$
$$b_{1,r}=6Nr\big(\theta_w-1\big)\Big[1+\big(\theta_w-1\big)\theta_r\Big]^2+Prf_r-PrNb\xi'_r+2PrNt\theta'_r,$$
$$b_{2,r}=\theta''_r\Big[1+3Nr\Big\{1+\big(\theta_w-1\big)\theta_r\Big\}^2\big(\theta_w-1\big)\Big]+6Nr\big(\theta_w-1\big)\Big\{1+\big(\theta_w-1\big)\theta_r\Big\}\big(\theta_w-1\big)\theta'^2_r,$$
$$b_{3,r}=Pr\theta'_r,\ \ b_{4,r}=-PrNb\theta'_r,$$
$$c_{0,r}=1,\ \ c_{1,r}=Scf_r,\ \ c_{2,r}=-ScK\Big(1-4\xi_r+3\xi_r^2\Big),\ \ c_{3,r}=Sc\xi'_r,\ \ c_{4,r}=-(Nt/Nb). \tag{37}$$

A Chebyshev pseudo-spectral method [30] was used to solve the system (33)–(35) using the Gauss-Lobatto points [31] defined by

$$x_i=\cos\Big(\frac{\pi i}{N}\Big),\quad i=0,1,2,...,N;\quad -1\le x_i\le 1, \tag{38}$$

where N represents the number of collocation points. The system is solved in the domain $[0,L]$ instead of $[0,\infty)$; where, L is the boundary condition at infinity and L must be a larger number. Thus, the interval $[0,L]$ transformed to $[-1,1]$ using the linear transformation formula $\eta=\frac{L(x+1)}{2}$.

The idea of the spectral collocation method is introduce a differentiation matrix in order to approximate the derivative of unknown variables at the collocation points as a matrix product:

$$\frac{dF_r}{d\eta}=\sum_{k=0}^{N}\mathbf{D}_{jk}f(\eta_k)=\mathbf{D}F_m,\ j=0,1,2,...,N, \tag{39}$$

where $\mathbf{D}=2D/L$ and $F=\Big[f(\eta_0),f(\eta_1),f(\eta_1),...,f(\eta_N)\Big]^T$ is the vector function at the collocation points. The high derivatives are defined as powers of $\mathbf{D}$, thence

$$F_r^{(p)}=\mathbf{D}^pF_r, \tag{40}$$

thus p represents the order of the derivative. Thus, Equation (33)–(35) with (36) yields

$$\mathbf{A}_{1,1}\mathbf{f}+\mathbf{A}_{1,2}\theta+\mathbf{A}_{1,3}\xi=R_f, \tag{41}$$
$$\mathbf{A}_{1,2}\mathbf{f}+\mathbf{A}_{2,2}\theta+\mathbf{A}_{2,3}\xi=R_\theta, \tag{42}$$
$$\mathbf{A}_{1,3}\mathbf{f}+\mathbf{A}_{2,3}\theta+\mathbf{A}_{3,3}\xi=R_\xi. \tag{43}$$

Here

$$\mathbf{A}_{1,1}=\mathbf{diag}\big(a_{0,r}\big)\mathbf{D}^4+\mathbf{diag}\big(a_{1,r}\big)\mathbf{D}^3+\big(a_{2,r}\big)\mathbf{D}^2+\mathbf{diag}\big(a_{3,r}\big)\mathbf{D}+\mathbf{diag}\big(a_{4,r}\big)\mathbf{I},$$
$$\mathbf{A}_{1,2}=0,\ \ \mathbf{A}_{1,3}=0, \tag{44}$$
$$\mathbf{A}_{2,1}=\mathbf{diag}\big(b_{3,r}\big)\mathbf{I},\ \ \mathbf{A}_{2,2}=\mathbf{diag}\big(b_{0,r}\big)\mathbf{D}^2+\mathbf{diag}\big(b_{1,r}\big)\mathbf{D}+\mathbf{diag}\big(b_{2,r}\big)\mathbf{I},$$
$$\mathbf{A}_{2,3}=\mathbf{diag}\big(b_{4,r}\big)\mathbf{D}, \tag{45}$$
$$\mathbf{A}_{3,1}=\mathbf{diag}\big(c_{3,r}\big)\mathbf{I},\ \ \mathbf{A}_{3,2}=\mathbf{diag}\big(c_{4,r}\big)\mathbf{D}^2,$$
$$\mathbf{A}_{3,3}=\mathbf{diag}\big(c_{0,r}\big)\mathbf{D}^2+\mathbf{diag}\big(c_{1,r}\big)\mathbf{D}+\mathbf{diag}\big(c_{2,r}\big)\mathbf{I}, \tag{46}$$

$$\mathbf{R}_f = \alpha \mathbf{f}_\mathbf{r}''^2 - \mathbf{f}_\mathbf{r}'^2 - 2\alpha \mathbf{f}_\mathbf{r}' \mathbf{f}_\mathbf{r}''' + \mathbf{f}_\mathbf{r} \mathbf{f}_\mathbf{r}'' + \alpha \mathbf{f}_\mathbf{r} \mathbf{f}_\mathbf{r}'''', \tag{47}$$

$$\mathbf{R}_\theta = PrNt\theta_\mathbf{r}'^2 + Pr\mathbf{f}_\mathbf{r}\theta_\mathbf{r}' - PrNb\xi_\mathbf{r}'\theta_\mathbf{r}' + 3Nr\theta_\mathbf{r}''\theta_\mathbf{r}\Big(\theta_w - 1\Big)\Big[1 + (\theta_w - 1)\theta_\mathbf{r}\Big]^2$$

$$+3Nr\Big(\theta_w - 1\Big)\Big[1 + (\theta_w - 1)\theta_\mathbf{r}\Big]^2\theta_\mathbf{r}'^2 + 6Nr\Big(\theta_w - 1\Big)^2\theta_\mathbf{r}\theta_\mathbf{r}'^2\Big[1 + (\theta_w - 1)\theta_\mathbf{r}\Big], \tag{48}$$

$$\mathbf{R}_\xi = Sc\mathbf{f}_\mathbf{r}\xi_\mathbf{r}' + 2ScK\xi_\mathbf{r}\big(\xi_\mathbf{r} - \xi_\mathbf{r}^2\big), \tag{49}$$

where **diag** and **I** are the diagonal matrices and identical matrix; $(N+1)\times(N+1)$ respectively, and $\mathbf{f}$, θ and ξ are the values of functions, f, θ and ξ respectively. The system in equations (41)–(43) is solved using the SQLM schemes. The iteration is started with initial guesses approximation which can be written as

$$f_0(\eta) = \frac{1}{1+\lambda}\big(1 - \exp(-\eta)\big),$$
$$\theta_0(\eta) = \exp(-\eta), \quad \xi_0(\eta) = 1 - \frac{K_s}{1+K_s}\exp(-\eta). \tag{50}$$

Equations (41)–(43) can be written in matrix form as

$$\begin{bmatrix} \mathbf{A}_{11} & \mathbf{A}_{12} & \mathbf{A}_{13} \\ \mathbf{A}_{21} & \mathbf{A}_{22} & \mathbf{A}_{23} \\ \mathbf{A}_{31} & \mathbf{A}_{32} & \mathbf{A}_{33} \end{bmatrix} \begin{bmatrix} F_{r+1} \\ \Theta_{r+1} \\ \xi_{r+1} \end{bmatrix} = \begin{bmatrix} \mathbf{R}_f \\ \mathbf{R}_\theta \\ \mathbf{R}_\xi \end{bmatrix} \tag{51}$$

DISCUSSION OF RESULTS

The study addresses entropy generation and the impact of the Bejan number in a steady two-dimensional MHD viscoelastic nanofluid flow that is subject to homogeneous and heterogeneous chemical reactions, the effect of the slip and the nonlinear thermal radiation. The spectral quasi-linearization method (SQLM) is used to solve the conservation equations. The SQLM is used in the literature because it gives accurate results for boundary layer type equations [32, 33]).

The effect of flow parameters on velocity, temperature and concentration profiles as well as the skin friction coefficient, local Nusselt number and Sherwood number is investigated and provided in tables and graphs. The variation in the skin friction coefficient with different values of the viscoelastic parameter the partial slip parameter and the Hartmann number are provided in Table 1. It is observed that the skin friction decreases with the viscoelastic parameter and the Hartmann number, in contrast, it increases with λ. Numerical values of the local Nusselt number and Sherwood number with variations in the homogeneous reaction parameter, the heterogeneous reaction parameter, the nonlinear thermal radiation parameter, the temperature ratio parameter and the Thermophoresis parameter are tabulated in Table 2. It is noted that the Nusselt number increases with the heterogeneous reaction parameter, the nonlinear thermal radiation parameter, the temperature ratio parameter and the Thermophoresis parameter whereas homogeneous reaction parameter reduces the Nusselt number. In addition, in Table 2, it is observed that the homogeneous reaction parameter enhances the value of Sherwood number which is decreasing with heterogeneous reaction parameter, the nonlinear thermal radiation parameter, the temperature ratio parameter and the Thermophoresis parameter.

Table 1: Numerical values of $f''(0)$ with various values of $\alpha, \lambda,$ and Ha when $Nb = 0.5$,$Sc = 2, Pr = 6, K = 0.5, K_s = 1, Nr = 0.5, Nt = 0.2, \theta_w = 1.01$

α	λ	Ha	$C_f Re^{1/2}$
0.5			−0.90425116
0.7	0.3	0.5	−0.97468978
0.9			−1.06029277
	0.1		−1.05590404
0.2	0.5	0.5	−0.67757017
	0.7		−0.58067315
		0.2	−0.75761100
0.2	0.3	0.7	−0.88164753
		1	−0.98974875

Table 2: Numerical values of $-\theta'(0)$ and $-\xi'(0)$ with different values of K, K_s, Nr, θ_w and Nt when $\alpha = 0.2, \lambda = 1, Nb = 0.5, Ha = 0.5, Sc = 2, Pr = 6$.

K	K_s	Nr	θ_w	Nt	$Re^{-1/2} Nu_x$	$Re^{-1/2} Sh_x$
0.1					−0.44290300	−0.29765451
0.3	1	0.5	1.01	0.2	−0.45256076	−0.24036655
0.7					−0.50454819	−0.09720213
	0.5				−0.49842157	−0.11927642
0.5	3	0.5	1.01	0.2	−0.43654921	−0.24314929
	7				−0.42046705	−0.28069503
		1			−0.39239089	−0.08202508
0.5	1	1.5	1.01	0.2	−0.36069650	−0.08361434
		2			−0.33377872	−0.08566399
			1.5		−0.33609133	−0.13436426
0.5	1	0.5	2	0.2	−0.23905902	−0.14421738
			2.5		−0.17085877	−0.14991236
				1.5	−0.18792574	−0.15174783
0.5	1	0.5	1.01	2	−0.14148245	−0.17675215
				2.5	−0.11188459	−0.19531184

Figures (1) illustrates the effect of the viscoelastic parameter on the velocity, temperature and concentration profiles while other parameters are kept fixed. It is observed that an increase in the viscoelastic parameter leads to a decrease in the velocity and concentration profiles respectively, whereas the temperature profile is positively related to viscoelastic parameter.

The variability on the velocity, temperature and concentration profiles with various values of the partial slip parameter is displayed in Figures (2). It is noted that the influence of increasing partial slip parameter shifts streamline to boundary layer such that the momentum boundary layer becomes thicker. Therefore, partial slip parameter decreases the boundary layer velocity and concentration while the temperature increases with partial slip parameter.

Figure (3) shows the effect of different values of the Hartmann number on the velocity, temperature and concentration profiles. It is observed that an increase in the Hartmann number leads to reduction in both velocity and concentration profiles whereas it leads to an increase in temperature profile. The depreciation in velocity profile can be attributed to the presence of Lorentz force which prevails over the boundary layer when Hartmann number increases and thus leads to an increase in the viscous force which, in turn, resists velocity profile.

The effects of various values of the Brownian motion parameter on the temperature and concentration profiles

is presented in Figure (4). It is deduced that Brownian motion parameter is proportionally related to temperature and concentration profiles. However, the large values of Brownian motion parameter leads to an enhancement of the concentration. Further, the variation in Brownian motion parameter produces homogeneous and heterogeneous mixing which promotes the thermal conductivity of the viscoelastic nanofluid. Thus, the higher thermal conductivity causes to increase both the temperature and the chemical specie concentration.

The variation in the temperature profile according to the varying values of the nonlinear thermal radiation parameter is demonstrated in Figure (5). It is noted that the temperature increases with increased nonlinear thermal radiation parameter, which is consistent with physical observations regarding to the affect of increasing thermal radiation.

Figure (6) shows the effect of the Thermophoresis parameter on the temperature profile. It is noted that as temperature profile increases, Thermophoresis parameter also increases. From Equation (12), Thermophoresis parameter is proportionally related to the temperature profile.

The behavior of the concentration profile with increasing values of the stretching homogeneous parameter and the stretching heterogeneous parameter is depicted in Figures (7) and (8). Further, from the figures, it is observed the boundary conditions at the wall ($y = 0$) and far way from the sheet (streamline $y = \infty$) are satisfied. The concentration profile increases negligibly with homogeneous parameter and heterogeneous parameter. This effect occurs only in the vicinity of the wall.

Figure (9) represents the influence of Prandtl number on the temperature and concentration profiles. It is noted that an increases in Pr tends to decreases in temperature profile and increases in concentration profile. The deterioration in the concentration profile as a result of increasing values of Prandtl can be liked to the thinner thermal boundary layer (low temperature) caused by reduction of thermal diffusion of the fluid layers which is directly related to increase in Prandtl number.

The changing in the temperature and concentration profiles with an increase in the temperature ratio parameter is exhibited in Figure (10). An increase of temperature ratio parameter results in the increase of temperature and concentration profiles, at the proximity of the sheet. However, in ranges not very far from the sheet (η>3.5), concentration profile decreases with increasing temperature ratio parameter.

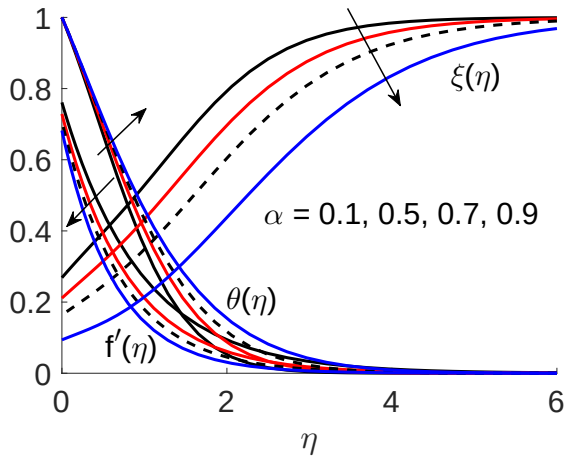

Figure 1: Effects of viscoelastic parameter (α) on the velocity profile ($f'(\eta)$), temperature ($\theta(\eta)$), concentration ($\xi(\eta)$) profiles for $K_s = 1, K = 0.5, Ha^2 = 0.5, \lambda = 0.3, Pr = 6, Nb = 0.5, Nt = 0.2, Sc = 2.0, \theta_w = 1.01, Nr = 0.5$

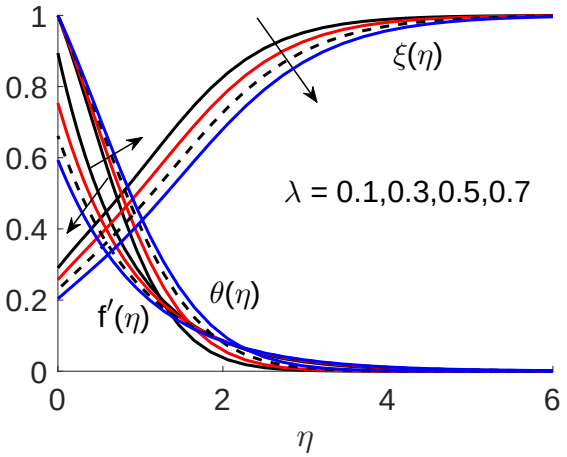

Figure 2: Effects of the partial slip parameter (λ) on the velocity $(f'(\eta))$, temperature $(\theta(\eta))$ and concentration $(\xi(\eta))$ profiles for $K_s = 1, K = 0.5, Ha^2 = 0.5, \alpha = 0.2, Pr = 6, Nb = 0.5, Nt = 0.2, Sc = 2.0, \theta_w = 1.01, Nr = 0.5$

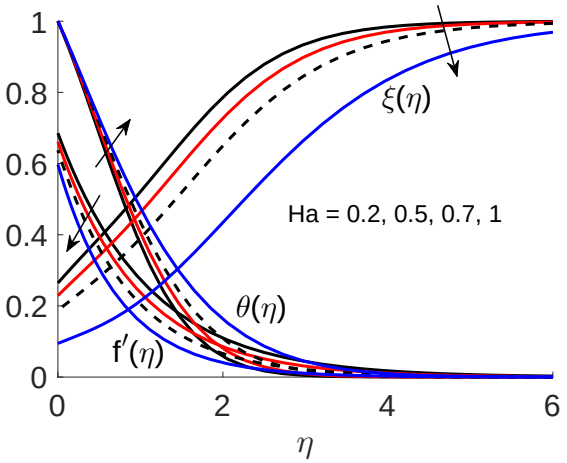

Figure 3: Effects of the Hartmann number (Ha) on the velocity $(f'(\eta))$, temperature $(\theta(\eta))$ and concentration $(\xi(\eta))$ profiles for $K_s = 1, K = 0.5, \lambda = 0.3, \alpha = 0.2, Pr = 6, Nb = 0.5, Nt = 0.2, Sc = 2.0, \theta_w = 1.01, Nr = 0.5$

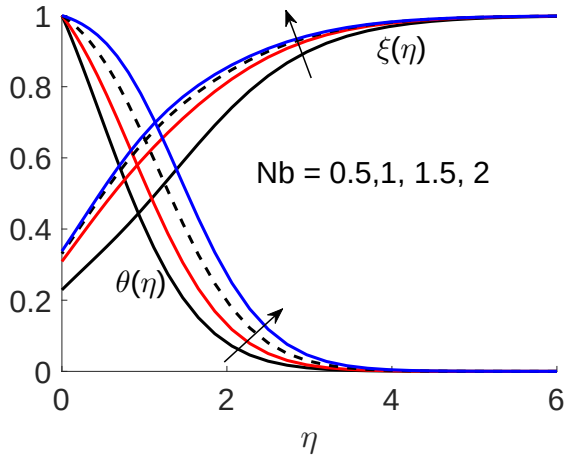

Figure 4: Effects of the Brownian mention parameter (Nb) on the velocity $(f'(\eta))$, temperature $(\theta(\eta))$ and concentration $(\xi(\eta))$ profiles for $K_s = 1, K = 0.5, \lambda = 0.3, \alpha = 0.2, Pr = 6, Ha^2 = 0.5, Nt = 0.2, Sc = 2.0, \theta_w = 1.01, Nr = 0.5$

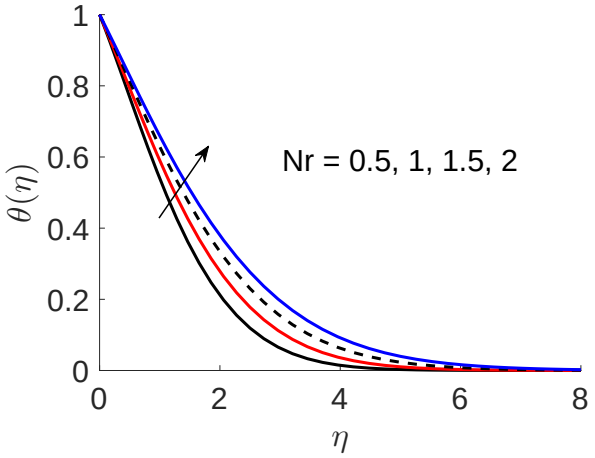

Figure 5: Effects of the thermal radiation parameter (Nr) on the temperature profile $(\theta(\eta))$ for $K_s = 1, K = 0.5, \lambda = 0.3, \alpha = 0.2, Pr = 6, Ha^2 = 0.5, Nt = 0.2, Sc = 2.0, \theta_w = 1.01, Nb = 0.5$

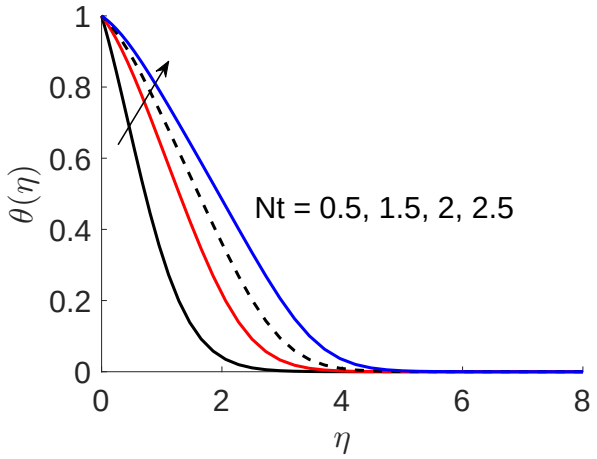

Figure 6: Effects of the Thermophoresis parameter (Nt) on the temperature profile $(\theta(\eta))$ for $K_s = 1, K = 0.5, \lambda = 0.3, \alpha = 0.2, Pr = 6, Ha^2 = 0.5, Nr = 0.5, Sc = 2.0, \theta_w = 1.01, Nb = 0.5$

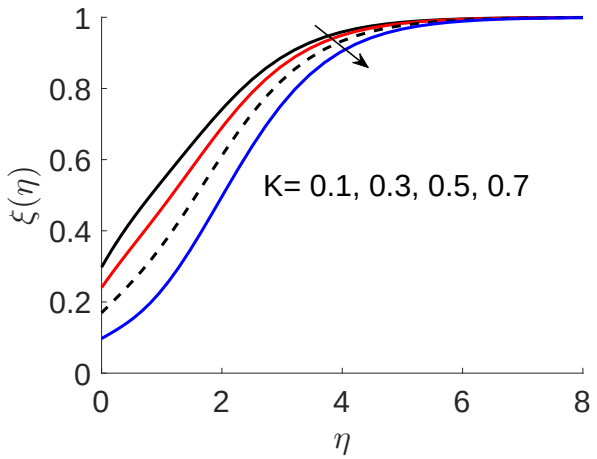

Figure 7: Effects of the stretching homogeneous parameter (K) on the concentration profile $(\xi(\eta))$ for $K_s = 1, Nt = 0.2, \lambda = 0.3, \alpha = 0.2, Pr = 6, Ha^2 = 0.5, Nr = 0.5, Sc = 2.0, \theta_w = 1.01, Nb = 0.5$

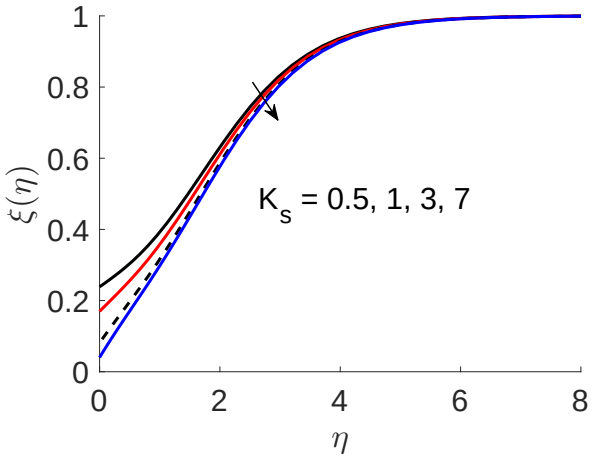

Figure 8: Effects of the stretching heterogeneous parameter (K_s) on the concentration profile ($\xi(\eta)$) for $K = 0.5, Nt = 0.2, \lambda = 0.3, \alpha = 0.2, Pr = 6, Ha^2 = 0.5, Nr = 0.5, Sc = 2.0, \theta_w = 1.01, Nb = 0.5$

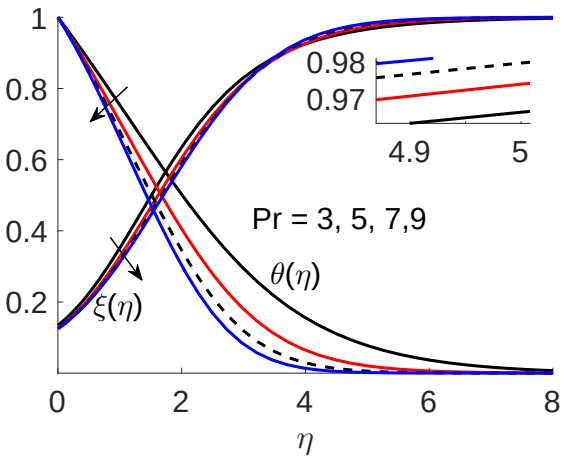

Figure 9: Effects of the Prandtl number (Pr) on the temperature ($\theta(\eta)$) concentration ($\xi(\eta)$) profiles for $K = 0.5, Nt = 0.2, \lambda = 3.5, \alpha = 0.2, K_s = 1, Ha^2 = 0.5, Nr = 0.5, Sc = 2.0, \theta_w = 1.01, Nb = 0.5$

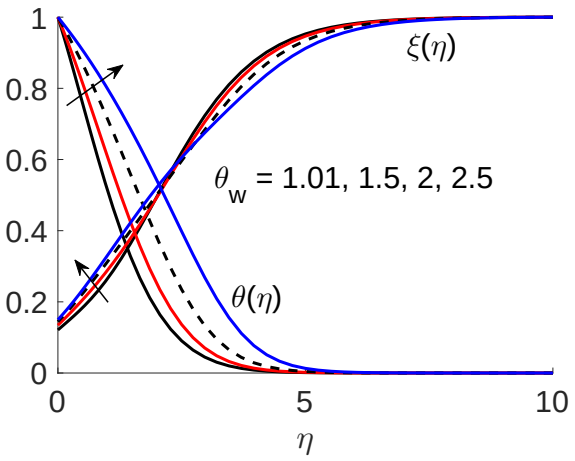

Figure 10: Effects of the temperature ratio parameter (θ_w) on the temperature ($\theta(\eta)$) concentration ($\xi(\eta)$) profiles for $K = 0.5, Nt = 0.2, \lambda = 3.5, \alpha = 0.2, K_s = 1, Ha^2 = 0.5, Nr = 0.5, Sc = 2.0, Pr = 6, Nb = 0.5$

The behavior of dimensionless entropy generation profile represents one of the most important characteristic of this study. The variation in entropy generation profile is examined and exhibited in different figures with different values of the pertinent parameters, namely, the Hartmann number, the Brinkman number, the dimensionless parameter, the viscoelastic parameter, the Reynolds number and the partial slip parameter respectively. It is worth noting that Figures (11)–(17) provide several ways to control the entropy generation number.

Figure (11) shows the effect of the Hartmann number on the entropy generation number. An increase in Hartmann number results in the increment of the entropy generation number. In the neighborhood of the sheet vicinity, Hartmann number has significant impact on the entropy generation number, whereas at regions far away from the sheet, the Hartmann number has slight effect on the entropy generation number. This effect tends to increase the resistance of the fluid motion, consequently the heat transfer rates increase, which result in an increase in the entropy generation number. However, at far from the sheet vicinity, the influence of Hartmann number is insignificant.

Figure (12) displays entropy generation with the Brinkman number, which represents a measure of the significance of the heat produced by viscous heating proportional to heat transported by molecular conduction. An increase in the Brinkman number tends to increase the entropy generation number especially in the vicinity of the sheet. Heat generated bey viscous dissipation prevails through the heat transported via the molecular conduction in the neighborhood of the sheet. In the vicinity of the sheet, essential heat generation occurs over the boundary layer of the moving fluid particles, which trends the entropy generation number to enhance by increasing the degree of disorder of the system.

The variation in the entropy generation number with different values of the Prandtl number is illustrated in Figure (13). It is noted that an increase in the Prandtl number leads to an increases in the entropy generation number in the neighborhood to the sheet. However, in ranges not very far from the sheet, entropy generation number decreases with increasing the value of the Prandtl number. Furthermore, in the proximity of the sheet, the entropy generation number increases with a rise in the Prandtl number because the concentration profile shows a substantial decrease as Prandtl number increases (see Figure 9). Further, for a fixed value of Prandtl number, entropy generation number decreases gradually as moving away from the sheet until it extinguishes completely.

Figure (14) shows the behavior of the entropy generation number with the temperature ratio parameter. It can be observed that in the neighborhood of the sheet, the entropy generation number decreases with increasing the temperature ratio parameter. However, in ranges not very far from the sheet, an increases in the temperature ratio parameter tends to an increase in the entropy generation number. Moreover, in the proximity of the sheet, the entropy generation number decreases with a rise in the temperature ratio parameter because the concentration profile illustrates a great increase with increasing the temperature ratio parameter (see Figure 10). Further, for a fixed value of the temperature ratio parameter, the entropy generation number increases gradually as moving away from the sheet.

Figure (15) shows the influence of the viscoelastic parameter on the entropy generation number. It is worth noting that the entropy generation number is proportionally related to the viscoelastic parameter especially in the vicinity of the sheet. Figure (16) relates the entropy generation number with the Reynolds number. It is noted that the Reynolds number has remarkable effects on the entropy generation number as an increase in the Reynolds number leads to a significant increase in the entropy generation number, in the vicinity of the sheet. As Reynolds number increases, the entropy generation number caused by the heat transfer dominates the entropy generation number caused by the diffusion effect and the magnetic field in the neighborhood of the stretching sheet. This effect makes the fluid motion more random to the extent that troubled fluid motions arise. Consequently, the entropy generation number increases due to the contribution of heat transfer. Moreover, when Reynolds number increases, the inertia forces are promoted, hence, the values of the viscous forces are decreased. By increasing the value of the Reynolds number, the acceleration of the fluid increases in the vicinity of the sheet. However, far away from the sheet these effects are negligible.

The variation in the entropy generation number with various values of the partial slip parameter is illustrated in Figure (17). It is noted that the entropy generation number decreases when partial slip parameter increase, in the vicinity of the sheet. However, when the distance becomes larger, this effect is negligible.

The entropy generation number can be due to (the diffusion effect and magnetic field) and heat transfer. Therefore, it is legitimate to investigate which of these three factors dominates the entropy generation number. To identity whether the entropy generation due to heat transfer dominates over the entropy generation due to (diffusive irreversibility and magnetic field) (and vice versa), the Bejan number is studied for different physical parameters. Moreover, the Bejan number can be used to identity the dominant irreversibility: either the heat irreversibilit or the diffusion and the magnetic field irreversibility.

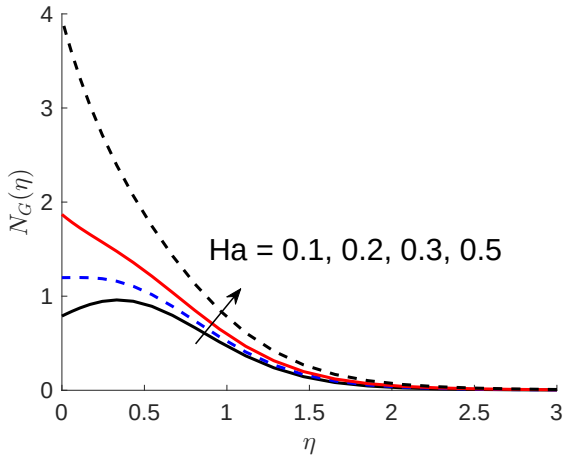

Figure 11: Effects of the Hartmann number (Ha^2) on the entropy generation number ($N_G(\eta)$) with $K_s = 1, K = 0.5, \lambda = 0.2, \alpha = 0.2, Nb = 0.5, Nt = 0.2, Nr = 0.5, Pr = 6, Sc = 2.0, \theta_w = 1.01, Re = 1, Br = 8, \chi = 0.2, \Sigma = 0.01$.

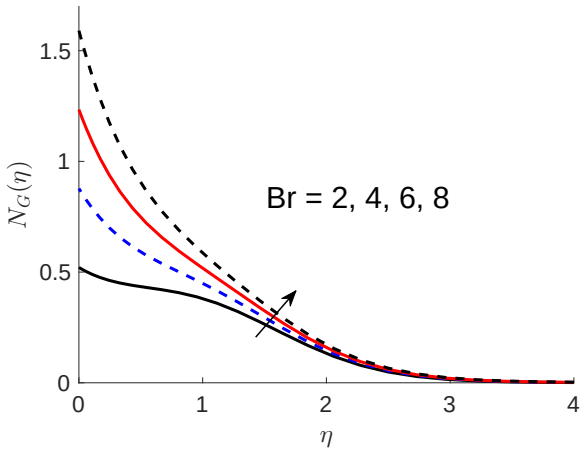

Figure 12: Effects of the Brinkman number (Br) on the entropy generation number ($N_G(\eta)$) with $K_s = 1, K = 0.5, \lambda = 2, \alpha = 0.2, Nb = 0.5, Nt = 0.2, Nr = 0.5, Pr = 6, Sc = 4.0, \theta_w = 1.01, Re = 1, Ha^2 = 0.5, \chi = 0.2, \Sigma = 0.01$.

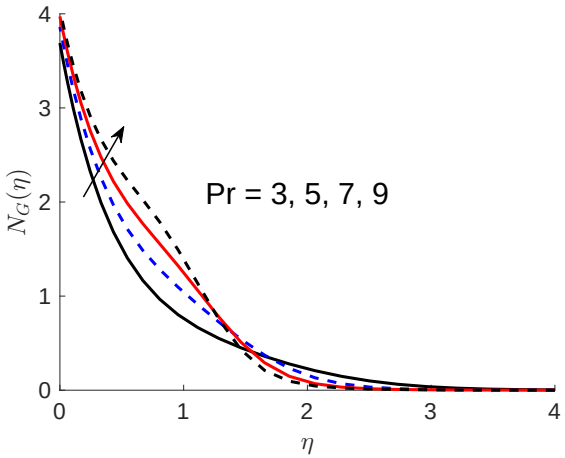

Figure 13: Effects of the Prandtl number (Pr) on the entropy generation number ($N_G(\eta)$) with $K_s = 1, K = 0.5, \lambda = 0.2, \alpha = 0.2, Nb = 0.5, Nt = 0.2, Nr = 0.5, Pr = 6, Sc = 4.0, \theta_w = 1.9, Br = 4, Re = 1, Ha^2 = 0.5, \chi = 0.2, \Sigma = 0.01$.

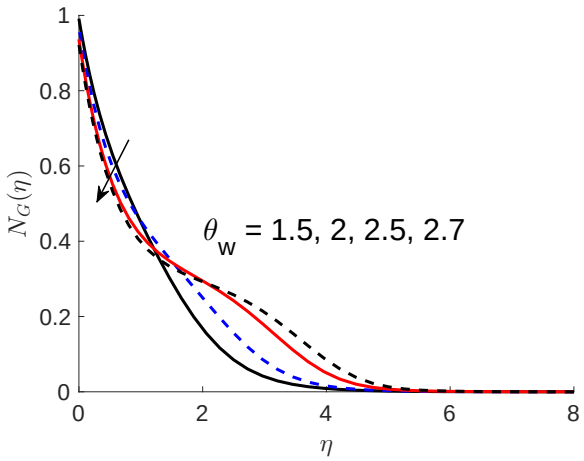

Figure 14: Effects of the temperature ratio parameter (θ_w) on the entropy generation number ($N_G(\eta)$) with $K_s = 1, K = 0.5, \lambda = 2, \alpha = 0.2, Nb = 0.5, Nt = 0.2, Nr = 0.5, Pr = 6, Sc = 2.0, \chi = 0.2, Re = 1, Ha^2 = 0.5, Br = 4, \Sigma = 0.01$.

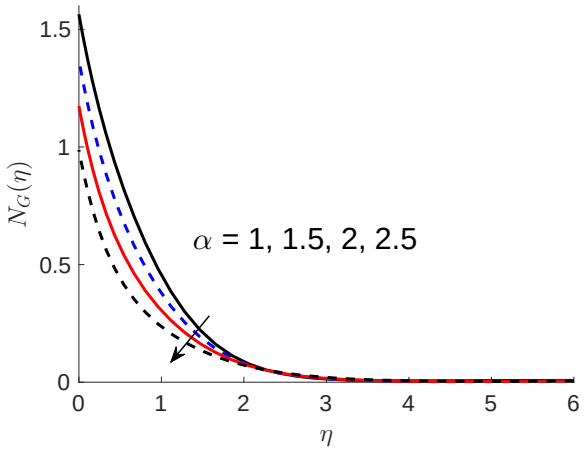

Figure 15: Effects of the viscoelastic parameter (α) on the entropy generation number ($N_G(\eta)$) with $K_s = 1, K = 0.5, \lambda = 2, Nb = 0.5, Nt = 0.2, Nr = 0.5, Pr = 6, Sc = 2.0, \theta_w = 1.01, Re = 1, Ha^2 = 0.5, Br = 8, \chi = 0.2, \Sigma = 0.01$.

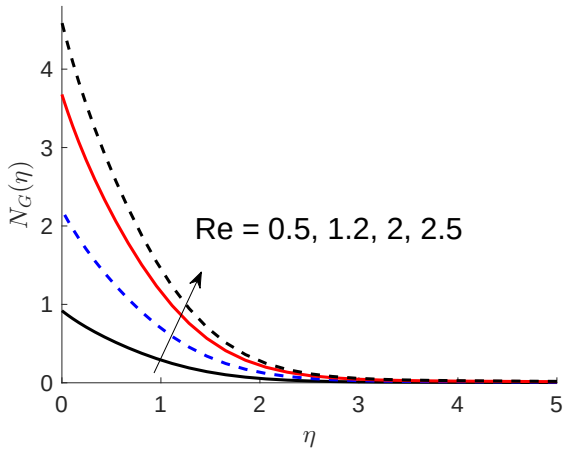

Figure 16: Effects of the Reynolds number (Re) on the entropy generation number ($N_G(\eta)$) with $K_s = 1, K = 0.5, \lambda = 2, Nb = 0.5, Nt = 0.2, Nr = 0.5, Pr = 6, Sc = 2.0, \theta_w = 1.01, \alpha = 0.2, Ha^2 = 0.5, Br = 8, \chi = 0.2, \Sigma = 0.01$.

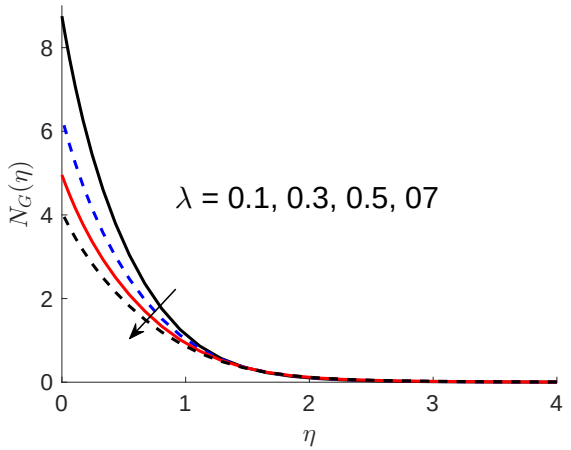

Figure 17: Effects of the partial slip parameter (λ) on the entropy generation number ($N_G(\eta)$) with $K_s = 1, K = 0.5, Re = 1, Nb = 0.5, Nt = 0.2, Nr = 0.5, Pr = 6, Sc = 2.0, \theta_w = 1.01, \alpha = 0.2, Ha^2 = 0.5, Br = 8, \chi = 0.2, \Sigma = 0.01$.

Figure (18) illustrates that the Bejan number is proportionally related to the Hartmann number. As Hartmann number increases, the entropy generation traced to diffusive irreversibility and magnetic field is totally controlled by the entropy generation due to heat transfer at the vicinity of the sheet.

The variation in the Bejan number with the viscoelastic parameter, the partial slip parameter and the dimensionless parameter respectively, are illustrated in Figures (19)–(21). It is noted that the value Bejan number increases in the neighborhood of the sheet, and it decreases gradually when the distance increases from the surface of the sheet, when viscoelastic parameter, partial slip parametre and dimensionless parameter related to the temperature ratio increasing. However, in ranges not far from the sheet, the entropy generation caused by the heat transfer is dominated as viscolastic parameter, partial slip parameter and dimensionless parameter are enhanced.

Figures (22) and (23) show the variations of the Bejan number with different values of the Brinkman number and the dimensionless parameter. It is observed that an increase in the Brinkman number and the dimensionless parameter leads to an increases in the Bejan number. From equation (31), it is noted that an increase in the Brinkman number and dimensionless parameter contribute to the increase in the magnitude of the diffusive irreversibility with the magnetic field irreversibility. However, Brinkman number and dimensionless parameter have no influence on heat transfer irreversibility, consequently, the irreversibility ratio increases and Bejan number decreases.

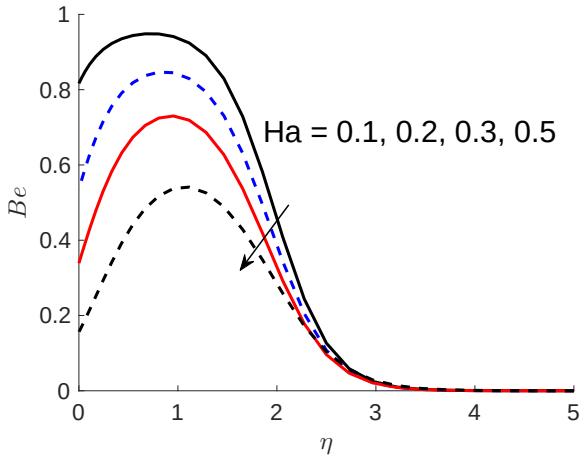

Figure 18: Effects of the Hartmann number (Ha^2) on the Bejan (Be) with $K_s = 1, K = 0.5, \lambda = 0.2, Nb = 0.5, Nt = 0.2, Nr = 0.5, Pr = 6, Sc = 2.0, \theta_w = 1.1, \alpha = 0.2, Re = 1, Br = 8, \chi = 0.2, \Sigma = 0.01$.

The behavior of the skin friction coefficient, the Nusselt number and the Sherwood number with variations in the pertinent parameters is expressed in Figures (24)–(30). Figures (24)–(26) show how the skin friction, the Nusselt number and Sherwood number vary according to different values of the viscoelastic parameter and the partial slip parameter, respectively. In Figures (24) and (26), it is observed that both skin friction and Sherwood number are proportionally related to the viscoelastic parameter. It is also noted that skin friction decreases with an increasing the partial slip parameter, while Sherwood number increases as partial slip parameter increases. Figure (25) shows that an increase in the viscoelastic parameter and the partial slip parameter leads to an decreases in the Nusselt number.

Figures (27) and (28) demonstrate the change in the Nusselt number and Sherwood number due to the effect of the homogeneous reaction parameter and the heterogeneous reaction parameter, respectively. It is observed that the Nusselt number and the Sherwood number are an decreasing function on the heterogeneous reaction parameter. It also noted that the Nusselt number and the Sherwood number increase with an increasing the homogeneous reaction parameter. The behavior of the Nusselt number and the Sherwood number with different values of the temperature ratio parameter and the Thermophoresis parameter are displayed in Figures (29) and (30) respectively. In Figure (29), it is noticed that the Nusselt number is an decreasing function on the temperature ratio parameter, moreover, it is decrease slightly as the Thermophoresis parameter increases. Figure (30) shows the effect of the temperature ratio parameter and the Thermophoresis parameter on the Sherwood number. These results show that the Sherwood number

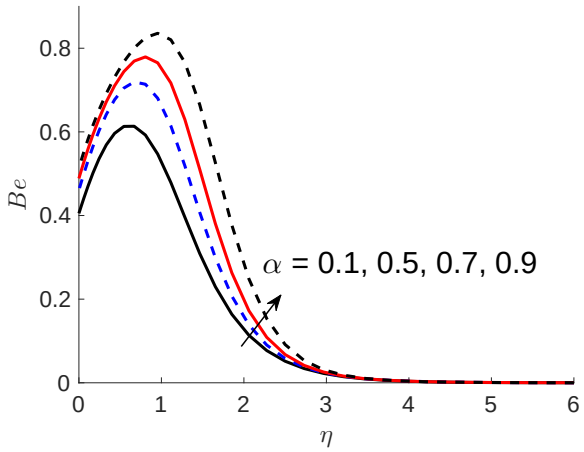

Figure 19: Effects of the viscoelastic parameter (α) on the Bejan (Be) with $K_s = 1, K = 0.5, \lambda = 2, Nb = 0.5, Nt = 0.2, Nr = 0.5, Pr = 6, Sc = 2.0, \theta_w = 1.01, Ha^2 = 0.5, Re = 1, Br = 8, \chi = 0.1, \Sigma = 0.1$.

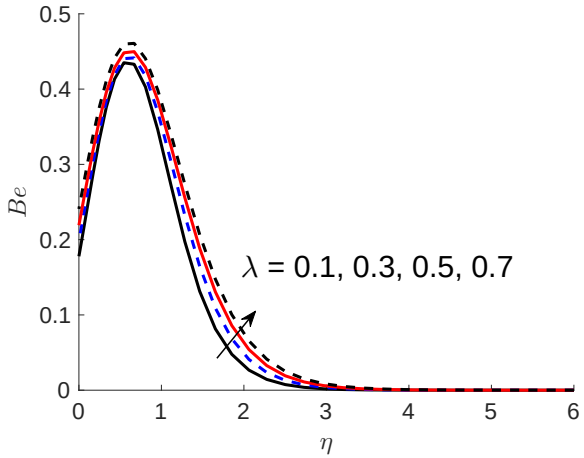

Figure 20: Effects of the partial slip parameter (λ) on the Bejan (Be) with $K_s = 1, K = 0.5, \alpha = 0.2, Nb = 0.5, Nt = 0.2, Nr = 0.5, Pr = 6, Sc = 2.0, \theta_w = 1.01, Ha^2 = 0.5, Re = 1, Br = 8, \chi = 0.1, \Sigma = 0.1$.

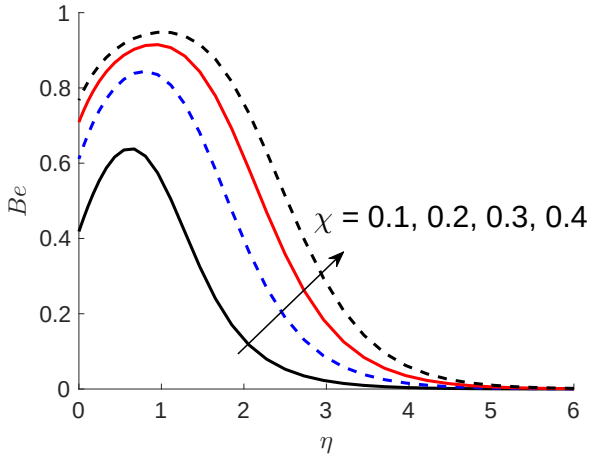

Figure 21: Effects of the dimensionless parameter (ξ) on the Bejan (Be) with $K_s = 1, K = 0.5, \alpha = 0.2, \lambda = 2, Nb = 0.5, Nt = 0.2, Nr = 0.5, Pr = 6, Sc = 2.0, \theta_w = 1.01, Ha^2 = 0.5, Re = 1, Br = 1, \Sigma = 0.1$.

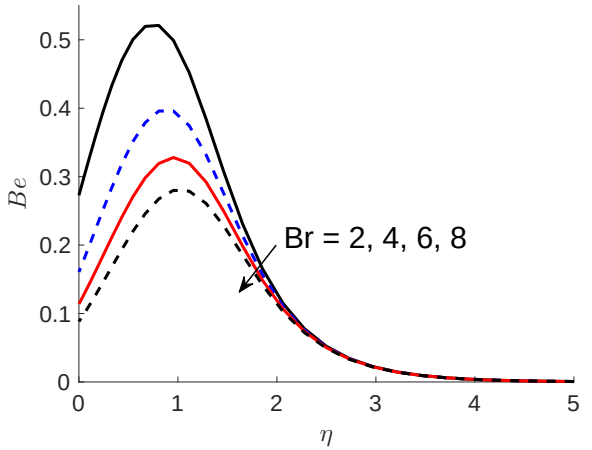

Figure 22: Effects of the Brinkman number (Br) on the Bejan (Be) with $K_s = 1, K = 0.5, \alpha = 0.2, \lambda = 2, Nb = 0.5, Nt = 0.2, Nr = 0.5, Pr = 6, Sc = 2.0, \theta_w = 1.01, Ha^2 = 0.5, Re = 1, \chi = 0.1, \Sigma = 0.1$.

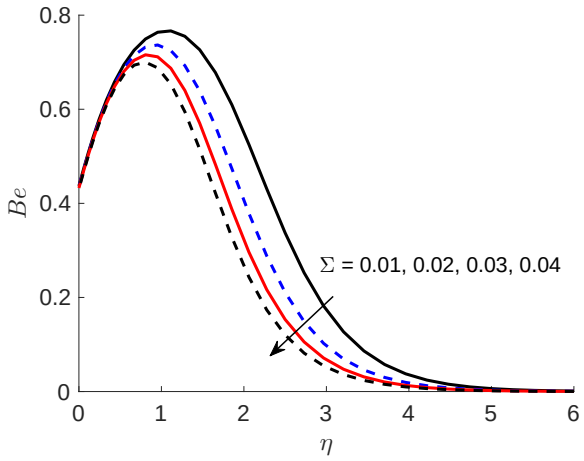

Figure 23: Effects of the dimensionless parameter (Σ) on the Bejan (Be) with $K_s = 1, K = 0.5, \alpha = 0.2, \lambda = 2, Nb = 0.5, Nt = 0.2, Nr = 0.5, Pr = 6, Sc = 2.0, \theta_w = 1.01, Ha^2 = 0.5, Re = 1, \chi = 0.1, Br = 8$.

decreases with an increasing temperature ration parameter, whereas it is increase as the Thermophoresis parameter increases.

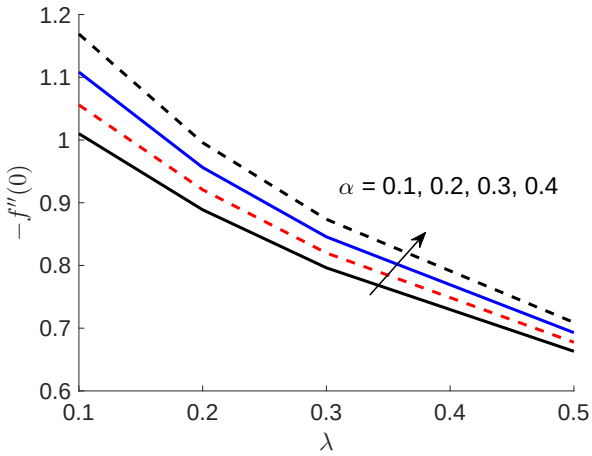

Figure 24: Effect of the viscoelastic parameter (α) and the partial slip parameter (λ) on the skin friction $f''(0)$ with $K_s = 1, K = 0.5, Nb = 0.5, Nt = 0.2, Nr = 0.5, Pr = 6, Sc = 2.0, \theta_w = 1.01, Ha^2 = 0.5$.

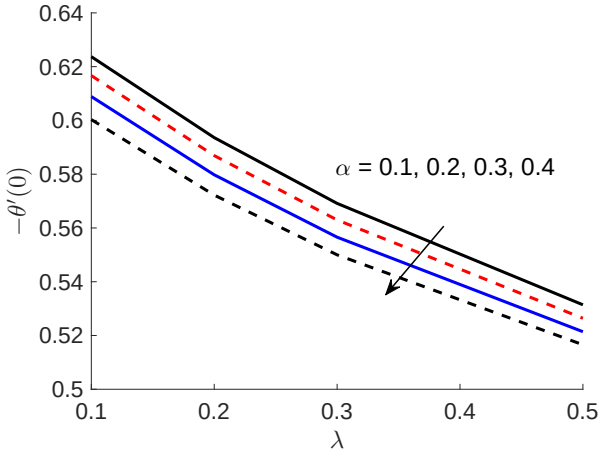

Figure 25: Effect of the viscoelastic parameter (α) and the partial slip parameter (λ) on the Nusselt number $-\theta'(0)$ with $K_s = 1, K = 0.5, Nb = 0.5, Nt = 0.2, Nr = 0.5, Pr = 6, Sc = 2.0, \theta_w = 1.01, Ha^2 = 0.5$.

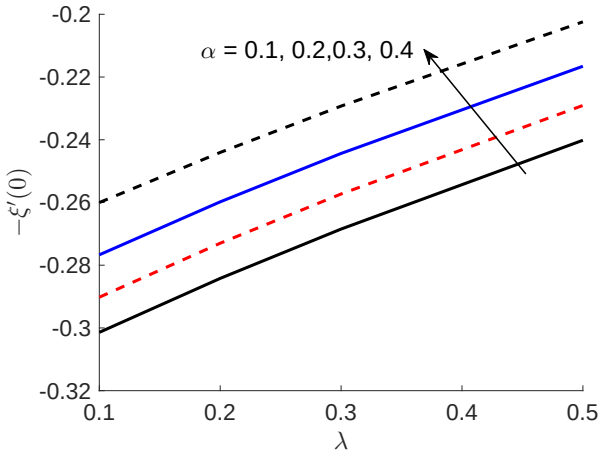

Figure 26: Effect of the viscoelastic parameter (α) and the partial slip parameter (λ) on the Sherwood number $-\xi'(0)$ with $K_s = 1, K = 0.5, Nb = 0.5, Nt = 0.2, Nr = 0.5, Pr = 6, Sc = 2.0, \theta_w = 1.01, Ha^2 = 0.5$.

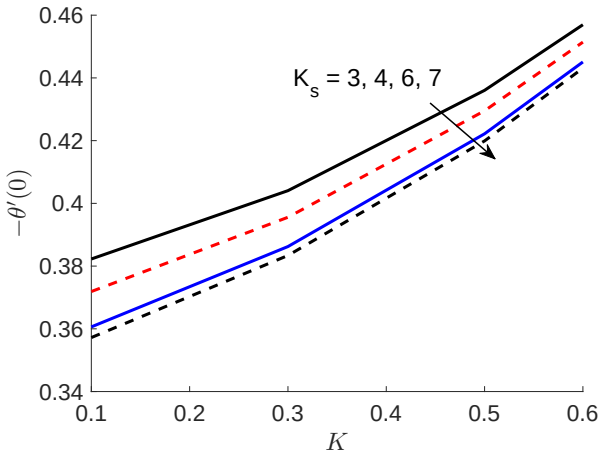

Figure 27: Effect of the homogeneous reaction parameter (K) and the heterogeneous reaction parameter (K_s) on the Nusselt number $-\theta'(0)$ with $\alpha = 0.2, \lambda = 1, Nb = 0.5, Nt = 0.2, Nr = 0.5, Pr = 6, Sc = 2.0, \theta_w = 1.01, Ha^2 = 0.5$.

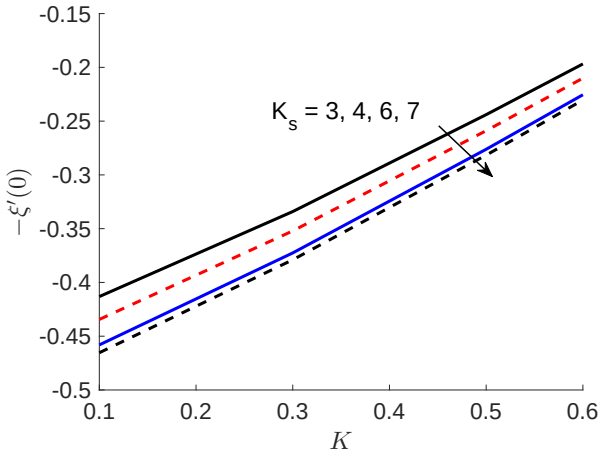

Figure 28: Effect of the heterogeneous reaction parameter (K_s) and the homogeneous reaction parameter (K) on the Sherwood number $-\xi'(0)$ with $\alpha = 0.2, \lambda = 1, Nb = 0.5, Nt = 0.2, Nr = 0.5, Pr = 6, Sc = 2.0, \theta_w = 1.01, Ha^2 = 0.5$.

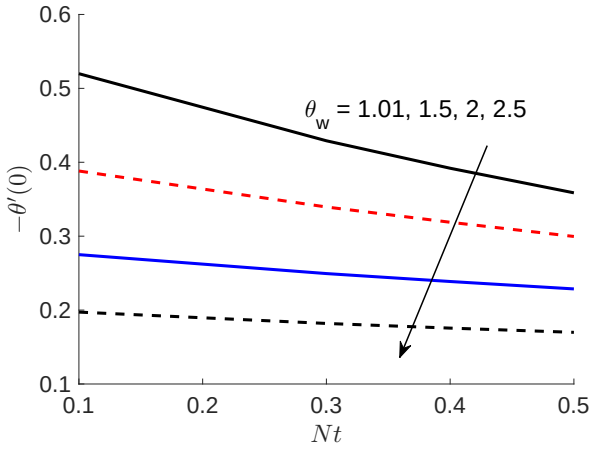

Figure 29: Effect of the temperature ratio parameter (θ_w) and the Thermophoresis parameter (Nt) on the Nusselt number $-\theta'(0)$ with $\alpha = 0.2, \lambda = 1, Nb = 0.5, Nr = 0.5, Pr = 6, Sc = 2.0, K_s = 1, K = 0.5, Ha^2 = 0.5$.

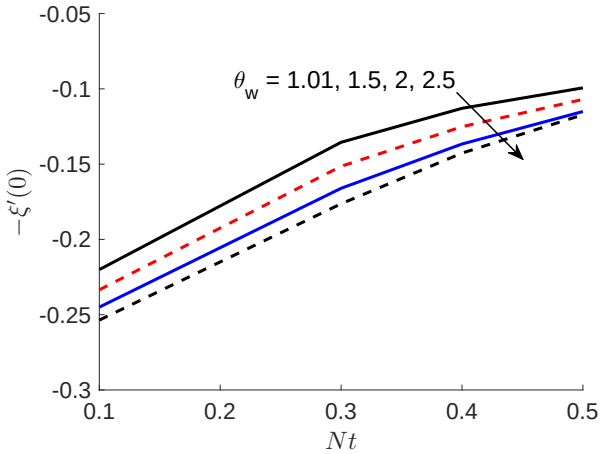

Figure 30: Effect of the temperature ratio parameter (θ_w) and the Thermophoresis parameter (Nt) on the Sherwood number $-\xi'(0)$ with $\alpha = 0.2, \lambda = 1, Nb = 0.5, Nr = 0.5, Pr = 6, Sc = 2.0, K_s = 1, K = 0.5, Ha^2 = 0.5$.

CONCLUSIONS

A numerical model was developed to study the entropy generation in MHD flow of viscoelastic nanofluids with homogeneous-heterogeneous reaction, partial slip and nonlinear thermal radiation. The resulting partial differential equations have been solved using the spectral quasi-linearization method. The graphical results were obtained to illustrate the details of flow, heat and mass transfer characteristics and their dependence on some physical parameter. The following conclusions can be derived from the numerical results:

(i) Enhancement occur in thermal boundary layer, whereas the concentration and momentum boundary layer reduces when the viscoelastic parameter increases.
(ii) The velocity and concentration profiles are strongly influenced by the magnetic field in the momentum boundary layer, which decreases with the increase in the Hartmann number and reverse trends are seen for temperature profile.
(iii) The velocity and concentration profiles are reduced due to increase the partial slip parameter but reverse effects are seen for temperature profiles.
(iv) The impact of the Brownian motion parameter and thermophoresis parameter on temperature are similar, while the effects on nanoparticles volume fraction are opposite for increasing the Brownian motion parameter.
(v) The effect of nonlinear thermal radiation is to increase temperature in the thermal boundary layer.
(vi) The concentration at the surface decreased with the strengths of the homogeneous and heterogeneous reactions.
(vii) The Prandtl number and temperature ratio parameter show a quite opposite behavior for temperature and concentration profile.
$(viii)$ The entropy generation number decreases with the increase of viscoelastic parameter and partial slip parameter, while the entropy generation number increases with the increase of Brinkman number and Reynolds number.
(ix) The Bejan number is strongly affected by variations in the viscoelastic parameter and dimensionless Brinkman groups.
(x) The local Nusselt number and Sherwood number decrease with the increase in homogeneous and heterogeneous chemical reaction parameter.

ACKNOWLEDGEMENT

The authors are grateful to the Claude Leon Foundation, DST-NRF Centre of Excellence-Mathematical and Statistical Sciences and the University of KwaZulu-Natal for financial support.

NOMENCLATURE

A	homogeneous chemical reaction
B	heterogeneous chemical reaction
Br	Brinkman number
B_0	magnetic field strength $(kg\ s^{-2}A^{-1})$
C	concentration (kgm^{-3})
C_a	concentration of homogeneous chemical reaction A (kgm^{-3})
C_b	concentration of heterogeneous chemical reaction B (kgm^{-3})
C_w	concentration at surface (kgm^{-3})
C_∞	ambient concentration (kgm^{-3})
c, k_1^*	are constants
c_p	specific heat $(m^2s^{-2}K^{-1})$
D_A	diffusion coefficient of specie A $(kgm^{-1}s^{-1})$
D_B	diffusion coefficient of specie B $(kgm^{-1}s^{-1})$
D_T	Thermophoretic diffusion coefficient $(kgm^{-1}s^{-1}K^{-1})$
E_{gen}	volumetric entropy generation per unit length $(Wm^{-4}K^{-1})$
E_0	dimensionless entropy generation rate
f	dimensionless velocity
Ha	Hartmann number
h_m	mass flux $(kgm^{-2}s^{-1})$
h_w	heat flux (Wm^{-2})
K	the stretch of the homogeneous reaction
K_s	the stretch of the heterogeneous reaction
k_f	thermal conductivity $(Wm^{-1}K^{-1})$
k_s, k_1	constants rate
k_0	material fluid parameter
k^*	mean absorption coefficient

Nb Brownian mention parameter
Nr thermal radiation parameter
Nt Thermophoresis parameter
p pressure $(kgm^{-1}s^{-2})$
Pr Prandtl number
q_r radiative heat flux (kgm^{-2})
Re Reynolds number
Sc Schmidt number
T temperature (K)
T_w uniform surface temperature (K)
T_∞ ambient temperature (K)
ΔT difference between $(T_W - T_\infty)(K)$
$U(x)$ velocity of the stretching sheet (ms^{-1})
u, v velocity components (ms^{-1})
x, y rectangular coordinate axis (m)

GREEK SYMBOLS

α viscoelastic parameter
α_m thermal diffusion of fluid (m^2s^{-1})
ε the ration diffusion coefficient
η dimensionless variable
θ dimensionless temperature
θ_w similarity variable related to the energy equation
λ dimensionless velocity slip parameter
μ dynamic viscosity $(kgm^{-1}s^{-1})$
ν kinematic viscosity (m^2s^{-1})
ξ dimensionless concentration of specie A
ρ density of fluid (kgm^{-3})
$(\rho c_p)_f$ heat capacity of base fluid
$(\rho c_p)_s$ heat capacity of the nanoparticle
Σ dimensionless parameter
σ electrical conductivity $(\Omega^{-1}m^{-1})$
σ^* Steaffan-Boltzman constant
τ ratio of nanoparticle heat capacity
τ_w shear stress at the surface
ϕ dimensionless concentration of specie B
χ constant parameter

References

[1] Choi, S. U., Eastman, J. A. Enhancing thermal conductivity of fluids with nanoparticles. Technical report, Argonne National Lab., IL (United States) (1995)

[2] Valyi, E. I. Extrusion of plastics. US Patent 5,082,604 (1992)

[3] Makinde, O. D., Aziz, A. Boundary layer flow of a nanofluid past a stretching sheet with a convective boundary condition. International Journal of Thermal Sciences 50, 7, 1326–1332 (2011)

[4] Chamkha, A. J. Mhd flow of a uniformly stretched vertical permeable surface in the presence of heat generation/absorption and a chemical reaction. International Communications in Heat and Mass Transfer 30, 3, 413–422 (2003)

[5] Putley, E. The development of thermal imaging systems. Recent Advances in Medical Thermology, 151–166. Springer (1984)

[6] Sandeep, N., Sulochana, C., Kumar, B. R. Mhd boundary layer flow and heat transfer past a stretching/shrinking sheet in a nanofluid. Journal of Nanofluids 4, 4, 512–517 (2015)

[7] Sandeep, N., Raju, C., Sulochana, C., Sugunamma, V. Effects of aligned magneticfield and radiation on the flow of ferrofluids over a flat plate with non-uniform heat source/sink. International Journal of Science and Engineering 8, 2, 151–158 (2015)

[8] Sheikholeslami, M., Ganji, D. D., Javed, M. Y., Ellahi, R. Effect of thermal radiation on magnetohydrodynamics nanofluid flow and heat transfer by means of two phase model. Journal of Magnetism and Magnetic Materials 374, 36–43 (2015)

[9] Hayat, T., Muhammad, T., Alsaedi, A., Alhuthali, M. Magnetohydrodynamic three-dimensional flow of viscoelastic nanofluid in the presence of nonlinear thermal radiation. Journal of Magnetism and Magnetic Materials 385, 222–229 (2015)

[10] Animasaun, I., Raju, C., Sandeep, N. Unequal diffusivities case of homogeneous–heterogeneous reactions within viscoelastic fluid flow in the presence of induced magnetic-field and nonlinear thermal radiation. Alexandria Engineering Journal 55, 2, 1595–1606 (2016)

[11] Chaudhary, M., Merkin, J. Homogeneous-heterogeneous reactions in boundary-layer flow: Effects of loss of reactant. Mathematical and computer modelling 24, 3, 21–28 (1996)

[12] Merkin, J. A model for isothermal homogeneous-heterogeneous reactions in boundary-layer flow. Mathematical and Computer Modelling 24, 8, 125–136 (1996)

[13] Shaw, S., Kameswaran, P. K., Sibanda, P. Homogeneous-heterogeneous reactions in micropolar fluid flow from a permeable stretching or shrinking sheet in a porous medium. Boundary Value Problems 2013, 1, 77 (2013)

[14] Goyal, M., Bhargava, R. Boundary layer flow and heat transfer of viscoelastic nanofluids past a stretching sheet with partial slip conditions. Applied Nanoscience 4, 6, 761–767 (2014)

[15] Sheikh, M., Abbas, Z. Homogeneous–heterogeneous reactions in stagnation point flow of casson fluid due to a stretching/shrinking sheet with uniform suction and slip effects. Ain Shams Engineering Journal (2015)

[16] Bachok, N., Ishak, A., Pop, I. On the stagnation-point flow towards a stretching sheet with homogeneous–heterogeneous reactions effects. Communications in Nonlinear Science and Numerical Simulation 16, 11, 4296–4302 (2011)

[17] Hayat, T., Imtiaz, M., Alsaedi, A. Effects of homogeneous-heterogeneous reactions in flow of powell-eyring fluid. Journal of Central South University 22, 8, 3211–3216 (2015)

[18] Mirzazadeh, M., Shafaei, A., Rashidi, F. Entropy analysis for non-linear viscoelastic fluid in concentric rotating cylinders. International Journal of Thermal Sciences 47, 12, 1701–1711 (2008)

[19] Aïboud, S., Saouli, S. Entropy analysis for viscoelastic magnetohydrodynamic flow over a stretching surface. International Journal of Non-Linear Mechanics 45, 5, 482–489 (2010)

[20] Butt, A. S., Munawar, S., Ali, A., Mehmood, A. Effect of viscoelasticity on entropy generation in a porous medium over a stretching plate. World Applied Sciences Journal 17, 4, 516–523 (2012)

[21] Chaudhary, M., Merkin, J. A simple isothermal model for homogeneous-heterogeneous reactions in boundary-layer flow. i equal diffusivities. Fluid dynamics research 16, 6, 311–333 (1995)

[22] Awad, M. M. A review of entropy generation in microchannels. Advances in Mechanical Engineering 7, 12, 1687814015590297 (2015)

[23] Bejan, A. Advanced engineering thermodynamics. John Wiley & Sons (2016)

[24] Awad, M. M. A new definition of bejan number. Thermal Science 16, 4, 1251–1253 (2012)

[25] Awad, M. M., Lage, J. L. Extending the bejan number to a general form. Thermal Science 17, 2, 631–633 (2013)

[26] Awad, M. M. Hagen number versus bejan number. Thermal Science 17, 4, 1245–1250 (2013)

[27] Awad, M. M. An alternative form of the darcy equation. Thermal Science 18, suppl. 2, 617–619 (2014)

[28] Awad, M. M. The science and the history of the two bejan numbers. International Journal of Heat and Mass Transfer 94, 101–103 (2016)

[29] Bellman, R. E., Kalaba, R. E. Quasilinearization and nonlinear boundary-value problems (1965)

[30] Agbaje, T., Mondal, S., Makukula, Z., Motsa, S., Sibanda, P. A new numerical approach to mhd stagnation point flow and heat transfer towards a stretching sheet. Ain Shams Engineering Journal (2016)

[31] Canuto, C., Hussaini, M. Y., Quarteroni, A., Thomas Jr, A., et al. Spectral methods in fluid dynamics. Springer Science & Business Media (2012)

[32] Motsa, S., Sibanda, P., Shateyi, S. On a new quasi-linearization method for systems of nonlinear boundary value problems. Mathematical Methods in the Applied Sciences 34, 11, 1406–1413 (2011)

[33] Almakki, M., Dey, S., Mondal, S., Sibanda, P. On unsteady three-dimensional axisymmetric mhd nanofluid flow with entropy generation and thermo-diffusion effects (2017)

[34] Chand, R., Rana, G., Hussein, A. On the onsetof thermal instability in a low prandtl number nanofluid layer in a porous medium. Journal of Applied Fluid Mechanics 8, 2, 265–272 (2015)

[35] Al-Rashed, A. A., Kolsi, L., Hussein, A. K., Hassen, W., Aichouni, M., Borjini, M. N. Numerical study of three-dimensional natural convection and entropy generation in a cubical cavity with partially active vertical walls. Case studies in thermal engineering 10, 100–110 (2017)

[36] Kolsi, L., Hussein, A. K., Borjini, M. N., Mohammed, H., Aïssia, H. B. Computational analysis of three-dimensional unsteady natural convection and entropy generation in a cubical enclosure filled with water-al 2 o 3 nanofluid. Arabian Journal for Science and Engineering 39, 11, 7483–7493 (2014)

[37] Chand, R., Rana, G., Hussein, A. Effect of suspended particles on the onset of thermal convection in a nanofluid layer for more realistic boundary conditions. International Journal of Fluid Mechanics Research 42, 5 (2015)

[38] Mallikarjuna, B., Rashad, A., Hussein, A., Hariprasad Raju, S. Transpiration and thermophoresis effects on non-darcy convective flow past a rotating cone with thermal radiation. Arabian Journal for Science & Engineering (Springer Science & Business Media BV) 41, 11 (2016)

Chapter 5

Entropy generation in Casson nanofluid flow with a binary chemical reaction and nonlinear thermal radiation

In Chapter 4, it was assumed that the velocity of the stretching surface is linear. In this chapter we consider nonlinear velocity to bring the model a step closer to reality. In addition, we also investigate a binary chemical reaction which is not considered in all previous chapters.

In this chapter we propose a model that captures the behaviour of a steady incompressible MHD Casson nanofluid flow over a stretching or shrinking sheet. It is assumed that the surface stretches in the vertical direction with exponential velocity. Subsequently, the model is used to analyse the entropy generation, heat and mass transfer in the laminar flow near the stagnation point. Viscous dissipation, nonlinear thermal radiation and a binary chemical reaction are assumed. The spectral quasiliearization method is used to solve the flow equations.

Entropy generation in Casson nanofluid flow with binary chemical reaction and nonlinear thermal radiation

Mohammed Almakki[1], Peri K. Kameswaran [2], Hiranmoy Mondal [1], Precious Sibanda [1]
[1]School of Mathematical Sciences, University of KwaZulu-Natal, Private Bag X01, Scottsville 3209, Pietermaritzburg, South Africa
[2] Department of Mathematics, School of Advanced Sciences, VIT University, Vellore 632014, India

November 29, 2018

1 Abstract

We present a model to describe the flow of an MHD Casson nanofluid over a stretching/shrinking surface. The model used to investigate entropy generation and heat transfer in the laminar boundary-layer stagnation point. The flow is subject to an external magnetic field, nonlinear thermal radiation, viscous disipation and binary chemical reaction. The sysyem is solved numerically using the spectral local lineralization method. The method is found to be accurate and convergent. The results show that entropy generation increases with an increase in the Reynolds number and Casson parameter.

Keywords: binary chemical reaction; Casson Nanofluids; Entropy generation; non-linear thermal radiation; spectral quasi-linearization method.

2 Introduction

A Casson nanofluid is a fluid that is generated by a suspending solid particles with dimensions less than 100 nm in a fluid. It has a liquid phase and and a solid phase. It also has enhanced thermophysical properties such as high thermal diffusivity, viscosity, and thermal conductivity compared to base liquids such as water, oil and ethylene glycol mixture, etc. These fluids have diverse uses in industry, for instance, in fuel cell, biomedicine, nuclear reactors and transportation. The flow of a viscous incompressible fluid driven by a moving surface is encountered in a number of industrial processes such as in metal and plastic extrusion, glass blowing and polymer extrusion. The study of fluid flow with a binary chemical reaction is encountered in a number of large scale manufacturing processes. The flow of fluid with a chemically reacting species over a stretching sheet play an important role in metallurgy and chemical engineering industries, such as food processing and polymer production [1]. All these applications involve some aspects of flow over a stretching sheet, free convection, heat transfer and so on. Running flow reactions

have a number of advantages over batch processes. The advantages include achieving mixing in smaller time scales, heat transfer is intensified, because the area to volume ration is large. Oxley et al [2] studied flow on a spinning disk used in the manufacturing of pharmaceuticals. They showed that the spinning disk reactor (SDR) displayed distinct advantages over batch processing in the commercial manufacture of pharmaceuticals. It was further postulated that the SDR is capable of generating a far higher mixing intensity than a stirred vessel and is also capable of maintaining a uniform concentration profiles within a rapidly reacting fluid.

The quality of most industrial products depends on the rate of heat and mass transfer during cooling. Heat is generated or absorbed during a chemical reaction [3]. Some of the strategies that have been used for controlling the heat transfer rate include the use of a transverse magnetic field [4] and the use of nanofluids. Nanofluids consist of nanopartices, normally aluminum, gold, iron oxide, platinum, silica, silver etc of sizes ranging from 1 to 100 nanometers suspended in a base fluid to increase/improve the thermal performance of base liquids. Nanofluids have a wide range of applications such as in cooling systems, solar water heating and improving diesel generator efficiency [5].

Another important factor in fluid flow with a chemical reaction is the activation energy. This is the minimum energy which must be available for potential reactants to produce a chemical reaction [6]. We include the activation energy in this model, which most researchers have not incorporated in previous studies. Pal and Mondal [7] investigated the effects of a chemical reaction on boundary layer flow past a vertical stretching surface with internal heat generation. They found that for positive buoyancy, the local skin friction and mass transfer coefficients increase with Eckert and Schmidt numbers while the heat transfer coefficient decreases with both the Eckert and Schmidt numbers. However, the study did not consider the activation energy, nanoparticle effects and order of the chemical reaction. These are new aspects that are incorporated in the current model. Olanrewaju et al [8] studied the effects of internal heat generation on a thermal boundary layer with a convective surface boundary condition. They observed that for weak plate heating, the surface temperature increased rapidly as the local internal heat generation increased. Their model however did not include mass transfer. Reddy et al [9, 10] studied free convection, heat and mass transfer flow in a chemically reactive and radiation absorption fluid in an aligned magnetic filed. The concentration was shown to decrease with increasing chemical reaction rates which also reduced the solutal boundary layer thickness. It was further noted that increasing the radiation parameter caused a decrease in the fluid velocity. The velocity attained a peak in the absence of the radiation parameter. Palani et al [11] studied the MHD flow of an upper-convected Maxwell fluid with a higher order chemical reaction. The main conclusion from this study was that the thickness of the species distribution increased with increasing order of a chemical reaction. However the study did not incorporate energy transport including the aspect of activation energy.

In this work, we are interested in investigating entropy generation in MHD Casson nanofluid flow in porous media with binary chemical reaction. In thermodynamical systems, factors such as heat transfer, mass transfer, viscous dissipation and magnetic field may give rise to entropy generation. In many engineering applications, e.g. heat exchangs, electronic cooling, fuel cells and turbomachinery the comprehensive analysis of the flow and thermodynamics is imperative. The study of entropy generation is relevant also in physiological processes. In phoysiological studies, blood pressure is measured periodically when the subjects are conducting physical/mental tasks. Depending on the temperature of the surrouding environment and the temperature of the subjects, heat transfer occurs between the subjects and the environment through sweating, radiation and conduction. Monitoring entropy generation is crucia characterizing such systems

[12]. Entropy generation defines the level of irreversibility and accounts for thermodynamic imperfections of engineering systems. It is an important factor in energy loss [13, 14]. As a consequence, by controlling entropy generation, the performance of engineering systems can be enhanced. Entropy generation is found through employing the first and second law of thermodynamics in order to optimize the thermodynamics [15]. This optimization is known as finite time thermodynamics. In this study, the impact of several factors on entropy generation are investigated in order to understand and control the entropy generation in porous media as the entropy analysis is particularly important for system efficiency [15] when porous media are considered. Some relevant studies on entropy generation include those of [16] whose were focus on entropy generation for Casson nanofluid flow induced by a stretching surface and Qing et al. [17] investigated entropy generation in Casson nanofluid subject to nonlinear thermal radiation and chemical reaction.

The novelty of this study is in the presentation of a single generalized model to describe the flow of Casson nanofluid with a binary chemical reaction. We assume thermal radiation, viscous dissipation, Brownian motion, temperature ratio and thermophoresis are significant factors that may alter the flow structure and the heat transfer properties of the fluid. A second important aspect of the study lies in the effect of entropy generation in Casson nanofluid. Here we use a recent spectral quasiliearization method to solve the conservation equations, see [18]. The technique has been used successfully in a few studies in the literature.

3 Problem formulation

Consider the steady incompressible MHD Casson nanofluid stagnation point boundary layer flow with vertical stretching/shrinking surface with u and v denoting $x-$ and $y-$ components of velocity respectively. The coordinate x extends along the surface and y is the coordinate axis normal to it (see Fig. 1). The magnetic force having uniform intensity B_0 acts normal to the plane of the sheet. We assume that the surface stretches in the vertical direction with exponential velocity $u_e = u_\infty e^{x/L}$.

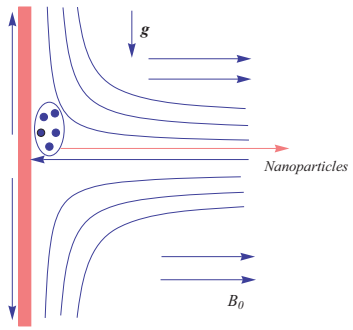

(a)

Figure 1: Geometry of the problem

The equations of the MHD Casson nanofluid model can be written as

$$\frac{\partial u}{\partial x}+\frac{\partial v}{\partial y}=0, \tag{3.1}$$

$$u\frac{\partial u}{\partial x}+v\frac{\partial u}{\partial y}=\nu\Big(1+\frac{1}{\beta}\Big)\frac{\partial^2 u}{\partial y^2}+\frac{\sigma B_0^2}{\rho}+u_e\frac{\partial u_e}{\partial x}+\frac{\epsilon\mu_{eff}}{\rho k_1}(u_e-u) + g\Big(B_t(T-T_\infty)+B_c(C-C_\infty)\Big), \tag{3.2}$$

$$u\frac{\partial T}{\partial x}+v\frac{\partial T}{\partial y}=\alpha\frac{\partial^2 T}{\partial y^2}+\frac{16\sigma^*}{3k^*(\rho c_p)_f}\frac{\partial}{\partial y}\left(T^3\frac{\partial T}{\partial y}\right)+\frac{\nu}{c_p}\Big(1+\frac{1}{\beta}\Big)\Big(\frac{\partial u}{\partial y}\Big)^2 + \tau\left(D_B\frac{\partial T}{\partial y}\frac{\partial C}{\partial y}+\frac{D_T}{T_\infty}\Big(\frac{\partial T}{\partial y}\Big)^2\right), \tag{3.3}$$

$$u\frac{\partial C}{\partial x}+v\frac{\partial C}{\partial y}=D_B\frac{\partial^2 C}{\partial y^2}+\frac{D_T}{T_\infty}\frac{\partial^2 T}{\partial y^2}-k_T^2\Big(\frac{T}{T_\infty}\Big)^m e^{(-Ea/k_T)}(C-C_\infty), \tag{3.4}$$

where ν is the kinematic viscosity which represents the ratio of the dynamic viscosity μ to the density of the fluid ρ, β is the Casson parameter, σ and B_0^2 are the electrical conductivity and the strength of the magnetic field respectively, $u_e(x)$ is the external velocity, k_1 is permeability of the porous medium, g is the acceleration, β_t and β_c are the thermal expansion and the expansion with concentration respectively, T is the temperature, C is the concentration, $\alpha=(k_f/\rho c_p)$ is the thermal diffusion which represents the ratio between the effective thermal conductivity and the effective specific heat, σ^* and k^* are the steaffan-Boltzman constant and mean absorption coefficient respectively, $(\rho c_p)_f$ is the specific heat of the base fluid, D_B is the Brownian motion, D_T is the thermophoretic diffusion. Moreover, k_T^2 is the chemical reaction, $(T/T_\infty)^m \mathrm{e}^{(-Ea/kT)}$ is the modified Arrhenius function, in which k is the Boltzmann and m is the constant where $-1<m<1$

The auxiliary conditions for this study are

$$\begin{aligned} &v=v_w=v_{w_0}\mathrm{e}^{x/2L},\ T=T_w(x),\ C=C_w(x),\ \mu\frac{\partial u}{\partial y}=\sigma_T\frac{\partial T}{\partial x}+\sigma_C\frac{\partial C}{\partial x}\ \text{ at }\ y=0\\ &u=u_e(x)=u_\infty\mathrm{e}^{x/L},\ T=T_\infty(x),\ C=C_\infty(x)\ \text{ at }\ y\to\infty, \end{aligned} \tag{3.5}$$

where v_w and u_e are the velocities at the wall and at the outer edge of the boundary layer respectively, and L is the stretching velocity. Moreover, the emperature distribution and concentration distribution are defined as respectively

$$\begin{aligned} &u_e=u_0\mathrm{e}^{x/L},\ \ T_w(x)=T_\infty+(T_0-T_\infty)\mathrm{e}^{x/2L},\\ &C_w(x)=C_\infty+(C_0-C_\infty)\mathrm{e}^{x/2L}, \end{aligned} \tag{3.6}$$

where u_0 is velocity parameter of the sheet, T_0 and C_0 are the temperature and concentration distributions in the stretching sheet respectively.

Equations (3.1)–(3.4) are converted into the couple of ordinary differential equations by using the following non-dimensional variable (see [19])

$$\begin{aligned} &\psi=\sqrt{2}\nu Re^{1/2}\mathrm{e}^{x/2L}f(\eta),\ \ \eta=\sqrt{\frac{Re}{2}}\frac{y}{L}\mathrm{e}^{x/2L},\\ &T=T_\infty+(T_0-T_\infty)\mathrm{e}^{x/2L}\theta(\eta),\ C=C_\infty+(C_0-C_\infty)\mathrm{e}^{x/2L}\phi(\eta). \end{aligned} \tag{3.7}$$

The system of Equations (3.1)–(3.4) become as

$$\Big(1+\frac{1}{\beta}\Big)f'''+ff''-2f'^{2}+2Rie^{(-3\xi/2)}(\theta+N\phi)+2e^{-\xi}(M^2+\kappa_p)(1-f')+2=0, \tag{3.8}$$

$$\frac{1}{Pr}\theta''+\theta' f-f'\theta+e^{(\xi/2)}\Big(Nb\theta'\phi'+Nt\theta'^{2}\Big)+Ec\Big(1+\frac{1}{\beta}\Big)e^{(3\xi/2)}f''^{2} + Rd\Big\{\Big(1+(\theta_f-1)e^{(\xi/2)}\theta\Big)^{3}\theta''+3(\theta_f-1)e^{(\xi/2)}\theta'^{2}\Big\}=0, \tag{3.9}$$

$$\frac{1}{Le}\phi''+f\phi'-f'\phi+\frac{1}{Le}\frac{Nt}{Nb}\theta''-\sigma e^{(-\xi)}\Big(1+(\theta_f-1)e^{(\xi/2)}\theta\Big)^{m}e^{\Big(\frac{-E}{1+(\theta_f-1)e^{(\xi/2)}\theta}\Big)}\phi=0, \tag{3.10}$$

with boundary conditions

$$\begin{aligned} &f(0)=s,\ f''(0)=1-\epsilon,\ \theta(0)=1,\ \phi(0)=1,\\ &f'(\infty)=1,\ \theta(\infty)=0,\ \phi(\infty)=0, \end{aligned} \tag{3.11}$$

where the prime denotes differentiation is with respect to η, $Gr=gB_t\Delta TL^3/\nu^2$ is the Grashof number, $Ri=Gr/Re^2$ is the Richardson number where $Re=u_0L/\nu$ is the Reynolds number, $\xi=x/L$ is the non-dimensional number along x-axis, $N=B_c\Delta C/B_t\Delta T$ is the buoyancy parameter, $M^2=\sigma B_0^2L^2/\rho\nu Re$ is the magnetic parameter, $\kappa_p=\epsilon\mu_{eff}L^2/k_1Re\nu$ is the permeability parameter, $Pr=\nu/\alpha$ is the Prandtl number, $Nb=\tau D_B\Delta C/\nu$ is the Brownian motion parameter, $Nt=\tau D_T\Delta T/\nu T_\infty$ is the Thermophoresis parameter, $Ec=\nu^2Re^2/\Delta TL^2c_p$ is the Eckert number, $Rd=16\sigma^*T_\infty^3/3\nu(\rho c_p)_f k^*$ is the radiation parameter, $\theta_f=T_f/T_\infty$ is the temperature ratio, $Le=\nu/D_B$ is the Lewis number, $E=/Ea/kT_\infty$ binary chemical reaction rate and $\sigma=2k_T^2L^2/Re\nu$. In Equation (3.11), $s=-v_{w0}\sqrt{2}L/\nu\sqrt{Re}$ is the suction/ injection parameter where $s>0$ is suction and $s<0$ is injection and $\epsilon=Ma_C/Ma_T=\sigma_C\Delta C/\sigma_T\Delta T$ is the Marangoni parameter, where Ma_C and Ma_T are the solutal Marangoni number and thermal Marangoni number respectively (see [20]).
The local Nusselt number Nu and the local Sherwood number Sh are defined as

$$Nu=\frac{xh_w}{k_f(T_w-T_\infty)},\quad Sh=\frac{xh_m}{\rho D_B(C_w-C_\infty)}, \tag{3.12}$$

where the heat flux h_w and the mass flux h_m at the wall are given as

$$h_w=-k_f\left[\frac{\partial T}{\partial y}\right]_{y=0},\quad h_m=-\rho D_B\left[\frac{\partial C}{\partial y}.\right]_{y=0} \tag{3.13}$$

Using variables in equation (3.7) and Equation (3.13), we get from equation (3.12)

$$\begin{aligned} &\sqrt{2}Re^{-1/2}Nu=-\Big[1+Nd(1+(\theta_f-1))^3\mathrm{e}^{\xi/2}\Big]\mathrm{e}^{\xi}\xi\theta'(0),\\ &\sqrt{2}Re^{-1/2}Sh=-\xi\mathrm{e}^{\xi}\phi'(0), \end{aligned} \tag{3.14}$$

where $Re=\frac{u_0L}{\nu}$ is the local Reynolds number.

4 Entropy Generation

Entropy generation is dependent on the reversibility of a particular process. For an isolated system entropy tends to increase with time, but remains constant for reversible reactions. With an increase in use of nanofluids and nanoparticles in engineering and medical applications, it is important to study and understand the impact of these nanoparticles on entropy generation on real devices, [14]. The volumetric rate of local entropy generation for the nanofluid according to the second law of thermodynamics, is given for two-dimensional flow as

$$S'''_{gen} = \frac{k_f}{T_\infty^2}\left(\left(\frac{\partial T}{\partial y}\right)^2 + \frac{16\sigma^* T^3}{3k_f k^*}\left(\frac{\partial T}{\partial y}\right)^2\right) + \frac{\mu}{T_\infty}\left(1+\frac{1}{\beta}\right)\left(\frac{\partial u}{\partial y}\right)^2 + \frac{\sigma B_0^2}{T_\infty}u^2 + \frac{\mu}{T_\infty k_1}u^2 + \frac{\mu}{k_1}u^2 + \frac{RD}{C_\infty}\left(\frac{\partial C}{\partial y}\right)^2 + \frac{RD}{T_\infty}\left(\frac{\partial T}{\partial y}\frac{\partial C}{\partial y}\right). \tag{4.1}$$

Equation (4.3) shows that entropy generation has several components . The first source is caused by the heat transfer through the thermal radiation; the second is caused by viscous dissipation; the third and fourth are caused by the magnetic field and mean absorption coefficient respectively; the last two sources are caused by mass transfer.
It is appropriate to obtain the entropy generation number as a ratio between the the local volumetric entropy generation S'''_{gen} and a characteristic rate of entropy generation S'''_0 such that S'''_0 is written as [12]

$$S'''_0 = \frac{k_f(T_w - T_\infty)^2}{L^2 T_\infty^2}. \tag{4.2}$$

The characteristic entropy generation rate S'''_0 is the optimal entropy generation at which the thermodynamic performance of a system is optimized [21]. Finding S'''_0 requires solving an optimization problem which is constrained by the irreversible operations of the system. The physical characteristics of the system are varied until minimum entropy generation is found Bejan [21].

The entropy generation number can be expressed as

$$N_G = \frac{S'''_{gen}}{S'''_0} = \frac{1}{2}\left[1 + Rd\Big(1+(\theta_f-1)\theta\Big)^3\right]Re\mathrm{e}^{2\xi}\theta'^2 + \frac{1}{2}\left(1+\frac{1}{\beta}\right)\frac{ReBr}{(\theta_f-1)^2}\mathbf{e}^{\xi}f''^2 + \frac{Re\Sigma\Omega^2}{2(\theta_f-1)^2}\mathrm{e}^{2\xi}\phi'^2 + Re\frac{Br}{(\theta_f-1)^2}\Big(M^2+\kappa_p\Big)f'^2 + \frac{Re\Omega\Sigma}{2(\theta_f-1)}\mathrm{e}^{2\xi}\theta'\phi', \tag{4.3}$$

where Br, Σ and Ω the Brinkman number, a constant parameter and the concentration difference respectively. These parameters are expressed as:

$$Br = \frac{\mu u_w(x)^2}{T_\infty k_f}, \quad \Sigma = \frac{C_\infty RD}{k_f}, \quad \Omega = \frac{C_0 - C_\infty}{C_\infty}. \tag{4.4}$$

5 Method of solution

The quasi-linearization method (QLM) is a generalization of the Newton-Raphson method (Bellman and Kalaba [22]). The nonlinear equations are linearized using a Taylor series assuming that the difference between the current iteration, $r+1$, and the previous iteration, r is negligible.

Applying the quasi-linearization method to Equations (3.8)–(3.10) and (3.11), gives the following iterative schemes:

$$a_{0,r}f'''_{r+1} + a_{1,r}f''_{r+1} + a_{2,r}f'_{r+1} + a_{3,r}f_{r+1} + a_{4,r}\theta_{r+1} + a_{5,r}\phi_{r+1} = R_f, \tag{5.1}$$
$$b_{0,r}\theta''_{r+1} + b_{1,r}\theta'_{r+1} + b_{2,r}\theta_{r+1} + b_{3,r}f_{r+1} + b_{4,r}f'_{r+1} + b_{5,r}f''_{r+1} + b_{6,r}\phi'_{r+1} = R_\theta, \tag{5.2}$$
$$c_{0,r}\phi''_{r+1} + c_{1,r}\phi'_{r+1} + c_{2,r}\phi_{r+1} + c_{3,r}f_{r+1} + c_{4,r}f'_{r+1} + c_{5,r}\theta_{r+1} + c_{6,r}\theta''_{r+1} = R_\phi, \tag{5.3}$$

subject to

$$\begin{aligned} &f_{r+1}(0) = s,\ f''_{r+1}(0) = 1-\epsilon,\ \theta_{r+1}(0) = 1,\ \phi_{r+1}(0) = 1,\\ &f'_{r+1}(\infty) = 1,\ \theta_{r+1}(\infty) = 0,\ \phi_{r+1}(\infty) = 0. \end{aligned} \tag{5.4}$$

The coefficients in Equations (5.1)–(5.3) are

$$\begin{aligned} &a_{0,r} = 1 + \frac{1}{\beta},\ a_{1,r} = f_r,\ a_{2,r} = -4f'_r - 2e^{-\xi}(M^2 + \kappa_p),\ a_{3,r} = f''_r,\\ &a_{4,r} = 2Rie^{(-3\xi/2)},\ a_{5,r} = 2NRie^{(-3\xi/2)},\\ &b_{0,r} = \frac{1}{Pr} + Rd\Big(1 + (\theta_f - 1)e^{(\xi/2)}\theta_r\Big)^3,\\ &b_{1,r} = f_r + e^{(\xi/2)}\Big(Nb\phi'_r + 2Nt\theta'_r\Big) + 6Rd(\theta_f - 1)e^{(\xi/2)}\theta'_r,\\ &b_{2,r} = -f'_r + 3Rd\Big(1 + (\theta_f - 1)e^{\xi/2}\theta_r\Big)^2\theta''_r(\theta_f - 1)e^{(\xi/2)},\ b_{3,r} = \theta'_r,\ b_{4,r} = -\theta_r,\\ &b_{5,r} = 2Ec\Big(1 + \frac{1}{\beta}\Big)e^{(3\xi/2)}f''_r,\ b_{6,r} = e^{\xi/2}Nb\theta'_r, \end{aligned} \tag{5.5}$$

$$\begin{aligned} &c_{0,r} = 1,\ c_{1,r} = Lef_r,\ c_{2,r} = -Lef'_r - Le\sigma e^{-\xi}\Big(1 + (\theta_f - 1)e^{(\xi/2)}\theta_r\Big)^m e^{-E/1+(\theta_f-1)e^{\xi/2}\theta_r},\\ &c_{3,r} = Le\phi'_r,\ c_{4,r} = -Le\phi_r,\ c_{6,r} = \frac{Nt}{Nb}, \end{aligned} \tag{5.6}$$

$$\begin{aligned} c_{5,r} = -\sigma\phi_r e^{-\xi}\Bigg\{&\Big(1 + (\theta_f - 1)e^{\xi/2}\theta_r\Big)^m e^{(-E/1+(\theta_f-1)e^{\xi/2}\theta_r)}\frac{E(\theta_f - 1)e^{\xi/2}}{\Big(1 + (\theta_f - 1)e^{\xi/2}\theta_r\Big)^2}\\ &+ me^{(-E/1+(\theta_f-1)e^{\xi/2}\theta_r)}\Big(1 + (\theta_f - 1)e^{\xi/2}\theta_r\Big)^{m-1}(\theta_f - 1)e^{\xi/2}\Bigg\} \end{aligned} \tag{5.7}$$

Equations (5.1)–(5.3) were solved using the Chebyshev pseudo-spectral method with the Gauss-Lobatto points [23]

$$x_i = \cos\Big(\frac{\pi i}{N}\Big),\quad i = 0, 1, 2, \ldots, N \qquad -1 \le x_i \ge 1, \tag{5.8}$$

where N is the number of collocation points. A linear transformation formula was used to transfer the interval $[0, L]$ to the $[-1, 1]$, where L represents the boundary condition at infinity.

The derivatives with respect to η are expressed is terms of the Chebyshev differentiation matrix such as

$$\left.\frac{df_r^{(p)}}{d\eta^p}\right|_{\eta=\eta_j} = \sum_{k=0}^{N}\mathbf{D}_{jk}f(\eta_k) = \mathbf{D}F, \quad j = 1, 2, \ldots, N, \tag{5.9}$$

where $\mathbf{D} = 2D/L$ and $F = \Big[f(\eta_0), f(\eta_1), f(\eta_2), \ldots, f(\eta_N)\Big]^T$ is the vector function at the collocation points. The derivative of the high order p can be written by

$$F_r^{(p)} = \mathbf{D}^p F. \tag{5.10}$$

The spectral collocation is applied at iteration r by using the differentiation matrix $\mathbf{D}$ to approximate derivative of unknown, yields

$$\mathbf{A}_{1,1}\mathbf{f} + \mathbf{A}_{1,2}\boldsymbol{\theta} + \mathbf{A}_{1,3}\boldsymbol{\phi} = R_f, \tag{5.11}$$
$$\mathbf{A}_{1,2}\mathbf{f} + \mathbf{A}_{2,2}\boldsymbol{\theta} + \mathbf{A}_{2,3}\boldsymbol{\phi} = R_\theta, \tag{5.12}$$
$$\mathbf{A}_{1,3}\mathbf{f} + \mathbf{A}_{2,3}\boldsymbol{\theta} + \mathbf{A}_{3,3}\boldsymbol{\phi} = R_\phi. \tag{5.13}$$

Here:

$$\begin{aligned}
&\mathbf{A}_{1,1} = a_{0,r}\mathbf{D}^3 + \mathbf{diag}(a_{1,r})\mathbf{D}^2 + \mathbf{diag}(a_{2,r})\mathbf{D} + \mathbf{diag}(a_{3,r}),\\
&\mathbf{A}_{1,2} = a_{4,r},\ \mathbf{A}_{1,3} = a_{5,r}, \qquad (5.14)\\
&\mathbf{A}_{2,2} = \mathbf{diag}(b_{0,r})\mathbf{D}^2 + \mathbf{diag}(b_{1,r})\mathbf{D} + \mathbf{diag}(b_{2,r}),\\
&\mathbf{A}_{2,1} = \mathbf{diag}(b_{3,r}) + \mathbf{diag}(b_{4,r})\mathbf{D} + \mathbf{diag}(b_{5,r})\mathbf{D}^2,\quad \mathbf{A}_{2,3} = \mathbf{diag}(b_{6,r})\mathbf{D}, \qquad (5.15)\\
&\mathbf{A}_{3,3} = (c_{0,r})\mathbf{D}^2 + \mathbf{diag}(c_{1,r})\mathbf{D} + \mathbf{diag}(c_{2,r}),\ \mathbf{A}_{3,1} = \mathbf{diag}(c_{3,r}) + \mathbf{diag}(c_{4,r})\mathbf{D},\\
&\mathbf{A}_{3,2} = \mathbf{diag}(c_{5,r}), \qquad (5.16)\\
&\mathbf{R}_f = f_r f_r'' - 2f_r'^2 - 2e^{-\xi}\Big(M^2 + \kappa_p\Big) - 2, \mathbf{R}_\theta = f_r\theta_r' - f_r'\theta_r + e^{\xi/2}\Big(Nb\theta_r'\phi_r' + Nt\theta_r'^2\Big)\\
&\qquad + 3Rd(\theta_f - 1)e^{\xi/2}\theta_r'^2 + Ec(1 + \frac{1}{\beta})e^{3\xi/2}f_r''^2 + 3Rd\Big(1 + (\theta_f - 1)e^{\xi/2}\theta_r\Big)^2 e^{\xi/2}\theta_r\theta_r'',\\
&\mathbf{R}_\phi =, \qquad (5.17)
\end{aligned}$$

where $\mathbf{diag}()$ is $(N+1)\times(N+1)$ diagonal matrices and $\mathbf{f}, \boldsymbol{\theta}$ and $\boldsymbol{\phi}$ are the values of the f, θ and ϕ respectively. Now applying the SQLM scheme on Equations (5.11)–(5.13), which can obtained as matrix form such as

$$\begin{bmatrix} \mathbf{A}_{11} & \mathbf{A}_{12} & \mathbf{A}_{13} \\ \mathbf{A}_{21} & \mathbf{A}_{22} & \mathbf{A}_{23} \\ \mathbf{A}_{31} & \mathbf{A}_{32} & \mathbf{A}_{33} \end{bmatrix} \begin{bmatrix} F_{r+1} \\ \Theta_{r+1} \\ \phi_{r+1} \end{bmatrix} = \begin{bmatrix} \mathbf{R}_f \\ \mathbf{R}_\theta \\ \mathbf{R}_\phi \end{bmatrix} \tag{5.18}$$

6 Results and Discussion

The nonlinear differential equations (3.7)–(3.10) with the boundary conditions (3.11) were solved numerically using the spectral quasi-linearization method for selected parameter values. Literature suggests that the SQLM is robust and gives accurate results for boundary layer problems [24, 25]. The iteration is started from the initial approximations which satisfy (3.11), specifically:

$$f_0(\eta) = (-1 - e)\exp(-\eta) + \eta - s + (1 + e), \tag{6.1}$$
$$\theta_0(\eta) = \exp(-\eta), \tag{6.2}$$
$$\phi_0(\eta) = \exp(-\eta). \tag{6.3}$$

We considered the significance of physical parameters for instance, the Casson parameter β, the Richardson number Ri, the non-dimensional number ξ, the radiation parameter Rd, the

temperature ratio θ_f and the binary chemical reaction rate E on the velocity profiles $f'(\eta)$, $\theta(\eta)$ the temperature profiles and the concentration profiles $\phi(\eta)$. The values of Ri and ξ are 0.1 and 1.2 respectively, which are determined from [19]. However, the rest of the other parameters $Pr = 6.7$, $Le = 4$, $Nt = 10^{-3}$, $\beta = 2$ $e = 1$, $s = 2$, $\kappa_p = 0.6$, $E = 0.5$, $Rd = 0.15$, $\theta_f = 2$, $Nb = 0.5$, $Ec = 0.3$, $\sigma = 1$, $m = 0.5$, $M = 0.5$, $N = 0.5$ [19, 20].

The variation in the local Nusselt number and the Sherwood number for various values of the Casson parameter, Richardson number, the radiation parameter, the temperature ratio and the non-dimensional number are provided in Table 1. We note that the Nusselt number increases as Casson parameter β increases, while the Sherwood number decrease with increasing with other parameters fixed. It is also observed that the Nusselt number reduces as Richardson number Ri increases, whereas the Sherwood number increase. The Nusselt number and Sherwood number are vary positively with Rd. The same result it is seen with respect to the temperature ratio. The Nusselt number and Sherwood number vary inversely with the non-dimensional number.

Table 1: Numerical values of $-\theta'(0)$ and $-\phi'(0)$ with different values of β, Ri, Rd, θ_f and ξ when $Pr = 6.7$, $Le = 4$, $Nt = 10^{-3}$, $e = 1$, $s = 2$, $\kappa_p = 0.6$, $E = 0.5$, $Nb = 0.5$, $Ec = 0.3$, $\sigma = 1$, $m = 0.5$, $M = 0.5$, $N = 0.5$

$\boldsymbol{\beta}$	$\boldsymbol{Ri}$	$\boldsymbol{Rd}$	$\boldsymbol{\theta_f}$	$\boldsymbol{\xi}$	$\boldsymbol{Re^{-1/2}Nu}$	$\boldsymbol{Re^{-1/2}Sh}$
1					−0.89826777	1.39934551
3	0.1	0.15	2	1.2	−0.18205046	1.27881276
5					−0.09225992	1.26745514
	0.5				−0.47888070	1.49772170
2	1	0.15	2	1.2	−0.76012804	1.72149615
	1.5				−1.05219374	1.90147611
		0.5			0.04856763	1.27101508
2	0.1	1	2	1.2	0.15337722	1.27337443
		1.5			0.16035341	1.27345065
			1.01		−2.03641215	1.18001097
2	0.1	1.5	1.3	1.2	−0.73187093	1.24466801
			3		−0.17183036	1.32679920
				0.5	−0.17620748	1.59246412
2	0.1	0.15	2	1.5	−0.45415417	1.24508669
				2.5	−1.00665598	1.12749275

Figs. 2(a)–(c) show the effect of the Casson parameter β on the fluid velocity, temperature and concentration profiles. In Figs. 2(a) and (b), we observe that the velocity profiles and the temperature profiles decrease as the Casson parameter increases. From Fig. 2(c), it is noted that the Casson parameter is an increasing function of the concentration profiles. For very large values of the Casson parameter, i.e. $\beta \to \infty$, the fluid becomes Newtonian.

The variation of velocity, temperature and concentration profiles with the mixed convection parameter Ri are depicted in Fig. 3(a)–(c), respectively. From Figs. 3(a)–(b), it is observed

that the effect of increasing the mixed convection parameter is to increase the velocity and the temperature profiles. When Ri increase, the bouyancy influences increase and subsequently the acceleration of the fluid flow increases. For the temperature profiles, as Ri increases, the convection cooling effect reduces such that the temperature increases. It is also note that from Fig. 3(b) the temperature profiles increase when $0 \leq \eta \leq 1.5$ while η>1.5, the temperature profiles decrease and hence becomes constant far from the stretching sheet. Fig. 3(c) reveals that the concentration profiles of the fluid decreases as the mixed convection parameter increases.

Figs. 4(a)–(b) show the velocity, temperature and concentration profiles for different non-dimensional number ξ. It is observed from Fig. 4(a) that the velocity profiles decrease with increase in the non-dimensional number in the momentum boundary layer. In Fig. 4(b) the thermal layer thickness increases as the non-dimensional number increases significantly near the stretching sheet. Furthermore, the same result also holds for the concentration profiles Fig. 4(c).

The effects of the thermal radiation parameter on the temperature profiles is shown in Fig. 5(a). It is observed that the temperature increases as thermal radiation increases, which is consistent with physical observations regarding to the affect of increasing thermal radiation.

Figs. 6(a)–(b) show the behaviour of temperature and concentration profiles for different values of temperature ratio θ_f. It is observed that an increase in the value of temperature ratio leads to an decrease of the temperature and concentration profiles. It is also obtained from Fig. 6(a) that increase in the values of temperature ratio leads to decrease in the temperature profiles close the values of $0 \leq \eta \leq 1.5$ whereas reverse trend is observed away from the sheet for η>1.5

The changes in the concentration profiles with binary chemical reaction rate E is depicted in Fig. 7(a). It is noted that increasing the binary chemical reaction rate trends to increases in the concentration profiles since binary chemical reaction rate enhances the concentration of species.

The variations of the local Nusselt number and local Sherwood number with the magnetic parameter for different values of Casson parameter β are depicted in Figs. 8(a) and (b) respectively. It is noted that the influence of increasing the magnetic field is to increase the Nusselt number which it is reduce for all values of Casson parameter β. Moreover, the magnetic filed and Casson parameter are varying inversely with the Sherwood number.

In the following, entropy generation is discussed which is an important attribute of the flow. The entropy generation is influenced by the quantum and changes in the physical characteristics of the fluid and the porous medium as can be seen in equation (4.3). We consider how physical parameters such as non-dimensional number ξ the permeability parameter κ_p, the Reynolds number Re, the temperature ratio θ_f and Casson parameter β influence entropy generation.

The influence of varying the non-dimensional number, the permeability parameter and the Reynolds number on entropy generation are depicted in Figs. 9(a), (b) and (c) respectively. An increase in the non-dimensional number causes an increase in entropy generation. A reduction in entropy generation is noted with an increase in κ_p as depicted in Fig. 9(b) close the values $0 \leq \eta \leq 0.5$ while reverse result is observed on the range is no far way from the sheet η>0.5. Fig. 9(c) illustrates the influence of Reynolds number on entropy generation. In alignment with equation (4.3), it is observed that the entropy generation increases in a response to the increase in Reynolds numbe. The physical interpretation of this observation is the increase of fluid friction and heat transfer due to the change in the structure of the flow which may be attributed to the increase in Reynolds number.

Figs. 10(a) and (b) show the effect of different values of temperature ratio and Casson parameter

on entropy generation, respectively. It is observed that in the proximity of the sheet, entropy generation increases with increasing the temperature ratio near the values $0 \leq \eta \leq 0.5$ while reverse result is viewed away from the sheet till it reached the value of η>0.5. It is viewed that from Fig. 10(b) that for a large β, the entropy generation decreases until it reaches a lowest value at $\eta = 0.5$ and then starts increasing for η>0.5. Since entropy generation is responsible for the irreversibility and our analysis has shown that in the neighborhood of the sheet the entropy generation is substantially high in comparison with other regions, we may conclude that the sheet is a strong source of irreversibility and the thermodynamics imperfections.

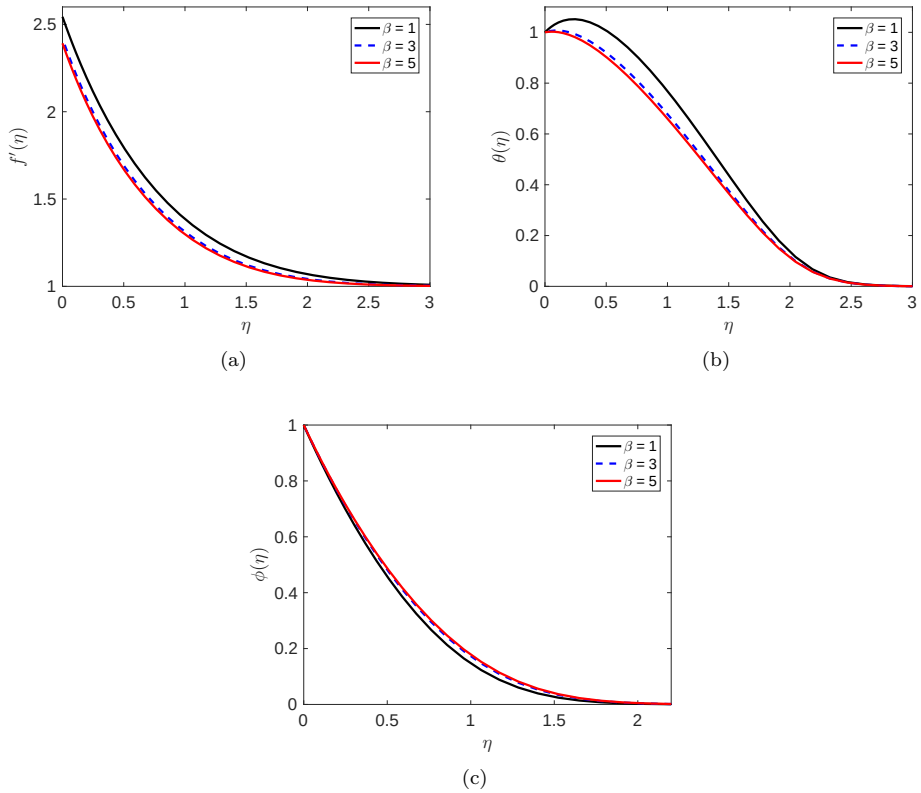

Figure 2: Effect of β on (a) the velocity profiles $f'(\eta)$, (b) the temperature profiles $\theta(\eta)$, and (c) the concentration profiles $\phi(\eta)$.

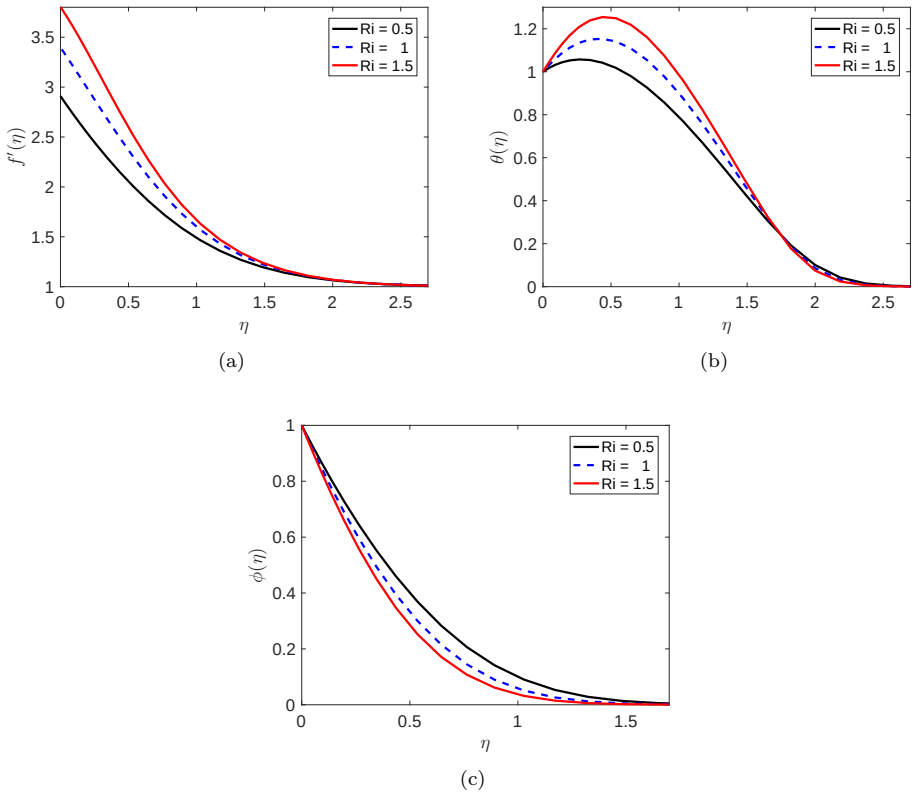

Figure 3: Effect of Ri on (a) the velocity profiles $f'(\eta)$, (b) the temperature profiles $\theta(\eta)$, and (c) the concentration profiles $\phi(\eta)$.

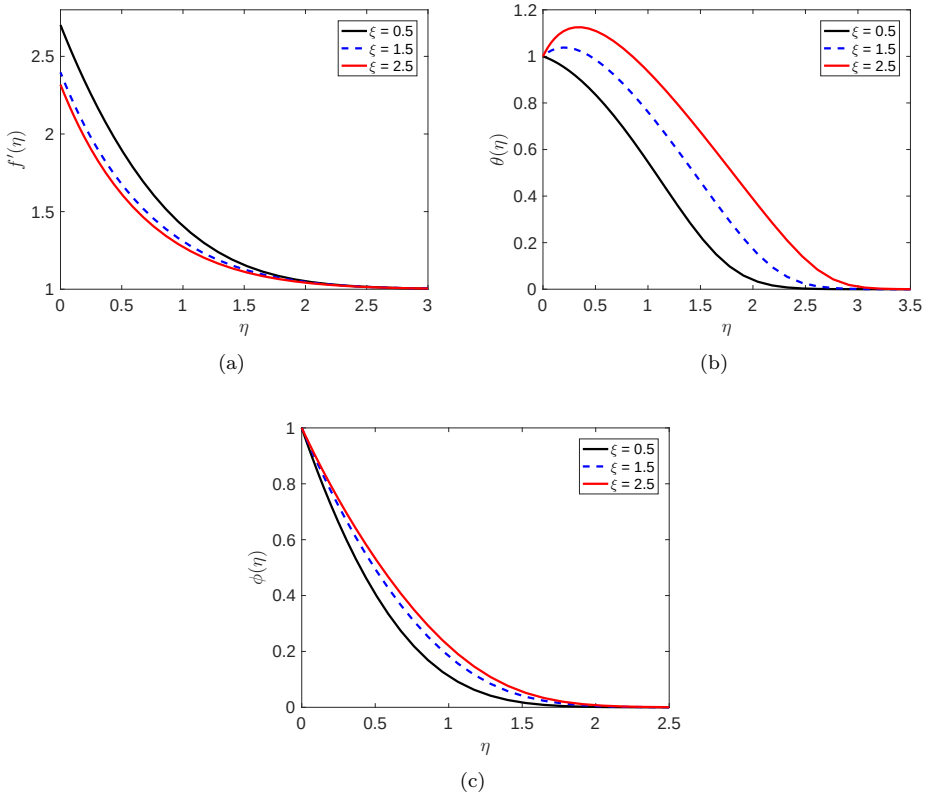

Figure 4: Effect of ξ on (a) the velocity profiles $f'(\eta)$, (b) the temperature profiles $\theta(\eta)$, and (c) the concentration profiles $\phi(\eta)$.

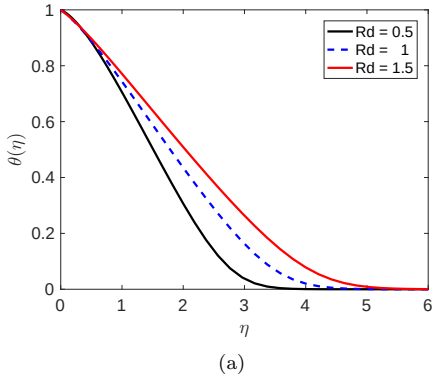

Figure 5: Effect of Rd on (a) the temperature profiles $\theta(\eta)$.

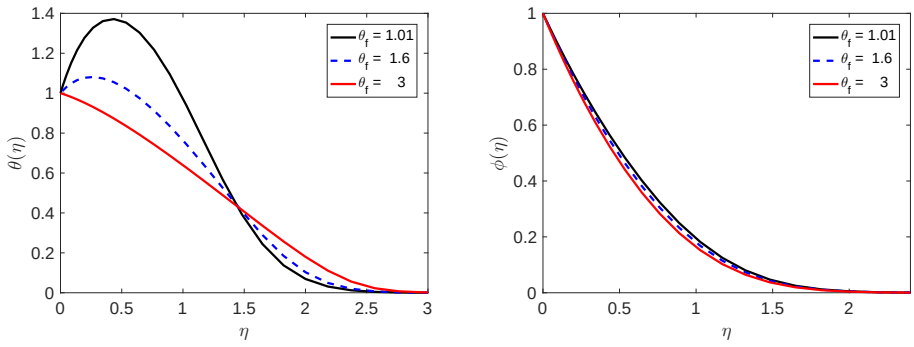

(a) (b)

Figure 6: Effect of θ_f on (a) the temperature profiles $\theta(\eta)$, and (b) the concentration profiles $\phi(\eta)$.

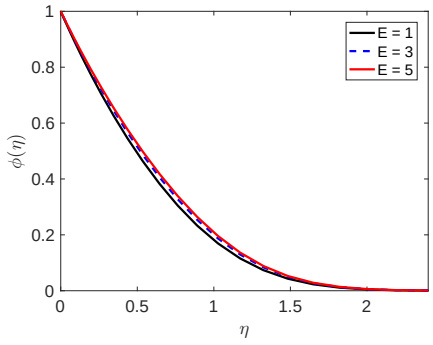

(a)

Figure 7: Effect of E on (a) the concentration profiles $\phi(\eta)$.

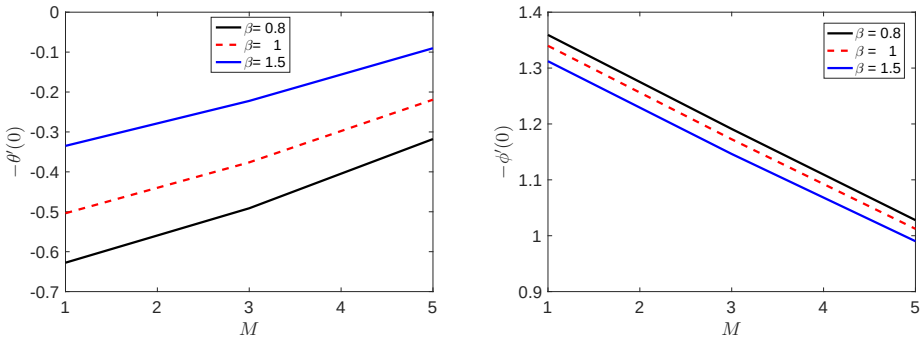

Figure 8: Effect of β and M on (a) the Nusselt number $-\theta'(0)$, and (b) the Sherwood number $-\phi'(0)$.

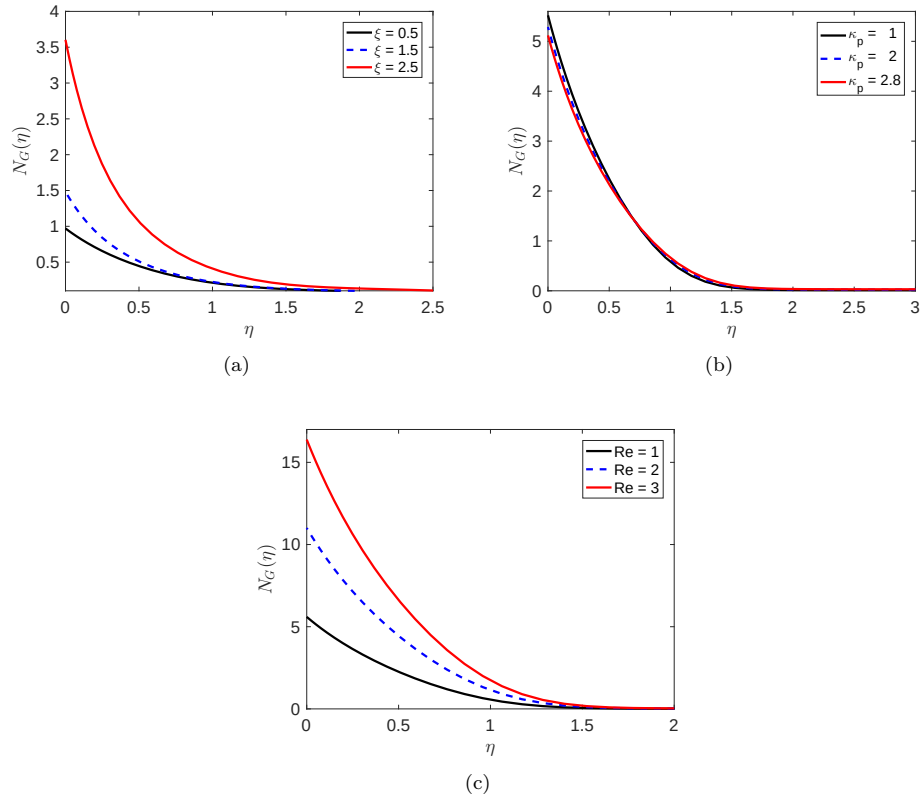

Figure 9: Effect of (a) the non-dimensional number ξ, (b) the permeability parameter κ_p, and (c) the Reynolds number Re on the entropy generation profiles.

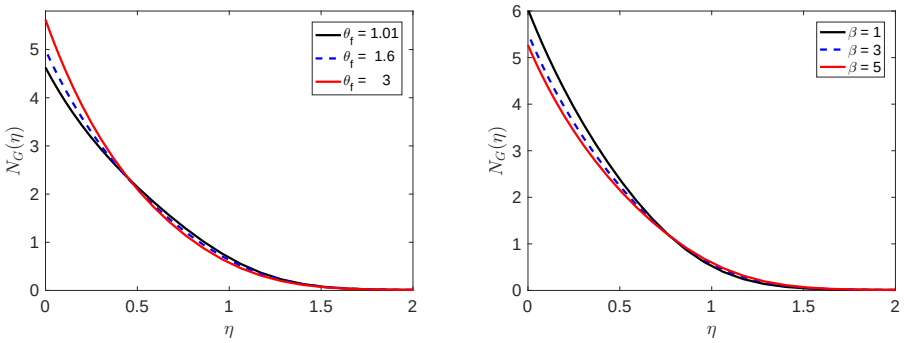

(a) (b)

Figure 10: Effect of (a) the temperature ratio parameter θ_f, and (b) the Casson parameter β on the entropy generation profiles.

7 Conclusions

In this manuscript we considered the effect of Casson nanofluid on a binary chemical reaction with convective boundary conditions. The nonlinear differential equations were solved using the spectral quasi-linearization method. The following observations were made.

- The velocity and temperature profiles decrease as the Casson parameter increases.
- The effect of increasing the mixed convection parameter is to increase the velocity and the temperature profiles.
- The velocity profiles decrease with increase in the non-dimensional number in the momentum boundary layer.
- The influence of increasing the magnetic field is to increase the Nusselt number.
- The entropy generation increases in a response to the increase in Reynolds number.
- The surface is hugely responsible for the irreversibility.

Acknowledgement: The authors would like to thank the University of KwaZulu-Natal South Africa, DST-NRF Centre of Excellence-Mathematical and Statistical Sciences for financing this research and for other necessary support.

References

[1] T. Hayat, T. Muhammad, S. A. Shehzad, and A. Alsaedi, "Temperature and concentration stratification effects in mixed convection flow of an oldroyd-b fluid with thermal radiation and chemical reaction," *PloS one*, vol. 10, no. 6, p. e0127646, 2015.

[2] P. Oxley, C. Brechtelsbauer, F. Ricard, N. Lewis, and C. Ramshaw, "Evaluation of spinning disk reactor technology for the manufacture of pharmaceuticals," *Industrial & engineering chemistry research*, vol. 39, no. 7, pp. 2175–2182, 2000.

[3] O. D. Makinde and P. Sibanda, "Effects of chemical reaction on boundary layer flow past a vertical stretching surface in the presence of internal heat generation," *International Journal of Numerical Methods for Heat & Fluid Flow*, vol. 21, no. 6, pp. 779–792, 2011.

[4] K. Bhattacharyya, "Effects of radiation and heat source/sink on unsteady mhd boundary layer flow and heat transfer over a shrinking sheet with suction/injection," *Frontiers of Chemical Science and Engineering*, vol. 5, no. 3, pp. 376–384, 2011.

[5] T. Hayat, I. Ullah, A. Alsaedi, and M. Farooq, "Mhd flow of powell-eyring nanofluid over a non-linear stretching sheet with variable thickness," *Results in physics*, vol. 7, pp. 189–196, 2017.

[6] Z. Shafique, M. Mustafa, and A. Mushtaq, "Boundary layer flow of maxwell fluid in rotating frame with binary chemical reaction and activation energy," *Results in physics*, vol. 6, pp. 627–633, 2016.

[7] D. Pal and H. Mondal, "Mhd non-darcian mixed convection heat and mass transfer over a non-linear stretching sheet with soret–dufour effects and chemical reaction," *International communications in heat and mass transfer*, vol. 38, no. 4, pp. 463–467, 2011.

[8] P. Olanrewaju, O. Arulogun, and K. Adebimpe, "Internal heat generation effect on thermal boundary layer with a convective surface boundary condition," *American journal of Fluid dynamics*, vol. 2, no. 1, pp. 1–4, 2012.

[9] V. P. Reddy, R. K. Kumar, G. V. Reddy, P. D. Prasad, and S. Varma, "Free convection heat and mass transfer flow of chemically reactive and radiation absorption fluid in an aligned magnetic filed," *Procedia Engineering*, vol. 127, pp. 575–582, 2015.

[10] D. Pal and H. Mondal, "Effects of soret dufour, chemical reaction and thermal radiation on mhd non-darcy unsteady mixed convective heat and mass transfer over a stretching sheet," *Communications in Nonlinear Science and Numerical Simulation*, vol. 16, no. 4, pp. 1942–1958, 2011.

[11] S. Palani, B. R. Kumar, and P. K. Kameswaran, "Unsteady mhd flow of an ucm fluid over a stretching surface with higher order chemical reaction," *Ain Shams Engineering Journal*, vol. 7, no. 1, pp. 399–408, 2016.

[12] M. A. Abbas, Y. Bai, M. M. Rashidi, and M. M. Bhatti, "Analysis of entropy generation in the flow of peristaltic nanofluids in channels with compliant walls," *Entropy*, vol. 18, no. 3, p. 90, 2016.

[13] M. Rashidi, F. Mohammadi, S. Abbasbandy, and M. Alhuthali, "Entropy generation analysis for stagnation point flow in a porous medium over a permeable stretching surface.," *Journal of Applied Fluid Mechanics*, vol. 8, no. 4, 2015.

[14] A. Bejan, "Entropy generation minimization: The new thermodynamics of finite-size devices and finite-time processes," *Journal of Applied Physics*, vol. 79, no. 3, pp. 1191–1218, 1996.

[15] H. F. Oztop and K. Al-Salem, "A review on entropy generation in natural and mixed convection heat transfer for energy systems," *Renewable and Sustainable Energy Reviews*, vol. 16, no. 1, pp. 911–920, 2012.

[16] M. H. Abolbashari, N. Freidoonimehr, F. Nazari, and M. M. Rashidi, "Analytical modeling of entropy generation for casson nano-fluid flow induced by a stretching surface," *Advanced Powder Technology*, vol. 26, no. 2, pp. 542–552, 2015.

[17] J. Qing, M. M. Bhatti, M. A. Abbas, M. M. Rashidi, and M. E.-S. Ali, "Entropy generation on mhd casson nanofluid flow over a porous stretching/shrinking surface," *Entropy*, vol. 18, no. 4, p. 123, 2016.

[18] S. S. Motsa, "A new spectral local linearization method for nonlinear boundary layer flow problems," *Journal of Applied Mathematics*, vol. 2013, 2013.

[19] D. Srinivasacharya and C. RamReddy, "Soret and dufour effects on mixed convection from an exponentially stretching surface," *International Journal of Nonlinear Science*, vol. 12, no. 1, pp. 60–68, 2011.

[20] R. Hamid, N. Arifin, R. Nazar, F. Ali, and I. Pop, "Dual solutions on thermosolutal marangoni forced convection boundary layer with suction and injection," *Mathematical Problems in Engineering*, vol. 2011, 2011.

[21] A. Bejan, "Entropy generation minimization," *Advanced Engineering Thermodynamics*, pp. 531–600, 2016.

[22] R. E. Bellman and R. E. Kalaba, "Quasilinearization and nonlinear boundary-value problems," 1965.

[23] T. Agbaje, S. Mondal, Z. Makukula, S. Motsa, and P. Sibanda, "A new numerical approach to mhd stagnation point flow and heat transfer towards a stretching sheet," *Ain Shams Engineering Journal*, 2016.

[24] S. Motsa, P. Sibanda, and S. Shateyi, "On a new quasi-linearization method for systems of nonlinear boundary value problems," *Mathematical Methods in the Applied Sciences*, vol. 34, no. 11, pp. 1406–1413, 2011.

[25] M. Almakki, S. Dey, S. Mondal, and P. Sibanda, "On unsteady three-dimensional axisymmetric mhd nanofluid flow with entropy generation and thermo-diffusion effects on a nonlinear stretching sheet," *Entropy*, vol. 19, no. 7, p. 168, 2017.

Chapter 6

A model for entropy generation at stagnation point flow of non-Newtonian Jeffrey, Maxwell and Oldroyd-B nanofluids

In previous chapters, a model is developed to describe a particular non-Newtonian fluid which might considered as a shortcoming from the perspective of generality. Further, we adapted a single method to solve the model equations. In this chapter a general model that encapsulates different types of non-Newtonian fluids is developed and solved using different solution methods.

In this chapter, we propose a single model for the steady laminar boundary-layer flow describing the behavior of Jeffrey, Maxwell and Oldroyd-B nanofluids. The model is used to study entropy generation, and heat and mass transfer near a stagnation point in the flow. The system of non-linear equations is solved numerically using three different methods; namely a spectral relaxation method, a spectral quasiliearization method and the spectral local linearization method. The residual errors is used to determine the most accurate solution method.

Received: 20 March 2018 | Accepted: 14 July 2018

DOI: 10.1002/htj.21366

ORIGINAL ARTICLE

WILEY

A model for entropy generation in stagnation-point flow of non-Newtonian Jeffrey, Maxwell, and Oldroyd-B nanofluids

Mohamed Almakki[1] | **Samir Kumar Nandy**[2] | **Sabyasachi Mondal**[3] | **Precious Sibanda**[1] | **Dora Sibanda**[4]

[1]School of Mathematics, Statistics and Computer Science, University of KwaZulu-Natal, Pietermaritzburg, South Africa

[2]Department of Mathematics, A. K. P. C. Mahavidyalaya, Hooghly, India

[3]Department of Mathematics, Amity University, Kolkata, Newtown, India

[4]School of Education, University of KwaZulu-Natal, Pinetown, South Africa

Correspondence
Sabyasachi Mondal, Department of Mathematics, Amity University, Kolkata, Newtown 700135, West Bengal, India.
Email: sabya.mondal.2007@gmail.com

Abstract

We present a generalized model to describe the flow of three non-Newtonian nanofluids, namely, Jeffrey, Maxwell, and Oldroyd-B nanofluids. Using this model, we study entropy generation and heat transfer in laminar nanofluid boundary-layer stagnation-point flow. The flow is subject to an external magnetic field. The conventional energy equation is modified by the incorporation of nanoparticle Brownian motion and thermophoresis effects. A hydrodynamic slip velocity is used in the initial condition as a component of the stretching velocity. The system of nonlinear equations is solved numerically using three different methods, a spectral relaxation method, spectral quasilinearization method, and the spectral local linearization method, first to determine the most accurate of these methods, and second as a measure to validate the numerical simulations. The residual errors for each method are presented. The numerical results show that the spectral relaxation method is the most accurate of the three methods, and this method is used subsequently to solve the transport equations and thus to determine the empirical impact of the physical parameters on the fluid properties and entropy generation.

KEYWORDS

Brownian motion, entropy generation, non-Newtonian nanofluids, spectral methods, thermophoresis

1 | INTRODUCTION

The study of non-Newtonian fluids has generated a significant amount of interest among researchers because of the broad spectrum of applications of these fluids in industrial and technological processes such as food processing, chemical engineering, biomedicine, and many other areas. Of interest is that, in general, the Navier-Stokes equation cannot effectively, and substantially describe the flow of non-Newtonian fluids. The physics of the flow, heat, and mass transfer in non-Newtonian fluids is complex compared to the case of Newtonian fluids. Consequently, the behavior of non-Newtonian fluid flows is described in terms of highly coupled and nonlinear equations, which, in general, precludes the existence of closed-form solutions.

Non-Newtonian fluids of interest in this study are Jeffrey, Maxwell, and Oldroyd-B nanofluids. Some studies have been done before, for example, the steady two-dimensional flow, heat and mass transfer in Jeffrey, Maxwell, and Oldroyd-B nanofluids along a porous stretching sheet with Brownian motion, thermophoresis, magnetic field, and suction/injection was analyzed by Sandeep et al.[1] The Runge-Kutta method and a shooting technique were used to solve the system of equations. The results showed that the wall skin friction for a Maxwell nanofluid is less than that of Jeffrey and Oldroyd-B nanofluids. Also, particle Brownian motion was found to have a significant influence on the flow and the behavior of a Maxwell nanofluid compared to the other nanofluids. The effect of the Lorentz force on a Jeffrey nanofluid was found to be higher than in the case of Maxwell and Oldroyd-B nanofluids. Sandeep et al[2] presented related results for steady hydromagnetic, incompressible flow of Jeffrey, Maxwell, and Oldroyd-B nanofluids through a stretching sheet. Hayat et al[3] obtained a solution for the equation of MHD flow of an upper-convected Maxwell fluid along a stretching sheet in a permeable medium. Abbasi et al[4] considered the flow and behavior of an MHD Jeffrey nanofluid along a linear stretching sheet subject to thermal radiation for prescribed heat and nanoparticle concentration flux conditions. The study of Jeffrey nanofluid flow over an exponential stretching sheet by Hussain et al[5] included an evaluation of the impact of Brownian motion, viscous dissipation, and thermophoresis on the behavior of the flow and heat transfer characteristics. Rashidi et al[6] proposed a semianalytical method for solutions to equations of a nanofluid flow through nonlinear a porous stretching sheet. The homotopy analysis method was used to solve the system of equations. The steady two-dimensional MHD mixed convection in a Jeffrey nanofluid with Joule heating was investigated by Ramzan et al.[7] Sheikholeslami et al[8] presented an analysis of heat transfer in a ferrofluid with a nonuniform magnetic field. The system of equations was solved using the finite element method.

Mustafa et al[9] presented an analysis of heat transfer near a stagnation-point flow of a Jeffrey fluid. The flow was subject to viscous dissipation. Mushtaq et al[10] considered heat transfer in steady incompressible Maxwell fluid flow over a linearly stretching sheet. Both viscous dissipation and thermal radiation were taken into account. The study by Narayana et al[11] of a Jeffrey fluid flow included an analysis of the impact of a chemical reaction and thermal radiation on the flow field. As expected, their results confirmed that an exothermic reaction has the effect of reducing the chemical concentration in the boundary layer, and thereby significantly impacting the concentration profiles. A mathematical model of two-dimensional steady mixed convection flow in a Maxwell nanofluid over an exponential stretching sheet was recently proposed by Mustafa et al.[12]

The Oldroyd-B nanofluid may be used to model the flow of dilute polymeric solutions and common fluids such as blood, Pires et al.[13] Heat transfer and the boundary-layer flow in an Oldroyd-B nanofluid has been considered by, among others, Nadeem et al[14] and Shehzad et al.[15] Hayat et al[16] studied the MHD flow of an Oldroyd-B nanofluid and obtained an analytical solution using a

convective surface boundary condition. The study addressed the importance of thermophoresis and Brownian motion in modifying the flow field.

In some earlier studies, for instance,[1,3,7,10] it has been assumed that the nanoparticles distribution is uniform across the nanofluid. In reality, however, there are slip velocities between the nanoparticles and the fluid molecules owing to Brownian motion and thermophoresis, migration of nanoparticles from hotter to colder regions. In this study, we are interested in investigating the entropy generation in the stagnation-point flow of non-Newtonian nanofluids. In thermodynamical systems, factors such as heat transfer, mass transfer, viscous dissipation, and magnetic field may give rise to entropy generation. In many engineering applications, for example, the design of heat exchangers, electronic cooling, fuel cells, and turbomachinery, the comprehensive analysis of the flow and thermodynamics is important.

The study of entropy generation is not only relevant in engineering applications, but it is also important in many physiological processes. In many physiological studies, blood pressure is measured periodically when conducting physical or mental tasks. Depending on the temperature of the surrounding environment, heat transfer occurs through evaporation, radiation, and conduction. In such studies, monitoring the entropy generation is crucial in characterizing such systems.[17] The entropy generation defines irreversibility and accounts for energy losses.[18,19] As a consequence, by controlling entropy generation, the performance of engineering systems can be enhanced. The minimum entropy generation is found employing the first and second laws of thermodynamics to optimize the thermodynamics.[20] This optimization is known as finite time thermodynamics. In this study, the impact of several factors on entropy generation are investigated to understand and control entropy generation in porous media.[20] Some relevant studies on entropy generation include those of Dalir[21] whose focus was on forced convection and heat transfer in a Jeffrey fluid and Rehmana et al[22] who investigated entropy generation in a Jeffrey nanofluid with zero normal nanoparticle flux at the wall. Dalir et al[23] investigated entropy generation in a Jeffrey nanofluid flow subject to viscous dissipation. Related studies, include, among others, Shateyi et al[24] who investigated entropy generation in a Maxwell flow in a Darcian porous medium. Entropy generation in MHD nanofluid flow over a permeable rotating disk was investigated by Rashidi et al.[25]

A novelty of the current study is the presentation of a single generalized model to describe the flow of three different nanofluids. This study further extends the earlier work by focusing on entropy generation in the stagnation-point flow of MHD Jeffrey, Maxwell, and Oldroyd-B nanofluids. We assume thermal radiation, viscous dissipation, Brownian motion, suction/injection, and thermophoresis are significant factors that may alter the flow structure and the heat transfer properties of the fluid. A second important aspect of the study lies in the method of solution of the coupled nonlinear differential equations. There are many numerical techniques in the literature. Here, we have opted to use three recent spectral collocation-based methods, namely, the spectral relaxation method, the spectral quasiliearization method, and local linearization method.[26,27] The techniques have been used successfully in a few prior studies in the literature, and for systems of varying complexities. We seek to distinguish between the methods in terms of numerical accuracy as determined through residual errors in the numerical results.

2 | PROBLEM FORMULATION

Consider the two-dimensional steady laminar boundary-layer stagnation-point flow of Jeffery, Maxwell, and Oldroyd-B nanofluids along a linear porous stretching sheet in the xy plane. The fluid velocity is $v = (u, v)$ where u is the velocity along the x-axis and v is the velocity along the

y-axis, C is the nanoparticle concentration, and the fluid temperature is T. The flow is subject to viscous dissipation, and we consider thermophoresis and nanoparticle Brownian motion to be significant. Viscous dissipation is amplified when the fluid is highly viscous or the fluid velocity is large. The uniform surface and ambient temperature are represented by T_ω and T_∞, respectively, C_ω is the reference concentration at the surface and C_∞ is the ambient concentration where T_ω > T_∞ and $C_\omega > C_\infty$.

The assumptions made to derive the flow equations are as follows:

- The velocity distribution far from the surface is $u \to U_\infty(x) = ax$, where $a > 0$ represents a constant and a measure of the strength of the stagnation-point flow.
- Magnetic field of strength B_0 is exerted in a transverse direction of the flow.
- There is a slip velocity between the nanoparticles and the fluid molecules.
- The velocity of the fluid near the stretch sheet is $u_\omega(x) = cx$, where $c > 0$.

The flow configuration is represented in Figure 1. With the assumptions above, the single set of nonlinear differential equations that describe the nanofluid motions in the boundary-layer is expressed as[1,3,4]

$$\frac{\partial u}{\partial x} + \frac{\partial v}{\partial y} = 0, \tag{1}$$

$$u\frac{\partial u}{\partial x} + v\frac{\partial v}{\partial y} + \beta_1\left(u^2\frac{\partial^2 u}{\partial y^2} + 2uv\frac{\partial^2 u}{\partial x \partial y} + v^2 + \frac{\partial^2 u}{\partial y^2}\right) = -\frac{1}{\rho}\frac{\partial \rho}{\partial x} + \frac{\nu_f}{(1+\beta_2)}\left[\frac{\partial^2 u}{\partial y^2} + \beta_3\left(u\frac{\partial^3 u}{\partial x \partial y^2} + \frac{\partial u}{\partial y}\frac{\partial^2 u}{\partial x \partial y} + v\frac{\partial^3 u}{\partial y^3} - \frac{\partial u}{\partial x}\frac{\partial^2 u}{\partial y^2}\right)\right] - u\left(\frac{\sigma B_0^2}{\rho_f} + \frac{\nu_f}{K}\right), \tag{2}$$

$$u\frac{\partial T}{\partial x} + v\frac{\partial T}{\partial y} = \frac{k_f}{\rho_f c_p}\frac{\partial^2 T}{\partial y^2} + \frac{\nu_f}{(1+\beta_2)}\left(\frac{\partial u}{\partial y}\right)^2 + \frac{1}{(\rho c)_f}\frac{16\sigma^* T_\infty^3}{3k^*}\frac{\partial^2 T}{\partial y^2} + \frac{\beta_3 \nu_f}{c_p(1+\beta_2)}\left(u\frac{\partial u}{\partial y}\frac{\partial^2 u}{\partial x \partial y} + v\frac{\partial u}{\partial y}\frac{\partial^2 y}{\partial y^2}\right), \tag{3}$$

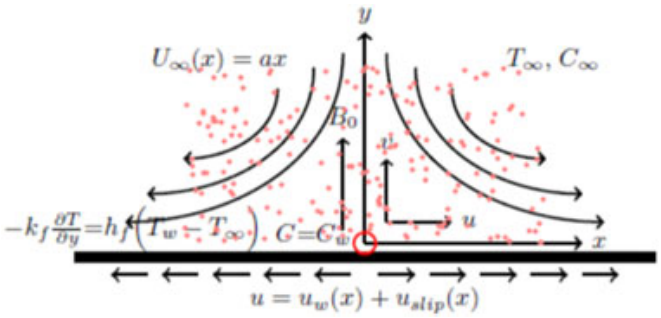

FIGURE 1 Physical configuration [Color figure can be viewed at wileyonlinelibrary.com]

$$u\frac{\partial C}{\partial x} + v\frac{\partial C}{\partial y} = D_B\frac{\partial^2 C}{\partial y^2} + \frac{D_T}{T_\infty}\left(\frac{\partial^2 T}{\partial y^2}\right), \tag{4}$$

where p is the pressure, σ is the electrical conductivity, B_0^2 is the constant applied magnetic field in the $y-$direction, ρ is the density of the fluid, ν_f is the kinematic viscosity, K is the permeability coefficient of the porous medium, c_p is the heat at fixed pressure, k_f is the thermal conductivity, $\tau = (\rho c)_p/(\rho c)_f$ is ratio between the effective heat capacity of the nanofluid and the heat capacity of the base fluid, D_T and D_B are the thermophoretic diffusion coefficient and the Brownian diffusion coefficient, respectively, k^*represents the Rosseland mean absorption coefficient and σ^* represents the Stefan-Boltzmann constant. The parameter β_1 represents the relaxation time, which is the time a reaction takes to reach the equilibrium. In general, there is more than one relaxation time; each is associated with an internal reaction. However, we adopt a black-box approach and employ one relaxation time that is related to the whole system Woods et al.[28] The parameter β_2 is a ratio of the relaxation time and retardation time. The parameter β_3 represents the retardation time, which is the time from the point where a force is exerted to the point where its effect is manifested by Yamaguchi.[29] The retardation time is a feature of the viscoelastic fluids as they do not respond instantaneously to a sudden change in stress (Yamaguchi[29]).

Equations (1) to (4) must be solved subject to the boundary conditions

$$u = u_w(x) + u_{slip}(x),\quad v = v_w(x),\quad -k_f\frac{\partial T}{\partial y} = h_f(T_w - T_\infty),$$

$$C = C_w \text{ at } y = 0,$$

$$u \to U_\infty(x) = ax,\quad \frac{\partial u}{\partial y} \to 0,\quad T \to T_\infty,\quad C \to C_\infty \text{ at } y\to\infty, \tag{5}$$

where h_f represents the convective heat transfer coefficient, $u_{slip}(x)$ is the slip velocity and $u_w(0)$ is the wall transfer velocity and v_0 is the constant mass velocity flux. We note that in the free stream, Equation 2 reduces to

$$-\frac{1}{\rho}\frac{\partial \rho}{\partial x} = a^2x + \frac{\sigma B_0^2}{\rho}U_\infty + \frac{\nu_f}{k}U_\infty. \tag{6}$$

Hence, Equation 2, reduces to

$$\begin{aligned} u\frac{\partial u}{\partial x} + v\frac{\partial v}{\partial y} + \beta_1\left(u^2\frac{\partial^2 u}{\partial y^2} + 2uv\frac{\partial^2 u}{\partial x\partial y} + v^2 + \frac{\partial^2 u}{\partial y^2}\right) \\ = a^2x + \frac{\nu_f}{(1+\beta_2)}\left[\frac{\partial^2 u}{\partial y^2} + \beta_3\left(u\frac{\partial^3 u}{\partial x\partial y^2} + \frac{\partial u}{\partial y}\frac{\partial^2 u}{\partial x\partial y} + v\frac{\partial^3 u}{\partial y^3} - \frac{\partial u}{\partial x}\frac{\partial^2 u}{\partial y^2}\right)\right] \\ - (u - U_\infty)\left(\frac{\sigma B_0^2}{\rho_f} + \frac{\nu_f}{K}\right). \end{aligned} \tag{7}$$

The conservation equation is reduced to a dimensionless form using the following variables[3,4]

$$u = \mathrm{cx}f'(\eta), v = -\sqrt{c\nu_\mathrm{f}}\, f(\eta), \quad \eta = y\sqrt{\frac{c}{\nu_\mathrm{f}}}$$

$$\theta(\eta) = \frac{T - T_\infty}{T_\omega - T_\infty}, \quad \phi(\eta) = \frac{C - C_\infty}{C_\omega - C_\infty}. \tag{8}$$

Thus, in terms of the nondimensional velocity $f(\eta)$, temperature $\theta(\eta)$, and concentration $\phi(\eta)$, respectively, the equations are

$$f''' + (1 + \beta_2)(ff'' - f'^2) + \gamma_1(1 + \beta_2)(2\mathrm{ff}'f'' - f^2f''') + \gamma_2(f''^2 - ff'''') + (1 + \beta_2)[\alpha^2 - (M+\Gamma)(f' - \alpha)] = 0, \tag{9}$$

$$\frac{(1+\mathrm{Nr})}{\mathrm{Pr}}\theta'' + f\theta' + \mathrm{Nt}\theta'^2 + \frac{\mathrm{Ec}}{(1 + \beta_2)}\left[f^{(''2)} + \gamma_2(f'f'' - ff'')\right] + \mathrm{Nt}\theta'\phi' = 0, \tag{10}$$

$$\phi'' + \mathrm{Sc}f\phi' + \left(\frac{\mathrm{Nt}}{\mathrm{Nb}}\right)\theta'' = 0, \tag{11}$$

with the boundary conditions

$$f(0) = s, f'(0) = -1 + \delta f''(0),\ f'(\infty) = f''(\infty) = 0,$$

$$\theta'(0) = -\mathrm{Bi}(1 - \theta(0), \theta(0) = 1,\ \phi(0) = 1,\ \phi(\infty) = 0, \tag{12}$$

where the prime denotes differentiation related to η, $\alpha = a/c$ is constant, $M = \sigma B_0^2/c\rho_\mathrm{f}$ is the magnetic field parameter, $\Gamma = \mu_\mathrm{f}/k{\sim}c$ is the porosity parameter, $\mathrm{Pr} = \mu_\mathrm{f}/\alpha$ is the Prandtl number, $\mathrm{Nr} = 16\sigma^* T_\infty^3/3k_\mathrm{f}k^*$ is the radiation parameter, $\mathrm{Nt} = \tau D_\mathrm{T}(T_\mathrm{w} - T_\infty)/\mu_\mathrm{f}$, $\mathrm{Ec} = u_\mathrm{w}^2/c_\mathrm{p}(T_\mathrm{w} - T_\infty)$ are the thermophoresis parameter and Eckert number, respectively, $\mathrm{Nb} = \tau D_\mathrm{B}(C_\mathrm{w} - C_\infty)/\nu_\mathrm{f}$ is the Brownian motion, $\mathrm{Sc} = \nu_\mathrm{f}/D_\mathrm{B}$ is the Schmidt number, $s = -v_0/(\nu_\mathrm{f}c)^{0.5}$ is the suction/injection parameter where $s > 0$ is suction and $s < 0$ is injection, $\delta = L(c/\nu_\mathrm{f})^{0.5}$ is the velocity slip parameter and $\mathrm{Bi} = (h_\mathrm{f}/k_0)(\nu_\mathrm{f}/c)^{0.5}$ is the Biot number.

The Jeffrey, Maxwell, and Oldroyd-B nanofluids are distinguished by different values of the parameters γ_1, γ_2, and β_2 where γ_1 is the Deborah number related to relaxation time, γ_2 is the Deborah number with respect to retardation time. These parameters are defined as

$$\gamma_1 = \beta_1 c \text{ and } \gamma_2 = \beta_3 c.$$

In particular, we note from Equation (9) that if

(i) $\gamma_1 = 0$, $\gamma_2 \neq 0$, and $\beta_2 \neq 0$ the system reduces to a Jeffrey nanofluid model.
(ii) $\gamma_1 \neq 0$, $\gamma_2 \neq 0$, and $\beta_2 = 0$ the system reduces to an Oldroyd-B nanofluid model.
(iii) $\gamma_1 \neq 0$, $\gamma_2 = 0$, and $\beta_2 = 0$ the system reduces to a Maxwell nanofluid model.

Equation (9) thus represents a single unified model for the flow of Jeffery, Maxwell, and Oldroyd-B nanofluids.

3 | ENTROPY GENERATION

Entropy is a measure of amount of disorder in a particular system. Entropy generation is dependent on the reversibility of a particular process. For an isolated system entropy tends to increase with time, but remains constant for reversible reactions. With an increase in use of nanofluids and nanoparticles in engineering and medical applications, it is important to study and understand the impact of these nanoparticles on entropy generation on real devices.[19] In this study, the focus is on entropy generation in the stagnation-point flow of Jeffrey, Maxwell, and Oldroyd-B nanofluids. The volumetric rate of local entropy generation is defined as

$$\begin{aligned} S'''_{\text{gen}} = {} & \frac{k_{\text{f}}}{T_\infty^2}\left[\left(\frac{\partial T}{\partial y}\right)^2 + \frac{16\sigma^* T_\infty^3}{3k^*}\left(\frac{\partial T}{\partial y}\right)^2\right] + \frac{\sigma B_0^2}{T_\infty}u^2 + \frac{\mu}{T_\infty k\sim}u^2 \\ & + \frac{\mu}{(1+\beta_2)T_\infty}\left[\left(\frac{\partial u}{\partial y}\right)^2 + \beta_3\left(u\frac{\partial u}{\partial y}\frac{\partial^2 u}{\partial x \partial y} + v\frac{\partial^3 u}{\partial y^3}\right)\right] \\ & + \frac{\text{RD}}{C_\infty}\left(\frac{\partial C}{\partial y}\right)^2 + \frac{\text{RD}}{T_\infty}\left(\frac{\partial T}{\partial y}\right)\left(\frac{\partial C}{\partial y}\right). \end{aligned} \tag{13}$$

Equation (13) shows that entropy generation is a contribution of four sources. The first source is due to heat transfer as well as thermal radiation, heat transfer irreversibility (HTI), (S_{th}); the second is due to the magnetic field and mean absorption coefficient (S_{m}); the third source is due to viscous dissipation and fluid friction irreversibility (FFI) (S_{fr}) and the fourth and fifth sources are due to concentration diffusion, diffusion irreversibility, (DI) (S_{dif}). Thus, the volumetric rate of local entropy generation is expressed as a linear combination of (S_{th}), (S_{m}), (S_{fr}) and (S_{dif}):

$$S'''_{\text{gen}} = S_{\text{th}} + S_{\text{m}} + S_{\text{fr}} + S_{\text{dif}}. \tag{14}$$

It is appropriate to write the entropy generation number as a ratio between the entropy generation rate S'''_{gen} and the characteristic entropy generation S'''_0 expressed as[17]

$$S'''_0 = \frac{k_f (T_\omega - T_\infty)^2}{T_\infty^2 x^2}. \tag{15}$$

The characteristic entropy generation rate S'''_0 is the optimal entropy generation at which the thermodynamic performance of a system is optimized.[30] Finding S'''_0 requires solving an optimization problem, which is constrained by the irreversible operations of the system. The physical characteristics of the system is varied until a minimum entropy generation is found.[30] The entropy generation number is, thus, written as

$$N_G(\eta) = \frac{S_{gen}'''}{S_0'''} = (1 + N_r)\mathrm{Re}\theta'^2(\eta) + \frac{\mathrm{Re}B_r}{\Omega(1+\beta_2)}[f''^2 + \gamma_2(f'f''^2 - ff''f''')] + \frac{\mathrm{Re}B_r}{\Omega}(M + \Gamma)f'^2(\eta) + \frac{\mathrm{Re}\Sigma\chi}{\Omega}\phi'(\eta)\theta'(\eta) + \mathrm{Re}\Sigma\left(\frac{\chi}{\Omega}\right)^2\phi'^2(\eta). \quad (16)$$

The parameters in Equation (16) are defined as follows:

$$\mathrm{Re} = \frac{u_\omega(x)x}{\nu_f}, \quad B_r = \frac{\mu u_\omega^2(x)}{k_f \Delta T}, \quad \Omega = \frac{\Delta T}{T_\infty} = \frac{T_\omega - T_\infty}{T_\infty},$$

$$\Sigma = \frac{C_\infty \mathrm{RD}}{k_f}, \quad \chi = \frac{\Delta C}{C_\infty} = \frac{C_\omega - C_\infty}{C_\infty}. \quad (17)$$

From Equation (16), there are four irreversibility sources that contribute to the entropy generation number N_G can be rewritten as $N_G = N_{th} + N_{fr} + N_m + N_{dif}$ where

$$N_{th} = (1 + N_r)\mathrm{Re}\theta'^2(\eta), \quad N_{fr} = \frac{\mathrm{Re}B_r}{\Omega(1+\beta_2)}[f''^2 + \gamma_2(f'f''^2 - ff''f''')],$$

$$N_m = \frac{\mathrm{Re}B_r}{\Omega}(M + \Gamma)f'^2(\eta), \quad N_{dif} = \frac{\mathrm{Re}\Sigma\chi}{\Omega}\phi'(\eta)\theta'(\eta) + \mathrm{Re}\Sigma\left(\frac{\chi}{\Omega}\right)^2\phi'^2(\eta). \quad (18)$$

The fraction of irreversibility from each source can be obtained by dividing the irreversibility source by the total irreversibility leading to nondimensional parameters:

$$\gamma_{th} = \frac{N_{th}}{N_G}, \quad \gamma_{fr} = \frac{N_{fr}}{N_G}, \quad \gamma_m = \frac{N_m}{N_G}, \quad \gamma_{dif} = \frac{N_{dif}}{N_G}, \quad (19)$$

where γ_{th} is the fraction of irreversibility due to thermal diffusion, γ_{fr} is the fraction of irreversibility due to viscous dissipation and fluid friction, γ_m is the fraction of irreversibility due to magnetic field and mean absorption coefficient and γ_{dif} is the fraction irreversibility due to concentration diffusion.

4 | METHOD OF SOLUTION

To determine the most appropriate method of solution, three recent spectral collocation-based techniques were selected. There are other popular methods such as finite difference schemes for nonlinear systems similar to Equations (9) to (11). However, the literature suggests that spectral methods are robust and give better accuracy compared to finite differences.

We seek first to determine the most appropriate scheme among the spectral relaxation (SRM), the spectral local linearization method (SLLM), and spectral quasiliearization method

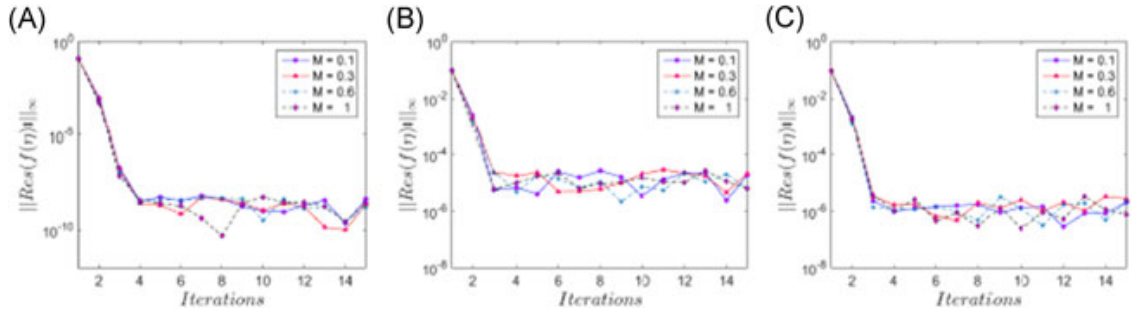

FIGURE 2 The residual errors in the velocity $f(\eta)$ for selected values of the magnetic field parameter M obtained using a, SRM; b, SLLM; c, SQLM methods when $\beta_2 = 0.3$, γ_1 0. 1, $\gamma_2 = 0.01$, $\alpha = 0.01$, $\Gamma = 0.01$, $\mathrm{Pr} = 5$, $\mathrm{Ec} = 0.1$, $N_r = N_b = N_t = 0.2$, $\mathrm{Sc} = 0.4$, $s = 2$, $\delta = 3$, $B_i = 0.2$ [Color figure can be viewed at wileyonlinelibrary.com]

(SQLM) as determined through the calculation of residual errors in the numerical results, and second, to use the perceived better scheme to solve the systems of Equations (9) to (11) subject to the boundary conditions (12). The three schemes were compared with respect to the residual errors in the fluid velocity $f(\eta)$, temperature $\theta(\eta)$ and the nanofluid volume fraction $\phi(\eta)$ profiles for the varying magnetic field parameter M and the suction/injection parameter s.

Figures 2 and 3 give the residual errors in $f(\eta)$ using the three methods for selected values of M and s, respectively. We observe that, for any given number of iterations, the SRM gives the smallest residual error of $|\mathrm{Res}_i| \approx 10^{-9}$ in comparison with the SLLM and SQLM with residual errors of $|\mathrm{Res}_i| \approx 10^{-5}$ and $|\mathrm{Res}_i| \approx 10^{-6}$, respectively.

In the evaluation of $\theta(\eta)$ as illustrated in Figures 4, the difference in the residual errors using the three methods is however marginal. Generally, the residual errors are of order $|\mathrm{Res}_i| \approx 10^{-10}$.

We have not sought to determine the efficiency of the various schemes in terms of the number of function evaluations per iteration. However, in general, all three schemes require approximately the same effort in coding and computational time. The schemes give good accuracy with the SRM giving the smallest residual errors compared to SLLM and SQLM for our system of equations.

The computational times (measured in seconds) for SRM, SLLM, and SQLM are presented in Table 1. All the methods were tested using Matlab (R2017b) on a Desktop Computer with an Intel Core i5 3.30 GHz processor, 4.00 GB of RAM and widows 10 (64-bit) operating system. It can be seen that all the methods perform comparably in terms of the computational time.

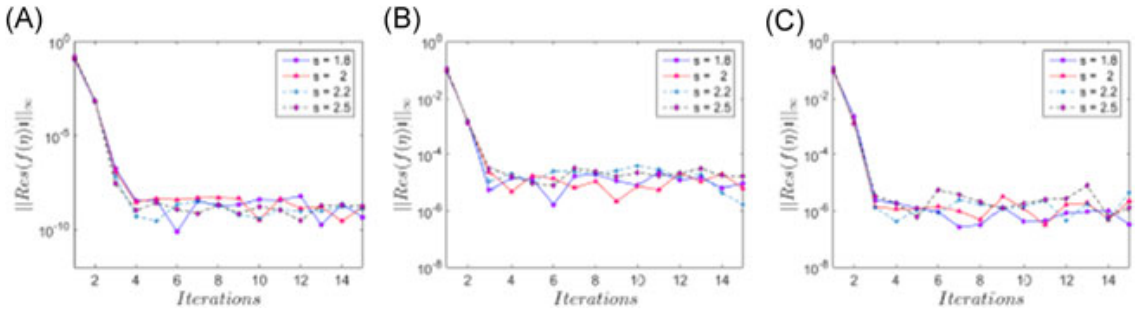

FIGURE 3 The residual errors in the velocity $f(\eta)$ for selected values of the suction parameter obtained using A, SRM; B, SLLM; C, SQLM methods when $\beta_2 = 0.3$, $\gamma_1 = 0.1$, $\gamma_2 = 0.01$, $\alpha = 0.01$, $\Gamma = 0.01$, $\mathrm{Pr} = 5$, $\mathrm{Ec} = 0.1$, $N_r = N_b = N_t = 0.2$, $\mathrm{Sc} = 0.4$, $s = 2$, $\delta = 3$, $B_i = 0.2$ [Color figure can be viewed at wileyonlinelibrary.com]

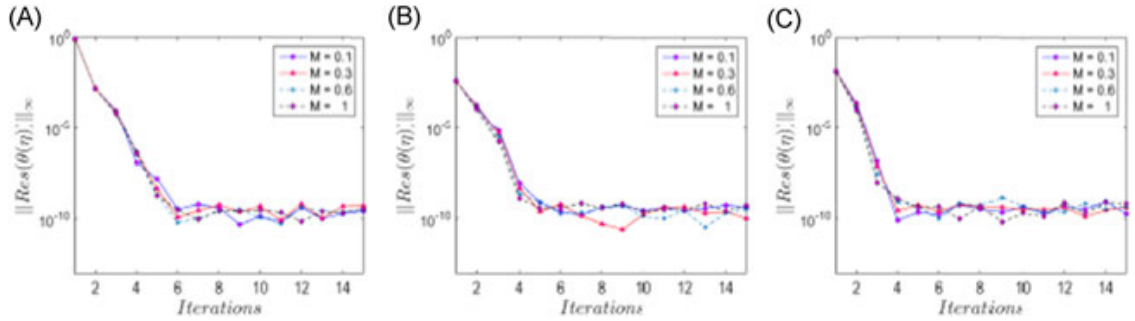

FIGURE 4 The residual errors in the velocity $\theta(\eta)$ for selected values of the magnetic field parameter obtained using a, SRM; b, SLLM; c, SQLM methods when $\beta_2 = 0.3$, $\gamma_1 = 0.1$, $\gamma_2 = 0.01$, $\alpha = 0.01$, $\Gamma = 0.01$, $\Pr = 5$, $\mathrm{Ec} = 0.1$, $N_r = N_b = N_t = 0.2$, $\mathrm{Sc} = 0.4$, $s = 2$, $\delta = 3$, $B_i = 0.2$ [Color figure can be viewed at wileyonlinelibrary.com]

TABLE 1 Computational times for SRM, SLLM, and SQLM with various values of M and s when $\beta_2 = 0.3$, $\gamma_1 = 0.1$, $\gamma_2 = 0.01$, $\alpha = 0.01$, $\Gamma = 0.01$, $\Pr = 5$, $\mathrm{Ec} = 0.1$, $N_r = N_b = N_t = 0.2$, $\mathrm{Sc} = 0.4$, $s = 2$, $\delta = 3$, $B_i = 0.2$

M	s	SRM	SLLM	SQLM
0.1	2	0.004350	0.001454	0.002509
0.3		0.003562	0.001418	0.003505
0.6		0.004198	0.002095	0.002465
1		0.006628	0.001261	0.002436
0.6	1.8	0.003933	0.002131	0.002537
	2	0.005087	0.001545	0.004132
	2.2	0.003213	0.001638	0.004465
	2.5	0.003247	0.001217	0.002667

5 | RESULTS AND DISCUSSION

The system described by Equations (9) to (11) with the boundary condition (12) was solved numerically using the spectral relaxation method for selected parameter values. Suitable initial approximations for the solution of Equations (9) to (11) that satisfy (12) are

$$f_0(\eta) = s\left(\frac{1}{1+\delta}\right)(\exp(-\eta)-1), \tag{20}$$

$$\theta_0(\eta) = \left(\frac{B_i}{1+B_i}\right)\exp(-\eta), \tag{21}$$

$$\phi_0(\eta) = \exp(-\eta). \tag{22}$$

The importance of physical parameters such as the Deborah numbers $\gamma_1$and γ_2, β_2, the suction/injection parameter s, the Schmidt number Sc and the slip parameter δ on the fluid velocity $f'(\eta)$, the temperature $\theta(\eta)$, concentration $\phi(\eta)$and the volumetric entropy generation $N_G(\eta)$ on Maxwell, Jeffrey, and Oldroyd-B nanofluids are discussed. The values of the parameters Pr and Re are 5 and

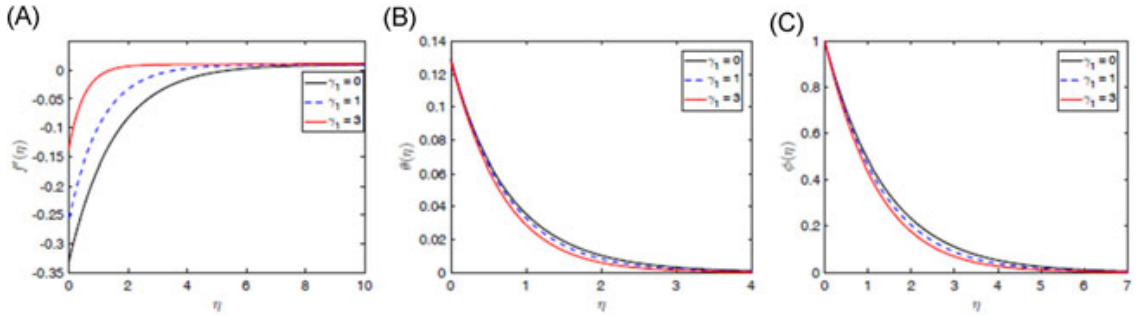

FIGURE 5 Influence of γ_1 on A, the velocity profile $f'(\eta)$; B, the temperature profiles $\theta(\eta)$; and C, the concentration profiles $\phi(\eta)$ [Color figure can be viewed at wileyonlinelibrary.com]

3, respectively, which are determined based on the literature.[23,31] Unless stated otherwise, we have used the parameter values $\mathrm{Nb} = 0.2$, $\mathrm{Nt} = 0.2$, $\mathrm{Nr} = 0.2$, $\alpha = 0.01$, $\mathrm{Sc} = 0.4$, $\beta_2 = 0.3$, $\Gamma = 0.01$, $\delta = 3$, $\mathrm{Bi} = 0.2$, $\mathrm{Ec} = 0.1$, $M = 0.6$, $s = 2$ and $2 = 4$. Maximum values of the parameters are chosen by considering the previously published results, which are mentioned in the references and some parameters values are chosen manually through trial and error.

Figure 5a-c shows the effect of the Deborah number γ_1 on the fluid velocity, the temperature, and the concentration profiles, respectively. Physically, the Deborah number is a dimensionless expression of the relaxation time, which is the time the fluid takes to reach equilibrium after experiencing a stress. Thus, it is expected that fluids behave like liquids with low Deborah number and behave like solids with high Deborah number. Therefore, it is not surprising to note that the velocity profile is affected negatively by high Deborah number as Figure 5A shows. The deterioration of the velocity profile with increasing Deborah number could be justified by the higher resistance of the solid-like fluids, which are associated with high Deborah numbers. In Figure 5B, we observe that the temperature distribution and thermal boundary layer thickness decrease as γ_1 increases. The justification of this behavior lies on the fact that γ_1 is inversely proportional to the retardation time β_3, which is related to the fluid viscosity. Small values of β_3 are associated with less viscous fluids, which have high motion resulting in weakening the thickness of the thermal boundary layer and lowering the temperature profile as the figure suggests. A similar behavior is observed for the concentration profile as Figure 5C shows. This observation can be physically justified in a similar way as explained for Figure 5B by linking the behavior to the fluid motion since it is the case that as the fluid moves faster, nanoparticles are washed downstream giving rise to the decrease of the boundary layer concentration.

The changes in velocity, temperature, and concentration profiles with β_2 are illustrated in Figure 6a-c. In Figure 6a, it is observed that as β_2 increases due to the increase in relaxation time and a reduction in retardation time, the fluid velocity increases. Figure 6b and 6c shows that as β_2 increase the temperature and concentration profiles become thinner.

Figure 7a-c shows the variation in the velocity, temperature, and the concentration profiles, respectively, with respect to the Deborah number γ_2. In Figure 7a, the velocity profiles decrease as γ_2 increases. In contrast, larger values of γ_2 yield increases in both the temperature and concentration profiles, Figure 7b and 7c.

The effect of the suction parameter s on the velocity, temperature, and concentration profiles is given in Figure 8. Positive values of the parameter s represent suction, whereas the negative values represent injection. The velocity profiles increase as the suction/injection increases. It is observed that as the suction/injection parameter increases, which represents increased

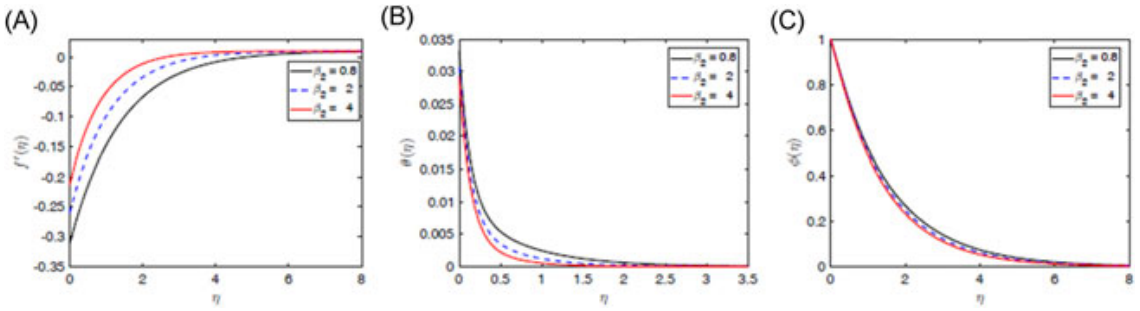

FIGURE 6 Effect of β_2 on A, the velocity profile $f'(\eta)$; B, the temperature profiles $\theta(\eta)$; and C, the concentration profiles $\phi(\eta)$ [Color figure can be viewed at wileyonlinelibrary.com]

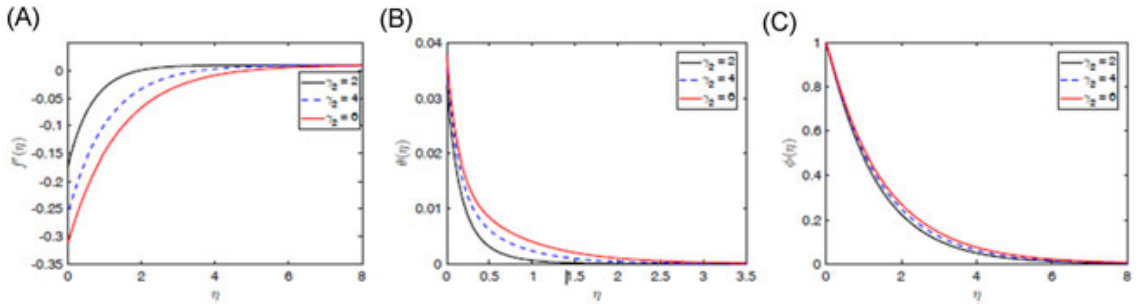

FIGURE 7 Effect of γ_2 on A, the velocity profile $f'(\eta)$; B, the temperature profiles $\theta(\eta)$; and C, the concentration profiles $\phi(\eta)$ [Color figure can be viewed at wileyonlinelibrary.com]

withdrawal of the fluid from the system, reduces the fluid temperature and concentration profiles. This has the same effect as increasing the flow velocity.

The concentration profiles are given for different Schmidt numbers in Figure 9. It is evident that nanoparticle concentration decreases to the ambient concentration values for small values of η and large Schmidt numbers.

Figure 10 demonstrates how the velocity, temperature, and concentration profiles change with the slip parameter δ. In Figure 10A, the velocity slip parameter varies from 0 to 4 with $\delta = 0$ representing no slip condition. The figure shows that as the slip condition becomes stronger, the velocity decreases causing less amount of the flow to move in the velocity direction. When $\delta = 0$, the distribution of nanoparticles is uniform. However, in reality, the

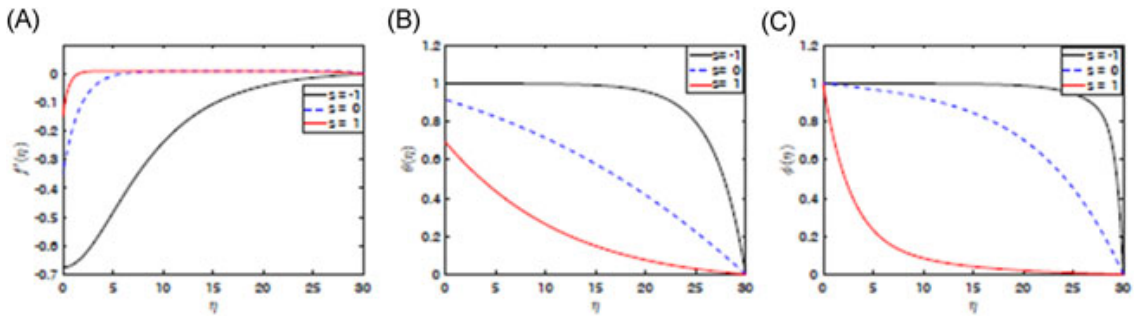

FIGURE 8 Influence of the suction/injection parameter s on A, the velocity profile $f'(\eta)$; B, the temperature profiles $\theta(\eta)$; and C, the concentration profiles $\phi(\eta)$ [Color figure can be viewed at wileyonlinelibrary.com]

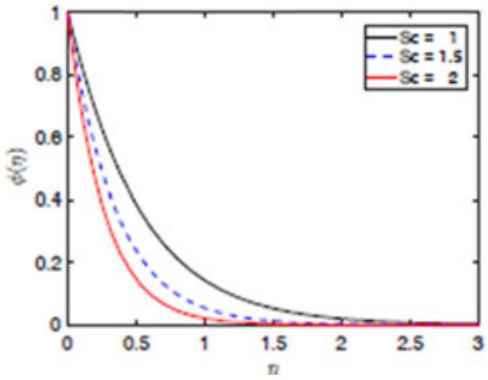

FIGURE 9 Influence of the Schmidt number Sc on the concentration profile [Color figure can be viewed at wileyonlinelibrary.com]

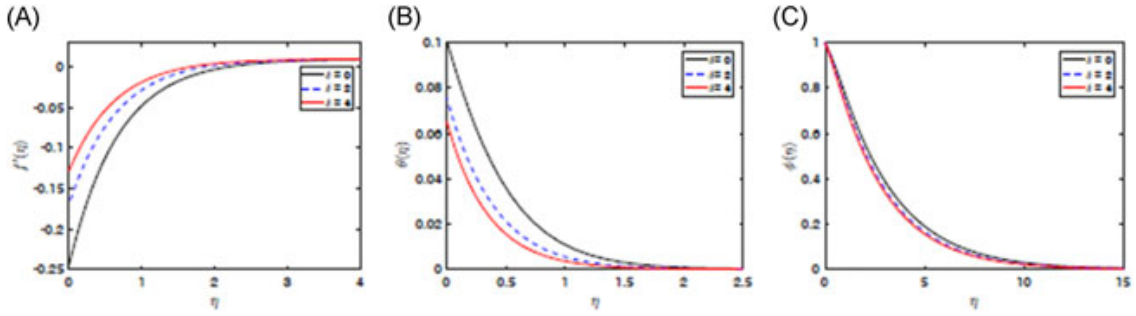

FIGURE 10 Influence of the velocity slip parameter δ on A, the velocity profile $f'(\eta)$; B, the temperature profiles $\theta(\eta)$; and C, the concentration profiles $\phi(\eta)$ [Color figure can be viewed at wileyonlinelibrary.com]

nanoparticles distribution is far from being uniform due to certain mechanics, mainly Brownian motion and thermophoresis (movement of nanoparticles from hotter to colder regions). Therefore, large values of δ is associated with high Brownian motion, which stems from the collision between the nanoparticles and the liquid molecules. The collision contributes to the decrease of the velocity when δ increases as the figure shows. In Figure 10B, it is observed that larger velocity slip enhances the thermal boundary layer thickness. Similar results were obtained for the concentration profiles.

Entropy generation, which is an important attribute of the flow is discussed below. The entropy generation is influenced by the quantum and changes in the physical characteristics of the fluid and the porous medium as can be seen in Equation (16). We consider how physical parameters such as the Deborah number, the porosity parameter Γ, the Reynolds number Re, and the slip parameter δ influence entropy generation.

Figures 11 shows how the entropy generation profiles change with the Deborah number and the ratio of relaxation to retardation times β_2. It is evident that the entropy generation is proportional to the Deborah number γ_1. This result is in agreement with Dalir[21] in which a non-Newtonian Jeffery fluid is considered.

The variation in entropy generation profiles with the Deborah number related to the retardation time γ_2 is shown in Figure 11B. Here, we observed that the entropy generation is inversely related to γ_2 with increasing γ_2 resulting in lower entropy generation. From the physical viewpoint, an increase in γ_2 is associated with a decrease in the velocity of the particles of the fluid within the boundary layer.

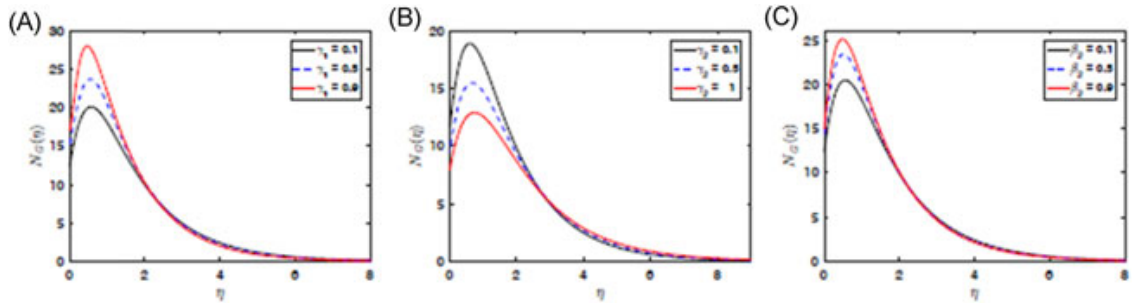

FIGURE 11 Effect of A, Deborah number γ_1; B, the Deborah number γ_2; and C, β_2 on entropy generation [Color figure can be viewed at wileyonlinelibrary.com]

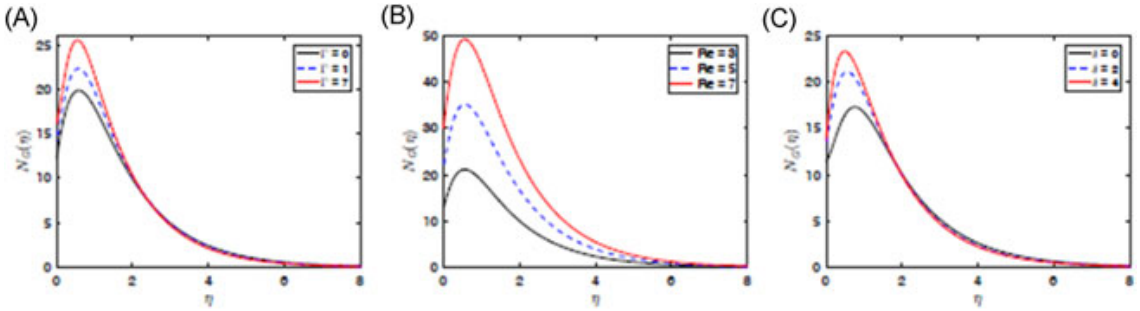

FIGURE 12 Influence of A, the porosity parameter Γ; B, Reynold number Re; and C, the slip parameter δ on the entropy generation [Color figure can be viewed at wileyonlinelibrary.com]

The slow motion of fluid particles contributes to reducing entropy generation. Figure 11C shows the variation of the volumetric entropy generation with the ratio of relaxation to retardation times β_2. It is evident that as β_2 increases entropy generation also increases. This may be explained by noting that an increase in the ratio of relaxation time to retardation time β_2 signifies an increase in the boundary-layer fluid velocity. Moreover, in a specific region in the proximity of the sheet, the combined effect of velocity, temperature, and concentration generates the maximum entropy. Thus, the surface is a main factor for generating irreversible processes.

We checked if medium porosity, the Reynolds number Re and the slip parameter δ have any meaningful influence on entropy generation. The variation in entropy generation due to changes in the porosity parameter Γ is displayed in Figure 12A. It is evident that the entropy generation is enhanced by the fluid flow over a porous medium.

Figure 12B illustrates how entropy generation varies with the Reynolds number Re. In line with Equation (16), we observe that increasing the Reynolds number causes higher entropy generation. The physical justification may further be that as the Reynolds number increases, the flow structure changes from its laminar phase, hence contributing to increased fluid friction and heat transfer. This, in turn, causes high entropy generation.

The variation of entropy generation with the slip parameter δ is presented in Figure 12C. We observe that the slip velocity has a positive impact on the entropy generation. Increasing slip velocity increases the fluid motions inside the boundary layer hence both the fluid velocity and temperature profiles increase leading to an increase in entropy generation. Since the entropy generation is responsible for the irreversibility and our analysis has shown that in the neighborhood of the sheet the entropy generation is substantially high in comparison with other regions, it can be concluded that the sheet is a strong source of irreversibility and the thermodynamics imperfections.

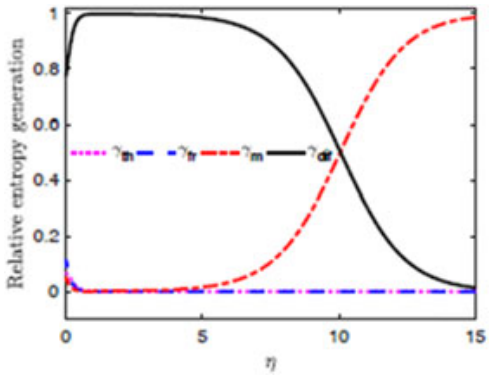

FIGURE 13 The impact of each source of irreversibility [Color figure can be viewed at wileyonlinelibrary.com]

In Section 2, it was shown that there are some sources of irreversibility, namely, thermal radiation, the magnetic field and mean absorption coefficient, viscous dissipation and fluid friction and concentration diffusion. In Figure 13, the contribution of each source to the total irreversibility is given as a function of distance from the sheet. First, it is observed, though not very noticeable, that in the proximity of the sheet all sources of irreversibility contribute positively to the total irreversibility. However, the irreversibility due to the concentration diffusion (γ_{dif}) is dominant due to the high Brownian motion of the nanoparticle species near the sheet. Moving away from the sheet the irreversibility due to the magnetic field and mean absorption coefficient (γ_{m}) takes over and becomes the dominant source of irreversibility as the temperature drops. On the other hand, the contribution of irreversibility due to concentration diffusion decreases moving away from the sheet due to a decrease in the Brownian motion. The combined effect of the increase in the magnetic field and the decrease in nanoparticle motion leads to the dominance of the irreversibility in the regions far from the sheet.

6 | CONCLUSION

We have presented a single generalized model for the study of steady two-dimensional MHD flow and heat transfer in Jeffrey, Maxwell, and Oldroyd-B nanofluids. Entropy generation, and how this is influenced by certain physical parameters has been investigated. The Deborah number has a significant impact on entropy generation in porous media systems. Consequently, by varying the Deborah the entropy generation can be adjusted and controlled. A comparison of the accuracy of three spectral collocation techniques for solving highly nonlinear equations has been given. The spectral relaxation method has been shown to give less residual errors, and this method has been used to find the numerical solutions presented in this study. The main results of the analysis are, that

1. The velocity profiles increase with the Deborah number γ_1, whereas the opposite trend was observed for temperature and concentration profiles.
2. The slip parameter has a negative impact on the velocity, temperature, and concentration profiles.
3. Entropy generation increased with the Deborah number related to relaxation time γ_1 and decreased with the Deborah number related to retardation time γ_2.
4. The velocity, temperature, and concentration profiles are determined and subsequently used to calculate the entropy generation number.
5. The surface is hugely responsible for the irreversibility.

6. The entropy generation due to concentration diffusion is the most dominant source of entropy generation.

There are emerging research directions, which extend the classical studies by consider the entropy generation in natural and mixed convection.

ACKNOWLEDGMENTS

The authors would like to thank the University of KwaZulu-Natal, South Africa, the DST-NRF Centre of Excellence-Mathematical and Statistical Sciences, and Amity University, Kolkata, India for financial support.

ORCID

Sabyasachi Mondal http://orcid.org/0000-0003-4666-0568

NOMENCLATURE

u	velocity in x direction ($m\,s^{-1}$)
v	velocity in $\boldsymbol{y}$ direction ($m\,s^{-1}$)
$(\boldsymbol{x}, \boldsymbol{y})$	coordinate axis (m)
β_1	fluid relaxation time (s)
p	pressure
ρ_f	density
υ_f	kinematic viscosity ($m^2\,s^{-1}$)
μ	viscosity of the fluid ($kg\,m^{-1}\,s^{-1}$)
β_2	ratio between relaxation time and retardation time
β_3	fluid retardation time (s)
σ	electrical conductivity ($\Omega^{-1}\,m^{-1}$)
B_0	magnetic field strength ($kg\,s^{-2}\,A^{-1}$)
K	permeability coefficient ($kg\,mN^{-1}\,s^{-1}$)
T	temperature (K)
T_∞	ambient temperature (K)
T_ω	temperature of the fluid at the sheet (K)
κ_f	thermal conductivity ($W\,m^{-1}\,K^{-1}$)
c_p	specific heat ($m^2\,s^{-2}\,K^{-1}$)
τ	effective heat capacity of nanoparticles (J K)
$(\rho c_p)_p$	heat capacity of the nanoparticles ($J\,kg^{-1}\,K^{-1}$)
D_B	Brownian motion coefficient ($kg\,m^{-1}\,s^{-1}$)
C	concentration of fluid ($kg\,m^{-3}$)
C_ω	concentration at the wall ($kg\,m^{-3}$)
C_∞	concentration away from the disk ($kg\,m^{-3}$)
D_T	thermophoretic diffusion coefficient ($kg\,m^{-1}\,s^{-1}\,K^{-1}$)
σ^*	Stefan-Boltzmann constant
κ^*	Roseland mean absorption coefficient ($m^2\,kg^{-1}$)
$u_\omega(x)$	velocity of the stretching sheet ($m\,s^{-1}$)
$u_{slip}(x)$	slip velocity ($m\,s^{-1}$)
h_f	heat transfer coefficient ($W\,m^{-2}\,K^{-1}$)

(a, c)	constants
$U_\infty(x)$	velocity of free stream ($m\,s^{-1}$)
f	dimensionless velocity
η	dimensionless variable
θ	dimensionless temperature
ϕ	dimensionless nanoparticle concentration
γ_1	Deborah number due to retardation time
γ_2	Deborah number due to relaxation time
α	constant
M	magnetic field parameter
Γ	porosity parameter
Nr	thermal radiation parameter
Pr	Prandtl number
Nt	thermophoresis parameter
Ec	Eckert number
Nb	Brownian motion parameter
Sc	Schmidt number
s	suction/injection parameter
δ	dimensionless velocity slip parameter
Bi	Biot number
$S_{\text{gen}}^{'''}$	volumetric entropy generation ($W\,m^{-3}\,K^{-1}$)
$S_0^{'''}$	dimensionless minimum entropy generation rate
Re	Reynold number
Br	Brinkman number
Ω	dimensionless
ΔT	difference between $(T_\omega - T_\infty)$(K)
χ	concentration difference

REFERENCES

1. Sandeep N, Rushi kumar B, Jagadeesh kumar MS. A comparative study of convective heat and mass transfer in non-newtonian nanofluid flow past a permeable stretching sheet. *J Mol Liq*. 2015;212:585-591.
2. Sandeep N, Sulochana C. Momentum and heat transfer behaviour of jeffrey, maxwell and oldroyd-b nanofluids past a stretching surface with non-uniform heat source/sink. *Ain Shams Eng J*. 2016. https://doi.org/10.1016/j.asej.2016.02.008
3. Hayat T, Abbas Z, Sajid M. Series solution for the upper-convected maxwell fluid over a porous stretching plate. *Phys Lett A*. 2006;358(5–6):396-403.
4. Abbasi F, Shehzad S, Hayat T, Alsaedi A, Obid MA. Influence of heat and mass flux conditions in hydromagnetic flow of jeffrey nanofluid. *AIP Adv*. 2015;5(3):037111.
5. Hussain T, Shehzad SA, Hayat T, Alsaedi A, Al-Solamy F, Ramzan M. Radiative hydromag-netic flow of jeffrey nanofluid by an exponentially stretching sheet. *PLOS One*. 2014;9(8):e103719.
6. Rashidi MM, Freidoonimehr N, Hosseini A, Bég OA, Hung T-K. Homotopy simulation of nanofluid dynamics from a non-linearly stretching isothermal permeable sheet with transpiration. *Meccanica*. 2014;49(2):469-482.
7. Ramzan M, Bilal M, Chung JD, Mann A. On mhd rditive jeffery nnofluid flow with convective heat and mass boundry conditions. *Neural Comput Appl*. 2017:1-10. https://doi.org/10.1007/s00521-017-2852-8
8. Sheikholeslami M, Rashidi MM, Ganji DD. Effect of non-uniform magnetic field on forced convection heat transfer of fe3o4–water nanofluid. *Comput Methods Appl Mech Eng*. 2015;294:299-312.
9. Mustafa M, Hayat T, Hendi AA. Influence of melting heat transfer in the stagnation-point flow of a jeffrey fluid in the presence of viscous dissipation. *J Appl Mech*. 2012;79(2):024501.

10. Mushtaq A, Mustafa M, Hayat T, Alsaedi A. Effects of thermal radiation on the stagnation-point flow of upper-convected maxwell fluid over a stretching sheet. *J Aerosp Eng*. 2013;27(no. 4):04014015.
11. Satya narayana PV, Harish babu D. Numerical study of mhd heat and mass transfer of a jeffrey fluid over a stretching sheet with chemical reaction and thermal radiation. *J Taiwan Inst Chem Eng*. 2016;59:18-25.
12. Mustafa M, Khan JA, Hayat T, Alsaedi A. Simulations for maxwell fluid flow past a convectively heated exponentially stretching sheet with nanoparticles. *AIP Adv*. 2015;5(3):037133.
13. Pires M, Sequeira A. Flows of generalized oldroyd-b fluids in curved pipes. *Parabolic Problems*. Springer; 2011:21-43.
14. Nadeem S, Ul haq R, Akbar NS, Lee C, Khan ZH. Numerical study of boundary layer flow and heat transfer of oldroyd-b nanofluid towards a stretching sheet. *PLOS One*. 2013;8(8):e69811.
15. Shehzad SA, Abdullah Z, Abbasi FM, Hayat T, Alsaedi A. Magnetic field effect in three-dimensional flow of an oldroyd-b nanofluid over a radiative surface. *J Magn Magn Mater*. 2016;399:97-108.
16. Hayat T, Muhammad T, Shehzad SA, Alsaedi A. An analytical solution for magnetohydrodynamic oldroyd-b nanofluid flow induced by a stretching sheet with heat generation/absorption. *Int J Therm Sci*. 2017;111:274-288.
17. Abbas M, Bai Y, Rashidi M, Bhatti M. Analysis of entropy generation in the flow of peristaltic nanofluids in channels with compliant walls. *Entropy*. 2016;18(3):90.
18. Rashidi M, Mohammadi F, Abbasbandy S, Alhuthali M. Entropy generation analysis for stagnation point flow in a porous medium over a permeable stretching surface. *J Appl Fluid Mech*. 2015;8(4):753-765.
19. Bejan A. Entropy generation minimization: The new thermodynamics of finite-size devices and finite-time processes. *J Appl Phys*. 1996;79(3):1191-1218.
20. Oztop HF, Al-Salem K. A review on entropy generation in natural and mixed convection heat transfer for energy systems. *Renewable Sustainable Energy Rev*. 2012;16(1):911-920.
21. Dalir N. Numerical study of entropy generation for forced convection flow and heat transfer of a Jeffrey fluid over a stretching sheet. *Alexandria Eng J*. 2014;53(4):769-778.
22. Rehman S, Haq R, Khan ZH, Lee C. Entropy generation analysis for non-newtonian nanofluid with zero normal flux of nanoparticles at the stretching surface. *J Taiwan Inst Chem Eng*. 2016;63:226-235.
23. Dalir N, Dehsara M, Nourazar SS. Entropy analysis for magnetohydrodynamic flow and heat transfer of a jeffrey nanofluid over a stretching sheet. *Energy*. 2015;79:351-362.
24. Shateyi S, Motsa S, Makukula Z. On spectral relaxation method for entropy generation on a mhd flow and heat transfer of a maxwell fluid. *J Appl Fluid Mech*. 2015;8(1):21-31.
25. Rashidi MM, Abelman S, Freidooni mehr N. Entropy generation in steady mhd flow due to a rotating porous disk in a nanofluid. *Int J Heat Mass Transfer*. 2013;62:515-525.
26. Motsa SS, Dlamini PG, Khumalo M. Spectral relaxation method and spectral quasilinearization method for solving unsteady boundary layer flow problems. *Adv Math Phys*. 2014;2014:1-12.
27. Motsa SS. A new spectral local linearization method for nonlinear boundary layer flow problems. *J Appl Math*. 2013;2013:1-15.
28. Woods LC. *The Thermodynamics of Fluid Systems*. Oxford University Press, New York: Oxford, Clarendon Press; 1975; 371p. http://adsabs.harvard.edu/abs/1975cp...book.....W
29. Yamaguchi H. *Engineering fluid mechanics*. 85. Springer Science & Business Media; 2008. https://doi.org/10.1007/978-1-4020-6742-6
30. Bejan A. Entropy generation minimization. *Adv Eng Thermodyn*. 2016:531-600. https://doi.org/10.1002/9781119245964.ch11
31. Awad FG, Ahamed SMS, Sibanda P, Khumalo M. The effect of thermophoresis on unsteady oldroyd-b nanofluid flow over stretching surface. *PLOS One*. 2015;10(8):e0135914.

How to cite this article: Almakki M, Nandy SK, Mondal S, Sibanda P, Sibanda D. A model for entropy generation in stagnation-point flow of non-Newtonian Jeffrey, Maxwell, and Oldroyd-B nanofluids. *Heat Transfer—Asian Res*. 2019;48:24-41. https://doi.org/10.1002/htj.21366

Chapter 7

Conclusion

In this thesis we sought to investigate entropy generation, and heat and mass transfer in Newtonian and non-Newtonian fluids in various geometrical settings and subject to different boundary conditions. The resultant systems of equations that model the fluid flows of interest are highly nonlinear, coupled, differential equations. Recent, spectral schemes were proposed for use in solving such complex systems of equations. The impact of key physical and chemical parameters of the fluid flows were analysed.

In Chapter 2, we investigated entropy generation and the combined effect of Soret and Dufour numbers in axisymmetric unsteady MHD nanofluid flow over a nonlinearly stretching sheet. The heat flux at the boundary layer was assumed to be controlled. The velocity of the surface stretch was assumed to be nonlinear in the radial direction. The magnetic field and chemical reaction were each considered to be functions of both space and time. Brownian motion and thermophoresis were considered to be significant. The spectral quasilinearization method was chosen as the solution method for the system. It was found that the Hartmann number is proportionally related to the skin friction, whereas the Sherwood and the Nusselt number decrease as the Hartmann number increases. The Brinkman and the Reynolds numbers both have a positive effect on entropy generation. The results obtained conform with those results from similar previous studies published in the literature.

In Chapter 3 we investigated heat and mass transfer and entropy generation in an unsteady two-dimensional MHD flow of a magneto-micropolar fluid with boundary layer flow along a linear

porous sheet. The viscous dissipation, thermophoesis, nanoparticle Brownian motion, chemical reaction and thermal radiation were taken into account. The bivariate spectral quasilinearization method was used to solve the partial differential equations. It was found that the method converges rapidly and gives accurate results. An increase in the Brownian motion parameter increases the temperature profiles whereas the same increase in the Brownian motion parameter reduces the concentration profiles. The Nusselt number and skin-friction coefficient increase with increasing thermal radiation. Perhaps, the most significant finding emerging from this Chapter is that the irreversibility due to thermal diffusion is the most dominant source of entropy generation. Further, the surface contributes significantly to the irreversibility.

In Chapter 4,we studied entropy generation and the impact of the Bejan number on an MHD viscoelastic nanofluid flow with partial slip and homogeneous and heterogeneous reactions. The nonlinear thermal radiation, thermophoresis and Brownian motion were considered to be significant factors that may alter the flow structure and the heat transfer properties of the fluid. The partial differential equations were solved using the spectral quasilinearization method. It was found that the Bejan number is strongly affected by variations in the viscoelastic parameter and the dimensionless Brinkman groups. The entropy generation decreases with an increase in the viscoelastic and partial slip parameters, while the entropy generation increases when the Brinkman and Reynolds numbers increase.

In Chapter 5, we generalized a mathematical model to describe the flow of a steady incompressible MHD Casson nanofluid with a binary chemical reaction flowing over a stretching or shrinking sheet. The model was used to investigate heat transfer and entropy generation in the laminar boundary-layer stagnation point. The external magnetic field, nonlinear thermal radiation and viscous dissipation were considered to be significant factors. The system of ordinary differential equations was solved numerically using the spectral quasilinearization method. We observed that the velocity and temperature profiles decrease as the Casson parameter increases. The entropy generation increases in response to an increase in Reynolds number.

In Chapter 6, a mathematical model was formulated to describe the behaviour of Jeffrey, Maxwell

and Oldroyd-B nanofluids. The model was used to investigate heat and mass transfer and entropy generation near a stagnation point. The flow was subject to the magnetic field, the Brownian motion, the slip velocity and the thermophoresis. Three different solution techniques were used; namely, the spectral relaxation method, the spectral quasilinearization method and the spectral local linearization method. A comparison of the accuracy of the three spectral collocation methods was carried out through calculation and analysis of residual errors. We showed that the spectral relaxation method gives smaller residual errors. For this reason, the spectral relaxation method was used to solve the system of equations. In terms of the chemical and physical parameters, the slip parameter has a negative influence on the velocity, temperature and concentration profiles. The velocity profiles are proportionally related to the Deborah number whereas the opposite trend is observed for temperature and concentration profiles. Entropy generation decreases with the Deborah number related to retardation time whereas the opposite behaviour is noted with the Deborah number related to relaxation time. The entropy generation due to concentration diffusion is the most dominant source of entropy generation.

For future work, the credibility of the findings of this study, which are obtained merely through mathematical modelling techniques, may be subjected to experiments for validation. The complexity of the full model equations necessitates improving solution methods to obtain higher convergence rates, greater stability and accuracy and improved portability of algorithms.

References

[1] M. Goyal and R. Bhargava, "Boundary layer flow and heat transfer of Viscoelastic nanofluids past a stretching sheet with partial slip conditions," *Applied Nanoscience*, vol. 4, no. 6, pp. 761–767, 2014.

[2] N. Dalir, "Numerical study of entropy generation for forced convection flow and heat transfer of a Jeffrey fluid over a stretching sheet," *Alexandria Engineering Journal*, vol. 53, no. 4, pp. 769–778, 2014.

[3] N. Freidoonimehr and A. B. Rahimi, "Exact-solution of entropy generation for MHD nanofluid flow induced by a stretching/shrinking sheet with transpiration: Dual solution," *Advanced Powder Technology*, vol. 28, no. 2, pp. 671–685, 2017.

[4] A. Bejan, "Entropy generation minimization: The new thermodynamics of finite-size devices and finite-time processes," *Journal of Applied Physics*, vol. 79, no. 3, pp. 1191–1218, 1996.

[5] M. I. Afridi, M. Qasim, I. Khan, S. Shafie, and A. S. Alshomrani, "Entropy generation in magnetohydrodynamic mixed convection flow over an inclined stretching sheet," *Entropy*, vol. 19, no. 1, p. 10, 2016.

[6] R. Ellahi, S. Z. Alamri, A. Basit, and A. Majeed, "Effects of MHD and slip on heat transfer boundary layer flow over a moving plate based on specific entropy generation," *Journal of Taibah University for Science*, pp. 1–7, 2018.

[7] M. H. Yazdi, S. Abdullah, I. Hashim, and K. Sopian, "Entropy generation analysis of open parallel Microchannels embedded within a permeable continuous moving surface: application to magnetohydrodynamics (MHD)," *Entropy*, vol. 14, no. 1, pp. 1–23, 2011.

[8] M. H. Matin, "Entropy analysis of combined heat and mass transfer over a plate embedded

in a porous medium," *Journal of Mechanical Engineering and Automation*, vol. 5, no. 3A, pp. 26–32, 2015.

[9] A. S. Butta, S. Munawara, A. Ali, and A. Mehmood, "Entropy analysis of mixed convective magnetohydrodynamic flow of a Viscoelastic fluid over a stretching sheet," *Zeitschrift für Naturforschung A*, vol. 67, no. 8-9, pp. 451–459, 2012.

[10] M. H. Abolbashari, N. Freidoonimehr, F. Nazari, and M. M. Rashidi, "Analytical modeling of entropy generation for Casson nanofluid flow induced by a stretching surface," *Advanced Powder Technology*, vol. 26, no. 2, pp. 542–552, 2015.

[11] J. Qing, M. M. Bhatti, M. A. Abbas, M. M. Rashidi, and M. E.-S. Ali, "Entropy generation on MHD Casson nanofluid flow over a porous stretching/shrinking surface," *Entropy*, vol. 18, no. 4, p. 123, 2016.

[12] Y. A. Cengel and A. Ghajar, *Heat and mass transfer (a practical approach, SI version)*. McGraw-Hill Education,, McGraw-Hill Education, New York, 2011.

[13] C. A. Yunus and J. G. Afshin, *Heat and mass transfer: fundamentals and applications*. Tata McGraw-Hill, New Delhi, 2011.

[14] T. L. Bergman, F. P. Incropera, D. P. DeWitt, and A. S. Lavine, *Fundamentals of heat and mass transfer*. John Wiley & Sons, Hoboken, 2011.

[15] J. Buongiorno, "Convective transport in nanofluids," *Journal of Heat Transfer*, vol. 128, no. 3, pp. 240–250, 2006.

[16] S. Chol and J. Estman, "Enhancing thermal conductivity of fluids with nanoparticles," *ASME-Publications-Fed*, vol. 231, pp. 99–106, 1995.

[17] W. Yu and H. Xie, "A review on nanofluids: preparation, stability mechanisms, and applications," *Journal of Nanomaterials*, vol. 2012, p. 1, 2012.

[18] A. Ghadimi, R. Saidur, and H. Metselaar, "A review of nanofluid stability properties and characterization in stationary conditions," *International Journal of Heat and Mass Transfer*, vol. 54, no. 17-18, pp. 4051–4068, 2011.

[19] A. Kuznetsov and D. Nield, "Natural convective boundary-layer flow of a nanofluid past a vertical plate," *International Journal of Thermal Sciences*, vol. 49, no. 2, pp. 243–247, 2010.

[20] A. M. Rohni, S. Ahmad, and I. Pop, "Flow and heat transfer over an unsteady shrinking sheet with suction in nanofluids," *International Journal of Heat and Mass Transfer*, vol. 55, no. 7-8, pp. 1888–1895, 2012.

[21] B. Gireesha and N. Rudraswamy, "Chemical reaction on MHD flow and heat transfer of a nanofluid near the stagnation point over a permeable stretching surface with non-uniform heat source/sink," *International Journal of Engineering, Science and Technology*, vol. 6, no. 5, pp. 13–25, 2014.

[22] O. D. Makinde and A. Aziz, "Boundary layer flow of a nanofluid past a stretching sheet with a convective boundary condition," *International Journal of Thermal Sciences*, vol. 50, no. 7, pp. 1326–1332, 2011.

[23] N. S. Akbar, S. Nadeem, R. U. Haq, and Z. Khan, "Radiation effects on MHD stagnation point flow of nanofluid towards a stretching surface with convective boundary condition," *Chinese Journal of Aeronautics*, vol. 26, no. 6, pp. 1389–1397, 2013.

[24] M. Rahman and I. Eltayeb, "Radiative heat transfer in a hydromagnetic nanofluid past a nonlinear stretching surface with convective boundary condition," *Meccanica*, vol. 48, no. 3, pp. 601–615, 2013.

[25] S. Nadeem and R. U. Haq, "Effect of thermal radiation for megnetohydrodynamic boundary layer flow of a nanofluid past a stretching sheet with convective boundary conditions," *Journal of Computational and Theoretical Nanoscience*, vol. 11, no. 1, pp. 32–40, 2014.

[26] N. Sandeep, B. R. Kumar, and M. J. Kumar, "A comparative study of convective heat and mass transfer in non-Newtonian nanofluid flow past a permeable stretching sheet," *Journal of Molecular Liquids*, vol. 212, pp. 585–591, 2015.

[27] T. Hayat, Z. Abbas, and M. Sajid, "Series solution for the upper-convected Maxwell fluid over a porous stretching plate," *Physics Letters A*, vol. 358, no. 5-6, pp. 396–403, 2006.

[28] M. Ramzan, M. Bilal, J. D. Chung, and A. Mann, "On MHD radiative Jeffery nanofluid flow with convective heat and mass boundary conditions," *Neural Computing and Applications*, pp. 1–10, 2017.

[29] A. Noghrehabadi, R. Pourrajab, and M. Ghalambaz, "Flow and heat transfer of nanofluids over stretching sheet taking into account partial slip and thermal convective boundary conditions," *Heat and Mass Transfer*, vol. 49, no. 9, pp. 1357–1366, 2013.

[30] W. Ibrahim and B. Shankar, "MHD boundary layer flow and heat transfer of a nanofluid past a permeable stretching sheet with velocity, thermal and solutal slip boundary conditions," *Computers & Fluids*, vol. 75, pp. 1–10, 2013.

[31] A. Noghrehabadi and A. Behseresht, "Flow and heat transfer affected by variable properties of nanofluids in natural-convection over a vertical cone in porous media," *Computers & Fluids*, vol. 88, pp. 313–325, 2013.

[32] N. Amirsom, M. Uddin, and A. Ismail, "Three dimensional stagnation point flow of bio-nanofluid with variable transport properties," *Alexandria Engineering Journal*, vol. 55, no. 3, pp. 1983–1993, 2016.

[33] P. Sanghera, *Quantum Physics for Scientists and Technologists: Fundamental Principles and Applications for Biologists, Chemists, Computer Scientists, and Nanotechnologists*. John Wiley & Sons, New Jersey, 2011.

[34] F. Abbasi, S. Shehzad, T. Hayat, A. Alsaedi, and M. A. Obid, "Influence of heat and mass flux conditions in hydromagnetic flow of Jeffrey nanofluid," *AIP Advances*, vol. 5, no. 3, p. 037111, 2015.

[35] M. Sheikholeslami, D. D. Ganji, M. Y. Javed, and R. Ellahi, "Effect of thermal radiation on magnetohydrodynamics nanofluid flow and heat transfer by means of two phase model," *Journal of Magnetism and Magnetic Materials*, vol. 374, pp. 36–43, 2015.

[36] D. Pal, "Heat and mass transfer in stagnation-point flow towards a stretching surface in the presence of buoyancy force and thermal radiation," *Meccanica*, vol. 44, no. 2, pp. 145–158, 2009.

[37] H. F. Oztop and K. Al-Salem, "A review on entropy generation in natural and mixed convection heat transfer for energy systems," *Renewable and Sustainable Energy Reviews*, vol. 16, no. 1, pp. 911–920, 2012.

[38] M. M. Rashidi, M. M. Bhatti, M. A. Abbas, and M. E.-S. Ali, "Entropy generation on MHD blood flow of nanofluid due to peristaltic waves," *Entropy*, vol. 18, no. 4, p. 117, 2016.

[39] M. M. Bhatti, T. Abbas, M. M. Rashidi, and M. E.-S. Ali, "Numerical simulation of entropy generation with thermal radiation on MHD Carreau nanofluid towards a shrinking sheet," *Entropy*, vol. 18, no. 6, p. 200, 2016.

[40] M. Magherbi, H. Abbassi, N. Hidouri, and A. B. Brahim, "Second law analysis in convective heat and mass transfer," *Entropy*, vol. 8, no. 1, pp. 1–17, 2006.

[41] A. S. Butt and A. Ali, "Entropy effects in hydromagnetic free convection flow past a vertical plate embedded in a porous medium in the presence of thermal radiation," *The European Physical Journal Plus*, vol. 128, no. 5, p. 51, 2013.

[42] S. Baag, S. Mishra, G. Dash, and M. Acharya, "Entropy generation analysis for Viscoelastic MHD flow over a stretching sheet embedded in a porous medium," *Ain Shams Engineering Journal*, vol. 8, no. 4, pp. 623–632, 2017.

[43] M. Almakki, S. Dey, S. Mondal, and P. Sibanda, "On unsteady three-dimensional axisymmetric MHD nanofluid flow with entropy generation and thermo-diffusion effects on a nonlinear stretching sheet," *Entropy*, vol. 19, no. 7, p. 168, 2017.

[44] E. B. Gil, *Experimental Design and Verification of a Centralized Controller for Irrigation Canals*. Elsevier, London, 2018.

[45] S. Alharbi and I. Hassanien, "Unsteady mixed convection flow in the stagnation region of a heated vertical plate embedded in a variable porosity medium with thermal dispersion effects," in *Developments in Heat Transfer*, pp. 217–226, Edited by Dr. Marco Aurelio Dos Santos Bernardes, InTech, Shanghai, 2011.

[46] P. Patil, S. Roy, and I. Pop, "Unsteady mixed convection flow over a vertical stretching sheet in a parallel free stream with variable wall temperature," *International Journal of Heat and Mass Transfer*, vol. 53, no. 21-22, pp. 4741–4748, 2010.

[47] Y. Lok, N. Amin, and I. Pop, "Unsteady mixed convection flow of a micropolar fluid near the stagnation point on a vertical surface," *International Journal of Thermal Sciences*, vol. 45, no. 12, pp. 1149–1157, 2006.

[48] A. J. Chamkha and S. Ahmed, "Similarity solution for unsteady MHD flow near a stagnation point of a three-dimensional porous body with heat and mass transfer, heat generation/absorption and chemical reaction," *Journal of Applied Fluid Mechanics*, vol. 4, no. 2, pp. 87–94, 2011.

[49] R. Seshadri, N. Sreeshylan, and G. Nath, "Unsteady mixed convection flow in the stagnation region of a heated vertical plate due to impulsive motion," *International Journal of Heat and Mass Transfer*, vol. 45, no. 6, pp. 1345–1352, 2002.

[50] R. Ravindran, M. Ganapathirao, and I. Pop, "Effects of chemical reaction and heat generation/absorption on unsteady mixed convection MHD flow over a vertical cone with non-uniform slot mass transfer," *International Journal of Heat and Mass Transfer*, vol. 73, pp. 743–751, 2014.

[51] S. Liao, "Notes on the Homotopy analysis method: some definitions and theorems," *Communications in Nonlinear Science and Numerical Simulation*, vol. 14, no. 4, pp. 983–997, 2009.

[52] G. Adomian, *Solving frontier problems of physics: The decomposition method*. Kluwer, MA, Boston, 1994.

[53] G. Adomian and G. Adomian, "A global method for solution of complex systems," *Mathematical Modelling*, vol. 5, no. 4, pp. 251–263, 1984.

[54] S.-J. Liao, "On the analytic solution of magnetohydrodynamic flows of non-Newtonian fluids over a stretching sheet," *Journal of Fluid Mechanics*, vol. 488, pp. 189–212, 2003.

[55] M. Ayub, A. Rasheed, and T. Hayat, "Exact flow of a third grade fluid past a porous plate using Homotopy analysis method," *International Journal of Engineering Science*, vol. 41, no. 18, pp. 2091–2103, 2003.

[56] A. A. Afify, "Similarity solution in MHD: effects of thermal diffusion and diffusion thermo on free convective heat and mass transfer over a stretching surface considering suction or injection," *Communications in Nonlinear Science and Numerical Simulation*, vol. 14, no. 5, pp. 2202–2214, 2009.

[57] R. Sharma, R. Bhargava, and P. Bhargava, "A numerical solution of unsteady MHD convection heat and mass transfer past a semi-infinite vertical porous moving plate using element free Galerkin method," *Computational Materials Science*, vol. 48, no. 3, pp. 537–543, 2010.

[58] J. Argyris and M. Haase, "An engineer's guide to soliton phenomena: Application of the Finite element method," *Computer Methods in Applied Mechanics and Engineering*, vol. 61, no. 1, pp. 71–122, 1987.

[59] T. Cebeci and P. Bradshaw, "Finite-difference solution of boundary-layer equations," in *Physical and Computational Aspects of Convective Heat Transfer*, pp. 385–428, Springer, 1984.

[60] A. Asaithambi, "A second-order Finite-difference method for the Falkner–Skan equation," *Applied Mathematics and Computation*, vol. 156, no. 3, pp. 779–786, 2004.

[61] S. S. Motsa, "A new spectral local linearization method for nonlinear boundary layer flow problems," *Journal of Applied Mathematics*, vol. 2013, Article ID 423628, 2013.

[62] S. S. Motsa, P. G. Dlamini, and M. Khumalo, "Spectral relaxation method and spectral quasilinearization method for solving unsteady boundary layer flow problems," *Advances in Mathematical Physics*, vol. 2014, Article ID 341964, 2014.

[63] S. Motsa, T. Hayat, and O. Aldossary, "MHD flow of upper-convected Maxwell fluid over porous stretching sheet using successive Taylor series linearization method," *Applied Mathematics and Mechanics*, vol. 33, no. 8, pp. 975–990, 2012.

[64] S. Motsa, V. Magagula, and P. Sibanda, "A bivariate Chebyshev spectral collocation quasilinearization method for nonlinear evolution parabolic equations," *The Scientific World Journal*, vol. 2014, Article ID 581987, 2014.

[65] S. Motsa and S. Shateyi, "Successive linearisation analysis of unsteady heat and mass transfer from a stretching surface embedded in a porous medium with suction/injection and thermal radiation effects," *The Canadian Journal of Chemical Engineering*, vol. 90, no. 5, pp. 1323–1335, 2012.

[66] S. Shateyi and S. Motsa, "Variable viscosity on magnetohydrodynamic fluid flow and heat transfer over an unsteady stretching surface with hall effect," *Boundary Value Problems*, vol. 2010, no. 1, p. 257568, 2010.

[67] S. Motsa, "A new spectral relaxation method for similarity variable nonlinear boundary layer flow systems," *Chemical Engineering Communications*, vol. 201, no. 2, pp. 241–256, 2014.

[68] S. S. Motsa and P. Sibanda, "A multistage linearisation approach to a four-dimensional hyperchaotic system with cubic nonlinearity," *Nonlinear Dynamics*, vol. 70, no. 1, pp. 651–657, 2012.

[69] S. Motsa, P. Dlamini, and M. Khumalo, "A new multistage spectral relaxation method for solving chaotic initial value systems," *Nonlinear Dynamics*, vol. 72, no. 1-2, pp. 265–283, 2013.

[70] C. Canuto, M. Y. Hussaini, A. Quarteroni, A. Thomas Jr, *et al.*, *Spectral methods in fluid dynamics*. Springer Science & Business Media, Virginia, 2012.

[71] J. P. Boyd, *Chebyshev and Fourier spectral methods*. Courier Corporation, New York, 2001.

[72] L. N. Trefethen, *Spectral methods in MATLAB*, vol. 10. Siam, 2000.

[73] R. E. Bellman and R. E. Kalaba, *Quasilinearization and nonlinear boundary-value problems*. Rand Corporation, New York, 1965.

[74] S. S. Motsa and S. Shateyi, "The effects of chemical reaction, hall, and ion-slip currents on MHD Micropolar fluid flow with thermal diffusivity using a novel numerical technique," *Journal of Applied Mathematics*, vol. 2012, Article ID 689015, 2012.

[75] J. S. Hesthaven, S. Gottlieb, and D. Gottlieb, *Spectral methods for time-dependent problems*, vol. 21. Cambridge University Press, Rhode Island, 2007.

[76] S. S. Motsa and M. S. Ansari, "Unsteady boundary layer flow and heat transfer of Oldroyd-B nanofluid towards a stretching sheet with variable thermal conductivity," *Thermal Science*, vol. 19, no. suppl. 1, pp. 239–248, 2015.

[77] G. Makanda, S. Shaw, and P. Sibanda, "Effects of radiation on MHD free convection of a Casson fluid from a horizontal circular cylinder with partial slip in non-Darcy porous medium with viscous dissipation," *Boundary Value Problems*, vol. 2015, no. 1, p. 75, 2015.